

A Thesis Submitted for the Degree of PhD at the University of Warwick

Permanent WRAP URL:

<http://wrap.warwick.ac.uk/126885>

Copyright and reuse:

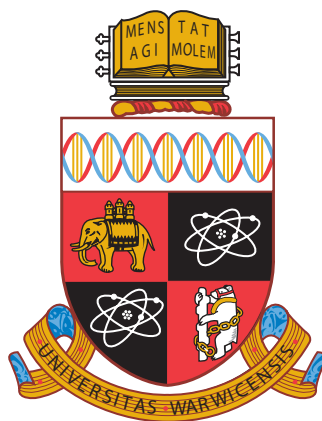
This thesis is made available online and is protected by original copyright.

Please scroll down to view the document itself.

Please refer to the repository record for this item for information to help you to cite it.

Our policy information is available from the repository home page.

For more information, please contact the WRAP Team at: wrap@warwick.ac.uk



**The Development of Solid-State NMR Methodology
to Study the Dynamics of Proteins and Ice**

by

Rebecca A. Stevens

Thesis

Submitted to the University of Warwick

for the degree of

Doctor of Philosophy

Department of Chemistry

September 2018



Contents

| | |
|---|-------------|
| Acknowledgments | vi |
| Declarations | vii |
| Abstract | viii |
| List of Tables | ix |
| List of Figures | x |
| List of Abbreviations | xiv |
| List of Symbols | xvi |
| Chapter 1 Introduction | 1 |
| Chapter 2 Theory | 6 |
| 2.1 Solid-State NMR Fundamentals | 6 |
| 2.1.1 Nuclear Spins | 6 |
| 2.1.2 NMR Interactions | 8 |
| 2.1.3 Magic Angle Spinning | 11 |
| 2.2 Pulsed Fourier Transform NMR | 12 |
| 2.2.1 The Basic SSNMR Experiment | 12 |
| 2.2.2 The Rotating Frame | 14 |
| 2.2.3 Cross Polarisation | 14 |
| 2.2.4 Proton Detection | 17 |
| 2.2.5 Heteronuclear Decoupling | 17 |
| 2.2.6 Solvent Suppression | 17 |
| 2.2.7 Isotopic Labelling | 18 |
| 2.2.8 Basics of 2D NMR Experiments | 21 |
| 2.3 Relaxation Theory | 23 |
| 2.3.1 The Origins of Relaxation | 23 |
| 2.3.2 The Correlation Time, Correlation Function and Spectral Density Function | 24 |
| 2.3.3 Transition Probabilities | 26 |

| | | |
|--------|---|----|
| 2.3.4 | Spin-Lattice Relaxation (R_1) | 30 |
| 2.3.5 | Spin-Spin Relaxation (R_2) | 32 |
| 2.3.6 | Spin-Lattice Relaxation in the Rotating Frame ($R_{1\rho}$) | 32 |
| 2.3.7 | The Model Free Approach | 33 |
| 2.3.8 | Relaxation Experiments | 34 |
| 2.3.9 | Relaxation Dispersion Measurements | 39 |
| 2.3.10 | Temperature and Relaxation | 39 |
| 2.3.11 | The Nuclear Overhauser Effect | 42 |
| 2.3.12 | Chemical Exchange | 42 |
| 2.3.13 | Spin Diffusion | 43 |
| 2.3.14 | Chemical Exchange Saturation Transfer | 45 |
| 2.3.15 | Cross-Correlated Relaxation | 47 |
| 2.4 | Solid-State NMR Applied to Biological Samples | 47 |
| 2.4.1 | Protein GB1 | 48 |

Chapter 3 Development of Tools to Aid the Packing of Proteins into Solid-State NMR Rotors

| | | |
|-------|--|-----------|
| | Solid-State NMR Rotors | 50 |
| 3.1 | Abstract | 50 |
| 3.2 | Introduction | 50 |
| 3.3 | Literature Review | 53 |
| 3.4 | Design and Development of the Packing Tools | 56 |
| 3.4.1 | Initial Packing Tools for 1.3 mm Rotors | 56 |
| 3.4.2 | First Development: Creating a Fixed Rotor to Swinging Bucket Adaptor | 61 |
| 3.4.3 | Initial Tests for 1.3 mm Packing Tools | 61 |
| 3.4.4 | Second Development: Creating Rotor Sleeves for 0.7 and 0.8 mm SSNMR Rotors | 62 |
| 3.4.5 | Third Development: Adapting the Rotor Sleeves and Funnel for 0.7 and 0.8 mm SSNMR Rotors to Avoid Leaks | 64 |
| 3.4.6 | The Final Design of the Ultracentrifuge Tools | 64 |
| 3.5 | Using the Tools to Pack Samples | 68 |
| 3.5.1 | Packing a Microcrystalline Protein Sample for NMR | 68 |
| 3.5.2 | Sedimentation and Packing of a Protein Sample | 68 |
| 3.6 | Experimental Considerations for Sedimentation | 71 |
| 3.6.1 | The Concentration and Molecular Weight Requirements for Suc- cessful Protein Sedimentation | 71 |
| 3.6.2 | Calculating the Time Required to Sediment a Protein Sample Us- ing the MLS-50 and MLA-150 Packing Tools | 74 |
| 3.7 | Conclusions and Outlook | 74 |
| 3.8 | Experimental Details | 77 |
| 3.8.1 | Information on the Ultracentrifuge | 77 |
| 3.8.2 | Dimensions and Materials of Tools | 77 |

| | | |
|--|--|-----|
| 3.8.3 | Testing of the Tools | 77 |
| 3.8.4 | Protein Samples | 79 |
| 3.8.5 | NMR Experiment(s) | 79 |
| Chapter 4 ^1H-Detected NMR Measurements of Aliphatic ^{13}C R_1 in Fully-Protonated Proteins in the Solid State 81 | | |
| 4.1 | Abstract | 81 |
| 4.2 | Introduction | 82 |
| 4.3 | Literature Review | 82 |
| 4.3.1 | Spin Diffusion | 82 |
| 4.4 | Results | 86 |
| 4.4.1 | Spin Diffusion Control Spectra at 60 and 100 kHz MAS | 88 |
| 4.4.2 | Spin Diffusion Saturation Transfer at 100 kHz MAS | 91 |
| 4.4.3 | Experimental ^{13}C R_1 Measurements at Variable MAS | 92 |
| 4.4.4 | Cross-Correlated Relaxation | 100 |
| 4.5 | Conclusions and Outlook | 100 |
| 4.6 | Experimental Details | 103 |
| 4.6.1 | Protein Samples | 103 |
| 4.6.2 | SSNMR Experimental Details | 103 |
| 4.6.3 | Determination of Relaxation Rates | 108 |
| Chapter 5 Variable-Temperature, Solid-State NMR Measurements to Investigate the Site-Specific Relaxation and Energy Landscape of GB1109 | | |
| 5.1 | Abstract | 109 |
| 5.2 | Introduction | 110 |
| 5.3 | Results | 112 |
| 5.3.1 | Variable Temperature R_1 and $R_{1\rho}$ Measurements | 112 |
| 5.3.2 | Use of the Extended Model Free Approach to Determine Order Parameters, Correlation Times and Activation Energies | 117 |
| 5.4 | Conclusions and Outlook | 124 |
| 5.5 | Experimental Details | 129 |
| 5.5.1 | Protein Samples | 129 |
| 5.5.2 | Assignment | 129 |
| 5.5.3 | SSNMR Experimental Details | 129 |
| 5.5.4 | Determination of Relaxation Rates | 131 |
| 5.5.5 | EMF-Arrhenius Analysis of the ^{13}C and ^{15}N R_1 and $R_{1\rho}$ | 131 |
| 5.5.6 | Monte Carlo Error Analysis | 132 |
| Chapter 6 Investigating the Effects of “Antifreeze” Molecules on Ice Growth Using Solid-State NMR 133 | | |
| 6.1 | Abstract | 133 |
| 6.2 | Introduction | 133 |

| | | |
|--|---|------------|
| 6.3 | Terminology | 134 |
| 6.4 | Literature Review | 137 |
| 6.4.1 | Binding Sites of AF(G)Ps | 139 |
| 6.4.2 | Is AF(G)P-Ice Binding Reversible? | 142 |
| 6.4.3 | Proposed Mechanisms for the Antifreeze Effect(s) of AF(G)Ps on Ice | 143 |
| 6.4.4 | Research into Antifreeze Proteins and Ice by Solid-State NMR | 146 |
| 6.4.5 | AFGP8, North Atlantic Pout AFP and Barfin Plaice AFP | 147 |
| 6.4.6 | Synthetic Antifreezes | 148 |
| 6.4.7 | Negative Controls | 152 |
| 6.4.8 | Applications of AFPs, AFGPs and Synthetic Antifreezes | 153 |
| 6.5 | Results | 154 |
| 6.5.1 | Variable Temperature ^1H R_1 of Ice in the Presence of Antifreezes | 155 |
| 6.5.2 | Variable Temperature ^1H R_2 of Ice in the Presence of Antifreezes | 158 |
| 6.5.3 | Variable Temperature ^1H Relaxation Dispersion of Ice in the Presence of Antifreezes | 163 |
| 6.5.4 | 2D ^1H - ^1H EXSY Spectra | 166 |
| 6.5.5 | Discussion | 168 |
| 6.6 | Conclusions and Outlook | 170 |
| 6.7 | Experimental Details | 172 |
| 6.7.1 | Antifreeze Samples | 172 |
| 6.7.2 | Temperature Calibration | 172 |
| 6.7.3 | NMR Experimental Details | 173 |
| Chapter 7 Summary and Outlook | | 177 |
| Appendices | | 181 |
| Appendix A Theory | | 182 |
| A.1 | Assignments of Protein GB1 | 182 |
| A.2 | Calculating the Effect of Spin Diffusion on PDSO | 184 |
| Appendix B Development of Tools to Aid the Packing of Proteins into Solid-State NMR Rotors | | 185 |
| B.1 | Detailed Protocol for the Ultracentrifuge Packing Tools | 185 |
| B.1.1 | Sedimenting Samples: | 185 |
| B.1.2 | Packing a Crystalline Sample into a Rotor: | 189 |
| B.2 | Sedimentation Calculations | 191 |
| Appendix C ^1H-Detected NMR Measurements of Aliphatic ^{13}C R_1 in Fully-Protonated Proteins in the Solid State | | 193 |

| | | |
|-------------------|--|------------|
| Appendix D | Variable-Temperature, Solid-State NMR Measurements to Investigate the Site-Specific Relaxation and Energy Landscape of GB1199 | |
| D.1 | $^{13}\text{C}'$ and ^{15}N R_1 and $R_{1\rho}$ Plotted Against the Inverse Absolute Temperature | 199 |
| D.2 | Calculation of the Correlation Times, Order Parameters and Activation Energies from $^{13}\text{C}'$ and ^{15}N R_1 and $R_{1\rho}$ | 205 |
| Appendix E | Investigating the Effects of “Antifreeze” Compounds on Ice Growth Using Solid-State NMR | 209 |
| E.1 | 1D ^1H Spectra of the Antifreeze Solutions as Solids and Liquids | 209 |

Acknowledgments

First and foremost, I would like to thank my supervisor, Dr. Józef Lewandowski, not only for his invaluable guidance and unrelenting enthusiasm, but also for providing me with many opportunities to travel, both across the UK and internationally, in order to present my work and attend workshops. I am also extremely grateful for the countless hours he has spent teaching me over the last 4 years.

I would also like to thank all of those who have helped me with SSNMR measurements and analysis, or produced protein samples, in particular Dr. Jonathan Lamley, Dr. Carl Öster, Dr. Trent Franks, Dr. Angelo Gallo, Dr. Simone Kosol and Sarah Mann. Additionally, I would like to express my gratitude towards Dr. Andy Howes and Dr. Gregory Rees for their technical assistance. Huge thanks go to Alice Fayter for all her work in the antifreeze project, whom it was truly a pleasure to collaborate with, and I would like to thank Christopher Stubbs and Dr. Muhammad Hasan for providing the PVA samples and antifreeze proteins. Financial support from the EPSRC is also gratefully acknowledged.

On a personal note, I am extremely grateful to past and present members of the Warwick Solid-State NMR group for the many friendships over the years that have made this PhD the experience it was. I've thoroughly enjoyed the climbing, board games and excessive amounts of cake! I will miss you all. Additionally, I will always be grateful for the fantastic teachers I have had throughout school, sixth form and university for sparking my interest in the sciences and truly inspiring me, I wouldn't be where I am today without them.

Special thanks go to my family for supporting me in everything I do, despite not always understanding what I do or why I do it. Finally, I am indebted to Seb for his superior grasp of the English language, attention to detail and his best attempts to keep me sane.

Declarations

The work in this thesis is original, and was conducted by the author, unless otherwise stated, under the supervision of Dr Józef R. Lewandowski (Department of Chemistry). The work has not been submitted for a degree or diploma or other qualification at any other University. Funding was provided by an EPSRC studentship. All sources of information have been acknowledged by means of reference throughout the text.

All collaborative results are indicated in the text, a brief summary is given here:

The initial designs for the 1.3 mm rotor packing tools presented in **Chapter 3** were developed by Dr W. Trent Franks and Georgina Charlton, supervised by Dr Józef Lewandowski. Later developments stemmed from discussions with Dr W. Trent Franks and Koorosh Fatemian. All versions of the tools were manufactured by Lee Butcher and Marcus Grant in the Department of Chemistry’s mechanical workshop (University of Warwick).

The SDST measurements presented in **Chapter 4** were performed by Dr. Angelo Gallo and the 60 kHz MAS PDSD spectra were recorded with guidance from Dr. Jonathan Lamley (both supervised by Dr. Józef R. Lewandowski).

All of the work presented in **Chapter 6** is in collaboration with Alice Fayter, supervised by Professor Matthew I. Gibson (Department of Chemistry, University of Warwick). The PVA samples were synthesised by Christopher Stubbs and the AFPs by Alice Fayter and Dr Muhammad Hasan (also supervised by Professor Gibson).

Abstract

Solid-state nuclear magnetic resonance (SSNMR) is an excellent tool for determining the molecular motions within a dynamic system. SSNMR relaxation measurements can access a vast range of timescales (ps - ms) and are able to simultaneously determine the frequency and amplitude of the motion that a particular nucleus is undergoing.

Recent developments in SSNMR instrumentation now allow for >100 kHz magic angle spinning (MAS) using 0.7 and 0.8 mm rotors. State-of-the-art MAS is especially beneficial for those wishing to investigate proteins in the solid state: only sub-milligram amounts of sample are required and the fast spinning yields incredible spectral resolution. This also enables proton detection and the associated improvements in sensitivity (for protonated samples). Unfortunately, these small rotors are extremely challenging to pack with the semi-solid protein samples. Furthermore, the proteins can become dehydrated in the slow packing process, making them unsuitable for NMR. To address this point, in Chapter 3, we present the design and application of an ultracentrifuge tool for the packing of proteins into 0.7 - 1.3 mm diameter SSNMR rotors. The tool helps to reduce the waste of expensive isotopically labelled proteins and decreases the packing time from several hours to minutes.

The work in Chapter 4 takes advantage of the mentioned fast MAS developments and demonstrates the accurate measurement of site-specific, spin-lattice relaxation rates (R_1) on $^{13}\text{C}^\alpha$ nuclei in a fully protonated, uniformly ^{13}C -labelled protein at 100 kHz MAS. Our approach overcomes the averaging effect of proton-driven spin diffusion that obscures site-specific information for the relaxation rates measured at slower spinning frequencies.

One area where measurements of relaxation in the solid state can yield significant insights is the understanding of the complex energy landscape describing conformational changes of proteins, which are often closely linked to their functions. In Chapter 5 we present some of the first extensive site-specific variable temperature measurements of ^{13}C and ^{15}N R_1 and spin-lattice relaxation rates in the rotating frame ($R_{1\rho}$) in a crystalline protein as a way to explore its conformational energy landscape. We observe $R_{1\rho}$ more than doubling over a narrow range of temperatures and minimal variation in R_1 over the same range. We model the relaxation data using an extended model free approach and Arrhenius relationship to extract activation energies for the motions dominating the dynamics, however find that further measurements are required for an accurate determination of the activation energies.

In Chapter 6 we show that relaxation measurements in the solid state are not only useful for characterising protein motions. In this chapter, we employ variable temperature measurements, including relaxation measurements, to investigate the effects of non-colligative antifreezes on ice dynamics. Antifreeze (glyco)proteins facilitate the survival of a diverse range of organisms at low temperatures by altering the freezing point, structure and growth of ice by modifying the dynamics of water molecules. These proteins and their synthetic mimics have many vital applications throughout science and engineering, but their mechanism of action is still not completely understood. In this PhD project, a combination of variable temperature relaxation measurements and 2D exchange spectra revealed that the antifreeze glycoproteins, type I antifreeze proteins, safranin and polyvinyl alcohols were exploiting a similar antifreeze mechanism involving reversible binding to ice, whereas the type III antifreeze protein was irreversibly binding to ice.

List of Tables

| | | |
|-----|---|-----|
| 2.1 | Common nuclei for NMR. | 7 |
| 2.2 | GB1 sequence. | 49 |
| 3.1 | Details on packing tools in the literature. | 55 |
| 3.2 | Ultracentrifuge conditions for using the tools. | 68 |
| 3.3 | Example minimum concentrations required for sedimentaion of various proteins. | 73 |
| 3.4 | Example sedimentation coefficients and times. | 75 |
| 3.5 | Maximum ultracentrifuge speeds and forces. | 77 |
| 3.6 | Testing conditions for the MLA-150 packing tool. | 79 |
| 3.7 | Testing conditions for the MLS-50 packing tool. | 80 |
| 4.1 | Conditions for VMAS measurements on (U- ¹ H, ¹³ C, ¹⁵ N)GB1. | 106 |
| 4.2 | Conditions for VMAS measurements on (2- ¹³ C(glucose), U- ¹ H, ¹⁵ N)GB1. . | 107 |
| 5.1 | Bond lengths | 120 |
| 5.2 | Sample temperatures | 131 |
| 6.1 | Colligative antifreezes. | 134 |
| 6.2 | AFPs and the ice planes they bind to. | 139 |
| 6.3 | PVA MWs and PDIs | 172 |
| A.1 | The ¹ H, ¹³ C and ¹⁵ N assignments for crystalline GB1. | 183 |
| B.1 | Parameters required for calculating whether sedimentation would be ef- fective. | 192 |
| B.2 | Parameters required for calculating sedimentation time. | 192 |

List of Figures

| | | |
|------|--|----|
| 1.1 | Timescales of dynamic processes and NMR techniques. | 2 |
| 1.2 | Magic Angle Spinning | 3 |
| 2.1 | CSA | 10 |
| 2.2 | Magic Angle Spinning | 12 |
| 2.3 | ‘One-pulse’ NMR experiment. | 13 |
| 2.4 | Fourier transform of an FID. | 13 |
| 2.5 | The laboratory and rotating frames. | 14 |
| 2.6 | Example of a cross polarisation pulse sequence. | 16 |
| 2.7 | The [1,3- ^{13}C]glycerol and [2- ^{13}C]glycerol labelling schemes. | 19 |
| 2.8 | The [2- ^{13}C]glucose labelling scheme. | 20 |
| 2.9 | A 1D and a 2D spectrum of protein GB1. | 22 |
| 2.10 | Example of a 2D pulse sequence. | 22 |
| 2.11 | Relaxation processes. | 23 |
| 2.12 | Correlation function and spectral density function. | 25 |
| 2.13 | Transition probabilities in a two-spin system. | 27 |
| 2.14 | Example spectral densities at $\omega = 0$, ω_0 and $2\omega_0$ | 29 |
| 2.15 | R_1 | 31 |
| 2.16 | R_2 | 32 |
| 2.17 | $R_{1\rho}$ | 33 |
| 2.18 | Example R_1 pulse sequence using the Torchia method. | 36 |
| 2.19 | ^1H saturation recovery R_1 pulse sequence. | 37 |
| 2.21 | R_2 pulse sequence | 38 |
| 2.22 | Effect of the the spin-echoes in a ^1H R_2 CPMG pulse sequence. | 38 |
| 2.23 | $R_{1\rho}$ | 40 |
| 2.24 | Examples of $R_{1\rho}$ and RD plots. | 40 |
| 2.25 | Variation in R_1 and R_2 with correlation time. | 42 |
| 2.26 | SD simulations. | 46 |
| 2.27 | CEST | 46 |
| 2.28 | Protein GB1 | 48 |
| 3.1 | Different techniques for the preparation of protein samples for SSNMR. | 52 |
| 3.2 | SSNMR rotors. | 52 |

| | | |
|------|---|-----|
| 3.3 | Previous packing method for 0.7 and 0.8 mm rotors. | 52 |
| 3.4 | Old method for packing proteins into rotors. | 53 |
| 3.5 | Ultracentrifuge tools in the literature. | 55 |
| 3.6 | The fixed rotor and swinging bucket ultracentrifuge rotors. | 57 |
| 3.7 | Packing with different ultracentrifuge rotors. | 57 |
| 3.8 | Initial packing tools. | 59 |
| 3.9 | Diagram of initial tools. | 60 |
| 3.11 | Future improvement for the adaptor. | 61 |
| 3.10 | Dimensions and photos of the adaptor. | 62 |
| 3.12 | Illustrations of different rotor sleeves - initial design. | 63 |
| 3.13 | Reasons for the tool leaking. | 65 |
| 3.14 | Ideas for better adapting the tool for 0.7 and 0.8 mm rotors. | 65 |
| 3.15 | Illustrations of different rotor sleeves - final design. | 66 |
| 3.16 | Photograph and illustration of packing tools. | 67 |
| 3.17 | Illustration of steps for using the tool. | 69 |
| 3.18 | Comparison of spectra of protein packed using the packing tools and a spatula. | 70 |
| 3.19 | A diagram of the ultracentrifuge tool parameters. | 72 |
| 3.20 | Conditions for successful sedimentation using the packing tools. | 73 |
| 3.21 | Time required for complete sedimentation. | 75 |
| 3.22 | Technical drawing of the swinging bucket MLS-50 tool, fixed angle MLA-150 tool and the adaptor. | 78 |
| 4.1 | Dipolar interactions in a protein. | 84 |
| 4.2 | ^2H -labelling | 84 |
| 4.3 | Partial ^{13}C -labelling. | 85 |
| 4.4 | 2D ^{13}C - ^1H at 100 kHz MAS. | 87 |
| 4.5 | PDSD spectra at 60 kHz | 89 |
| 4.6 | RFSD spectra at 60 kHz | 90 |
| 4.7 | Control PDSD spectra at 100 kHz MAS. | 91 |
| 4.8 | Example SDST profiles. | 93 |
| 4.9 | $^{13}\text{C}^\alpha$ SDST profiles for residues 1 - 32. | 94 |
| 4.10 | $^{13}\text{C}^\alpha$ SDST profiles for residues 33 - 56. | 95 |
| 4.11 | The ^{13}C - ^{13}C chemical shift difference between the neighbouring $^{13}\text{C}^\alpha$ and sidechain nuclei. | 96 |
| 4.12 | Example ^{13}Ca VMAS plots. | 97 |
| 4.13 | VMAS $^{13}\text{C}^\alpha$ R_1 measured in fully-protonated, uniformly-labelled crystalline GB1. | 97 |
| 4.14 | ^{13}C R_1 measured in fully-protonated, uniformly-labelled crystalline GB1 . | 98 |
| 4.15 | VMAS $^{13}\text{C}^\alpha$ R_1 for uniformly and partially ^{13}C -labelled GB1. | 99 |
| 4.16 | $^{13}\text{C}^\alpha$ R_1 measured both with and without ^1H decoupling during the relaxation delay. | 101 |

| | | |
|------|--|-----|
| 4.17 | PDSD and RFSD pulse sequences. | 104 |
| 4.18 | A ^1H - ^{13}C - ^1H PDSD control pulse sequence. | 104 |
| 4.19 | ^{13}C SDST pulse sequence. | 105 |
| 4.20 | ^{13}C R_1 pulse sequence. | 107 |
| 5.1 | Example energy landscape and timescale of motions within a protein. . . | 111 |
| 5.2 | $^{13}\text{C}'$ and ^{15}N R_1 and $R_{1\rho}$ at 28.0°C. | 113 |
| 5.3 | VT $^{13}\text{C}'$ and ^{15}N R_1 | 115 |
| 5.4 | VT $^{13}\text{C}'$ and ^{15}N $R_{1\rho}$ | 116 |
| 5.5 | Correlation times, order parameters and activation energies from the EMF analysis. | 122 |
| 5.6 | Reproducing the $^{13}\text{C}'$ and ^{15}N R_1 and $R_{1\rho}$ rates at 34.85°C. | 125 |
| 5.7 | Reproducing relaxation rates that were not involved in the initial model. . | 126 |
| 5.8 | ^1H - ^{15}N assignments. | 130 |
| 5.9 | Pulse sequences used for $^{13}\text{C}'$ and ^{15}N R_1 and $R_{1\rho}$ | 130 |
| 6.1 | I_h structure and the conditions for other phases of ice. | 136 |
| 6.2 | Planes of ice. | 136 |
| 6.3 | Ostwald ripening. | 136 |
| 6.4 | Dynamic Ice Shaping | 137 |
| 6.5 | Quasi-liquid layer. | 138 |
| 6.6 | AFGP structure. | 138 |
| 6.7 | Examples of AFPs from a range of organisms. | 140 |
| 6.8 | Regularly ordered threonine groups on AFPs. | 140 |
| 6.9 | DIS | 142 |
| 6.10 | Examples of AFP I binding planes. | 143 |
| 6.12 | Adsorption-inhibition mechanism. | 144 |
| 6.13 | Adsorption-inhibition models for ice growth in the presence of AF(G)P. . | 145 |
| 6.14 | The anchored clathrate water mechanism. | 146 |
| 6.15 | AFPIII interaction with its hydration shell and ice. | 147 |
| 6.16 | Structure of AFGP8 and North Atlantic Pout AFP III. | 148 |
| 6.17 | Structure of PVA. | 149 |
| 6.18 | PVA binds to primary and secondary prism planes of ice. | 149 |
| 6.19 | Effect of PVA concentration and DP on the IRI activity of PVA. | 151 |
| 6.20 | Structure of safranin chloride, phenosafranin chloride and safranin nitrate. | 151 |
| 6.21 | Structure of PEG and lysozyme. | 153 |
| 6.22 | VT R_1 of ice in the presence of antifreezes and controls. | 156 |
| 6.23 | VT R_2 of ice in the presence of antifreezes and controls. | 160 |
| 6.24 | The contributions to R_2 | 161 |
| 6.25 | VT R_2 of ice in the presence of PVA at different concentrations. | 162 |
| 6.26 | VT RD of ice in the presence of proteins. | 164 |
| 6.27 | VT RD of ice in the presence of polymers. | 165 |

| | | |
|------|---|-----|
| 6.28 | VT RD of ice in the presence of dyes. | 165 |
| 6.29 | 2D ^1H - ^1H EXSY measurements | 167 |
| 6.30 | 2D ^1H - ^1H EXSY measurements on liquid samples. | 169 |
| 6.31 | Summary of SSNMR measurements on ice in the presence of various an- tifreezes. | 169 |
| 6.32 | Temperature calibration using methanol. | 173 |
| 6.33 | The pulse sequence for measurement of ^1H R_1 | 174 |
| 6.34 | The pulse sequence for measurement of ^1H R_2 | 175 |
| 6.35 | The pulse sequence for measurement of ^1H $R_{1\rho}$ | 175 |
| 6.36 | The pulse sequence for measurement of 2D ^1H EXSY spectra. | 176 |
| | | |
| C.1 | All VMAS spectra. | 194 |
| C.2 | VMAS $^{13}\text{C}^\alpha$ R_1 | 195 |
| C.3 | VMAS $^{13}\text{C}^\alpha$ R_1 continued. | 196 |
| C.4 | Sidechain VMAS ^{13}C R_1 | 197 |
| | | |
| D.1 | VT $^{13}\text{C}'$ R_1 | 200 |
| D.2 | VT $^{13}\text{C}'$ $R_{1\rho}$ | 201 |
| D.3 | VT ^{15}N R_1 | 202 |
| D.4 | VT ^{15}N $R_{1\rho}$ | 203 |
| D.5 | VT ^{13}C R_1 sidechains | 203 |
| D.6 | VT ^{13}C $R_{1\rho}$ sidechains | 204 |
| D.7 | VT ^{15}N R_1 sidechains | 204 |
| D.8 | VT ^{15}N $R_{1\rho}$ sidechains | 205 |
| | | |
| E.1 | 1D ^1H spectra of 1 mg/ml DP150 PVA solution freezing. | 210 |
| E.2 | 1D ^1H spectra of AFGP | 210 |
| E.3 | 1D ^1H spectra of Lysozyme | 211 |
| E.4 | 1D ^1H spectra of PVA | 211 |
| E.5 | 1D ^1H spectra of PEG | 212 |
| E.6 | 1D ^1H spectra of Safranin | 212 |
| E.7 | 1D ^1H spectra of Phenoafranin | 213 |

List of Abbreviations

| | |
|----------------|---|
| AFGP(s) | Antifreeze Glycoprotein(s) |
| AFP(s) | Antifreeze Protein(s) |
| CD | Circular Dichroism |
| CEST | Chemical Exchange Saturation Transfer |
| CFRP | Carbon Fibre Reinforced Polymer |
| CP | Cross Polarisation |
| CPMG | Carr-Purcell-Meiboom-Gill |
| Cryo-EM | Cryogenic Electron Microscopy |
| CSA | Chemical Shift Anisotropy |
| DIS | Dynamic Ice Shaping |
| DSC | Differential Scanning Calorimetry |
| DSS | 4,4-Dimethyl-4-Silapentane-1-Sulphonic Acid |
| DP | Degree of Polymerisation |
| EMF | Extended Model Free |
| EPR | Electron Paramagnetic Resonance |
| EXSY | Exchange Spectroscopy |
| FA | Fixed Angle (Ultracentrifuge Rotor) |
| GB1 | Immunoglobulin Binding Domain B1 of Streptococcal Protein G |
| I _h | Hexagonal Ice |
| IBS | Ice-Binding Site |
| IR | Infrared spectroscopy |
| IRI | Ice Recrystallisation Inhibition |
| ISP | Ice-Structuring Protein |
| MAS | Magic Angle Spinning |
| MD | Molecular Dynamics |
| MF | Model Free |
| MLA-150 | Fixed Angle Ultracentrifuge Rotor (Speed \leq 150,000 rpm) |
| MLGS | Mean Largest Grain Size |
| MLS-50 | Swinging Bucket Ultracentrifuge Rotor (Speed \leq 50,000 rpm) |
| MPD | 2-Methyl-2,4-Pentanediol |

| | |
|----------------|--|
| MRI | Magnetic Resonance Imaging |
| MW | Molecular Weight |
| NMR | Nuclear Magnetic Resonance |
| NOE | Nuclear Overhauser Effect |
| PBS | Phosphate-Buffered Saline |
| PCTFE | Polychlorotrifluoroethylene |
| PDI | Polydispersity Index |
| PDSD | Proton Driven Spin Diffusion |
| PEEK | Polyether Ether Ketone |
| PEG | Polyethylene Glycol |
| Phenosafranin | Phenosafranin Chloride |
| POM | Polyoxymethylene |
| PVA | Polyvinyl Alcohol |
| PVP | Poly(<i>N</i> -Vinyl Pyrrolidone) |
| QLL | Quasi-Liquid Layer |
| RAFT | Reversible Addition-Fragmentation Chain Transfer |
| RD | Relaxation Dispersion |
| RF | Radio Frequency |
| RFSD | RF-Driven Spin Diffusion |
| Safranin | Safranin Chloride |
| SAXS | Small-Angle X-Ray Scattering |
| SB | Swinging Bucket (Ultracentrifuge Rotor) |
| SD | Spin Diffusion |
| SDST | Spin Diffusion Saturation Transfer |
| SMF | Simple Model Free |
| SNR | Signal-to-Noise Ratio |
| SSNMR | Solid-State Nuclear Magnetic Resonance |
| T _F | Freezing Point |
| TH | Thermal Hysteresis |
| T _M | Melting Point |
| TOCSY | Total Correlation Spectroscopy |
| TTMSS | Tris(trimethylsilyl)silane |
| VMAS | Variable Magic Angle Spinning |
| VT | Variable Temperature |
| VTU | Variable Temperature Unit |
| XRD | X-Ray Diffraction |

List of Symbols

| | |
|-------------|--|
| D | Dipolar Interaction |
| I | Spin Angular Momentum |
| R | Gas Constant |
| R_1 | Spin-Lattice Relaxation Rate |
| $R_{1\rho}$ | Spin-Lattice Relaxation Rate in the Rotating Frame |
| R_2 | Spin-Spin Relaxation Rate |
| S | Svedburg Unit (10^{-13} s) |
| S^2 | Order Parameter |
| T_1 | Spin-Lattice Relaxation Time |
| t_1 | Indirect Evolution Time |
| $T_{1\rho}$ | Spin-Lattice Relaxation Time in the Rotating Frame |
| T_2 | Spin-Spin Relaxation Time |
| t_2 | Direct Evolution Time |
| h | Planck Constant |
| \hbar | Reduced Planck Constant |
| γ | Gyromagnetic Ratio |
| μ | Magnetic Moment |
| μ_0 | Vacuum Permeability Constant |
| σ | Proton Driven Spin Diffusion Exchange Rate |
| τ_c | Correlation Time |

Chapter 1

Introduction

Over the last few decades significant developments in solid-state nuclear magnetic resonance (SSNMR) have moulded it into an extremely powerful technique for the determination of dynamics in a wide range of proteins, including challenging systems, such as amyloid fibrils¹⁻³ and large non-crystalline protein-protein complexes.⁴⁻⁶ Proteins are incredibly complex biomolecules that perform an impressive range of functions in living cells and are critical for life. One of the huge challenges facing biologists is the determination and understanding of protein functions. Vast amounts of research have focused on the relationship between protein function and structure. However, these biomolecules are not rigid, they are highly flexible and undergo continual fluctuations in their conformations, thus a stationary structure can only represent a weighted average of the possible conformations. It is a combination of the protein's structure and dynamics that ultimately determine its function. Furthermore, dynamics are crucial for various biological processes, such as ligand binding, enzymatic catalysis and protein folding.⁷⁻⁹

Research into the dynamics of proteins can be challenging due to the vast range of timescales upon which these may occur (see Figure 1.1).¹⁰ Over the years, nuclear magnetic resonance (NMR) has developed into an ideal technique for investigating protein dynamics at atomic-resolution on almost all functionally-relevant timescales. NMR has the ability to probe all (NMR-active) nuclei within a protein simultaneously, but can also selectively focus on specific regions. With suitable experimental set-up and resolution it is possible to individually monitor each nucleus within the protein, whereas most analytical techniques can either focus on only a few specific sites (e.g. fluorescence microscopy) or observe an average response from the entire protein (e.g. neutron diffraction). Historically, most proteins were investigated using solution-state NMR. Recent advances in SSNMR methodology and equipment, combined with the fact that many proteins are insoluble or too large to monitor in the solution state, have made the use of SSNMR extremely valuable. It has been questioned whether proteins prepared for SSNMR accurately represent the native environment, but there is increasing evidence suggesting that, as long as the protein is correctly hydrated, this is the case.¹¹⁻¹⁷

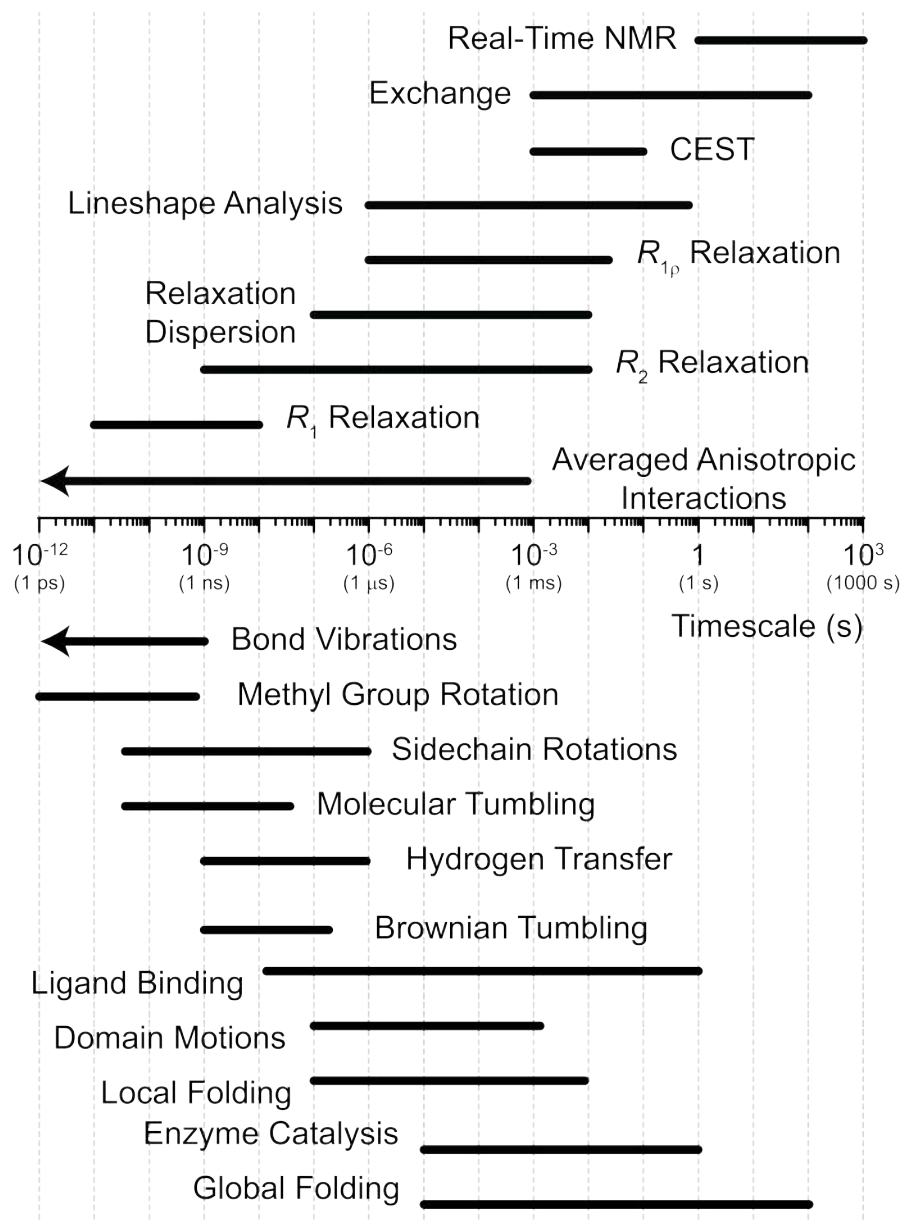


Figure 1.1: The timescales of particular NMR measurements and the dynamic processes commonly found within proteins.

The very first solid-state and solution-state NMR spectra were reported in 1946 by Purcell *et al.*¹⁸ and Block *et al.*,¹⁹ respectively. Ever since, solution-state measurements have dominated the field due to an inherent advantage of rapidly tumbling molecules, allowing various anisotropic interactions, which would otherwise cause extremely broad peaks, to be averaged out. Whereas solid samples have restricted motion and producing broad, often difficult to interpret, peaks in the spectra. Independently, Andrew *et al.*²⁰ and Lowe²¹ realised that this problem might be mitigated by macroscopic rotation of the solid in a way which mimics the tumbling of a solution. As described in Section 2.1.3 and Figure 1.2, fast rotation of the solid sample at a 54.7° angle with respect to the strong magnetic (B_0) field can sufficiently narrow the peaks. Faster spinning at this “magic angle” improves the averaging out of the anisotropic interactions and so narrows the linewidths. However, there are technical limits to achievable spinning speeds. Most modern rotors are made of zirconia and have decreased in diameter over the years as magic angle spinning (MAS) technology has advanced. The first rotor designed by Andrew *et al.* had an outer diameter of 8 mm and would spin at a maximum of 0.83 kHz. Now it is common to use 4 mm to 1.3 mm (external diameter) rotors that have maximum spinning speeds of 10 kHz to 70 kHz.²² Furthermore, state-of-the-art MAS uses 0.7 mm rotors that are capable of spinning at 110 kHz.

The rapid developments in MAS are especially beneficial for those wishing to investigate proteins in the solid state. Proteins are often costly and challenging to produce and so are typically available only in milligram amounts. Therefore these 0.7 mm rotors, which are filled by sub-milligram amounts of sample, are ideal, providing that sufficient sensitivity can be achieved. More importantly, the fast spinning aids obtaining excellent spectral resolution. For example it becomes possible to conduct proton-detected experiments on protein samples, which results in achieving significant gains in sensitivity that often compensates for the small sample size.^{23–25}

The spectra obtained at extremely fast MAS are impressive, but the smaller SSNMR rotors have made the packing of protein samples increasingly challenging. The sub-milligram amounts of protein are too sticky to be packed into a rotor using a spatula

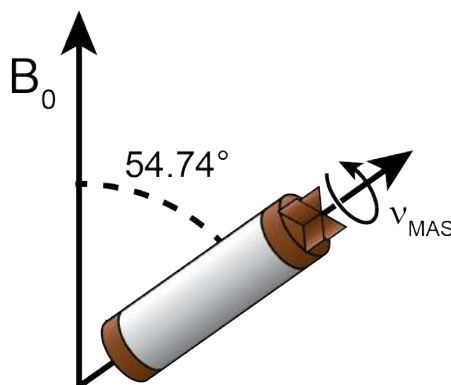


Figure 1.2: An SSNMR rotor spinning at the “magic angle” (54.74° from the B_0 field) at a frequency of ν_{MAS} .

or other standard tools, but also too viscous to be packed using a pipette. Most labs use home-made contraptions involving various pipette tips and a benchtop centrifuge to force their protein into the rotor, often a long-winded process. The longer the process takes, the higher the chance of the valuable protein sample becoming dehydrated, rendering it unsuitable for NMR. In response to this, in Chapter 3, I present the design and application of an ultracentrifuge tool for the packing of such samples into 0.7 - 1.3 mm diameter SSNMR rotors. The tool helps to reduce the waste of expensive isotopically labelled proteins and decreases the packing time from several hours to minutes.

There are further benefits to the development of such fast MAS. The work in Chapter 4 demonstrates the measurement of certain dynamics within a protein that would not be possible without 100 kHz MAS. The spin-lattice relaxation rate is particularly important for learning about fast, ps - ns motions, but the main challenge when measuring this type of relaxation is the suppression of an effect called “spin diffusion”. Spin diffusion causes the magnetisation of neighbouring sites to exchange via dipolar couplings, which averages out the measured relaxation rates so that they are no longer site-specific. Fast spinning is an important technique for decreasing the effects of spin diffusion (via averaging the dipolar couplings). It is often combined with specific isotopic labelling schemes and deuteration to make sure that spin diffusion is negligible during relaxation measurements. However, for some nuclei in certain systems, spin diffusion can be particularly challenging to remove. This is the case for aliphatic nuclei in proteins due to their strong ^1H - ^{13}C and ^{13}C - ^{13}C dipolar couplings. It is possible to measure the spin-lattice relaxation rates of aliphatic sites using extensive deuteration, partial ^{13}C labelling and 60 kHz MAS, however it can be very expensive and often challenging to isotopically label proteins in this way. Thus, with the recent development of 100 kHz MAS, Chapter 4 investigates whether the spin-lattice relaxation rates of aliphatic ^{13}C nuclei, in particular $^{13}\text{C}^\alpha$, can simply be measured with 100 kHz MAS in a fully protonated and uniformly ^{13}C labelled protein. Alongside the relaxation rate measurements themselves, spin diffusion control spectra and spin diffusion saturation transfer (SDST) measurements were conducted to analyse the extent of spin diffusion at the aliphatic sites under these conditions. The $^{13}\text{C}^\alpha$ nuclei throughout the protein backbone were especially interesting because they are not part of the rigid peptide plane and thus undergo dynamics distinct from the $^{13}\text{C}'$ and ^{15}N backbone sites.

Relaxation measurements are one of the most powerful SSNMR tools since they allow simultaneous measurement of the timescale, amplitude and occasionally directionality of each motion.^{16,26,27} The “model free” approach, developed by Lipari and Szabo in 1982, is a very popular method for accurate estimation of the order parameters (i.e. effective amplitudes) and correlation times (i.e. effective timescales) of the motions from relaxation rate data.^{28,29} This approach is used extensively in Chapter 5. Figure 1.1 summarises the dynamics commonly found within protein samples and the timescale upon which they occur. Each type of relaxation measurement is sensitive to a specific range of motion. For example, spin-lattice relaxation rates are dominated by

motions on the ps - ns timescale, such as methyl group rotations. Whereas spin-spin relaxation rates are sensitive to slower dynamics (ns - ms), such as local folding. Together this hierarchy of dynamics forms the overall energy landscape of the protein and its function(s).^{7,9,30} SSNMR relaxation measurements across a range of temperatures are well-suited for characterising the hierarchy of protein dynamics, since the combination of the Arrhenius equation and the model free approach allow the quantitative determination of activation energies. Chapter 5 explores the use of ^{13}C and ^{15}N variable temperature relaxation measurements to further understand the energy landscape throughout a protein backbone.

Relaxation rates are not only extremely valuable for determining the motions within a protein, they can be applied to many other dynamic systems. The research in Chapter 6 investigates the use of variable temperature relaxation measurements and 2D exchange spectra to determine the ice dynamics within frozen non-colligative antifreeze solutions. Non-colligative antifreezes are those that depress the freezing point of water significantly more than predicted by concentration alone. Since the first observation of antifreeze glycoproteins in polar fish, many more antifreeze glycoproteins and antifreeze proteins have been discovered across a vast range of organisms. These naturally-occurring antifreezes are extremely effective at very low concentrations and are vital for the survival of many species in cold habitats. Considering the huge quantities of research on these complicated proteins, relatively little is known about their mechanism for such effective antifreeze activity. The applications of these impressive biomolecules are vast and spread across the biomedical, agricultural and engineering industries. However, these proteins are challenging and costly to produce in significant quantities, so synthetic mimics of antifreeze (glyco)proteins are extremely sought after. Only a handful of synthetic antifreezes have been discovered and as such there is limited knowledge of their mechanisms too. In this work, the dynamics of frozen aqueous solutions of antifreeze (glyco)proteins and two synthetic mimics, polyvinyl alcohol and safranin chloride, are explored using SSNMR. In the literature there is little use of SSNMR to explore such systems. Moreover, the majority of measurements focus on the antifreezes themselves, whereas this research monitors changes in the motions of the ice protons in the presence of the antifreezes. This chapter aims to develop the knowledge of ice-antifreeze dynamics and aid the determination of a mechanism, complementing the research from other techniques, such as splat assays, nanolitre osmometry, fluorescence microscopy and molecular dynamics simulations.

The research presented in this thesis starts with an important practical consideration for SSNMR of proteins, the development of a packing tool (Chapter 3). It is followed by two chapters focusing on advancing SSNMR methodology for the determination of protein dynamics (Chapters 4 and 5) and finally, in Chapter 6, similar techniques are applied to investigate the dynamics of ice in the presence of various non-colligative antifreezes.

Chapter 2

Theory

In order to understand the results presented in this thesis, a basic knowledge of SSNMR and relaxation theory is required. In this light, this chapter starts with a walk-through of the fundamentals of SSNMR theory and followed by a section on the specifics of relaxation and relaxation measurements.

Large amounts of the theory presented here come from *Understanding NMR Spectroscopy* (J. Keeler),³¹ *Spin Dynamics* (M. H. Levitt),³² *NMR* (P. J. Hore),³³ *NMR: The Toolkit* (P. J. Hore, J. Jones and S. Wimperis),³⁴ *Solid-State NMR: Basic Principles and Practice* (D. C. Apperley, R. K. Harris and P. Hodgkinson),³⁵ *Introduction to Solid-State NMR Spectroscopy* (M. Duer)³⁶ and *SSNMR Studies of Biopolymers* (A. E. McDermott and T. Polenova).³⁷

2.1 Solid-State NMR Fundamentals

One of the most important differences between NMR in the solid state and in the solution state is the lack of rapid overall motion in solids. In a solution the molecules are tumbling very quickly and undergoing random motions, therefore any NMR parameters that are orientation dependent (anisotropic) will be averaged out to their orientation independent (isotropic) values, but in the solid state this is not the case. Thus a primary challenge when measuring dynamics using SSNMR is separating the incoherent contributions (due to random motions) from the coherent contributions (due to incomplete averaging of anisotropic interactions). Many experiments have been designed and developed to address this and these will be discussed in Section 2.3, but first the basic concepts and key interactions of SSNMR are described.

2.1.1 Nuclear Spins

All atomic nuclei possess three important physical properties: mass, electric charge and spin. The latter is an intrinsic angular momentum, critical for NMR. The overall magnitude of the spin of a nucleus is determined by the spin quantum number (I), which is a positive integer or half integer ($I = 0, \frac{1}{2}, 1, \frac{3}{2}, 2, \dots$). The spin quantum number of common nuclei are presented in Table 2.1. Note that isotopes with $I = 0$, such as ^{12}C , have zero overall spin and therefore are NMR-inactive.

Table 2.1: Common nuclei and their spin quantum numbers, gyromagnetic ratios, natural abundances and Larmor frequencies at 14.1 T (600 MHz ^1H Larmor frequency).

| Nucleus | Spin (I) | Natural Abundance (%) | Gyromagnetic Ratio (MHz T $^{-1}$) | Larmor Frequency at 14.1 T (MHz) |
|-----------------|--------------|-----------------------|-------------------------------------|----------------------------------|
| ^1H | 1/2 | 99.98 | 42.577 | 600.0 |
| ^2H | 1 | 0.02 | 6.536 | 92.1 |
| ^{12}C | 0 | 98.9 | N/A | N/A |
| ^{13}C | 1/2 | 1.1 | 10.708 | 150.9 |
| ^{14}N | 1 | 99.6 | 3.077 | 43.3 |
| ^{15}N | 1/2 | 0.4 | -4.316 | 60.8 |

All nuclei with a non-zero spin quantum number are inherently magnetic, they possess a magnetic moment (μ):

$$\mu = \gamma I_z \quad (2.1)$$

Where γ is the gyromagnetic ratio, a constant of proportionality between the angular momentum (I_z) and the magnetic moment. γ has a different value for each type of nucleus. I_z is the angular momentum of these spin states, which is quantised as:

$$I_z = m\hbar \quad (2.2)$$

Where $m = I, I - 1, I - 2, \dots, -I + 1, -I$.

All NMR-active nuclei have $2I + 1$ spin states. The nuclei studied in this work (^1H , ^{13}C and ^{15}N) are all spin $I = \frac{1}{2}$, therefore each has two states: $m_I = +\frac{1}{2}\hbar$ and $m_I = -\frac{1}{2}\hbar$. In these cases the lower energy state will be aligned with the external magnetic field (B_0), known as the α spin state ($m_I = +\frac{1}{2}\hbar$) and the higher energy state will be aligned against the magnetic field, known as the β spin state ($m_I = -\frac{1}{2}\hbar$), if γ is positive.

Each of the spin states has an energy associated with it (Equation 2.3):

$$E_Z = -\gamma m_I \hbar B_0 \quad (2.3)$$

The energy difference between these spin state relates to a transition between these states (Equation 2.4), this is known as the *Zeeman effect*.

$$|\Delta E_Z| = |\gamma \hbar B_0| \quad (2.4)$$

These transitions are critical for NMR. They can be related to a resonance frequency for NMR, known as the *Larmor frequency* (ω_0), through equations 2.5 and 2.6:

$$\Delta E_Z = \hbar \omega_0 \quad (2.5)$$

$$\omega_0 = \gamma B_0 \quad (2.6)$$

Where B_0 is the applied magnetic field strength. Note that in the NMR community the spectrometers are often referred to by their ^1H Larmor frequency rather than their B_0 field strength. For example, 600 MHz rather than 14.1 T.

The energy difference between spin states can be used to calculate the proportion of nuclear spins in the α and β states (i.e. aligned with or against the external magnetic field) at thermal equilibrium:

$$\frac{p_\beta}{p_\alpha} = e^{\frac{\Delta E_Z}{kT}} \quad (2.7)$$

Where $\frac{p_\beta}{p_\alpha}$ is the ratio of spins in the β and α states, k is the Boltzmann constant and T is temperature.

When describing NMR experiments, it is often much more convenient to consider the behaviour of the net magnetisation (also called the “bulk magnetisation”) rather than considering individual spins. Unfortunately the net magnetisation is extremely small meaning that NMR is a very insensitive analytical technique. For example, in the case of ^{13}C nuclei at a B_0 field of 9.4 T, for every 1,000,000 spins in the β state there will only be 1,000,017 in the α state. Due to its inherently poor sensitivity a lot of research has been dedicated to developing techniques to improve the signal-to-noise ratio (SNR) of NMR experiments, these will be discussed in detail further on.

In this work the hydrogen, carbon and nitrogen nuclei are used as probes to investigate proteins and ice since these are the most abundant elements in these systems. These elements have multiple isotopes and so the choices behind studying ^1H (rather than ^2H), ^{13}C (rather than ^{12}C) and ^{15}N (rather than ^{14}N) are outlined below. The natural abundances, gyromagnetic ratios and calculated Larmor frequencies at a field strength of 14.1 T are presented in Table 2.1 for these isotopes.

^1H nuclei have a very high natural abundance and gyromagnetic ratio. The combination of these properties results in a relatively high signal-to-noise ratio. Alternatively ^2H could be used, however the natural abundance of ^2H is very low (0.02%), therefore ^2H labelling would be necessary which can be expensive and challenging. Furthermore, ^2H has a gyromagnetic ratio 6.5 times smaller than that of ^1H , resulting in a much lower signal-to-noise ratio. It is also a quadrupolar (spin $>1/2$) which results in significantly broader signals. ^{12}C is by far the most abundant isotope of carbon, however it has a spin quantum number of zero and therefore is NMR-inactive. This leaves ^{13}C (1.1 % abundance), which often calls for the sample to be isotopically labelled to achieve a good signal in reasonable experimental time. ^{15}N is the most suitable isotope of nitrogen for these experiments due to ^{14}N being quadrupolar. However, ^{15}N has a very low natural abundance (0.36%) and so isotopic labelling is usually required.

2.1.2 NMR Interactions

It is important to understand some of the key NMR interactions that affect the Larmor frequency of a nucleus. These are briefly described here. Each interaction will have contributions to the overall Larmor frequency in varying magnitudes: The Zeeman inter-

action is on the scale of hundreds of MHz, dipolar coupling and chemical shift anisotropy are both on the scale of tens of kHz and J-couplings are typically 1-100 Hz.

$$\omega_0 \approx Zeeman + Dipolar + CSA + ChemicalShielding + J-Coupling \quad (2.8)$$

The precise Larmor frequency of nucleus in a magnetic field does not just depend upon the type of nucleus (i.e. gyromagnetic ratio), but also the environment surrounding it. Local magnetic fields induced by currents of electrons in the molecular orbitals will slightly shield nearby nuclei from the B_0 field, this well-known effect is called **chemical shift** or **chemical shielding**. It is one of the most important effects in solution-state NMR for the determination of chemical structure. The chemical shift, like the Larmor frequency, is proportional to the external magnetic field. So it is practical to describe the chemical shift in terms of its ratio to the Larmor frequency, thus providing an instrument-independent description:

$$\delta(ppm) = \frac{\omega_0 - \omega_{0,REF}}{\omega_{0,REF}} \times 10^6 \quad (2.9)$$

Where δ is the chemical shift (in parts per million), ω_0 is the Larmor frequency of the nucleus of interest and $\omega_{0,REF}$ is the Larmor frequency of a reference compound exposed to the same external magnetic field.

In most cases, electrons are not spherically distributed around a nucleus, therefore shielding from the electrons will be anisotropic. This means that the orientation of the nucleus with respect to the B_0 field will affect the chemical shift, this is known as **chemical shift anisotropy** (CSA). In the solution state, where the molecules are rapidly tumbling through all orientations, this anisotropy is averaged out and just the isotropic chemical shift is observed. But in the solid state CSA is an important factor to consider because the molecules will be in a variety of orientations with respect to the B_0 field, and each will produce a slightly different chemical shift. The resulting peak will be a superposition of all possible orientations and therefore have a broad characteristic shape. The CSA tensor of this lineshape can be described by three components: δ_{11} , δ_{22} and δ_{33} , which are defined as $\delta_{11} \geq \delta_{22} \geq \delta_{33}$ (i.e. the δ_{11} component corresponds to the direction of highest shielding and the δ_{33} component corresponds to the direction of lowest shielding).³⁸ A nucleus is described as being “axially symmetric” if two of the components are equal. The isotropic chemical shift is the mean of these three components (Equation 2.10).

$$\delta_{iso} = \frac{\delta_{11} + \delta_{22} + \delta_{33}}{3} \quad (2.10)$$

Figure 2.1 illustrates the effect CSA can have on the chemical shift of a peak in the solid state.

J-coupling is through-bond spin-spin coupling mediated by the bonding electrons. This coupling slightly raises or lowers the energy of the system, producing splitting

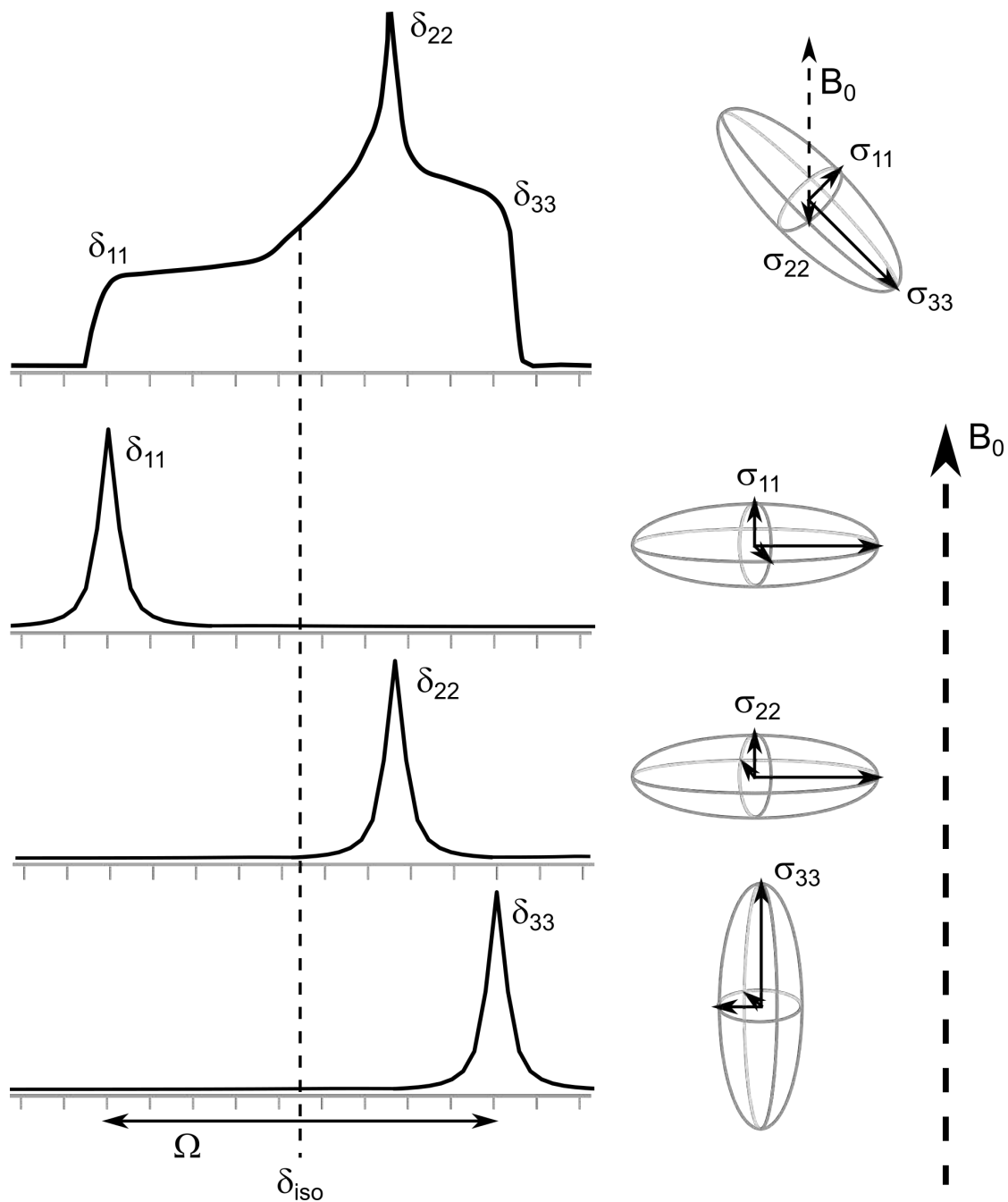


Figure 2.1: The effect of CSA on a static powder sample. The δ_{11} , δ_{22} and δ_{33} components are indicated, showing examples of how their orientation with respect to B_0 can cause variation in chemical shift. The overall spectrum is a superposition of all components. δ_{iso} is the isotropic chemical shift and Ω is the span.

patterns, which are very useful in the solution state for structure determination. In the solid state the effects of J-coupling are rarely resolved, because its interaction usually has the smallest magnitude by far.

Dipolar coupling is a through-space interaction between a pair of dipole moments. The secular approximation, valid in strong external magnetic fields, of the dipolar coupling between two spins (D), j and k , is defined by Equation 2.11:

$$D = -\frac{\mu_0}{4\pi} \frac{\gamma_j \gamma_k \hbar}{r^3} \frac{1}{2} (3 \cos^2 \theta_{jk} - 1) \quad (2.11)$$

Where μ_0 is the magnetic moment, γ_j and γ_k are the gyromagnetic ratios of the spins, r is the distance between the spins and θ_{jk} is the angle between the dipolar vector and the B_0 field.

Like CSA, this interaction is also anisotropic: each orientation will give a different splitting, which causes the overall NMR signal to become broad. It is important to note that the dipolar interaction is strongly distance dependent, therefore a spin will have the strongest dipolar interactions with those closest in space to it. It is also dependent on the gyromagnetic ratios of the involved nuclei, thus the strongest dipolar interactions will involve ^1H nuclei.

2.1.3 Magic Angle Spinning

It is routine to apply magic angle spinning (MAS) in SSNMR experiments to assist in the removal of the line-broadening effects of CSA and dipolar couplings, which have a common dependence on orientation (at least to the first order approximation):

$$\frac{1}{2} (3 \cos^2 \theta - 1) \quad (2.12)$$

Where θ is the angle between the B_0 field and the CSA principle axes or dipolar tensor.

Andrew²⁰ and Lowe²¹ independently discovered that rotation of a solid sample at 54.74° to the B_0 field reduces Equation 2.12 to zero on average (see Figure 2.2), mimicking the tumbling of a solution sample:

$$\frac{1}{2} (3 \cos^2 54.74^\circ - 1) = 0 \quad (2.13)$$

This angle has been termed the “magic angle”. To effectively average CSA or dipolar interactions, the frequency of the magic angle spinning (MAS) has to be significantly larger than the size of the interaction. The extent of precisely how much faster the spinning frequency needs to be is dependent on the nature of the interaction. For example, homonuclear dipolar couplings are typically more difficult to average out than heteronuclear dipolar couplings (due to a difference in an element of the dipolar coupling Hamiltonian when the chemical shifts of the coupled spins are similar i.e. in a homonuclear interaction).³⁶ MAS of up to 60 kHz is typical in protein SSNMR experiments, however more recent advances in NMR equipment now allow for MAS up to 150 kHz. It is important to note that fast MAS does not reduce the effects of inhomogeneous

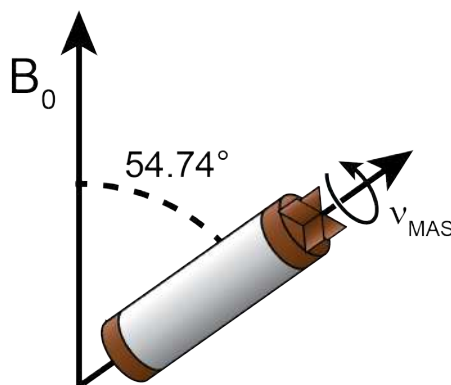


Figure 2.2: An SSNMR rotor spinning at the “magic angle” (54.74° from the B_0 field) at a frequency of ν_{MAS} .

broadening, for example broadening caused by a distribution of isotropic chemical shifts due to structural inhomogeneity.³⁹

2.2 Pulsed Fourier Transform NMR

2.2.1 The Basic SSNMR Experiment

The initial set up of an SSNMR experiment involves placing the sample (packed inside a rotor) into a strong external magnetic field (usually 10 - 20 Tesla). Around the rotor there is a coil of wire for both the application of radiofrequency (RF) pulses to the sample and the detection of signal. The strong B_0 field causes the nuclear spins to align either with or against the field, producing a very small net magnetic field (aligned with the B_0). It is this net magnetisation that is manipulated and detected in the NMR experiments.

The simplest “one-pulse” NMR experiment is illustrated in Figure 2.3 as a bulk magnetisation vector and as a pulse sequence. In this experiment the bulk magnetisation vector starts on the z -axis aligned with the B_0 field. Only magnetisation in the plane perpendicular to B_0 is detectable, therefore, to produce an NMR signal, an RF pulse along the y -axis is applied to rotate the bulk magnetisation by 90° into the xy -plane (i.e. spins transition from the α to the β energy levels). The magnetisation vector will now precess around the z -axis in the xy -plane and induce a current in the coil that surrounds the sample. The detected current will be a superposition of oscillations at the Larmor frequencies of the observed spins over time (each nucleus in a unique environment will produce a slightly different frequency). This signal is called a **free induction decay** (FID) and will decay over time due to **relaxation**, which is the process by which the system returns to equilibrium. The FID, a time-domain signal, is complicated to analyse directly and so it is **Fourier transformed** to produce a frequency-domain spectrum, separating out the components of the signal into peaks (Figure 2.4). The equation for a Fourier transform is shown below:

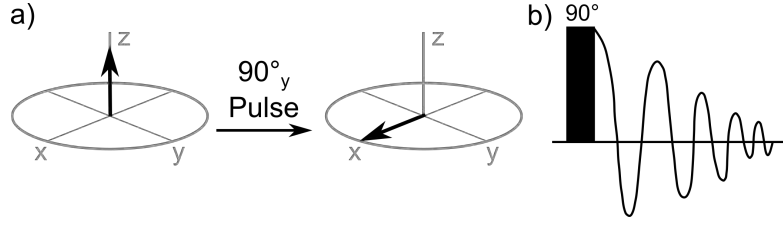


Figure 2.3: The “one-pulse” NMR experiment represented as a) bulk magnetisation vectors and b) the pulse sequence (where the x -axis is time). The black rectangle represents a 90°_y pulse that rotates the magnetisation (grey arrow) into the xy -plane ready for acquisition of the signal (damped sine wave).

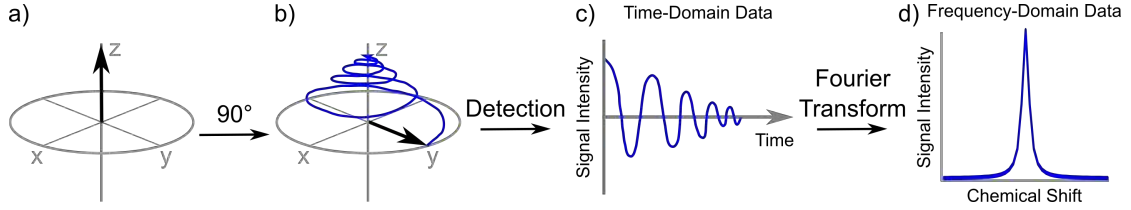


Figure 2.4: A vector model of a) magnetisation on the z -axis and then b) precession and returning to equilibrium after a 90° pulse. c) Detection during this period produces the FID (time-domain data), which is then Fourier transformed to d) an NMR spectrum (frequency-domain data).

$$S(\omega) = \sum_{i=1}^{i=N} S(t_i) e^{-i\omega t_i} \quad (2.14)$$

Where $S(\omega)$ is the signal at frequency ω , N is the number of digital points recorded, $S(t)$ is the signal at time t , t_i is the time of the i th data point.

In the case of a 90° pulse, the signal at time t (i.e. the voltage induced in the coil) can be described as:

$$S(t) = S_0 e^{i\Omega t} e^{-R_2 t} \quad (2.15)$$

Where R_2 is the rate of decay of magnetisation in the xy -plane and Ω is the angle between the bulk magnetisation and the axis.

The Fourier transform of Equation 2.15 is:

$$S(\omega) = \frac{S_0 R_2}{(\omega - \Omega)^2 + R_2^2} + i \frac{-S_0(\omega - \Omega)}{(\omega - \Omega)^2 + R_2^2} \quad (2.16)$$

The left-hand term in Equation 2.16 is the **real** part, which is an absorption mode Lorentzian lineshape, and the right-hand term is the **imaginary** part, which is an dispersion mode Lorentzian lineshape. Usually the real part of the spectrum is presented, however often the spectrum will neither be an absorption nor dispersion mode Lorentzian lineshape due to an arbitrary initial phase of the signal. In this case the spectrum can be corrected using either frequency-independent (also known as *zero-order*) or frequency-dependent (also known as *first-order*) phasing. For further details on phasing

see *Understanding NMR Spectroscopy*³¹ or *Spin Dynamics*.³²

Most NMR experiments are more complex than the one described in Figure 2.3, normally with multiple pulses, transfer of the magnetisation between different types of nuclei (e.g. cross polarisation) and evolution periods (for 2D or 3D spectra). The net magnetisation is manipulated by RF pulses of various lengths and powers. These two variables can be controlled to produce pulses that cause the net magnetisation to move by precise angles and at exact speeds. The relationship between pulse angle (θ), power of the RF pulse (B_1), pulse length (τ_p) and gyromagnetic ratio (γ) is shown in Equation 2.17. Normally when setting up experiments, the length and power for a 90° pulse (for a particular nucleus) are determined experimentally and then any other pulses can be calculated from this pulse.

$$\theta = \gamma B_1 \tau_p \quad (2.17)$$

2.2.2 The Rotating Frame

So far all diagrams of bulk magnetisation have been shown in the **laboratory frame** with the coordinates x , y and z but, since the magnetisation precesses around the z -axis, this frame of reference is not ideal. Instead a new coordinate system will be used from now on, which moves around the z -axis at the Larmor frequency. This means that any spins precessing at exactly the Larmor frequency will appear still and any spins at a slight variation of this frequency will only move very slowly. This new frame of reference is known as the **rotating frame** (Figure 2.5).

2.2.3 Cross Polarisation

The signal from an NMR experiment is intrinsically low and so often the same experiment is repeated many times to increase the signal-to-noise ratio. Cross polarisation (CP) is an important technique used to provide information on multiple types of nuclei (i.e. different isotopes) in a single experiment, it is also used to increase the SNR and decrease experimental time. CP involves the transfer of magnetisation from the nuclei of one

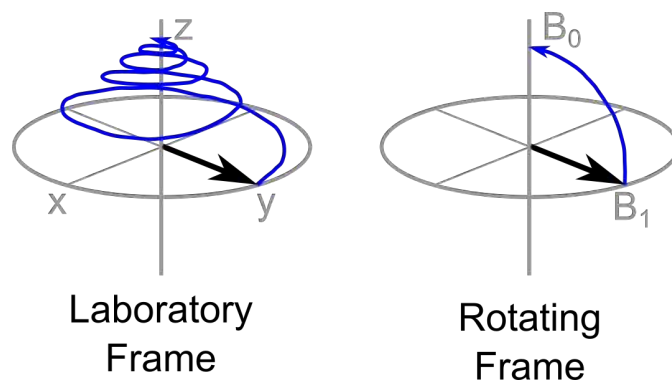


Figure 2.5: An example of the laboratory and rotating frames in the case of magnetisation in the xy -plane relaxing back to thermal equilibrium. The path of the bulk magnetisation vector is indicated in blue.

element to another, most commonly from the nuclei of an abundant isotope (e.g. ^1H) to a more dilute isotope of interest (such as ^{13}C or ^{15}N). In the case of 100% magnetisation transfer there will be a signal enhancement of $\frac{\gamma^1\text{H}}{\gamma^X}$ compared to direct excitation of the X nuclei. In this research ^1H - ^{13}C and ^1H - ^{15}N CPs are frequently used, these give theoretical signal enhancements of approximately 4 and 10, respectively. Note that the enhancement actually achieved in the experiment does depend on quality of the set up (i.e. the pulse powers and lengths chosen in the pulse sequence), type of CP used and the sample type. Normally the theoretical efficiency of CP is limited to approximately 60 % of $\frac{\gamma^1\text{H}}{\gamma^X}$, but can be up to 100 % if particular adiabatic CP pulse sequences are used.^{40,41}

Using CP instead of direct excitation can potentially reduce experimental time. After running the pulse sequence the magnetisation needs to fully relax back to equilibrium before repeating the experiment. The time that this takes is sample dependent and known as the **spin-lattice relaxation time** (T_1). At the end of a pulse sequence there is always a wait time known as the **recycle delay** that allows plenty of time for this relaxation. Often ^1H T_1 s are much shorter than ^{13}C or ^{15}N T_1 s. In the case of a ^1H -X CP, the recycle delay is limited by the ^1H T_1 (not the T_1 of the X nuclei), so typically this experiment can be repeated faster than a direct excitation experiment.

A final, very important, advantage of CPs is that it allows the transfer of magnetisation between different types of nuclei within an experiment. Therefore information on these different nuclei and their relationships to each other can be gathered in a single experiment. This is a vital tool in many SSNMR experiments, for example protein structure assignment sequences and dynamics measurements.

CPs are critical for the research presented in this thesis and many of the pulse sequences used involve two or three. For example, in the case of measuring relaxation in a protein sample a pulse sequence involving ^1H , ^{15}N and ^{13}C could be used. The magnetisation starts on the abundant ^1H nuclei and is transferred to the ^{15}N nuclei using a CP and then, after an indirect acquisition period on the ^{15}N , the magnetisation is transferred to the ^{13}C nuclei for detection, producing a 2D ^{15}N - ^{13}C spectrum.

Before further explanation of how CP works, the term “**spin-lock**” must be defined. A spin-lock pulse is simply a strong pulse applied along the same axis as the magnetisation vector (e.g. if the magnetisation is along the x -axis then the pulse will be applied along the x -axis). This strong pulse ensures that the magnetisation remains along the axis since the RF field strength will be greater than any of the typical offsets that would normally cause deviation from this axis, for example coherent contributions.

An example of a basic ^1H -X CP pulse sequence is shown in Figure 2.6. It starts with a ^1H 90° pulse which brings the ^1H spins from the z -axis into the xy -plane. Simultaneously, spin-lock pulses are applied on both the ^1H nuclei and the X nuclei for a length of time known as the **contact time** (usually a few ms). Under the correct conditions, described below, the magnetisation will transfer from the ^1H nuclei to the X nuclei during the contact time. Afterwards the X signal is detected, ^1H decoupling is applied during this

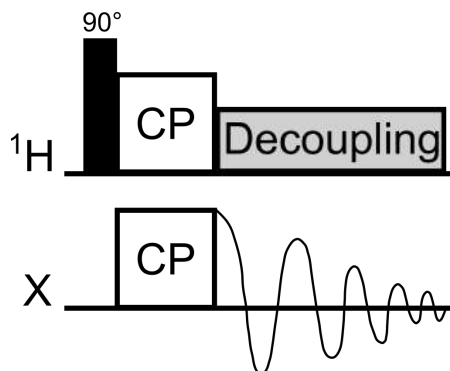


Figure 2.6: Example of a ^1H -X cross polarisation pulse sequence. The x-axis is always time and each type of nucleus has its own row. The black narrow rectangle represents a 90° pulse, the two boxes labelled “CP” are the cross polarisation pulses, the damped sine wave represents the decay (and detection) of the X magnetisation and the grey box is the decoupling pulse.

acquisition time. (Further information on decoupling can be found in Section 2.2.5).

During the contact time, both the ^1H and X spins are spin-locked (into the xy -plane). Naturally these nuclei will have different Zeeman splittings (energy difference between the spin states). The ^1H and X spin-lock B_1 fields can be applied in a way so that they do have the same Zeeman splitting (quantised in $B_{x/y}$ rather than B_0), this is known as the **Hartmann-Hahn matching condition**. Fulfilling the Hartmann-Hahn condition (Equation 2.18) will cause both the ^1H and X nuclei to have the same energy gap between their spin states, so that the ^1H -X dipolar coupling allows a redistribution of energy between them. The fact that the net spin polarisation must be preserved combined with the initial large ^1H magnetisation ultimately leads to a transfer of magnetisation from the ^1H to X nuclei.

$$\gamma^H B_1^H = \gamma^X B_1^X \quad (2.18)$$

Cross polarisation was originally developed for static SSNMR (i.e. without MAS). Although the Hartmann-Hahn matching condition still holds for relatively slow MAS, if fast MAS is employed the spinning speed needs to be taken into account using Equation 2.19.

$$\nu_1^H = \nu_1^X \pm n\nu_{MAS} \quad (2.19)$$

Where ν_1^H and ν_1^X are the ^1H and X nutation frequencies respectively, ν_{MAS} is the MAS frequency and n is 1 or 2.

This highlights the importance of optimising the CP conditions at the target MAS frequency to maximise the signal of the X nuclei. Under fast MAS the matching conditions are much narrower, and inhomogeneity in the B_1 fields can result in the matching condition varying throughout the sample. Using ramped or adiabatic CP is a good solution to this problem. During ramped or adiabatic CP the nutation rate is

varied by sweeping the RF pulse through the matching condition, therefore achieving the matching condition for all parts of the sample at some point within the sweep. In practice, using a ramped or adiabatic CP at high MAS frequencies tends to provide a more intense signal and be more robust than a constant CP.^{40–42} It is for these reasons that adiabatic CPs are used throughout this work.

2.2.4 Proton Detection

It was mentioned that often a ^1H -X experiment will be used to produce an X spectrum instead of a direct X experiment because the extra magnetisation transferred from the ^1H nuclei will significantly improve the signal. The overall sensitivity of the experiment also depends on which nucleus the magnetisation is detected. It generally improves if it is detected on nuclei with a higher gyromagnetic ratio. In particular, experiments in which the magnetisation is transferred from X to ^1H for detection provide large gains in sensitivity.^{43–46} **Proton detection** is used throughout this work to improve sensitivity.

2.2.5 Heteronuclear Decoupling

If, during an NMR experiment, a dilute spin (for example ^{13}C or ^{15}N) is observed while being surrounded by abundant spins (such as ^1H), heteronuclear dipolar coupling will cause substantial broadening of the spectrum, even under fast MAS. It is common practice to incorporate specific RF pulses in the experiment in order to reduce this effect, this is known as **heteronuclear decoupling**.

A technique commonly applied in this research, high-power heteronuclear decoupling, involves applying continuous high-power RF irradiation on the ^1H nuclei during the FID acquisition of ^{13}C , for example. The high-power pulse causes the ^1H spins to rapidly undergo repeated transitions between the α and β spin states at a rate determined by the RF pulse amplitude. If these spin state transitions are faster than the dipolar coupling, the ^{13}C spectrum will only be affected by the time-averaged dipolar coupling which will be zero in this case due to the rapid spin-state oscillations of the ^1H spins. At fast (> 50 kHz) spinning frequencies, where MAS is quite effective in removal of heteronuclear couplings, low power decoupling sequences become viable and sometimes even superior to high power approaches.^{47,48}

The specific types of decoupling used in these experiments (e.g. *WALTZ-16*⁴⁹ and *WALTZ-64*⁵⁰) are described in detail in the relevant experimental sections.

2.2.6 Solvent Suppression

Proton detection provides fantastic improvements in the sensitivity of SSNMR experiments on proteins, however it comes coupled with intense ^1H signals from the solvent that overwhelm the spectra. In this work, *Multiple Intense Solvent Suppression Intended for Sensitive Spectroscopic Investigation of Protonated Proteins, Instantly* (MISSISSIPPI)⁵¹ uses ^1H saturation pulses to effectively suppress the solvent signals.

2.2.7 Isotopic Labelling

^{13}C and ^{15}N Labelling

As shown in Table 2.1, the natural abundance of many interesting isotopes is low, which makes their NMR applications challenging. In this PhD project we investigated proteins and ice through measurements on the ^1H , ^{13}C and ^{15}N nuclei. ^{12}C and ^{14}N are far more naturally abundant, however ^{12}C is NMR-inactive and ^{14}N is quadrupolar, which poses serious challenges in terms of resolution, sensitivity and general spin manipulation. The inherently low signal of NMR has already been discussed, but by probing extremely low natural abundance isotopes (1.1 % and 0.4 %, respectively) this signal problem becomes orders of magnitude worse.

One partial solution to this problem is to isotopically label the samples so that they contain a much higher proportion of these ^{13}C and ^{15}N nuclei. Isotopic labelling is achieved by expressing the proteins in minimal media with isotopically-labelled ^{13}C or ^{15}N sources, such as $[\text{U-}^{13}\text{C}]$ -glycerol or $[15\% \text{ }^{15}\text{N}]$ -ammonium chloride, as the sole carbon or nitrogen sources.^{52, 54–57} The specific isotopically-labelled ^{13}C or ^{15}N source chosen defines the labelling in the resulting protein. It is common to use uniformly labelled sources to produce a $[\text{U-}^{13}\text{C}, ^{15}\text{N}]$ protein, but in some cases, such as those discussed in Chapter 4, partial labelling is desirable to effectively turn “on” and “off” specific interactions. For example, $[1,3\text{-}^{13}\text{C}]$ -glycerol or $[2\text{-}^{13}\text{C}]$ -glucose can be used to introduce ^{13}C nuclei into specific sites within the protein. The presence of these isotopes at each particular site within each amino acid is well defined by a specific labelling scheme for each isotope source. The labelling schemes used in this work are presented in Figures 2.7 and 2.8.

Deuteration

Proton detection is a good method of improving sensitivity, since ^1H nuclei have a high natural abundance and gyromagnetic ratio. Protons are also very abundant within proteins, but this becomes a problem in the solid state: the dense network of ^1H - ^1H dipolar couplings creates substantial line broadening, which offsets the advantages of improved sensitivity. Often moderate MAS is combined with significant dilution of the ^1H network with deuterium to reduce these linewidths. This is typically achieved by expressing the protein in deuterated media. Followed by exchanging of labile sites, such as amide ^2H s, by preparation in fully or partially protonated solvents.

The overall sensitivity obtained in deuterated samples is a balance between the level of dilution, resolution and sensitivity. As a rule of thumb, higher levels of dilution are required for applications at slow spinning frequencies and larger fractions of protons are tolerated at faster spinning frequencies.

Improvements in MAS technology have reduced the level of ^1H dilution required for well-resolved, proton-detected spectra. Now as frequencies of 110 kHz MAS are achieved is it questioned whether deuteration is still necessary at all.⁴³ In fact, many of the measurements in Chapter 4 successfully use proton-detection on a fully-protonated

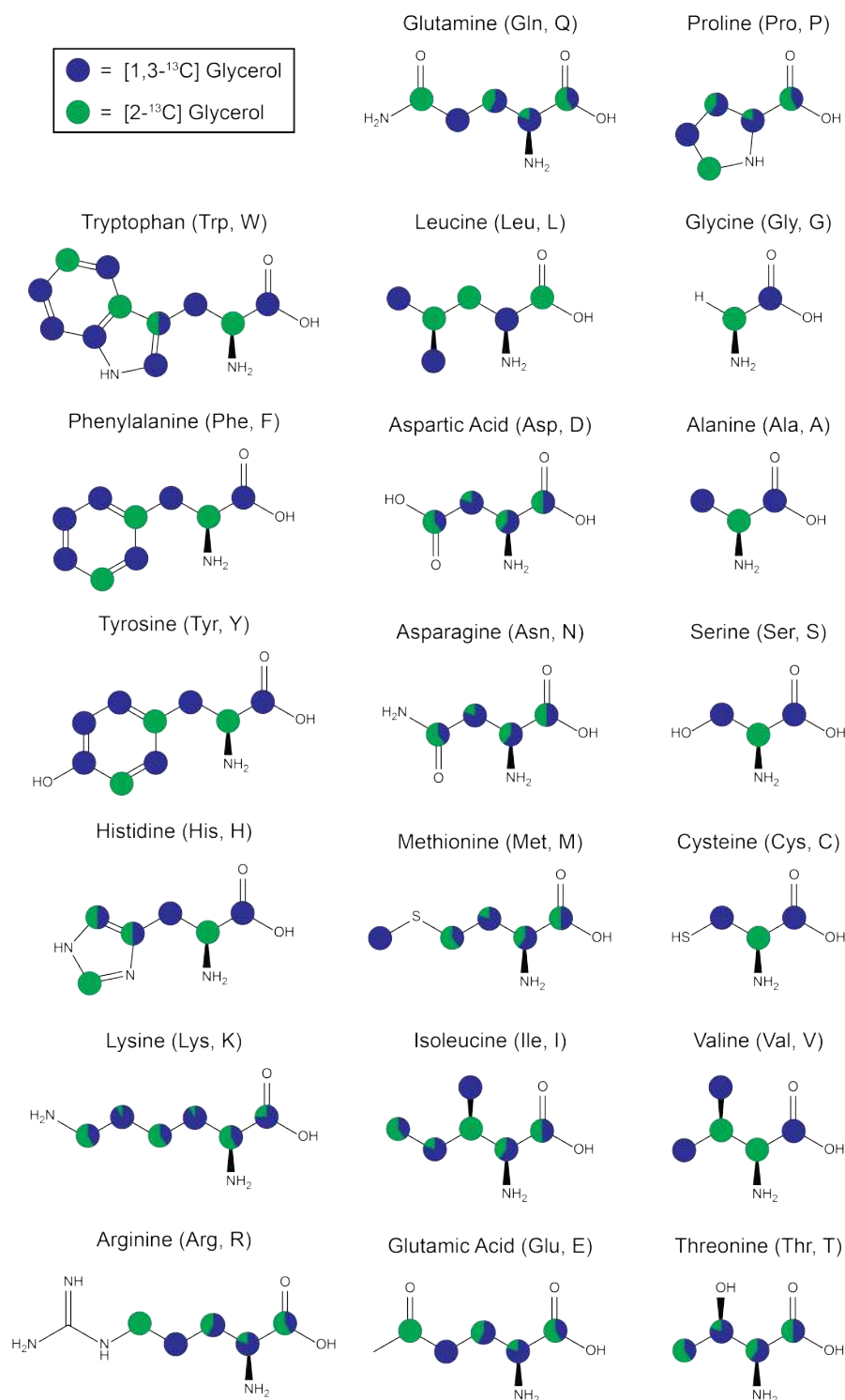


Figure 2.7: The [1,3- ^{13}C]glycerol and [2- ^{13}C]glycerol labelling schemes. The ^{13}C labelled nuclei are indicated in blue and green, respectively. For the amino acids that are synthesised via the citric acid cycle several isotopomers are produced, resulting in the average labelling indicated in the diagram. Adapted from LeMaster *et al.*⁵²

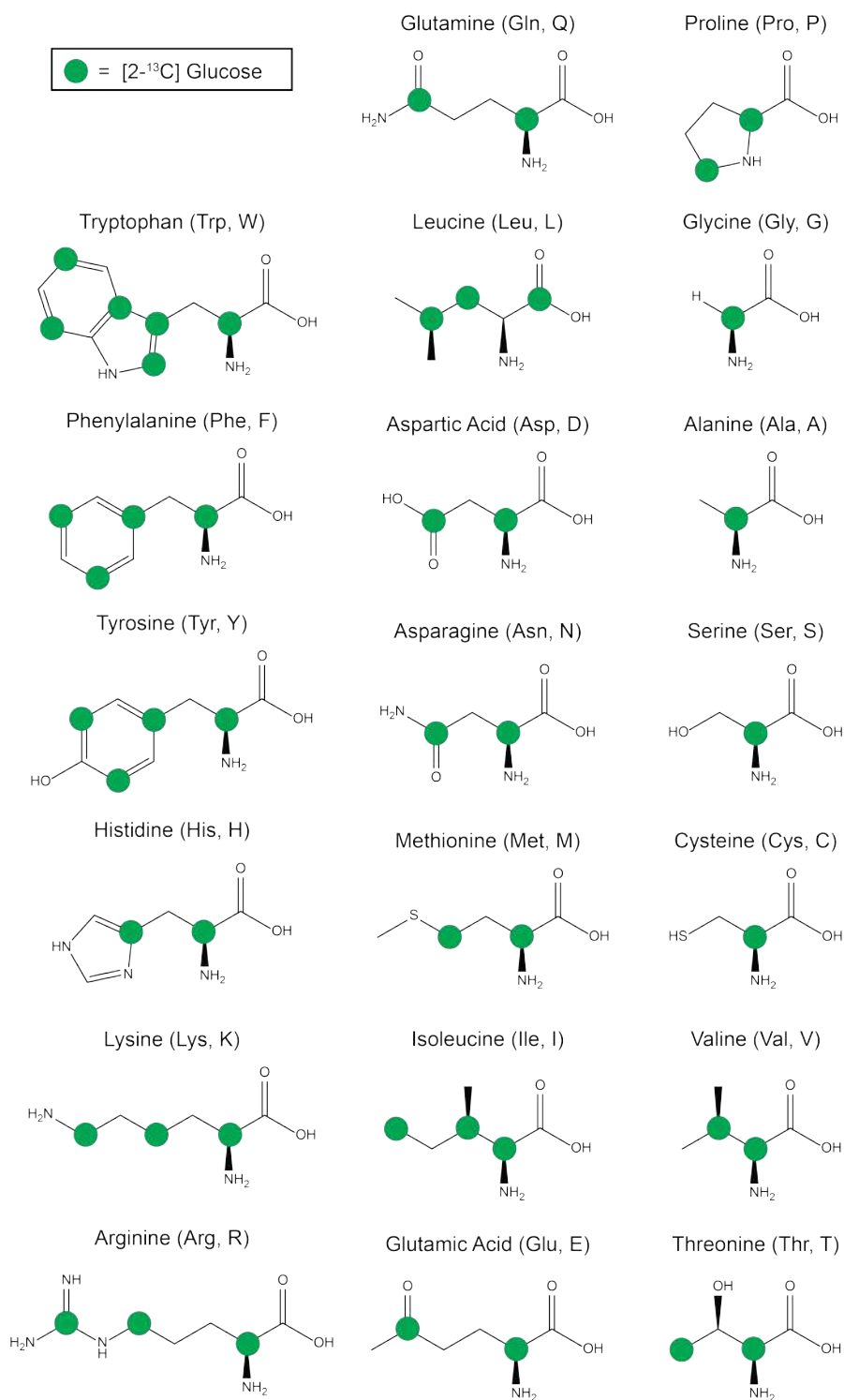


Figure 2.8: The [2-¹³C]glucose labelling scheme. The ¹³C labelled nuclei are indicted in green. Adapted from Lundstrom *et al.*⁵³

sample.

2.2.8 Basics of 2D NMR Experiments

In biological samples, the ^1H , ^{13}C and ^{15}N chemical shifts throughout the biomolecule all appear within a relatively small range, this leads to crowded spectra. For this reason it is extremely rare to assign the structure of a biological sample using just a 1D spectrum, normally 2D and 3D spectra are needed. To illustrate this, examples of 1D and 2D spectra of the same protein sample are presented in Figure 2.9, the advantages of multidimensional spectra are evident.

2D spectra can either be homonuclear or heteronuclear. An example of a basic homonuclear 2D pulse sequence is presented in Figure 2.10. After the initial 90° pulse, there is a variable **indirect evolution time (t_1)** in which the magnetisation evolves, under the chemical shift of the first nucleus. Next there is a “**mixing time**” that allows magnetisation to exchange between nearby sites. Finally the NMR signal is detected as a function of the time variable t_2 . This **direct evolution time** involves chemical shift evolution on the second nucleus. The experiment is repeated many times incrementing t_1 and then recording the FID as a function of t_2 . The dataset is Fourier transformed twice (with respect to t_1 and t_2) to produce a 2D spectrum that is a function of both frequency variables.⁵⁸ A similar concept can be applied to produce 3D or n D spectra. In the case of multidimensional heteronuclear pulse sequences, the same concepts can be applied alongside cross polarisation, which enables the transfer of the magnetisation between the different nuclei.

2.3 Relaxation Theory

In NMR, the relaxation rates of a nucleus are sensitive to both its environment and its dynamics. In this section the origins of relaxation, links between relaxation rates and motion, and fundamentals of NMR relaxation rate experiments are discussed in detail, since this is critical to understanding the research presented in this thesis.

2.3.1 The Origins of Relaxation

In an NMR experiment, after an RF pulse has perturbed the magnetisation from the z -axis to the xy -plane for example, the magnetisation does not precess there indefinitely. Relaxation is the process by which magnetisation returns to thermal equilibrium. There are two key relaxation processes: **spin-lattice relaxation** (also known as longitudinal relaxation, described by rate R_1), which describes the return of longitudinal magnetisation back to the equilibrium state determined by the Boltzmann distribution, and **spin-spin relaxation** (also known as transverse relaxation, described by rate R_2), which describes the decay of transverse magnetisation (in the xy -plane) to zero (Figure 2.11).

Many motional processes can be studied by measuring the rate of these relaxation mechanisms because relaxation is driven by the random thermal motion of the molecules. The motion experienced by the nucleus causes fluctuating magnetic fields that interact with the spins, driving the magnetisation to equilibrium. In the context of this work, such fluctuations can be caused by two key mechanisms: variations in the **dipolar interaction** between two spins or in the **chemical shift anisotropy** of the spin itself. The magnitude of both these types of anisotropic interactions is varied due to reorientation of molecules as a result of dynamic process, which results in the mentioned fluctuating magnetic fields. If these fluctuations occur at the required frequencies they induce transitions between spin energy levels driving the bulk magnetisation back to equilibrium.

Because these contributions to the relaxation rates originate from random motions they are said to be **incoherent**. One of the challenges for relaxation measurements in the solid state is separating the effects of incoherent contributions, which contain useful information on the molecular motions, from the **coherent** contributions that occur due to the incomplete averaging of strongly coupled network of anisotropic interactions. Often this challenge can be addressed through careful sample preparation and experi-

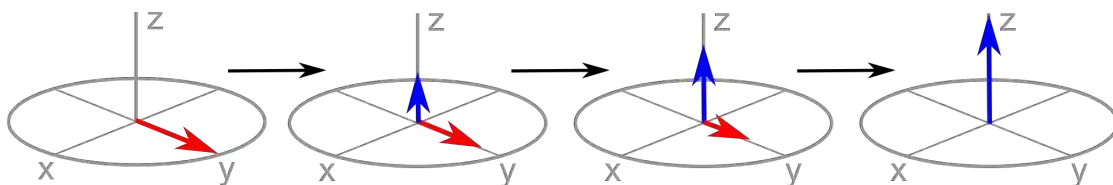


Figure 2.11: Illustrations of the magnetisation vectors affected by spin-lattice (blue) and spin-spin relaxation (red). The left-most diagram shows the net magnetisation after a 90° pulse and the right-most diagram shows the magnetisation back at equilibrium.

mental design.

Figure 1.1 in the introduction can be used as an approximate guide to understanding the timescales of various motions the nuclei or molecules may be undergoing, as well as the timescales that different relaxation measurements are typically sensitive to.¹⁰

2.3.2 The Correlation Time, Correlation Function and Spectral Density Function

In order to further understand the relationship between motion and relaxation rates, first there must be a way of describing the random motion that provides the time dependence to the local fields. Here the correlation time and correlation function are used to define how quickly a magnetic field randomly fluctuates and therefore whether it is at the correct frequency to cause relaxation. These concepts can then be used to estimate the frequency and amplitude of motions from the measured relaxation rates of a nucleus.

The **correlation time** (τ_c) is defined as the average time taken for a molecule to rotate one radian away from its starting position. As a rough guide, in solution, proteins will often have τ_c s for the overall tumbling on the nanosecond timescale, whereas small molecules will have faster τ_c s on the picosecond timescale. The reciprocal of the correlation time ($1/\tau_c$) provides a guide to the average frequency of the motion. The **correlation function** ($G(\tau_c)$) is used to characterise the time dependence of the random motion, and its Fourier transform, the **spectral density function** ($J(\omega)$), allows simple extraction of the amount of motion at a particular frequency. This is required when determining whether a motion is at the correct frequency to contribute to the relaxation process. Example plots of the correlation function and the spectral density function for various correlation times are presented in Figure 2.12.

The correlation function shows the change in local field over time (τ), where the maximum is always at $\tau = 0$ and provides information on the average size of the interaction. This maximum is equal to the average square of the local field ($\overline{B_{loc}^2}$). The correlation function undergoes a monotonic decay, often modelled as an exponential, as τ increases, the rate of this decay is dependent on the correlation time, as shown in Equation 2.20 and Figure 2.12. After the correlation time (i.e. $\tau = \tau_c$), the correlation function will have decayed to 50 %.

$$G(\tau) = \overline{B_{loc}^2} \exp\left(\frac{-|\tau|}{\tau_c}\right) \quad (2.20)$$

Since the exponential part of Equation 2.20 is independent of the magnitude of the local magnetic field (B_{loc}) and therefore the overall magnitude of $G(\tau)$, a reduced form of the correlation function may be used ($g(\tau)$):

$$g(\tau) = \exp\left(\frac{-|\tau|}{\tau_c}\right) \quad (2.21)$$

Taking the Fourier transform of the correlation function produces the spectral

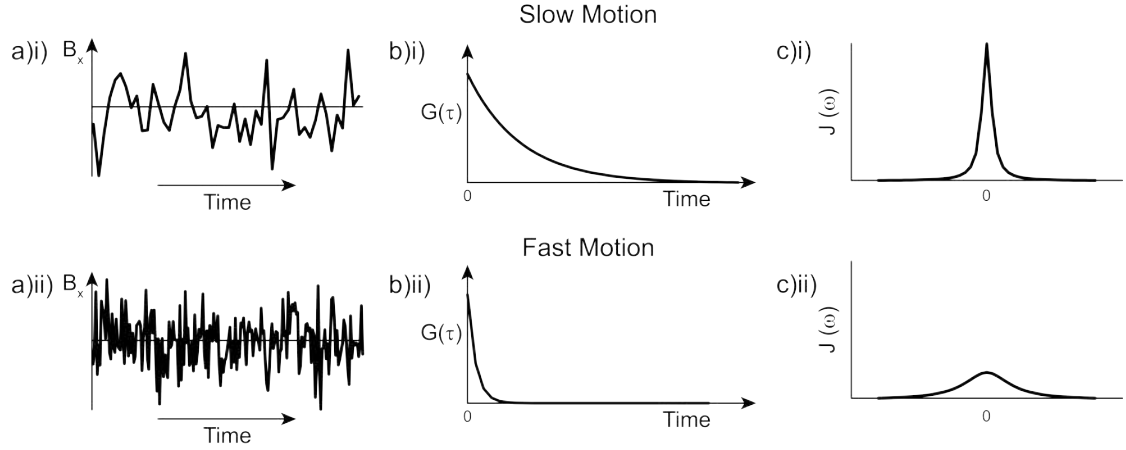


Figure 2.12: a) Example plots of i) slow and ii) fast random motions and their corresponding b) correlation functions and c) spectral density functions.

density function ($J(\omega)$), this allows for a simpler extraction of the amount of motion at the Larmor frequency. The spectral density function plotted against frequency (ω) forms a Lorentzian centred at $\omega = 0$, as shown in Figure 2.12c and Equation 2.22:

$$J(\omega) = \overline{B_{loc}^2} \frac{2\tau_c}{1 + \omega^2\tau_c^2} \quad (2.22)$$

The spectral density at the Larmor frequency is:

$$J(\omega_0) = \overline{B_{loc}^2} \frac{2\tau_c}{1 + \omega_0^2\tau_c^2} \quad (2.23)$$

$J(\omega_0)$ reaches its maximum value when $\tau_c = 1 / \omega_0$, confirming that motions will have the most influence on relaxation when they are close to the Larmor frequency. As with the correlation function, there is also a reduced spectral density function ($j(\omega)$):

$$j(\omega_0) = \frac{2\tau_c}{1 + \omega_0^2\tau_c^2} \quad (2.24)$$

It is important to note that the spectral density function can be simplified further if the motion is considered to be in either the fast motion or slow motion regime.

The **fast motion regime** is defined as when $\omega_0\tau_c \ll 1$. In this regime it is assumed that $1 + \omega_0^2\tau_c^2 \approx 1$ and therefore the reduced spectral density is independent of Larmor frequency:

$$j(\omega_0) = 2\tau_c \quad (2.25)$$

The **slow motion limit** is defined as when $\omega_0\tau_c \gg 1$. Therefore $1 + \omega_0^2\tau_c^2 \approx \omega_0^2\tau_c^2$ and since $j(0) = 2\tau_c$ the reduced spectral density in the slow motion regime is:

$$j(\omega_0) = \frac{j(0)}{\omega_0^2\tau_c^2} \quad (2.26)$$

Now that there is a system in place for quantifying the random motion that can influence relaxation, these spectral densities need to be linked to particular mechanisms of relaxation. This is achieved through **transition probabilities**.

2.3.3 Transition Probabilities

In a dipolar-coupled, two-spin system there are 4 energy levels. The dipolar interaction between the two spins can cause relaxation induced transitions between any of these energy levels. As illustrated in Figure 2.13, there are 6 possible transitions which can be divided into 3 categories: **single-quantum**, **double-quantum** and **zero-quantum**. Each of these transitions has a different probability: W_1 , W_2 and W_0 , respectively. The W_2 transition involves two aligned spins flipping simultaneously, W_0 is the same except the spins are anti-parallel and W_1 involves just one of the spins flipping.

The change in population of each of these energy levels can be written in terms of the transition probabilities:

$$\frac{dp_{\alpha\alpha}}{dt} = -W_1p_{\alpha\alpha} - W_1p_{\alpha\alpha} - W_2p_{\alpha\alpha} + W_1p_{\beta\alpha} + W_1p_{\alpha\beta} + W_2p_{\beta\beta} \quad (2.27)$$

$$\frac{dp_{\beta\alpha}}{dt} = -W_1p_{\beta\alpha} - W_1p_{\beta\alpha} - W_0p_{\beta\alpha} + W_1p_{\alpha\alpha} + W_1p_{\beta\beta} + W_0p_{\alpha\beta} \quad (2.28)$$

$$\frac{dp_{\alpha\beta}}{dt} = -W_1p_{\alpha\beta} - W_1p_{\alpha\beta} - W_0p_{\alpha\beta} + W_1p_{\alpha\alpha} + W_1p_{\beta\beta} + W_0p_{\beta\alpha} \quad (2.29)$$

$$\frac{dp_{\beta\beta}}{dt} = -W_1p_{\beta\beta} - W_1p_{\beta\beta} - W_2p_{\beta\beta} + W_1p_{\beta\alpha} + W_1p_{\alpha\beta} + W_0p_{\alpha\alpha} \quad (2.30)$$

Where p_{xx} is the population of the xx energy level ($x = \alpha$ or β).

The first three terms in each equation represent the loss of population from that state and the latter three terms represent the gain in population from other states. These expressions are only correct when the equilibrium populations are equal and this is not the case. Therefore these equations must be adjusted to take this into account by replacing the populations with the deviation of the population from its equilibrium value ($p_{xx} - p_{xx}^0$):

$$\begin{aligned} \frac{dp_{\alpha\alpha}}{dt} = & -W_1(p_{\alpha\alpha} - p_{\alpha\alpha}^0) - W_1(p_{\alpha\alpha} - p_{\alpha\alpha}^0) - W_2(p_{\alpha\alpha} - p_{\alpha\alpha}^0) \\ & + W_1(p_{\beta\alpha} - p_{\beta\alpha}^0) + W_1(p_{\alpha\beta} - p_{\alpha\beta}^0) + W_2(p_{\beta\beta} - p_{\beta\beta}^0) \end{aligned} \quad (2.31)$$

$$\begin{aligned} \frac{dp_{\beta\alpha}}{dt} = & -W_1(p_{\beta\alpha} - p_{\beta\alpha}^0) - W_1(p_{\beta\alpha} - p_{\beta\alpha}^0) - W_0(p_{\beta\alpha} - p_{\beta\alpha}^0) \\ & + W_1(p_{\alpha\alpha} - p_{\alpha\alpha}^0) + W_1(p_{\beta\beta} - p_{\beta\beta}^0) + W_0(p_{\alpha\beta} - p_{\alpha\beta}^0) \end{aligned} \quad (2.32)$$

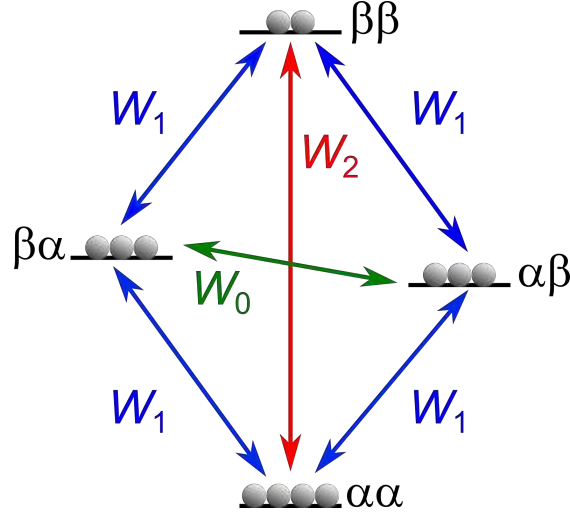


Figure 2.13: The six possible transitions in a two-spin system: four single-quantum (blue), one double-quantum (red) and one zero-quantum (green). The spins in higher energy states are aligned against the B_0 magnetic field.

$$\begin{aligned} \frac{dp_{\alpha\beta}}{dt} = & -W_1(p_{\alpha\beta} - p_{\alpha\beta}^0) - W_1(p_{\alpha\beta} - p_{\alpha\beta}^0) - W_0(p_{\alpha\beta} - p_{\alpha\beta}^0) \\ & + W_1(p_{\alpha\alpha} - p_{\alpha\alpha}^0) + W_1(p_{\beta\beta} - p_{\beta\beta}^0) + W_0(p_{\beta\alpha} - p_{\beta\alpha}^0) \end{aligned} \quad (2.33)$$

$$\begin{aligned} \frac{dp_{\beta\beta}}{dt} = & -W_1(p_{\beta\beta} - p_{\beta\beta}^0) - W_1(p_{\beta\beta} - p_{\beta\beta}^0) - W_2(p_{\beta\beta} - p_{\beta\beta}^0) \\ & + W_1(p_{\beta\alpha} - p_{\beta\alpha}^0) + W_1(p_{\alpha\beta} - p_{\alpha\beta}^0) + W_0(p_{\alpha\alpha} - p_{\alpha\alpha}^0) \end{aligned} \quad (2.34)$$

Now instead of considering the changes in populations of the energy levels, these equations will be re-written in terms of the z -magnetisation of the spins. Initially the z -magnetisation of the first spin, $I_{j,z}$, is considered. Figure 2.13 shows that $I_{j,z}$ magnetisation will be affected by $\alpha\alpha - \beta\alpha$ and $\alpha\beta - \beta\beta$ transitions (i.e. the transitions in which the left spin (j) changes between α and β):

$$I_{j,z} = (p_{\alpha\alpha} - p_{\beta\alpha}) + (p_{\alpha\beta} - p_{\beta\beta}) \quad (2.35)$$

Following the same logic, the $\alpha\alpha - \alpha\beta$ and $\beta\alpha - \beta\beta$ transitions involve the second spin:

$$I_{k,z} = (p_{\alpha\alpha} - p_{\alpha\beta}) + (p_{\beta\alpha} - p_{\beta\beta}) \quad (2.36)$$

Each of these magnetisations has an equilibrium value:

$$I_{j,z}^0 = (p_{\alpha\alpha}^0 - p_{\beta\alpha}^0) + (p_{\alpha\beta}^0 - p_{\beta\beta}^0) \quad (2.37)$$

$$I_{k,z}^0 = (p_{\alpha\alpha}^0 - p_{\alpha\beta}^0) + (p_{\beta\alpha}^0 - p_{\beta\beta}^0) \quad (2.38)$$

These equations allow the rate equations for the populations (Equations 2.31, 2.32, 2.33 and 2.34) to be re-written in terms of magnetisation in Equations 2.39 and 2.40.

$$\frac{dI_{j,z}}{dt} = -R_{auto}^{(j)}(I_{j,z} - I_{j,z}^0) - R_{cross}(I_{k,z} - I_{k,z}^0) \quad (2.39)$$

$$\frac{dI_{k,z}}{dt} = -R_{auto}^{(k)}(I_{k,z} - I_{k,z}^0) - R_{cross}(I_{j,z} - I_{j,z}^0) \quad (2.40)$$

$R_{auto}^{(j)}$ and $R_{auto}^{(k)}$ are the **auto relaxation rates** of spins j and k , respectively. This is the rate at which the magnetisation returns to equilibrium by dissipating energy to the surroundings. R_{cross} is the **cross relaxation rate**, which represents the rate at which magnetisation from spin j is transferred to spin k via a relaxation process. The opposite process, transfer of magnetisation from spin k to spin j , is also described using the same cross relaxation rate constant since the processes are equal. These equations show that spin j , for example, is only influenced by its self relaxation ($R_{auto}^{(j)}$) and the auto relaxation rate between spin j and k .

The constants $R_{auto}^{(j)}$, $R_{auto}^{(k)}$ and R_{cross} are defined below in terms of transition probabilities. Note that in these cases $W_1^{(j,\alpha)} = W_1^{(j,\beta)}$ and $W_1^{(k,\alpha)} = W_1^{(k,\beta)}$, so some of the expressions below have been simplified accordingly:

$$\mathbf{R}_{auto}^{(j)} = W_1^{(j,\alpha)} + W_1^{(j,\beta)} + W_2 + W_0 = 2\mathbf{W}_1^{(j)} + \mathbf{W}_2 + \mathbf{W}_0 \quad (2.41)$$

$$\mathbf{R}_{auto}^{(k)} = W_1^{(k,\alpha)} + W_1^{(k,\beta)} + W_2 + W_0 = 2\mathbf{W}_1^{(k)} + \mathbf{W}_2 + \mathbf{W}_0 \quad (2.42)$$

$$\mathbf{R}_{cross} = \mathbf{W}_0 - \mathbf{W}_2 \quad (2.43)$$

In order to link these relaxation rates to the frequencies of random motion that cause the relaxation, each of the transition probabilities must be written in terms of spectral densities. Figure 2.14 shows examples of spectral density plots for “fast” and “slow” motions, with some common frequencies used in the transition probability equations below indicated.

The **single-quantum transition probability** for spin j in a dipolar coupled two-spin system jk is:

$$W_1^{(j)} = \frac{3}{20}b^2J(\omega_{0,j}) \quad (2.44)$$

Where $J(\omega_{0,j})$ is the spectral density of the dipolar coupling at the Larmor frequency and b is the dipolar coupling constant defined by:

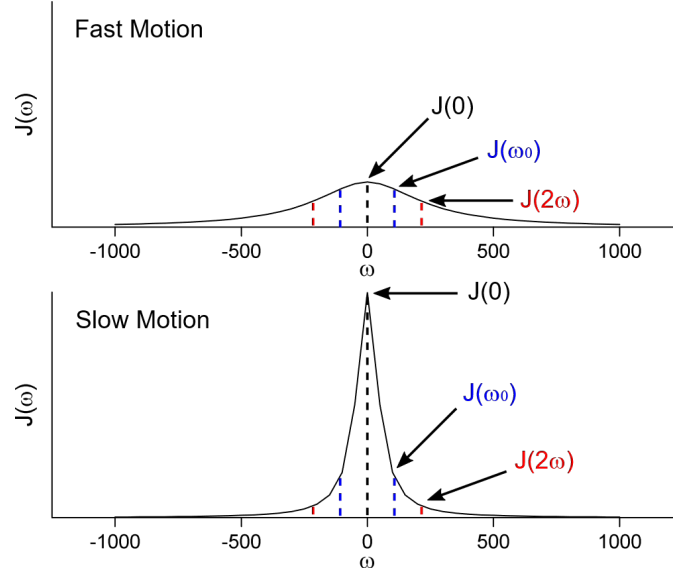


Figure 2.14: Example spectral densities plots for a “fast” and a “slow” motion with the spectral densities at $\omega = 0$, ω_0 and $2\omega_0$ highlighted.

$$b = -\frac{\mu_0}{4\pi} \frac{\gamma_1 \gamma_2 \hbar}{r^3} \quad (2.45)$$

The **double-quantum transition probability** is:

$$W_2^{(j)} = \frac{3}{5} b^2 J(\omega_{0,j} + \omega_{0,k}) \quad (2.46)$$

Which can often be simplified to:

$$W_2^{(j)} = \frac{3}{5} b^2 J(2\omega_0) \quad (2.47)$$

Where $J(2\omega_0)$ is the spectral density of the dipolar coupling at twice the Larmor frequency.

The **zero-quantum transition probability** is:

$$W_0^{(j)} = \frac{1}{10} b^2 J(\omega_{0,j} - \omega_{0,k}) \quad (2.48)$$

Which can often be simplified to:

$$W_0^{(j)} = \frac{1}{10} b^2 J(0) \quad (2.49)$$

Where $J(0)$ is the spectral density of the dipolar coupling at a frequency of zero.

With this new set of transition probabilities in terms of spectral densities, the $R_{auto}^{(j)}$ and R_{cross} rate constants can be re-defined once more:

$$R_{auto}^{(j)} = b^2 \left[\frac{6}{20} J(\omega_{0,j}) + \frac{3}{5} J(\omega_{0,j} + \omega_{0,k}) + \frac{1}{10} J(\omega_{0,j} - \omega_{0,k}) \right] \quad (2.50)$$

$$R_{cross}^{(j)} = b^2 \left[\frac{1}{10} J(\omega_{0,j} - \omega_{0,k}) - \frac{3}{5} J(\omega_{0,j} + \omega_{0,k}) \right] \quad (2.51)$$

These are further simplified as:

$$R_{auto}^{(j)} = b^2 \frac{1}{10} [3J(\omega_{0,j}) + 6J(\omega_{0,j} + \omega_{0,k}) + J(\omega_{0,j} - \omega_{0,k})] \quad (2.52)$$

$$R_{cross}^{(j)} = b^2 \frac{1}{10} [J(\omega_{0,j} - \omega_{0,k}) - 6J(\omega_{0,j} + \omega_{0,k})] \quad (2.53)$$

In the situation where both nuclei are the same isotope, the chemical shift difference is insignificant in terms of relaxation and therefore difference between Larmor frequencies is also negligible. Thus $J(\omega_{0,j} + \omega_{0,k})$ and $J(\omega_{0,j} - \omega_{0,k})$ can be simplified to $J(2\omega_0)$ and $J(0)$ respectively:

$$R_{auto} = b^2 \frac{1}{10} [3J(\omega_0) + 6J(2\omega_0) + J(0)] \quad (2.54)$$

As already mentioned, Equation 2.54 is known as the **auto-relaxation rate**, it is used to describe a spin relaxing by itself.

$$R_{cross} = b^2 \frac{1}{10} [J(0) - 6J(2\omega_0)] \quad (2.55)$$

Equation 2.55 is known as the **cross-relaxation rate** and it is used to determine the rate at which magnetisation is exchanged between two spins via relaxation processes. These equations will be used to establish how dynamic processes contribute to specific types of relaxation, such as spin-lattice or spin-spin relaxation.

2.3.4 Spin-Lattice Relaxation (R_1)

During an NMR experiment RF pulses cause the magnetisation to deviate from the thermal equilibrium. The return of the longitudinal magnetisation back to this equilibrium (i.e. the Boltzmann distribution) is known as spin-lattice relaxation (Figure 2.15). The time taken for this relaxation process to occur is known as the spin-lattice relaxation time (T_1), alternatively the relaxation process can be described by a rate (R_1):

$$T_1 = \frac{1}{R_1} \quad (2.56)$$

Relaxation is generally multi-exponential, however in most cases the deviation from a mono-exponential decay is not significant and so a mono-exponential decay can serve as a reasonable approximation. R_1 is often described by a single exponential of the form shown in Equation 2.57. However, the exact equation used to extract the value of R_1 from an experiment will vary slightly depending on the specific R_1 experiment used.

$$M(t) \propto [M(0) - M_{eq}]e^{-tR_1} \quad (2.57)$$

Where $M(t)$ is the magnetisation at time t after the perturbation, M_0 is the magneti-

sation at time zero and M_{eq} is the equilibrium magnetisation.

The basic method of measuring this relaxation rate involves preparing the system in a non-equilibrium state and repeatedly recording the amplitude of the signal in a spectrum while varying time t , during which the system relaxes back to equilibrium. The relaxation rate can then be extracted from an exponential fit of signal intensity against t . As mentioned above, there are a few different experiments for measuring R_1 , which manipulate the spins in slightly different ways. The experimental details of these pulse sequences are covered in Section 2.3.8.

The spin-lattice relaxation rate contains a large amount of information about the **picosecond - nanosecond** dynamics of a particular nucleus. This is because the motions that are most effective at causing R_1 (i.e. transitions between the α and β states) are on a timescale that is close to the Larmor frequency (i.e. energy gap between the α and β states), this is typically in the ps - ns range. In order to extract this information the various contributions to R_1 must be considered. In this case the important contributions to R_1 are from the dipolar interaction and the CSA:

$$R_1 = R_{1,CSA} + R_{1,DD} \quad (2.58)$$

Where $R_{1,CSA}$ and $R_{1,DD}$ are the contributions to R_1 from the CSA and dipolar couplings, respectively.

Both parts can be described in terms of spectral densities using Equations 2.54 and 2.55. The dipolar contribution to R_1 will be determined by the auto-relaxation rate:

$$R_{1,DD} = \frac{1}{10}b^2\{3J(\omega_{0,j}) + 6J(\omega_{0,j} + \omega_{0,k}) + J(\omega_{0,j} - \omega_{0,k})\} \quad (2.59)$$

The CSA can also contribute to R_1 , the following expression accounts for this:

$$R_{1,CSA} = \frac{2}{15}\omega_0^2(\sigma_{11}^2 + \sigma_{22}^2 + \sigma_{33}^2 - \sigma_{11}\sigma_{22} - \sigma_{11}\sigma_{33} - \sigma_{22}\sigma_{33})J(\omega_0) \quad (2.60)$$

Where σ_{xx} are the components of the CSA ($\sigma_{11} > \sigma_{22} > \sigma_{33}$).

The specific equations used to link R_1 to the spectral densities must be considered on an individual basis depending on the particular experiment and sample used. Section 2.3.7 explains the models used to extract the amplitudes and timescales of dynamics from the measured relaxation rates.

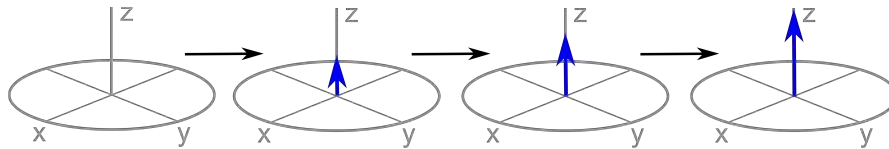


Figure 2.15: The mechanism of spin-lattice relaxation (R_1): the longitudinal magnetisation, represented by the blue arrow, returns to its equilibrium value.

2.3.5 Spin-Spin Relaxation (R_2)

An RF pulse will create magnetisation in the xy -plane. The decay of this transverse magnetisation to zero at equilibrium is known as spin-spin relaxation (Figure 2.16). It is quantified by the spin-spin relaxation time (T_2) or the spin-spin relaxation rate (R_2) where:

$$T_2 = \frac{1}{R_2} \quad (2.61)$$

Spin-spin relaxation can also be described in terms of spectral densities. It is particularly sensitive to slower dynamics, on the **nanosecond - millisecond** timescale through its $J(0)$ term. In the case of dipolar relaxation and the CSA contributions are described by Equation 2.62 and 2.63, respectively:

$$R_{2,DD} = \frac{3}{20}b^2\{3J(\omega_{0,j} - \omega_{0,k}) + 5J(\omega_{0,j}) + 2J(\omega_{0,j} + \omega_{0,k})\} \quad (2.62)$$

$$R_{2,CSA} = \frac{1}{3}\omega_0^2(\sigma_{11}^2 + \sigma_{22}^2 + \sigma_{33}^2 - \sigma_{11}\sigma_{22} - \sigma_{11}\sigma_{33} - \sigma_{22}\sigma_{33})\frac{2}{3}J(0) + \frac{1}{2}J(\omega_{0,j}) \quad (2.63)$$

2.3.6 Spin-Lattice Relaxation in the Rotating Frame ($R_{1\rho}$)

Another important type of relaxation to consider is spin-lattice relaxation in the rotating frame, known as $R_{1\rho}$. This is the measurement of R_1 under the presence of a spin-lock pulse (B_1) in the same direction as the magnetisation. The spin-lock pulse suppresses the free evolution of transverse magnetisation, “locking” it into a particular direction in the rotating frame. $R_{1\rho}$ is similar to R_1 , which is the relaxation along the B_0 field, except in this case it is the relaxation along the applied, significantly smaller, B_1 field (Figure 2.17).

$$R_{1\rho} = \frac{1}{T_{1\rho}} \quad (2.64)$$

$R_{1\rho}$ is sensitive to motion on the **nanosecond - millisecond** timescale through its $J(\omega_1)$ term (i.e. motions on a similar timescale to the spin-lock pulse), similar to R_2 , and is also sensitive to the MAS frequency (through terms involving $J(\omega_r)$). However $R_{1\rho}$ measurements are much more suitable for determining slow protein dynamics than

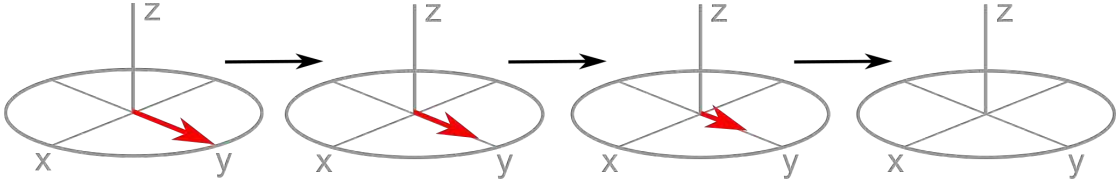


Figure 2.16: The mechanism of spin-spin relaxation (R_2): the transverse magnetisation, represented by the red arrow, returns to equilibrium.

R_2 measurements, since in R_2 measurements it is far more challenging to remove the coherent processes originating from incompletely averaged anisotropic interactions.

The spectral density equations for the contributions to $R_{1\rho}$ from the dipolar interaction ($R_{1\rho,DD}$) and CSA ($R_{1\rho,CSA}$) are presented below in which ω_1 is the frequency of the spin-lock pulse and ω_r is the MAS frequency, together these equations form the total $R_{1\rho}$:

$$R_{1\rho,DD} = \frac{1}{20}b^2\left\{\frac{2}{3}J(\omega_1 + 2\omega_r) + \frac{2}{3}J(\omega_1 - 2\omega_r) + \frac{4}{3}J(\omega_1 + \omega_r) + \frac{4}{3}J(\omega_1 - \omega_r) \right. \\ \left. + 4J(\omega_1) + 3J(\omega_{0,k}) + J(\omega_{0,j} - \omega_{0,k}) + 6J(\omega_{0,j}) + 6J(\omega_{0,j} + \omega_{0,k})\right\} \quad (2.65)$$

$$R_{1\rho,CSA} = \frac{1}{45}\omega_j^2(\sigma_{11}^2 + \sigma_{22}^2 + \sigma_{33}^2 - \sigma_{11}\sigma_{22} - \sigma_{11}\sigma_{33} - \sigma_{22}\sigma_{33})\{(4J\omega_1) + (3J\omega_{0,j})\} \quad (2.66)$$

2.3.7 The Model Free Approach

These relaxation rate measurements contain a wealth of information on the molecular dynamics. However, in order to estimate the correlation time and amplitude of such motions, these rates need to be fitted to a model. Particularly popular models for relaxation rate data are the **simple model free** (SMF) and **extended model free** (EMF) approaches developed by Lipari and Szabo.^{28,29}

The SMF approach allows the estimation of the order parameters (i.e. effective amplitudes) and correlation times (i.e. effective timescales) of the motions occurring throughout the molecule. As described previously, the **correlation time** (τ_c) describes how fast motion takes place; a shorter correlation time represents a motion with higher frequency. In the absence of a specific model of motion, the **order parameter** (S^2) can be used to provide a general measure of the amplitude of motion. S^2 ranges from 0 to 1, where 0 represents unrestricted motion and 1 indicates a rigid case. S^2 and τ_c can be extracted from measured relaxation rates via the spectral density equations for the particular relaxation rate (discussed in the previous section) and the following SMF expression for spectral density:

$$J(\omega) = (1 - S^2) \frac{\tau_c}{1 + (\omega\tau_c)^2} \quad (2.67)$$

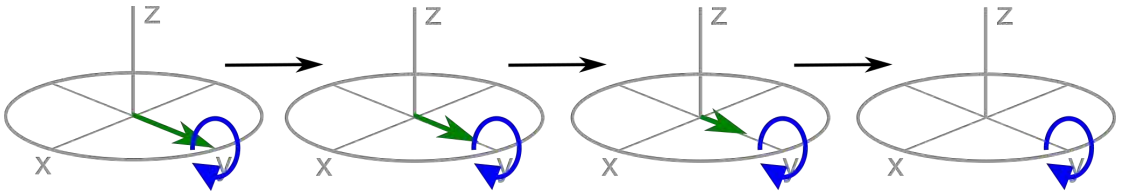


Figure 2.17: The mechanism of spin-lattice relaxation in the rotating frame. The blue circular arrow represents the spin-lock pulse along the y -axis.

The SMF approach provides a simple method of estimating the order parameter and correlation time of a site from its relaxation rate. However this model assumes that only a single motion contributes to the relaxation rate and so produces an average representation of the potentially complex dynamics. A more detailed model, such as the extended model free approach,⁵⁹ may be used if enough data is available. The EMF equation for spectral density is used for fitting both a “slow” and “fast” motion to the relaxation data and so has the potential to produce a more realistic representation of the dynamics (Equation 2.68).

$$J(\omega) = (1 - S_f^2) \frac{\tau_f}{1 + (\omega\tau_f)^2} + S_f^2(1 - S_s^2) \frac{\tau_s}{1 + (\omega\tau_s)^2} \quad (2.68)$$

Where S_f^2 and S_s^2 are the order parameters and τ_f and τ_s are the correlation times for the fast and slow motions, respectively.

It must be noted however that the EMF approach involves the fitting of four parameters (S_f^2 , τ_f , S_s^2 and τ_s) and so should only be used in the cases where ample data is present, otherwise an accurate fit will not be possible.

2.3.8 Relaxation Experiments

Now that the theory behind different types of relaxation (R_1 , R_2 and $R_{1\rho}$) has been presented and the methods of extracting dynamic information from the relaxation rates have been described, it is appropriate to discuss how to measure relaxation rates experimentally.

Throughout this thesis a handful of important relaxation experiments are referred to on multiple occasions: The saturation recovery and “Torchia” methods are implemented for measuring fast dynamics (R_1) in the protein experiments and the ice experiments, respectively. To investigate slower motions, $R_{1\rho}$ is implemented in the protein experiments and both $R_{1\rho}$ and R_2 are used in the ice experiments. These pulse sequences and experiments are explained below.

Measuring R_1 : The “Torchia” Method

The significant advantages of using cross polarisation to enhance the sensitivity of measurements on more dilute nuclei were highlighted in Section 2.2.3. When measuring ^{13}C and ^{15}N R_1 in proteins, it is vital that cross polarisation is used. Some techniques for measuring R_1 , such as *inversion-recovery*⁶⁰ and *saturation-recovery*,⁶¹ are not compatible with using cross polarisation in the pulse sequence and so the “Torchia” method,⁶² which will be explained in detail here, is most suitable. An additional benefit of using this experiment is that it is limited by the ^1H T_1 rather than the ^{13}C T_1 and so it can be repeated faster, reducing the experimental time.

Published in 1978, this method combines the improved signal of a ^1H -X CP with an R_1 measurement on the, now enhanced, X magnetisation. An example Torchia pulse sequence is illustrated in Figure 2.18 for X R_1 measurements. This pulse sequence uses two steps of phase cycling in order to cancel out the effects of the direct X Boltzmann

magnetisation. First, the steps of the pulse sequence are explained with the two different phase cycles (coloured in red and blue for clarity) and finally result of combining them is discussed.

An initial 90° pulse rotates the ^1H magnetisation into the xy -plane and then cross polarisation is used to transfer the magnetisation from the ^1H to the X nuclei. After the CP, either a 90°_{-y} or 90°_{+y} pulse on X rotates the magnetisation onto the $+z$ -axis or $-z$ -axis. It is here that a variable delay provides time for relaxation to the X equilibrium Boltzmann value to start. (Note that after the 90°_{-y} pulse, the X magnetisation on the z -axis is far greater than the equilibrium value due to the CP from ^1H , hence the following decrease in magnetisation to the Boltzmann value.) At the end of the relaxation delay there is a final 90°_x pulse on X to rotate the magnetisation into the xy -plane. Finally, the X magnetisation is recorded (^1H decoupling is applied during the acquisition). Examples of the magnetisation throughout this pulse sequence with short and long relaxation delays for both parts of the phase cycles are illustrated in Figure 2.18. The resulting plots of signal against relaxation delay for both and the combined plot are also presented.

Overall this pulse sequence will give maximum signal if no delay is used. If a very long delay is used, allowing the signal to fully relax, the resulting spectrum will have no signal. For a complete R_1 experiment, the pulse sequence is repeated with various delay lengths (for example from 0.01 s to 15 s) and the integrals of the resulting peaks are recorded. During this “**relaxation delay**” (τ) the magnetisation relaxes and so the signal intensity decreases. A plot of this intensity against the delay length should give an exponential decay, which can be fitted to the following equation:

$$M_\tau = M_0 e^{(-R_1 \tau)} \quad (2.69)$$

Where τ is the variable delay, M_τ is the magnetisation at time τ and M_0 is the magnetisation at time 0.

A final complication to this experiment is that usually, while studying proteins, it is necessary to record 2D spectra to achieve reasonable resolution (rather than just 1D as implied above). It is also worth noting that typical R_1 values for proteins are 1 - 200 ms for ^{15}N and 50 - 600 ms for ^{13}C .

Measuring R_1 : Saturation Recovery

Saturation recovery,^{63,64} an alternative method for measuring R_1 , is used for the ^1H R_1 experiments on ice samples. Typical ^1H R_1 values for ice are in the range of 100 - 1000 ms. This method is selected in this situation because it is a simple method that allows a very rapid repetition of experiments because there is no T_1 wait time at the end of the experiment. It is worth noting that cross polarisation is not needed for these ^1H relaxation experiments and so using the Torchia method (described above) would be inappropriate.

Figure 2.19 shows a saturation recovery pulse sequence. It starts, as the name suggests, by saturating the spins using a series of non-selective 90° pulses.⁶⁴ This causes

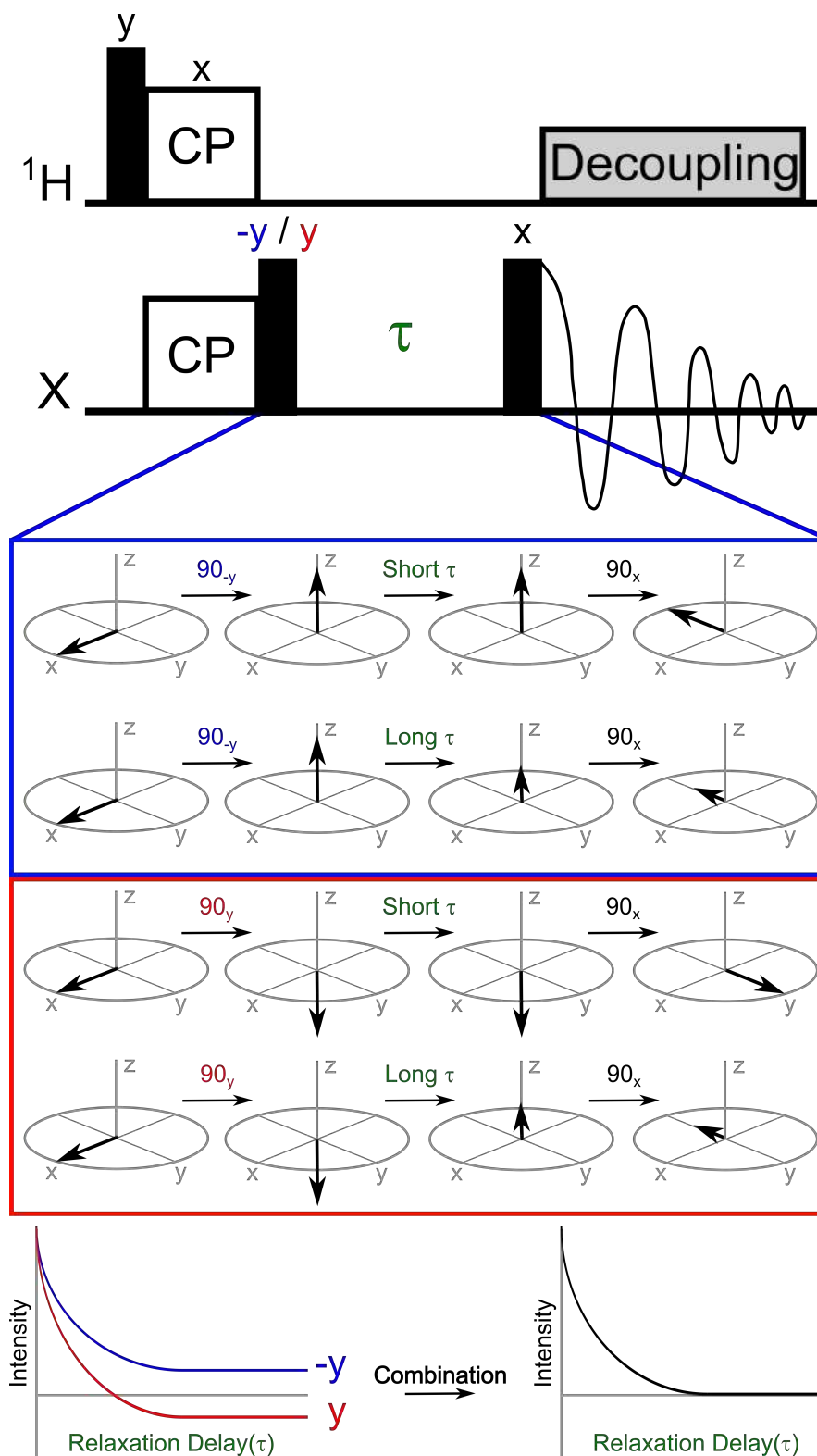


Figure 2.18: Example R_1 pulse sequence using the Torchia method. The effect of short and long relaxation delays on the bulk magnetisation for both parts of the phase cycle are illustrated, alongside the resulting plots of signal against relaxation delay. In both cases, the magnetisation vector after the “long τ ” represents the X magnetisation at its equilibrium value (i.e. fully relaxed).

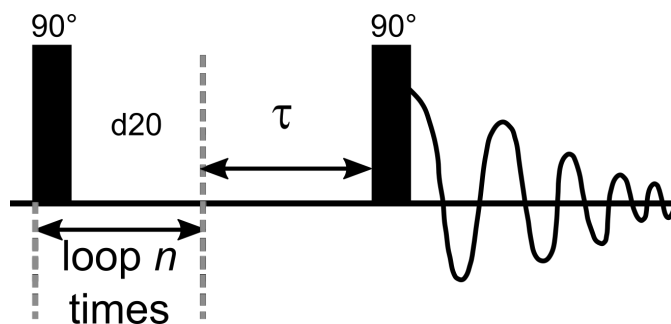


Figure 2.19: ^1H saturation recovery R_1 pulse sequence. The spins are saturated by the series of n non-selective 90° pulses. The relaxation delay (τ) is varied in order to observe the relaxation process.

the spins equally populate the states, thus there is no net magnetisation. After time τ , a 90° pulse rotates any z -magnetisation into the xy -plane for detection. During time τ the spins start to return to their equilibrium state resulting in an increased signal over time (Figure 2.20). This signal recovery is fitted to the following equation:

$$M_\tau = M_0(1 - e^{-R_1\tau}) \quad (2.70)$$

Where M_0 is a constant related to the initial magnetisation.

Measuring R_2 : CPMG

Many ^1H R_2 measurements are taken on the frozen antifreeze solutions in Chapter 6 using a pulse sequence known as **Carr-Purcell-Meiboom-Gill** (CPMG). This sequence starts with a 90° pulse to create magnetisation in the xy -plane, followed by a spin-echo period repeated n times before acquisition (see Figures 2.21 and 2.22). The effect of the spin-echo period on the spins is to reverse the *inhomogeneous* part of the T_2 signal decay (i.e. the distribution of offset frequencies due to magnetic field inhomogeneity) while allowing the *homogeneous* part of the T_2 decay (i.e. the natural distribution of frequencies due to the T_2 relaxation process) to be measured. Homogeneous broadening is caused by fluctuations in the microscopic magnetic fields and it is quantified by R_2 , whereas inhomogeneous broadening is caused by variations in the B_0 field throughout the sample. The separation of these effects is key to accurately measuring R_2 . The spin-echo period has to be very small to ensure diffusion effects are negligible, otherwise the spins will not be refocussed completely. Thus, a train of spin-echoes with short τ delays is used. As the number of these spin-echo repeats (n) is increased, the resulting signal decreases due to the homogeneous broadening.

The value of R_2 can be calculated from monitoring the intensity of the NMR signal as a function of length of the total spin-echo period ($\tau = n \times \text{time for a single spin-echo}$), see Equation 2.71. In these experiments a single spin-echo period was on the order of a few microseconds and n was varied from 2 into the hundreds.

$$M_\tau = Ae^{(-R_2\tau)} \quad (2.71)$$

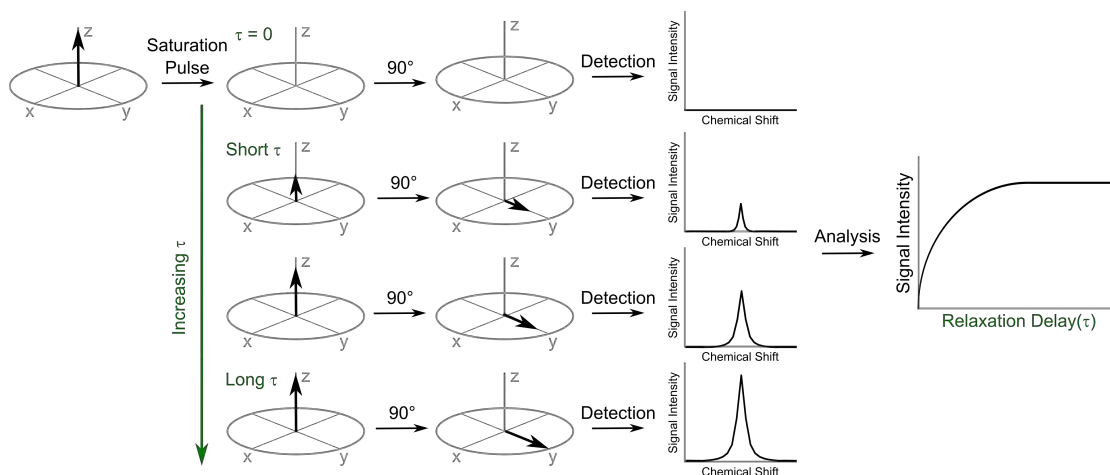


Figure 2.20: An illustration of how the spins react to this R_1 saturation recovery pulse sequence with an example spectrum at different values of τ . An example of a saturation decay R_1 plot is included on the right-hand side.

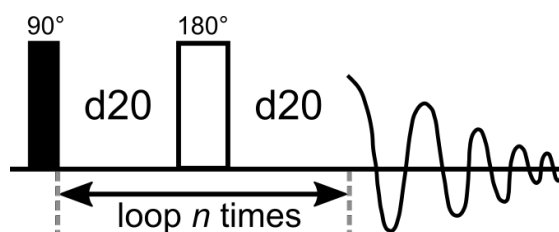


Figure 2.21: ^1H R_2 CPMG pulse sequence. The spin-echo is repeated n times. Varying n allows the decay of the transverse magnetisation to be observed.

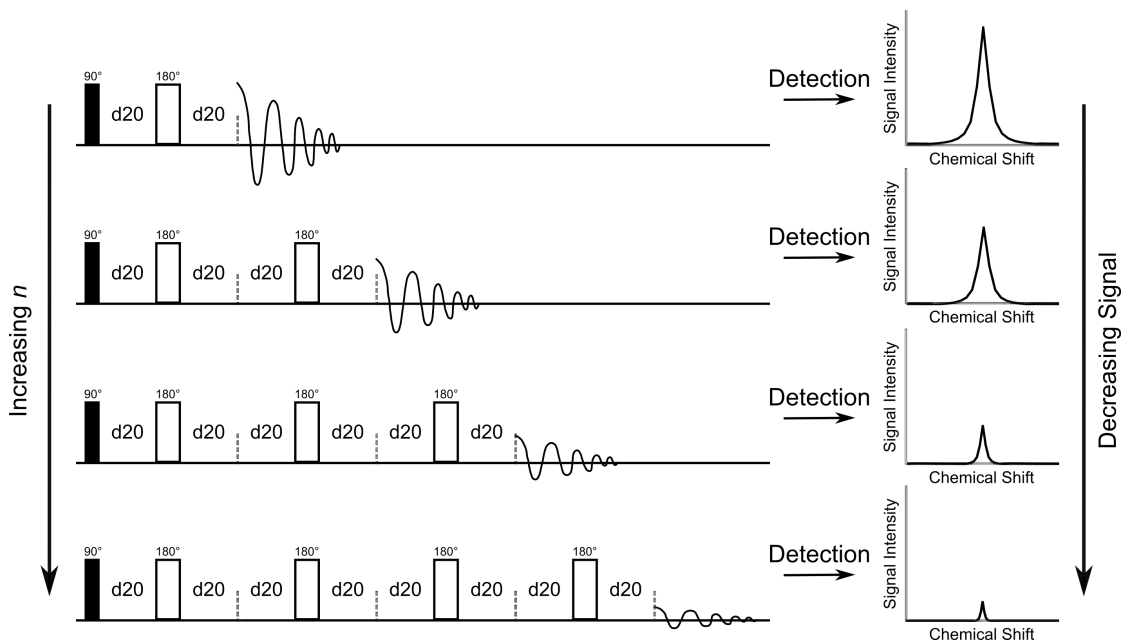


Figure 2.22: Effect of increasing the number of spin-echoes on the resulting signal in a ^1H R_2 CPMG pulse sequence.

Measuring $R_{1\rho}$:

$R_{1\rho}$ is measured in a similar way to R_1 except that, instead of a variable relaxation delay, a variable length spin-lock pulse (of length τ) is applied. $R_{1\rho}$ is much faster than R_1 and so significantly shorter times will be used for these spin-lock pulses (for example, 0.1 ms - 200 ms).

The minimum power of the spin-lock pulse needed to accurately measure $R_{1\rho}$ will vary depending on a variety of conditions, including nucleus and sample type (as an example 8 kHz is used for ^{13}C nuclei in a protein in Chapter 4). In a similar manner to the R_1 measurement, a plot of peak intensity versus spin-lock pulse length should result in an exponential decay (Figure 2.23) and the value of $R_{1\rho}$ can be extracted from the exponential fit of the graph through Equation 2.72.

$$M_\tau = M_0 e^{(-R_{1\rho}\tau)} \quad (2.72)$$

2.3.9 Relaxation Dispersion Measurements

Relaxation dispersion (RD) is measured on the frozen antifreeze solutions in Chapter 6 in order to extract further information on microsecond exchange processes. Here, the relationship between RD and exchange is discussed.

The presence of chemical exchange on the microsecond timescale will cause an increase in the measured $R_{1\rho}$, due to the nuclei spending time in different chemical environments during the spin-lock pulse. This effect can be suppressed by using a higher spin-lock power, which effectively flips the magnetisation more frequently and therefore it has less time to change to the other state. Spin-lock pulses are typically in the range of 1 - 50 kHz, hence why these measurements provide insight to microsecond exchange processes. The process of measuring $R_{1\rho}$ with a range of spin-lock powers is known as **relaxation dispersion**.

Figure 2.24 shows an example of relaxation dispersion measurements on a sample: Firstly the measured $R_{1\rho}$ plots for a range of spin-lock powers are presented and then the extracted $R_{1\rho}$ rates from these are plotted against the spin-lock power. In this example it is clear that $R_{1\rho}$ rapidly increases with decreased spin-lock power, showing that this sample is undergoing a microsecond exchange process. If there is no exchange on the relevant timescale, $R_{1\rho}$ will not vary in this way. Note that coherent contributions, which originate from insufficiently averaged anisotropic interactions, can also contribute to the relaxation dispersion effect (pseudodispersion).

2.3.10 Temperature and Relaxation

Molecular motion, which causes fluctuating magnetic fields, is the dominant cause of relaxation. Thus it is only logical that variation in temperature will affect these motions and alter relaxation rates. In certain cases, the relationship between a relaxation rate and temperature can aid in the extraction of dynamic information from the data. This concept is used in Chapter 4 to help determine the trends in motion throughout the

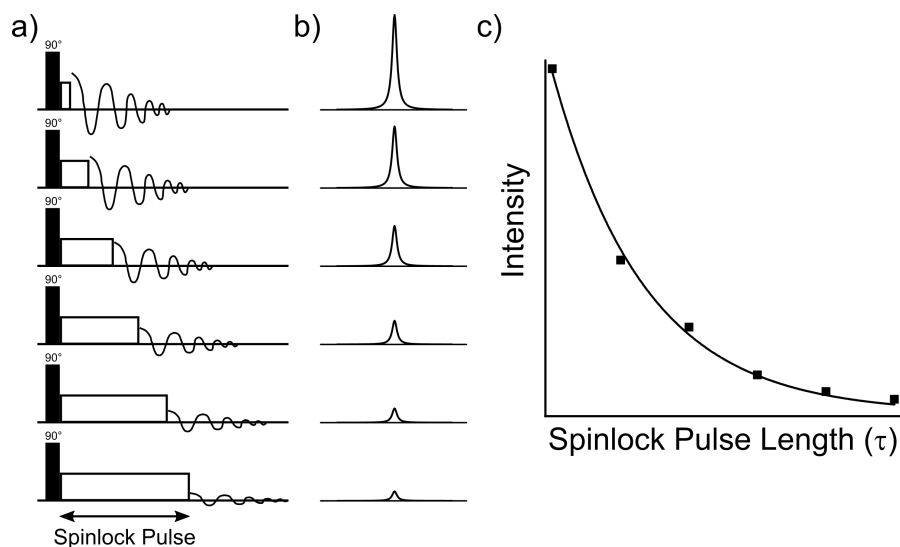


Figure 2.23: An example of a) an $R_{1\rho}$ pulse sequence with the spin-lock pulse of varying length, b) the resulting spectra (with decreasing intensity) and c) the plot of intensity against the delay time used to calculate $R_{1\rho}$.

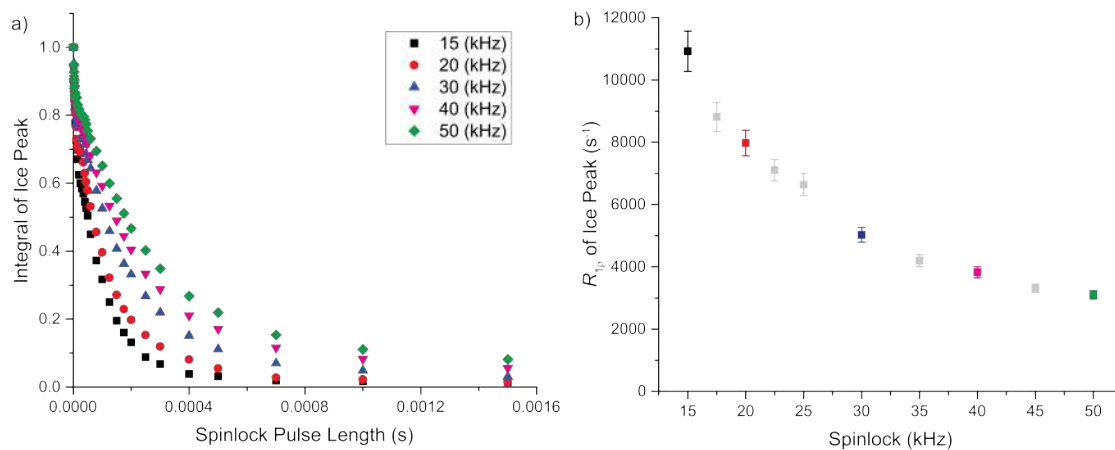


Figure 2.24: a) Examples of the exponential decay due to $R_{1\rho}$ using different spin-lock frequencies. b) These $R_{1\rho}$ rates (plus others) plotted against spin-lock frequency. It is clear that the measured value of $R_{1\rho}$ is strongly affected by the spin-lock frequency and therefore that this site is undergoing exchange on the microsecond timescale.

backbone of a protein and in Chapter 6 to compare the dynamics of ice protons within different frozen antifreeze solutions.

Firstly the approximate relationships of the spin-lattice and spin-spin relaxation times (T_1 and T_2) with correlation time are presented in Figure 2.25. Note that T_1 passes through a minimum, whereas T_2 decreases with increased correlation time. Additionally, at very short correlation times T_1 and T_2 are equal, this is known as the **extreme narrowing limit** and is valid in cases of very fast motion, such as in a liquid. Correlation times are inversely proportional to temperature: increasing the temperature will speed up motions, decreasing their correlation time. This suggests that T_2 will always increase with warming. Whereas T_1 will have a clear minimum at the correlation time at which relaxation is most efficient ($\tau_c = 1/\omega_0$).

The **Arrhenius** equation defines the relationship between temperature and the rate of a thermally-activated process, such as molecular motion. This equation can be adapted so that an activation energy (E_a) can be obtained from a plot of the correlation time as a function of temperature:

$$\tau_c = Ae^{\frac{E_a}{RT}} \quad (2.73)$$

Where A is a pre-exponential factor, R is the gas constant and T is temperature.

In certain cases, such as in the extreme narrowing limit (where T_1 has a linear relationship with correlation time and therefore also with temperature), the gradient of a plot of $\ln(T_1^{-1})$ against the inverse temperature will be proportional to the activation energy. However, in most cases, the relationship between the relaxation rate and temperature is more complex and so a different approach for obtaining activation energies is required.

One common method for analysing relaxation data with a temperature dependence is to combine the Arrhenius equation with the model free approach (see Section 2.3.7). In the model free approach, each relaxation rate consists of various spectral densities at particular frequencies and these spectral densities are related to the correlation times and order parameters of motions. To elaborate, in the spectral density equation presented below the correlation time now has a temperature dependency, defined by Equation 2.75:

$$J(\omega) = (1 - S^2) \frac{\tau_c}{1 + \omega^2 \tau_c^2} \quad (2.74)$$

$$\tau_c = \tau_0 e^{\left(\frac{E_a}{RT}\right)} \quad (2.75)$$

Now, instead of the spectral density equations fitting just τ_c and S^2 to a relaxation rate, they can be used to fit τ_0 , S^2 and E_a to a set of variable-temperature relaxation rates. τ_0 is a temperature-independent constant relating to the correlation time. The correlation time at any temperature can then be calculated from τ_0 and E_a using Equation 2.75. In this example the equations are based on the SMF approach and therefore depend on the

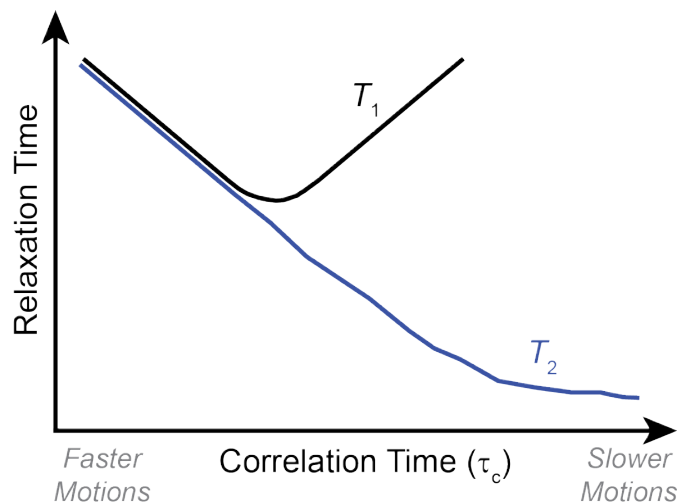


Figure 2.25: Approximate variation in T_1 and T_2 with correlation time. Adapted from Bloembergen *et al.*⁶⁵

assumption that a single motion dominates these relaxation measurements. Of course this method of incorporating the temperature-dependence of the correlation time into the spectral density equations can also be applied to the EMF approach if sufficient data is present.

2.3.11 The Nuclear Overhauser Effect

The nuclear Overhauser effect (NOE) is the transfer of magnetisation from one spin to another via dipolar cross-relaxation. The differential equation for the rate of change in the z-magnetisation of spin j will have a contribution from the cross-relaxation rate constant (σ_{jk}) if spin k is not at equilibrium:

$$\frac{dI_{j,z}}{dt} = -R_z^j(I_{j,z} - I_{j,z}^0) - \sigma_{jk}(I_{k,z} - I_{k,z}^0) \quad (2.76)$$

This cross-relaxation, which has a $\frac{1}{r^6}$ distance dependence, leads to the nuclear Overhauser effect (NOE). NOE measurements involve the saturation of particular nuclei and then the observation of which nuclei are affected. In 2D NOESY (nuclear Overhauser effect spectroscopy) spectra, the nuclear Overhauser cross relaxation between spins during the mixing period is used to establish the correlations. The resulting 2D spectrum has non-diagonal cross peaks that connect resonances from nuclei that are spatially close. The relative intensities and signs of the crosspeaks are dependent on the cross-relaxation rate constant and thus provide information on internuclear distances.

2.3.12 Chemical Exchange

A chemical exchange process between two state can either be described as “slow” ($k \ll |\Delta\nu|$) or “fast” ($k \gg |\Delta\nu|$) relative to the difference in chemical shift between the two states. The rate of exchange has important effects on NMR spectra and relaxation rates. In the case of slow exchange, both states will be distinctly observed in an NMR spectrum at their respective chemical shifts. As the rate of exchange increases the peaks will merge

into a single peak representing the population-weighted average of the chemical shifts. Exchange spectroscopy (EXSY)^{66,67} is used to quantify slow exchange processes. An EXSY measurement is actually the same as a NOESY measurement, they both produce crosspeaks for nuclei that are close in space and nuclei that are undergoing exchange. The name used typically depends on the purpose of the experiment.

Exchange processes can significantly contribute to relaxation rates, which can be used to provide an insight into the dynamics and chemical exchange rate of the nuclei. Slow exchange processes will contribute to R_2 in the following way:

$$R_2^{Obs} = R_2^0 + k \quad (2.77)$$

Where R_2^{Obs} is the observed relaxation rate, R_2^0 is relaxation in the absence of exchange and k is the rate of the exchange.

Increasing the exchange rate, for example by increasing the temperature, will increase its contribution to the observed relaxation rate. Whereas the contribution of fast exchange processes will decrease as the exchange rate increases:

$$R_2^{Obs} = R_2^0 + \frac{p_a p_b \Delta\omega^2}{k} \quad (2.78)$$

Where p_a and p_b are the populations of states a and b , and $\Delta\omega^2$ is the chemical shift difference between the two states.

In the case of $R_{1\rho}$, chemical exchange on the microsecond timescale will have the following contribution, which depends on the spin-lock frequency:

$$R_{1\rho}^{Obs} = R_{1\rho}^0 + \frac{p_a p_b \Delta\omega^2 k}{\omega_{eff}^2 + k^2} \quad (2.79)$$

Where $R_{1\rho}^{Obs}$ is the observed $R_{1\rho}$, $R_{1\rho}^0$ is the $R_{1\rho}$ in the absence of any microsecond exchange contributions, k is the exchange rate and ω_{eff} is the spin-lock frequency.

2.3.13 Spin Diffusion

Spin diffusion is a coherent process that promotes spontaneous exchange of magnetisation between spins. If this magnetisation transfer happens sufficiently fast compared to relaxation times during relaxation rate measurements, the measured rates are averaged over several sites, meaning that they are no longer site specific.⁶⁸⁻⁷¹ Thus it is important that the effects of spin diffusion are effectively suppressed in relaxation measurements. It is particularly challenging to do so in R_1 measurements.

During protein ^{13}C and ^{15}N R_1 measurements the most efficient spin diffusion is assisted by the dipolar couplings to protons. This is known as proton-driven spin diffusion (PDS) and its rate is dependent on the cross terms involving $^1\text{H-X}$ and X-X dipolar couplings, where $\text{X} = ^{13}\text{C}$ or ^{15}N . ^{15}N measurements tend to be less affected by PDS than ^{13}C due to their lower gyromagnetic ratio and therefore smaller dipolar couplings, as well as being sparsely spread throughout the protein. The rate of PDS can be reduced by fast MAS, dilution of the ^1H network or application of RF pulses.

Although, the latter technique is rarely used in practice due to the requirement of high RF pulses that may damage the equipment or sample.

Suppressing PDS is huge problem for aliphatic ^{13}C nuclei in particular, due to their strong one-bond ^1H - ^{13}C and ^{13}C - ^{13}C dipolar couplings. As previously discussed, if the coupled nuclei have a small chemical shift difference, relative to the dipolar coupling constant, higher-order terms will become relevant. This is the case for some $^{13}\text{C}^\alpha$ $^{13}\text{C}^\beta$ nuclei that are close in chemical shift, and therefore fast MAS will only eliminate some of the dipolar interaction terms.

In addition to fast spinning, partial ^{13}C labelling or deuteration can be used to remove some of these pathways for PDS. This combination of techniques allows for accurate, site-specific R_1 measurements on aliphatic ^{13}C nuclei, but there are various disadvantages to using these isotopic labelling schemes. In this light, Chapter 4 focuses on methods of eliminating the effects of proton-driven spin diffusion from site-specific $^{13}\text{C}^\alpha$ R_1 measurements on fully-protonated, uniformly ^{13}C labelled proteins.

Calculating the Effect of Spin Diffusion on R_1

In the case of a two-spin system coupled by spin diffusion, the spin diffusion can be described by the following equation:⁶⁹

$$\frac{\partial}{\partial t} \begin{bmatrix} I \\ S \end{bmatrix} = -(K + R) \cdot \left(\begin{bmatrix} I \\ S \end{bmatrix} - \begin{bmatrix} M^0 \\ M^0 \end{bmatrix} \right) \quad (2.80)$$

Where $K = \begin{bmatrix} -\sigma & \sigma \\ \sigma & -\sigma \end{bmatrix}$, $R = \begin{bmatrix} R_1^I & 0 \\ 0 & R_1^S \end{bmatrix}$ and M^0 is the magnetisation at thermal equilibrium. In this system, two spins are considered, I and S, with spin-lattice relaxation rates R_1^I and R_1^S , magnetisations I and S (at time t) and an exchange rate of σ (due to PDS).

The evolution of the above system can be described by Equations 2.81 and 2.82:

$$\frac{\partial I}{\partial t} = -R_1^I(I - M^0) - \sigma(I - S) \quad (2.81)$$

$$\frac{\partial S}{\partial t} = -R_1^S(S - M^0) - \sigma(S - I) \quad (2.82)$$

Equations 2.81 and 2.82 were solved (using *Matlab*) allowing the effect of PDS on the true R_1 to be calculated. Calculating the time dependence of the magnetisation of spins I and S will simulate the relaxation of this nucleus over time when coupled to the other spin, and fitting an exponential curve to this allows for calculation of the effective R_1 . The solution to Equations 2.81 and 2.82, and *Matlab* scripts used for these calculations are included in Appendix A.2.

The simulations presented in Figure 2.26 highlight just how effective PDS is at altering the measured relaxation rates from their true values. If the exchange rate is faster than either of the relaxation rates it will completely dominate the system and the

measured relaxation rates will no longer contain any site-specific information. Even a PDSD exchange rate an order of magnitude smaller than the true relaxation rates can still significantly alter the measured rates, so it is critical to reduce the PDSD exchange rate as much as possible during relaxation measurements.

There are two limiting cases for magnetisation exchange due to PDSD: $2\sigma \gg |R_1^I - R_1^S|$ and $2\sigma \ll |R_1^I - R_1^S|$.⁷² In the former case the PDSD rate will clearly dominate the measured relaxation rates, causing the magnetisation to decay bi-exponentially for both spins at an averaged rate. In this situation it is not possible to determine reliable dynamics data. The latter case, where the difference in relaxation rates is much greater than the rate of spin diffusion, will produce independent mono-exponential decays for the spins I and S with the rates of $R_1^I + \sigma$ and $R_1^S + \sigma$, respectively. In this case if σ is sufficiently small compared to the relaxation rates it will be possible to obtain reliable dynamics data.

Further simulations revealed that the system that causes the largest deviation in the measured R_1 of spin I is one where spin I relaxes much faster and is much less polarised than spin S. This, in the majority of cases, matches the situation between the adjacent $^{13}\text{C}^\alpha$ and $^{13}\text{C}^\beta$ nuclei in the relaxation measurements throughout Chapter 4: $^{13}\text{C}^\beta$ R_1 is typically far greater than $^{13}\text{C}^\alpha$ R_1 due to the increased dynamics of a sidechain, however the $^{13}\text{C}^\alpha$ peaks tend to be far more intense. This suggests why it can be so challenging to suppress PDSD at during these $^{13}\text{C}^\alpha$ relaxation measurements.

2.3.14 Chemical Exchange Saturation Transfer

Chemical exchange saturation transfer (CEST) was originally developed for use with contrast agents in magnetic resonance imaging (MRI).⁷³ In this situation, a low concentration contrast agent that has exchangeable protons is selectively saturated and then detected indirectly through the water, causing significant changes in the water signal. If the experiment is conducted with and without the saturation pulse, the difference between these two spectra will provide a huge enhancement in the area affected by the contrast agent. Subsequently, there has been a substantial amount of interest in developing CEST and compatible contrast agents for improved MRI.^{74–84}

CEST (also related to dark-state exchange saturation transfer, “DEST”^{85,86}) has also been applied to solution-state NMR in cases where an “invisible” (or low concentration) state is in exchange with a visible, higher concentration state. For successful CEST, the exchange rate should approximately be on the order of 20 - 300 s⁻¹ and the population of the invisible minor state(s) should be $\geq 1\%$.⁸⁷ During CEST, a weak RF pulse is applied step-by-step across the range of frequencies for a particular nucleus and a spectrum will be recorded at each step. If this RF pulse is applied on-resonance with the major state, it will be saturated and there will be a complete loss of signal. Critically, if this RF pulse is applied on-resonance with a minor state, the minor state will be saturated, which is then transferred to the major state via the exchange mechanism. This results in a decrease in intensity of the major state peak. By repeating this experiment while sweeping the frequency of the RF pulse, any invisible minor states in

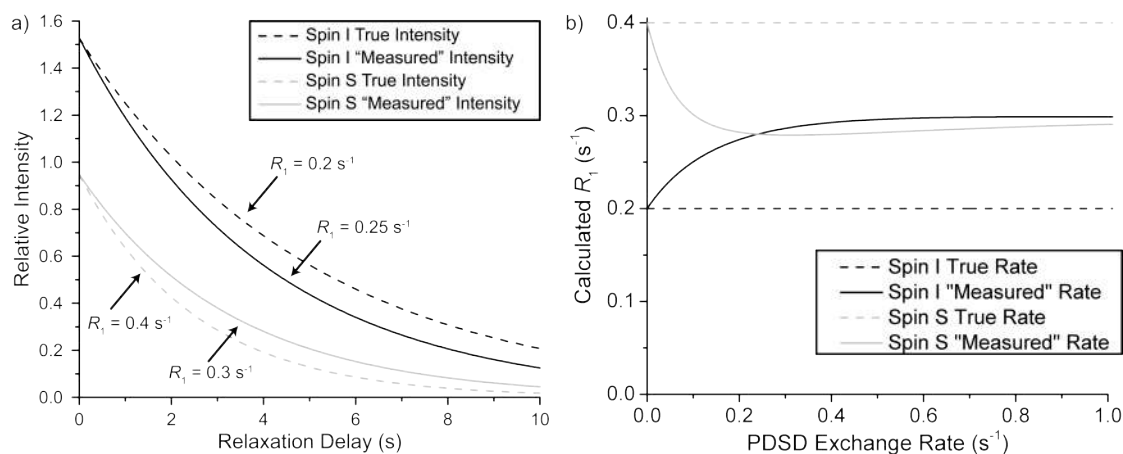


Figure 2.26: a) A comparison of the calculated “measured” and true relaxation decays for spins I and S with a PDSD exchange rate of 0.1 s^{-1} . b) A plot demonstrating how the calculated “measured” $^{13}\text{C}\alpha R_1$ varies from its true value as the PDSD exchange rate is varied. In both cases, the true R_1 of spins I and S are 0.2 and 0.4 s^{-1} and the relative initial polarisations are 1.5 and 1 respectively.

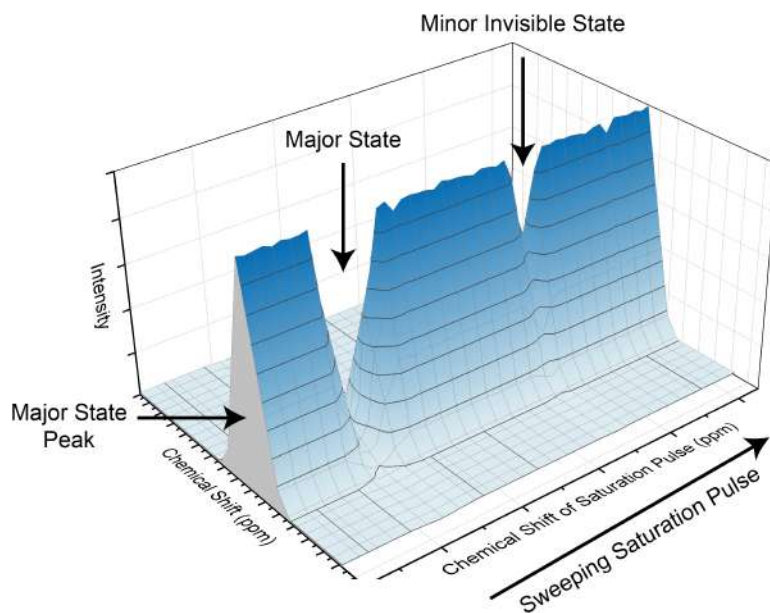


Figure 2.27: CEST: The major (visible) peak changes intensity as the saturation pulse sweeps across the spectrum. It decreases in intensity as the major and minor (invisible) peaks are saturated.

exchange with the major state will be revealed indirectly via the major state spectra. The resulting data can then be presented as a plot of major peak intensity as a function of the RF pulse frequency. This concept is illustrated in Figure 2.27.

Solution-state CEST has been used in many cases to identify minor or unfolded states of various proteins,^{87–92} such as amyloid- β ^{85,86} and SOD1,⁹³ which are known to be involved in Alzheimer’s disease and amyotrophic lateral sclerosis, respectively. In Chapter 4, SSNMR $^{13}\text{C}^\alpha$ “CEST-like” measurements are presented, which are used to observe polarisation transfer between neighbouring ^{13}C sites due to proton-driven spin diffusion.

2.3.15 Cross-Correlated Relaxation

First observed in the 1970s,^{94–96} cross-correlated relaxation describes the interference between multiple relaxation mechanisms acting simultaneously^{97–100} and can provide insights into the structure and dynamics of proteins.^{97,101–104} For example, Fischer *et al.* used the cross correlations between the $^{13}\text{C}'$ CSA and $^{13}\text{C}'$ - $^{13}\text{C}^\alpha$ dipolar couplings in a protein to produce dynamic models for the peptide planes¹⁰⁵ and Fiala *et al.* revealed ion coordination sites in DNA using cross-correlated relaxation rates.¹⁰⁶ Despite its uses, it is critical to suppress cross-correlated relaxation during relaxation measurements because it will alter the measured rates of the involved nuclei (i.e. the rates will no longer be quantitative).

In solution-state NMR, cross-correlated relaxation tends to be prominent and it is common practise to apply decoupling during the relaxation delay to suppress its effects. This decoupling must invert the magnetisation on a time scale substantially faster than the relaxation itself.^{71,97,107} In the solid state ^1H spin diffusion is typically fast enough to suppress cross-correlated relaxation (for interactions involving protons). However some of the measurements presented here use very fast MAS and under these conditions ^1H SD is slowed down. Thus in Chapter 4 it will be important to check that cross-correlated relaxation is still negligible during relaxation measurements at MAS speeds of up to 100 kHz.

2.4 Solid-State NMR Applied to Biological Samples

A significant amount of the research presented in this thesis focuses on extracting dynamic information from SSNMR relaxation measurements on proteins. These relaxation rates are most influenced by fluctuations in the local anisotropic interactions, which are caused by molecular motion. The timescales of the different dynamics that may occur within a protein are summarised in Figure ???. Different NMR measurements are sensitive to particular ranges of motion, these are also outlined in the same figure.

Within a protein different types of nuclei can be probed, which not only allows motions in the sidechain or backbone to be differentiated, but also the dynamics in specific parts of the backbone to be determined, for example ^{15}N , $^{13}\text{C}'$ or $^{13}\text{C}^\alpha$. Furthermore, if the NMR data is well resolved, the motions of these sites within each specific residue can be identified. This allows for a thorough analysis of a huge number of sites through-

out the whole biomolecule. In general, the protein backbone motions will be slower than sidechain motions, particularly the ^{15}N and ^{13}C nuclei that are within the peptide plane. Typically ^{15}N sites will have slower relaxation rates than ^{13}C s due to their lower gyromagnetic ratio. The sidechains will be very mobile, especially the rapidly rotating methyl groups, and therefore produce fast relaxation rates.

Finally, it is critical to highlight the importance of careful sample preparation: Even after the protein production, isotopic labelling and crystallisation, care must be taken throughout the packing and storage of the proteins. The primary concern is keeping the sample properly hydrated, which retains the biological context and improves the resolution of the resulting spectra.^{108,109} Various studies across the years suggest that these crystalline proteins samples still accurately represent their native state as long as the protein is correctly hydrated.^{11–17}

2.4.1 Protein GB1

The protein “GB1” (Figure 2.28) is used as a model protein in Chapters 3, 4 and 6, thus it is worthwhile providing background information on this useful protein.

GB1 is the β -1 immunoglobulin binding domain of protein G, expressed from *Escherichia coli*. It is commonly used as a model protein in SSNMR studies because it is a robust,^{110,111} fairly small (56 residues, MW = 6.2 kDa), well-characterised^{13,112–115} and extensively-studied^{110,116–119} protein that is relatively easy to crystallise. GB1 has a T_m of 87.0°C (at pH 5.4), which is particularly relevant to the measurements in Chapter 5 that are conducted between -2.2 and 34.85°C.¹¹⁰ The ^{13}C and ^{15}N SSNMR assignments and the crystallisation process of GB1 have been well-documented by Franks *et al.*¹³ The sequence and structure of GB1 are presented in Table 2.2 and Figure 2.28. In both cases the different regions of secondary structure are highlighted. A full list of assignments can be found in Appendix A.1.

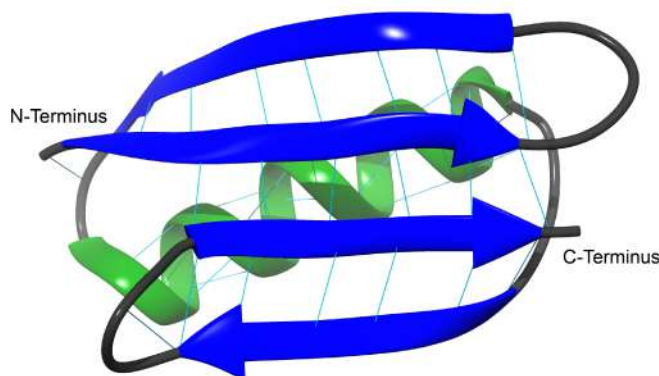


Figure 2.28: The structure of protein GB1. The α -helix is coloured green (residues 23 - 36), the β -sheets are blue (residues 2 - 8, 13 - 19, 42 - 46 and 51 - 55, respectively) and the loops are grey.

Table 2.2: The sequence of GB1. The residues that are part of the α - helix are coloured green and those that are part of a β -sheet are blue.

| | | | | | | | | | | | | | | | | | | |
|----|----|----|----|----|----|----|----|----|----|----|----|----|----|----|----|----|----|----|
| 1 | 2 | 3 | 4 | 5 | 6 | 7 | 8 | 9 | 10 | 11 | 12 | 13 | 14 | 15 | 16 | 17 | 18 | 19 |
| M | Q | Y | K | L | I | L | N | G | K | T | L | K | G | E | T | T | T | E |
| 20 | 21 | 22 | 23 | 24 | 25 | 26 | 27 | 28 | 29 | 30 | 31 | 32 | 33 | 34 | 35 | 36 | 37 | 38 |
| A | V | D | A | A | T | A | E | K | V | F | K | Q | Y | A | N | D | N | G |
| 39 | 40 | 41 | 42 | 43 | 44 | 45 | 46 | 47 | 48 | 49 | 50 | 51 | 52 | 53 | 54 | 55 | 56 | |
| V | D | G | E | W | T | Y | D | D | A | T | K | T | F | T | V | T | E | |

Chapter 3

Development of Tools to Aid the Packing of Proteins into Solid-State NMR Rotors

The initial designs for the 1.3 mm rotor packing tools were developed by Dr W. Trent Franks and Georgina Charlton, supervised by Dr Józef Lewandowski. Later developments stemmed from discussions with Dr W. Trent Franks and Koorosh Fatemian. All versions of the tools were manufactured by Lee Butcher and Marcus Grant in the Department of Chemistry's mechanical workshop (University of Warwick).

3.1 Abstract

Crystallisation,^{13,120,121} sedimentation^{122–124} and often precipitation,^{54,125} provide the homogeneous local environment for all chemically equivalent nuclei needed for high resolution NMR spectra of proteins. However, once prepared using such techniques, the delicate proteins become extremely challenging to pack into small SSNMR rotors (0.7 - 1.3 mm diameter). Custom tools were developed that allow careful, controlled packing of such samples into these rotors whilst ensuring that the samples do not degrade or dehydrate in the process. Additionally, the tools have been designed to allow sedimentation of protein samples in the tool before being directly packed into a rotor, minimising waste.

After thorough testing, the tools were used to pack a crystalline protein sample in 10 minutes (compared to several hours previously) and the resulting NMR spectra showed that the protein was neither dehydrated nor degraded. The tools were also used to sediment protein samples and then pack them into SSNMR rotors.

3.2 Introduction

For a relevant investigation of a biomolecule using SSNMR, it is critical that the sample is in an appropriate state. This means that the protein must be suitably hydrated; correct hydration of a protein is vital for normal activity, proper folding and dynamics,^{126–130} additionally dehydration may have further adverse effects specific to

that biomolecule.^{131–133} Furthermore, sample dehydration significantly reduces the SS-NMR spectral resolution, thus it is immediately obvious if the protein is poorly hydrated.^{121,134,135} Therefore it is absolutely critical to have a suitably-hydrated protein both to ensure the sample is biologically relevant and to obtain high quality spectra.

Techniques such as crystallisation,^{13,120,121} precipitation,^{54,125} and sedimentation^{122–124} are commonly used to produce immobilised, homogeneous and well-hydrated protein samples suitable for high-resolution SSNMR. Each of these protein preparation techniques results in a subtly different sample, as outlined in Figure 3.1. Crystallisation is commonly used for sample preparation, but it can be very challenging to determine the correct crystallisation conditions for a particular protein due to its sensitivity to temperature, pH and ionic strength.¹³⁶

When crystallisation is not tenable or if the protein is large, sedimentation may be used to immobilise the protein by centrifugation while retaining the homogeneous local environment.^{122–124} Sedimentation has no upper size limit and in fact becomes more efficient with higher molecular weights. It is important to note that centrifugation produces large shear forces, and in some cases may destroy large complexes if the force is too high. However, the forces in the SSNMR rotor caused by MAS are typically greater than any ultracentrifuge can achieve, so such samples may only be amenable to both low-g sedimentation and slower MAS.

Freezing, lyophilisation, and some precipitation conditions can be used to immobilise proteins, but have proven to be less suitable for SSNMR due to the multiple local environments introduced.¹³⁷ For example, lyophilisation followed by rehydration does not guarantee uniform hydration throughout the sample,¹³⁸ and imperfect precipitation can lead to a mixture of crystal lattices with different unit cells present.^{115,121} Furthermore it has been shown that freezing, precipitation and lyophilisation may deteriorate the quality of resulting spectra.^{121,139,140} This leaves crystallisation and sedimentation as the most suitable methods of preparing protein samples for SSNMR.

Once the protein has been prepared, a simple, reliable packing method is required, which retains the hydration (i.e. biological relevance) of the sample, maximises the quantity of sample in the rotor and packs it evenly, so that stable MAS is not compromised. Hydrated proteins are semi-solids and typically stick to the tools used to pack dry samples, while simultaneously being too viscous to be transferred using a pipette. Moreover, it is vital that crystallised proteins are transferred to the rotor with as little waste of the costly sample as possible, while also not changing the hydration of the protein. Packing these semi-solid samples into small SSNMR rotors (0.7 - 1.3 mm diameter, see Figure 3.2) is challenging, potentially wasteful of labelled material, and time consuming. Many methods involve several transfers between multiple tubes and pipette tips before ending up in the rotor.¹⁴¹ Previously, in the Lewandowski lab, proteins were packed into 0.7 and 0.8 mm rotors using a spatula (Figure 3.3) and into 1.3 mm rotors using a benchtop centrifuge (Figure 3.4). The latter method, which packed the sample at an angle, had the added risk of uneven packing that can cause unstable MAS.

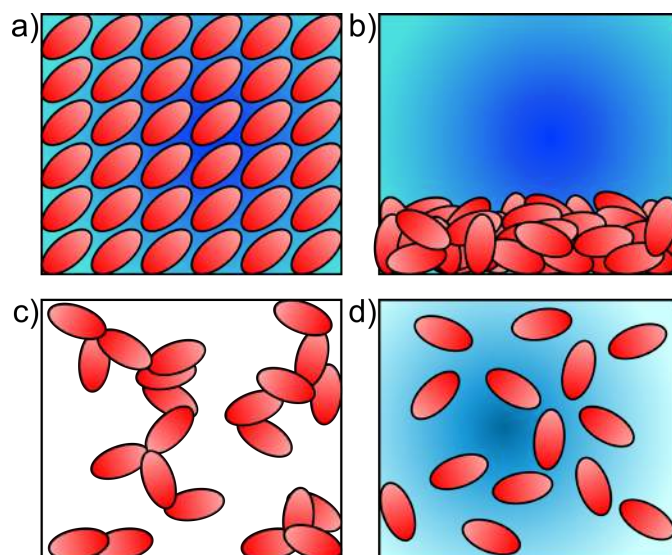


Figure 3.1: The results of different techniques for the preparation of SSNMR protein samples: a) Crystallisation, b) sedimentation, c) lyophilisation and d) freezing. *Figure adapted from Bertini et al.*¹²⁴

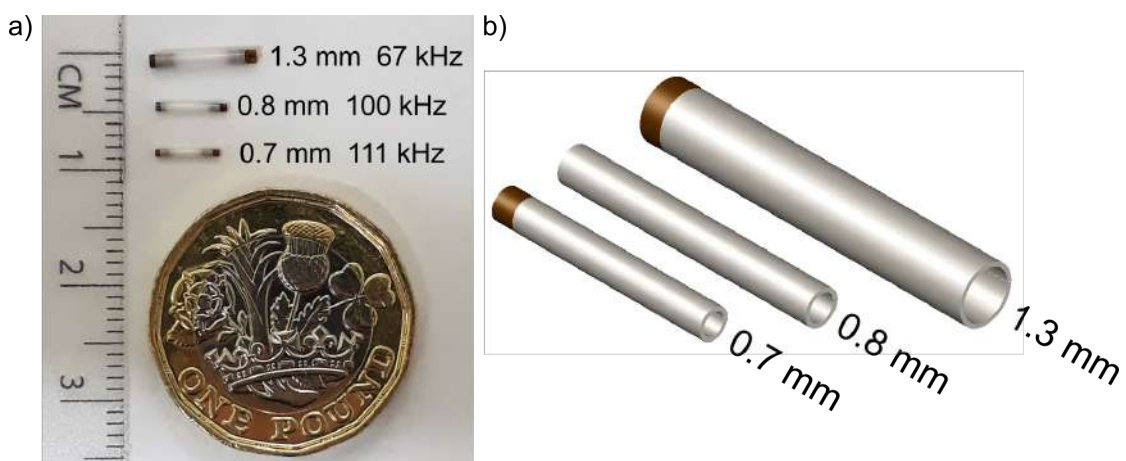


Figure 3.2: a) A photograph and b) a diagram of 0.7, 0.8 and 1.3 mm SSNMR rotors, showing the maximum MAS frequency of each rotor type. (Top caps are not included in the diagrams.)

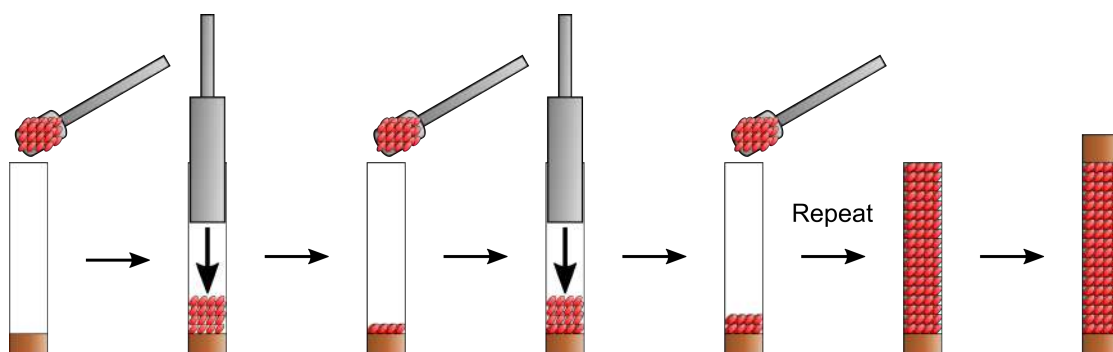


Figure 3.3: The previous method for packing proteins into 0.7 and 0.8 mm rotors using a spatula, which typically takes several hours.

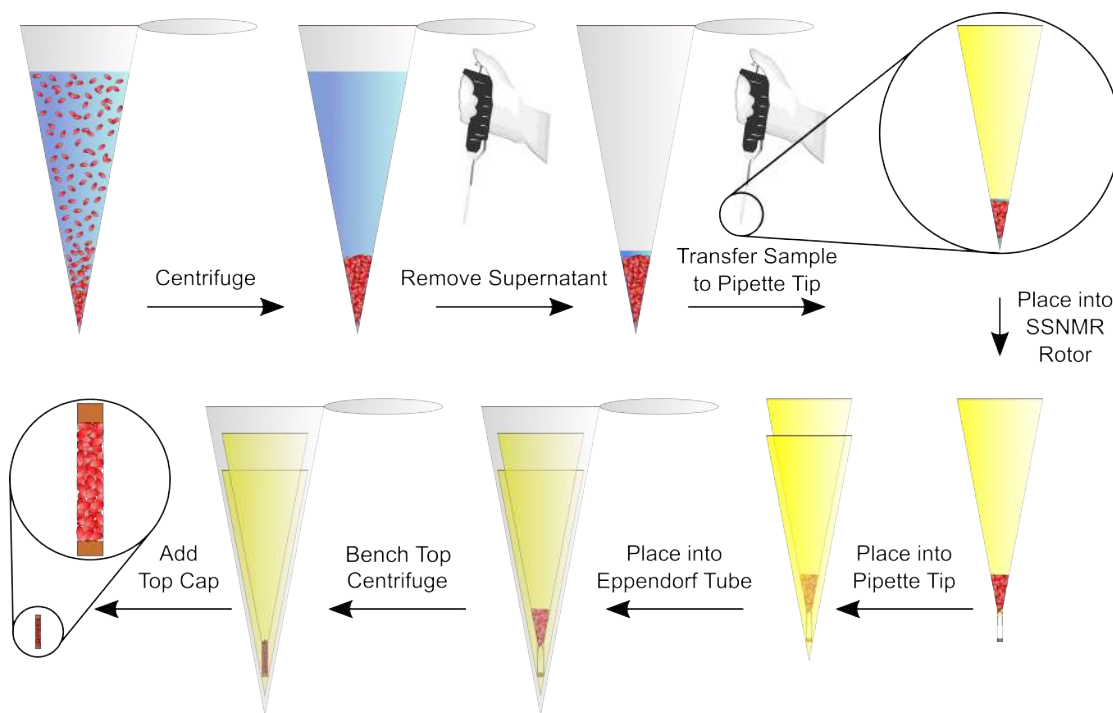


Figure 3.4: An older method for packing crystalline protein samples into 1.3 mm rotors in the Lewandowski lab. The sample is transferred into the rotor using a benchtop centrifuge meaning that the protein will be packed at an angle, potentially leading to unstable MAS.

In this chapter, ultracentrifuge tools to sediment the sample at up to 700,000 \times g and then pack the sample into an SSNMR rotor at moderate g-forces (10,000 - 50,000 \times g) are presented. These tools are for use with 0.7, 0.8 and 1.3 mm rotors, matching the recent developments in MAS technology, however the designs can also be adapted for larger rotors. The motivation behind these tools was to create an efficient, robust, reliable method of packing both crystalline and sedimented proteins into small SSNMR rotors that would also minimise the loss of sample and avoid dehydration.

3.3 Literature Review

The use of an ultracentrifuge device to pack SSNMR rotors was first mentioned in the literature by Bockmann *et al.* in 2009.¹⁴² The device, used to pack crystalline protein samples into 1.3 - 4 mm rotors using an ultracentrifuge, was a huge development in the packing of such samples. (For further comparison, Das *et al.* describe a typical home-made device which would have been used to pack these types of samples previously.¹⁴¹) Subsequently, various designs aiming to sediment soluble proteins directly into 1.3 - 4 mm rotors have been published.^{108,143-145} Prior to these devices, concentrated samples would have been sedimented into a normal ultracentrifuge tube before being transferred into a rotor, either using a spatula or transferring to a pipette tip and then being centrifuged into the rotor. These multiple steps increase the amount of valuable sample lost and greatly raise the chance of dehydration, emphasising that direct sedimentation

into the rotor is very advantageous. All of the designs presented here for sedimenting protein into a rotor can also be used to pack crystallised proteins.

The packing tool designs currently in the literature are presented in Figure 3.5. Table 3.1 highlights important details of these different ultracentrifuge devices, such as the reservoir volume, which is important when considering sedimentation conditions, and whether they allow for both sedimentation and packing of a sample. It is critical to note that, while these tools have been created for a wide range of SSNMR rotor sizes, currently there are none available for 0.7 and 0.8 mm rotors. Fast MAS (60 - 100 kHz), using 0.7 - 1.3 mm rotors, is often required to sufficiently resolve the complex spectra produced by proteins. Moreover, the sub-milligram amounts of sample required to fill 0.7 and 0.8 mm rotors are advantageous when the samples can be challenging to produce in large quantities and are expensive to isotopically label. For these reasons our ultracentrifuge sedimentation and packing tools are designed for use with 0.7, 0.8 and 1.3 mm rotors.

The packing tool created by Hisao *et al.* can be used to pack sedimented samples in addition to crystallised samples, but first requires the sample to be sedimented in a normal ultracentrifuge tube.¹³⁸ The supernatant is removed before the tube is inverted into the packing tool and the sample is transferred into a rotor using ultracentrifugal force (see Figure 3.5). This has the benefit of a simple sedimentation step where high forces can be used without any concern over damaging the rotor. However, when transferring the sediment to the rotor the chances of protein getting stuck on the walls of the packing device and ultracentrifuge tube are greatly increased, potentially wasting the valuable sample and limiting the amount that reaches the rotor. This highlights the importance of either direct sedimentation into the rotor or minimising the distance that the sediment has to travel to the rotor. The designs by Gardiennet *et al.*¹⁴⁴ and Gelis *et al.*¹⁴⁵ both allow for direct sedimentation into the rotor, an improvement on the design by Hisao *et al.*

In our design presented below, the sample is sedimented into a narrow reservoir and then directly transferred to a rotor in a second step. The key factor in this decision was to avoid having the rotor present during the sedimentation process, which provides access to more extreme sedimentation conditions. Thus making it possible for this packing tool to be used for a greater range of proteins, including those that are typically more challenging to sediment. Although the literature shows that 1.3 mm rotors can survive relatively harsh g-forces,^{142,143} it is unknown what forces the more delicate 0.7 and 0.8 mm rotors can withstand.

It is important to note that in the ultracentrifuge device by Bockmann *et al.*,¹⁴² a metal dummy cap was used in place of the bottom rotor cap in order to prevent damage to the delicate rotor caps from the high forces in the ultracentrifuge. This complicates the packing procedure and, more critically, adds a further opportunity for loss or dehydration of the protein. Therefore using a dummy cap should be avoided, if possible, when designing a packing tool.

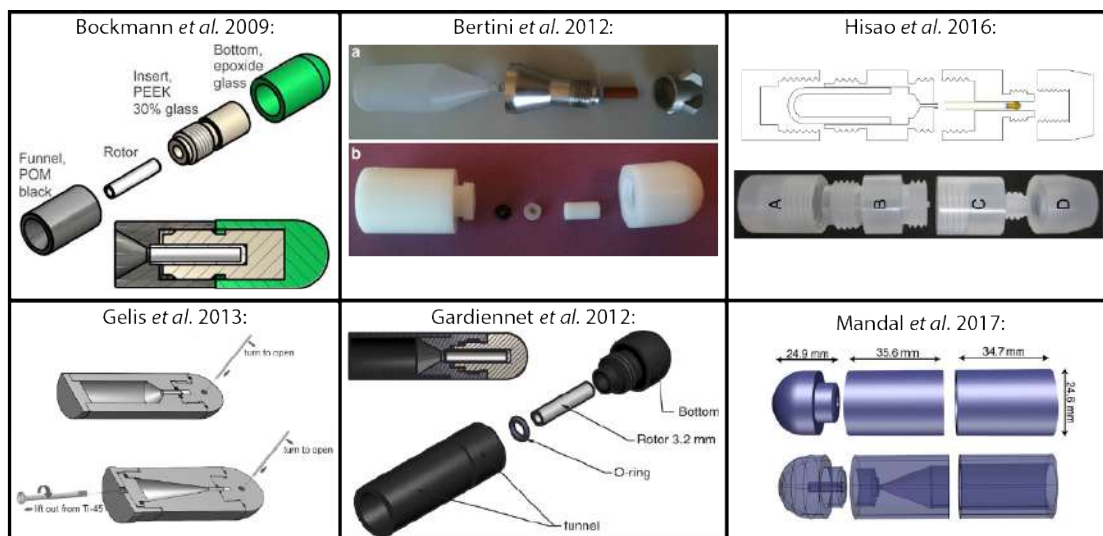


Figure 3.5: Ultracentrifuge tools in the literature for packing sedimented or crystallised protein into SSNMR rotors: Bockmann *et al.*,¹⁴² Bertini *et al.*,¹⁴³ Hisao *et al.*,¹³⁸ Gelis *et al.*,¹⁴⁵ Gardiennet *et al.*,¹⁴⁴ and Mandal *et al.*¹⁰⁸

Table 3.1: Key details on ultracentrifuge SSNMR rotor packing tools in the literature. (POM is polyoxymethylene, PEEK is polyether ether ketone, CFRP is carbon fibre reinforced polymer and PCTFE is polychlorotrifluoroethylene. SB and FA stand for “swinging bucket” and “fixed angle” ultracentrifuge rotors, respectively.)

| Reference | Rotors | Sediment -ation? | Conditions | Material | Volume |
|---|---------------------|---------------------|--------------------------------------|---|-------------------|
| Bockmann <i>et al.</i> (2009) ¹⁴² | 1.3 – 4 mm | No | 210,000 x g (SB) | POM, PEEK 30% glass & epoxide glass | Unknown |
| Bertini <i>et al.</i> (2012) ¹⁴³ | 1.3, 3.2, & 4 mm | Direct | 175,000 x g | Polycarbonate, aluminium & POM | 20 or 1.38 ml. |
| Gardiennet <i>et al.</i> (2012) ¹⁴⁴ | 3.2 mm | Direct | 210,000 x g | CFRP | 1 ml |
| Gelis <i>et al.</i> (2013) ¹⁴⁵ | 3.2 mm | Direct | 121,000 x g (SB) 201,000 x g (FA) | Aluminium & POM | 6 –7 ml |
| Hisao <i>et al.</i> (2016) ¹³⁸ | 1.6 & 3.2 mm | Indirect | 3,000 x g | PCTFE | Unknown |
| Mandal <i>et al.</i> (2017) ¹⁰⁸ | 3.2 mm & 4 mm | Direct | 143,000 x g 175,000 x g | PEEK | 1 – 1.5 ml |

The size of the funnel is also an important consideration when designing a sedimentation device as this limits the volume of the protein solution and subsequently the total amount of protein in the device. Two different ultracentrifugal devices are presented by Bertini *et al.* (labelled as “A” and “B” in Figure 3.5).¹⁴³ Device A has a very large reservoir (20 ml), which is necessary when sedimenting less concentrated solutions. However, there are downsides to this tool: the polycarbonate funnel in which the solution is placed must be cut to size each time and the tools includes aluminium components, which may corrode. Device B has a much smaller funnel (1.38 ml) and therefore is more suitable for the sedimentation of concentrated samples. It is made from the more chemically resistant polyoxymethylene (POM) and as such can be cleaned with acids or bases if necessary.

Two types of ultracentrifuge rotors are used with these tools: fixed angle and swinging bucket (Figure 3.6). A fixed angle rotor can typically reach higher speeds than a swinging bucket rotor, however the force produced by the rotor will not be parallel to the SSNMR rotor due to its fixed angle and may even cause damage to the MAS rotor.¹⁰⁸ If the SSNMR rotor is not packed in an axially symmetric fashion, it will not spin stably in the SSNMR probe (Figure 3.7). While the sample is generally viscous and will rearrange itself under MAS, occasionally the critical spinning rate required for this to happen cannot be reached. On the other hand, the swinging bucket rotor, which allows the SSNMR rotor to become parallel to the g-force, is ideal. For the designs presented here, the extreme forces produced by the fixed angle ultracentrifuge rotor (up to 700,000 x g) are initially exploited to sediment the protein sample (SSNMR spectra of proteins sedimented under similar conditions show that the high forces involved do not affect the protein structure).^{23,123,144} The packing device is then transferred to the swinging bucket ultracentrifuge rotor for uniform packing of the sediment into the SSNMR rotor.

The most recent devices designed by Mandal *et al.* allow sedimentation and packing into 3.2 and 4 mm rotors.¹⁰⁸ They are comprised of 3 pieces each and have a relatively large volume. However the process of sedimentation into a rotor is quite tedious: it requires three separate hour-long runs (at 154,000 x g) with manual rinsing in between each step. The long packing time is probably due to the limited speed of the swinging bucket rotor. This highlights the advantage of using a fixed angle rotor, which is capable of reaching significantly greater speeds, in a separate packing step. The design presented in this chapter uses forces up to 700,000 x g for sedimentation in comparison to others in the literature which range from 3,000 x g to 210,000 x g.

3.4 Design and Development of the Packing Tools

3.4.1 Initial Packing Tools for 1.3 mm Rotors

The initial packing tools had gone through several stages of development (by Trent Franks and Georgina Charlton) before my work, described in this chapter, commenced. The tools were at the stage that they could be used to pack crystallised protein into a 1.3 mm rotor, although this had not been tested with a real NMR sample, and large

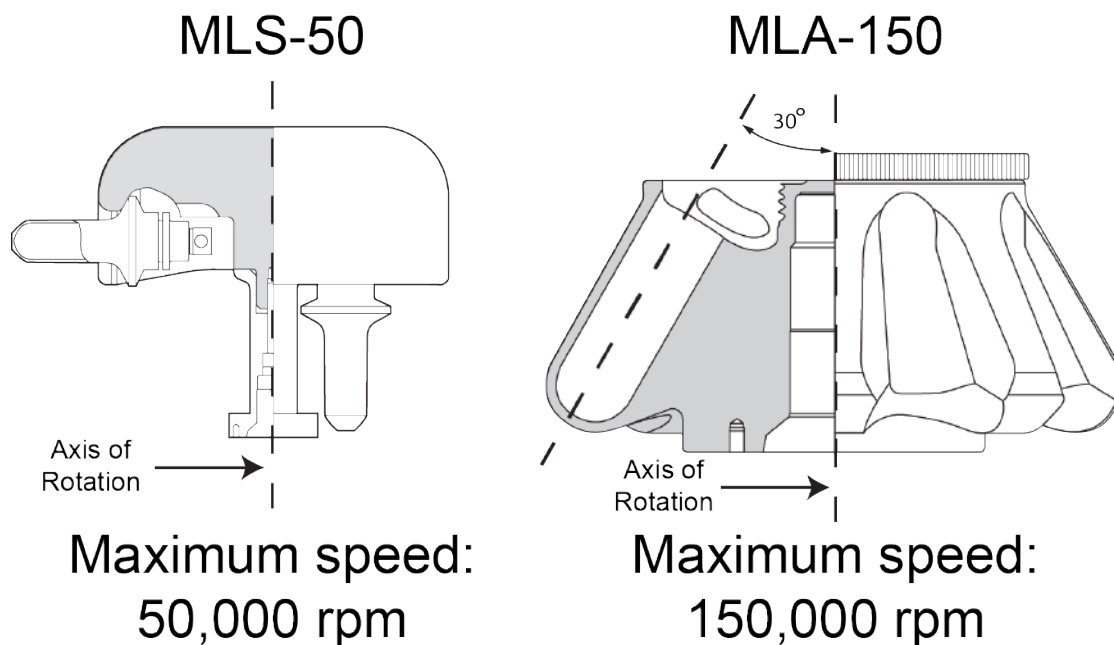


Figure 3.6: The swinging bucket (MLS-50) and fixed angle (MLA-150) rotors. Adapted from the *Beckmann Coulter Optima MAX-XP Ultracentrifuge* MLA-150¹⁴⁶ and MLS-50¹⁴⁷ manuals.

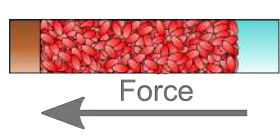
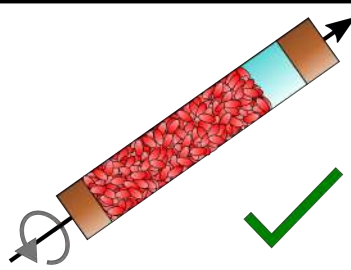
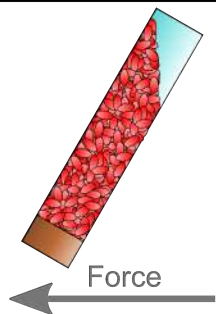
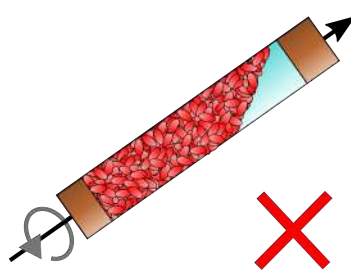
| | Sedimentation in Ultracentrifuge | Stable Magic Angle Spinning? |
|-----------------------|---|--|
| Swinging Bucket Rotor |  |  |
| Fixed Angle Rotor |  |  |

Figure 3.7: The result of packing samples using the swinging bucket and fixed angle rotors, and the possibility of stable MAS in each case.

proteins could be sedimented in the tool and then manually pushed into a 1.3 mm rotor. Photographs and designs of the tools at this stage are presented in Figures 3.8 and 3.9, respectively. The key ideas behind this design, and any important problems that were encountered along the way, are discussed below.

One of the critical ideas behind the design of these tools was to separate out the sedimentation and packing stages. This meant that the high forces of the fixed angle rotor could be exploited for sedimentation and then the swinging bucket rotor could be used to pack the sample evenly into the SSNMR rotor, which is critical for stable MAS. This led to the design of two differently sized tools, one to fit the MLA-150 (fixed angle) rotor to use with sedimented samples and the other to fit the MLS-50 (swinging bucket) rotor for crystallised samples. The plugs and rotor sleeves are interchangeable between the two tools.

These tools have to withstand forces of up to 700,000 x g and so a strong material is vital. The first iteration of tools was created from polycarbonate because of its low density, therefore allowing greater ultracentrifuge speeds, and transparency, allowing visual checks on the sedimentation process. However cracks appeared in the tool during the manufacturing process and, unexpectedly, they cracked further when tested in the ultracentrifuge at 5,000 x g. Additional points of weakness were observed at places where the material was particularly thin and it was noted that a minimum thickness of 3 mm is required throughout the tool. The material was changed to polyether ether ketone (PEEK), a much stronger material, and even after 12 days exposed to 700,000 x g there were no signs of wear on any part of the tools.

Another important consideration was to design the tool in such a way that the amount of sediment returning to the bulk solution post-sedimentation is minimal. This simply meant reducing the sediment-solution surface area by forcing the sediment to collect in a narrow reservoir at the end of the funnel and then quickly removing the excess solution post-sedimentation. The reservoir had the internal diameter of a 1.3 mm rotor to allow smooth transfer of the protein into the rotor. Since the tools must work with both fixed angle and swinging bucket centrifuge rotors, the angle of the funnel with respect to the ultracentrifuge rotor axis must be less than 30° to prevent sedimentation on the edges of the funnel, rather than in the long reservoir.

The initial design involved a polycarbonate disk in combination with a plug to prevent the funnel leaking and the funnel was screwed into the holder. Significant leaks caused these parts of the tools to be re-designed twice, ending up with the final tools presented in Figures 3.8 and 3.9. These use a combination of a rubber disk, silicon glue and a PEEK plug to prevent the funnel leaking, and an O-ring to avoid any leaked protein being forced out of the tool into the ultracentrifuge rotor.

Originally, three sizes of tools were created. These were for the MLA-50 (fixed angle, maximum speed 50,000 rpm), MLA-150 (fixed angle, maximum speed 150,000 rpm) and MLS-50 (swinging bucket, maximum speed 50,000 rpm) rotors. Eventually the MLA-50 tool was discontinued, since it had neither the benefit of the axially symmetric

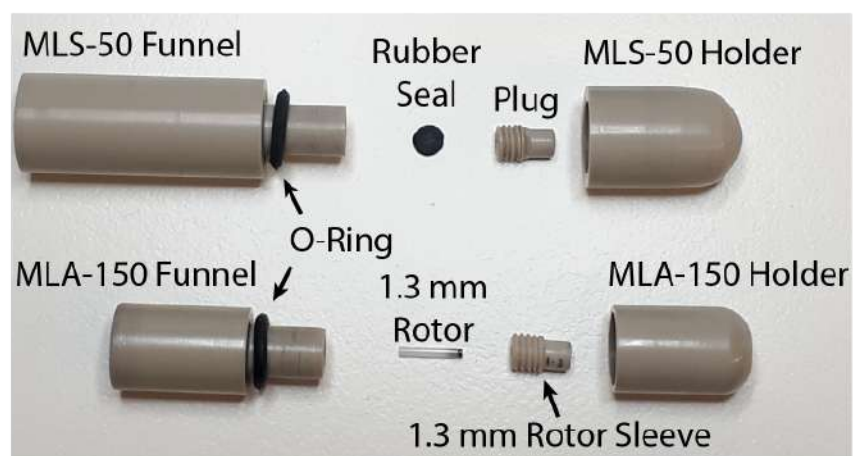
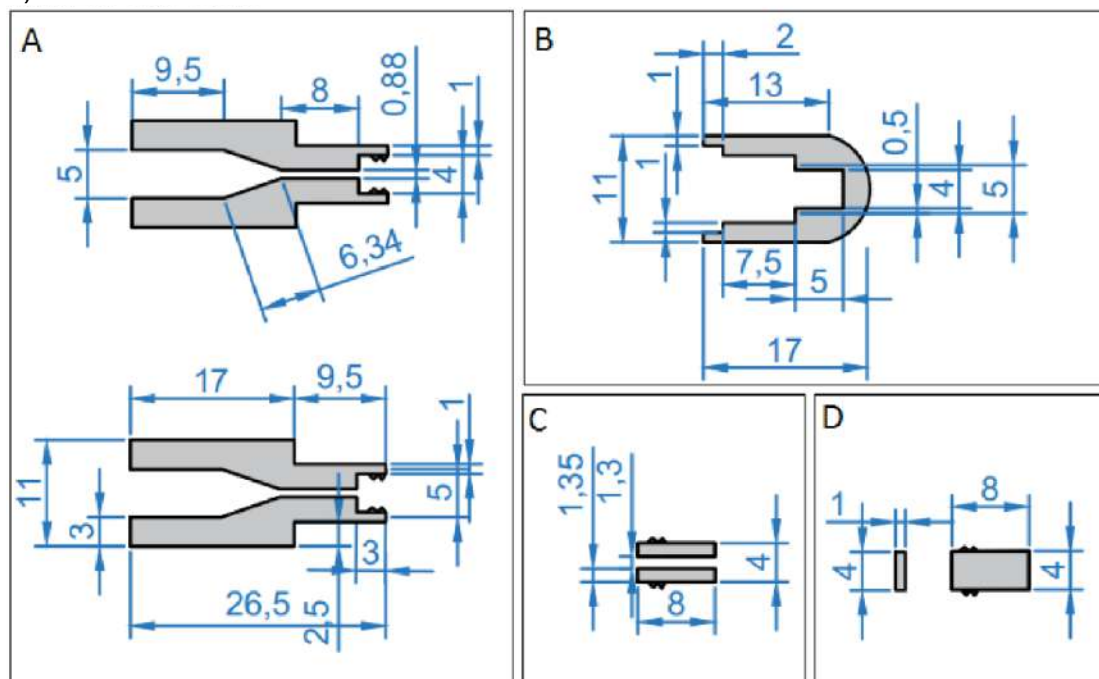


Figure 3.8: The initial tools used for packing crystallised samples into 1.3 mm SSNMR rotors and sedimenting samples.

a) MLA-150 Tools



b) MLS-50 Tools

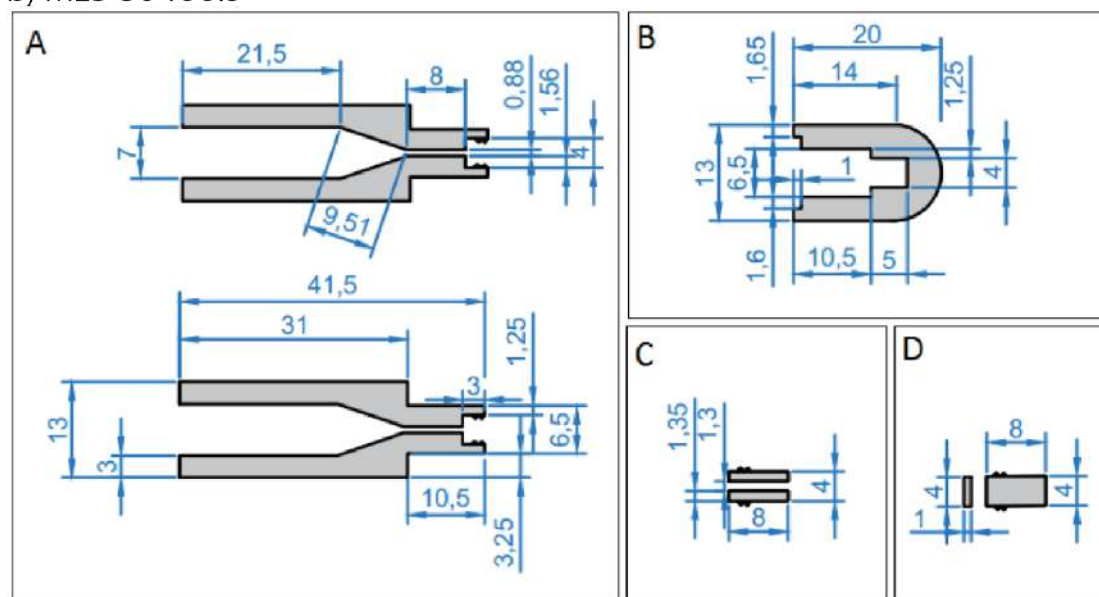


Figure 3.9: The initial a) MLA-150 and b) MLS-50 packing tools for 1.3 mm SSNMR rotors where A is the funnel (O-ring not included in diagram), B is the holder, C is the 1.3 mm rotor sleeve, and D is the rubber disk and plug. *Drawings from Georgina Charlton's MSc Thesis.*¹⁴⁸

packing produced by the swinging bucket rotor, or the higher g-forces of the MLA-150 rotor.

3.4.2 First Development: Creating a Fixed Rotor to Swinging Bucket Adaptor

In order to efficiently transfer a freshly sedimented sample from the MLA-150 tool into a rotor, an adaptor is required to fit the MLA-150 tool into the MLS-50 rotor. This adaptor, also made out of PEEK, was designed by calculating the difference in internal dimensions of the fixed angle and swinging bucket ultracentrifuge rotors (Figure 3.10). Note that the adaptor is not made to the full length of the larger MLS-50 tool, this allows the SSNMR rotor to be further from the axis of rotation, making better use of the ultracentrifuge. Additionally, a small (1 mm diameter) hole is drilled into the bottom of the adaptor to aid with removal of the MLA-150 tool after packing. Technical drawings for all parts of the tool are found in Figure 3.22.

This straightforward adaptor allows efficient sedimentation and packing of a protein into an SSNMR rotor. Successful tests and use of the adaptor have highlighted one future improvement: shortening the adaptor by 3 mm causing the MLA-150 tool to protrude slightly, allowing the use of forceps to aid with the removal of the MLA-150 tool from the adaptor after packing (Figure 3.11).

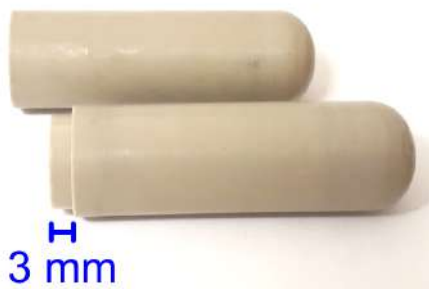


Figure 3.11: Future improvement: Reducing the length of the adaptor by 3 mm allowing for easier removal of the MLA-150 tool.

3.4.3 Initial Tests for 1.3 mm Packing Tools

In order to thoroughly understand the capabilities of the tools and to check for leaking, the sedimentation and packing processes were tested using water followed by lysozyme crystals or solution. There were no signs of leaking after 30 hours at 60,000 x g for the MLS-50 tool and 18.5 hours at 700,000 x g for the MLA-150 tool. Both the MLS-50 and MLA-150 (with the use of the adaptor) tools could be used to efficiently pack samples into 1.3 mm rotors.

Next, since these tools had not yet been tested on a real NMR sample, crystalline [U- ^1H , ^{13}C , ^{15}N]GB1 was packed into a 1.3 mm rotor in 10 minutes at 20,000 x g using the MLS-50 tool. It was noted that the tools were easy to use and the process was efficient.

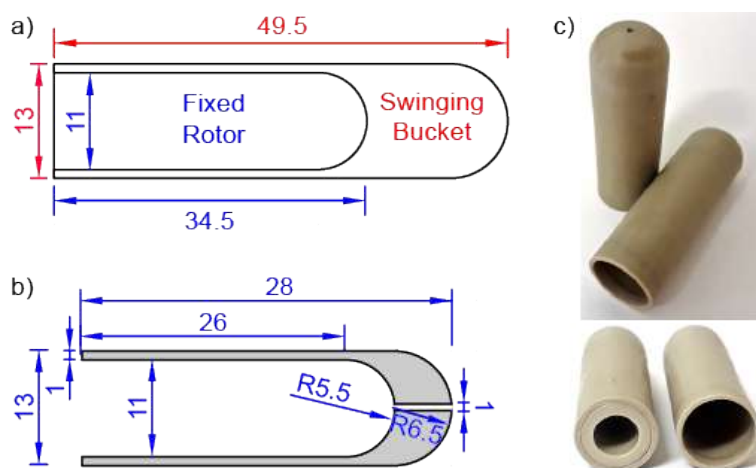


Figure 3.10: a) An overlay of the swinging bucket and fixed rotor internal dimensions, highlighting the difference, b) the dimensions of the adaptor and c) photographs of the adaptor with, and without, the MLA-150 tool inside. “R” preceding a value denotes the radius of a curve.

3.4.4 Second Development: Creating Rotor Sleeves for 0.7 and 0.8 mm SSNMR Rotors

Over the last few years, 0.7 and 0.8 mm rotors have been increasingly used for protein SSNMR experiments in the Lewandowski lab. The significantly faster MAS achievable (up to 110 kHz, compared to 60 kHz with a 1.3 mm rotor) and the sub-milligram samples required, make use of the 0.7 and 0.8 mm rotors particularly desirable.

A disadvantage of these extremely small rotors is that they are even more challenging to pack. Up until now the method for packing 0.7 and 0.8 mm rotors involved scooping sub-milligram amounts of protein into the top of the rotor using a micro-spatula, compacting it down and repeating until the rotor was full (see Figure 3.3). This process takes several hours, so the probability of the protein becoming dehydrated during the procedure, and therefore rendering the sample unusable, is high. It is obvious that a more efficient method would not only save time, but also reduce the waste of expensive, isotopically-labelled protein samples. This motivated the modification of these packing tools so that they could be used for 0.7 and 0.8 mm rotors, as well as 1.3 mm rotors.

To make these packing tools compatible with 0.7 and 0.8 mm rotors, the rotor sleeves need to be customised so that each size of rotor has a secure fit inside the tool. This will avoid any damage to the rotor and minimise loss of protein (a tight fit should mean that the sample is forced to enter the rotor rather than going around the outside of it). The dimensions of the rotor sleeves for the 0.7 and 0.8 mm rotors compared to the rotor sleeve for the 1.3 mm rotors are presented in Figure 3.12 alongside 3D illustrations and photographs.

One of the concerns prior to testing the new rotor sleeves to pack 0.7 and 0.8 mm rotors is whether the rotors and caps can withstand the extreme conditions of the ultracentrifuge. Additional complications occur when testing the packing process with

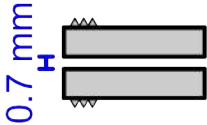
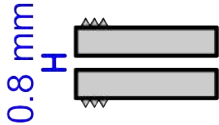
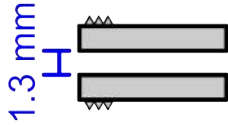
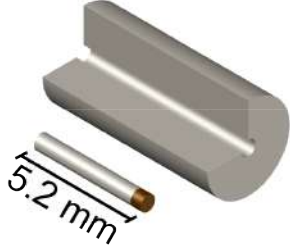
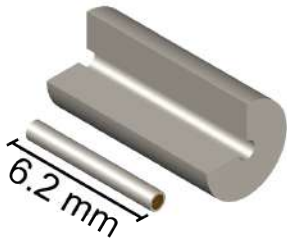
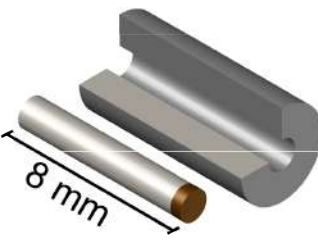



| | 0.7 mm Rotor | 0.8 mm Rotor | 1.3 mm Rotor |
|-------|---|---|---|
| 2D |  |  |  |
| 3D |  |  |  |
| Photo |  |  |  |

Figure 3.12: A summary of the differences between the initial designs of the rotor sleeves for 0.7 mm, 0.8 mm and 1.3 mm rotors: 2D diagrams showing the internal diameters, 3D illustrations of the rotor sleeves (with a quarter cut out to reveal the inside) and the rotors, and finally photographs of the rotor sleeves. (Screw thread not shown on 3D illustrations.) The critical difference to note is the variation of the internal diameter.

the new tools since the delicate 0.7 mm rotors are effectively one-use, and both 0.7 and 0.8 mm rotors are very expensive. Therefore tests on these tools become costly, so initially, to make the best use of resources, a real sample was packed into the rotors during testing. The MLA-150 tool was used to sediment this protein with the aim of packing it into a 0.7 mm rotor. Unfortunately, there were significant leaks in the packing step causing little sediment to end up in the rotor and the remaining sample was lost. This highlighted a critical problem with the design of tools when used with 0.7 or 0.8 mm rotors.

3.4.5 Third Development: Adapting the Rotor Sleeves and Funnel for 0.7 and 0.8 mm SSNMR Rotors to Avoid Leaks

The most likely cause of this leak was thought to be down to the set of tools not being fully adapted for the 0.7 and 0.8 mm rotors. Firstly, the diameter of the narrow reservoir (0.88 mm) is the same as the internal diameter of the 1.3 mm rotors, but wider than the 0.7 and 0.8 mm rotors. Secondly, the rotor sleeves are all the length of a 1.3 mm rotor (8 mm), while the 0.7 and 0.8 mm rotors are significantly shorter (5.2 and 6.2 mm, respectively), which leaves a large gap between the bottom of the reservoir and the top of the rotor. This combination provides ample opportunity for the protein to seep around the outside of the rotor and pool in the rotor holder under the high g-forces the ultracentrifuge produces (illustrated in Figure 3.13).

It was a simple decision to narrow the reservoir diameter to 0.5 mm, which is the same as or smaller than the internal dimensions of the 0.7 and 0.8 mm rotors. There were two ideas to account for the differences in rotor length: shortening the rotor sleeve itself, which also requires changes in the holder, or reducing the internal diameter in the rotor sleeve to 0.5 mm above the rotor, which effectively extends the reservoir into the top of the rotor sleeve. Both of these ideas are illustrated in Figure 3.14.

The latter idea is a simpler approach since it involves fewer unique parts and, after checking that the mechanical workshop staff could make these slightly more complex pieces, this idea was selected. Details on the dimensions of these rotor sleeves with 3D illustrations and photographs of the final tools are shown in Figure 3.15.

3.4.6 The Final Design of the Ultracentrifuge Tools

The final centrifuge tools (Figure 3.16) were machined from polyether ether ketone (PEEK), a strong material able to withstand up to 700,000 x g. The top is a funnel with a long, narrow reservoir to restrict the surface between the sediment and the supernatant, which is seated into the holder. The angle of the funnel with respect to the tool axis is less than 30° to prevent sedimentation on the edges of the funnel rather than in the long reservoir. The sedimentation tool for the MLA-150 centrifuge rotor has a reservoir size of 0.5 ml, allowing for a relatively large volume for the sedimentation of less concentrated solutions. The assembly is sealed with a 5.4 mm O-ring and the plug and rotor sleeve pieces are interchangeable between the two tools. The tool is counter-weighted with a second tool and water as needed. Points of contact between the pieces

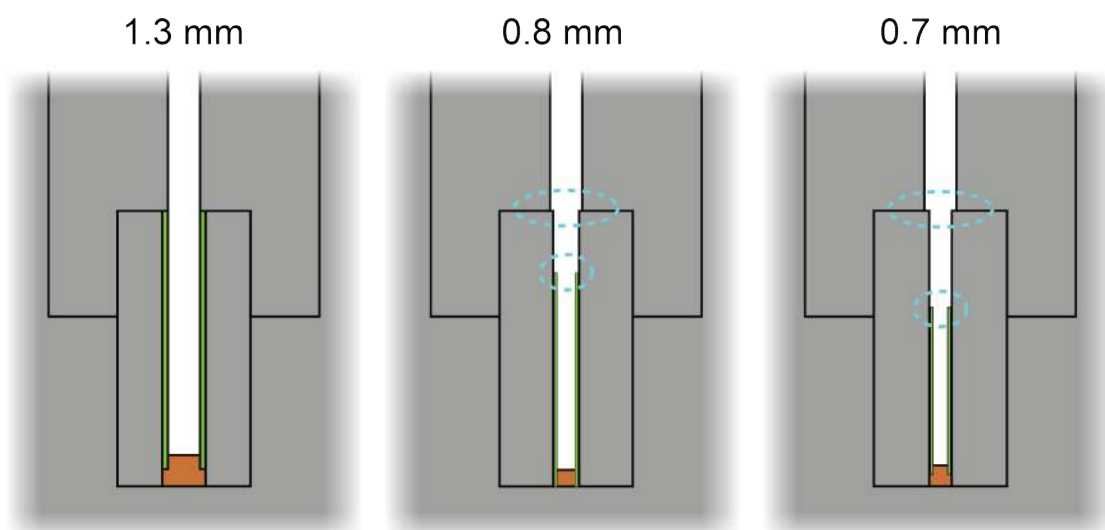


Figure 3.13: A zoomed-in illustration of the tool showing how the protein leaks by avoiding the 0.7 or 0.8 mm rotor during packing. Note that while the inside of the 1.3 mm rotor is flush with the rest of the tool, this is not the case for with the 0.8 and 0.7 mm rotors (circled). (The SSNMR rotors are highlighted in green.)

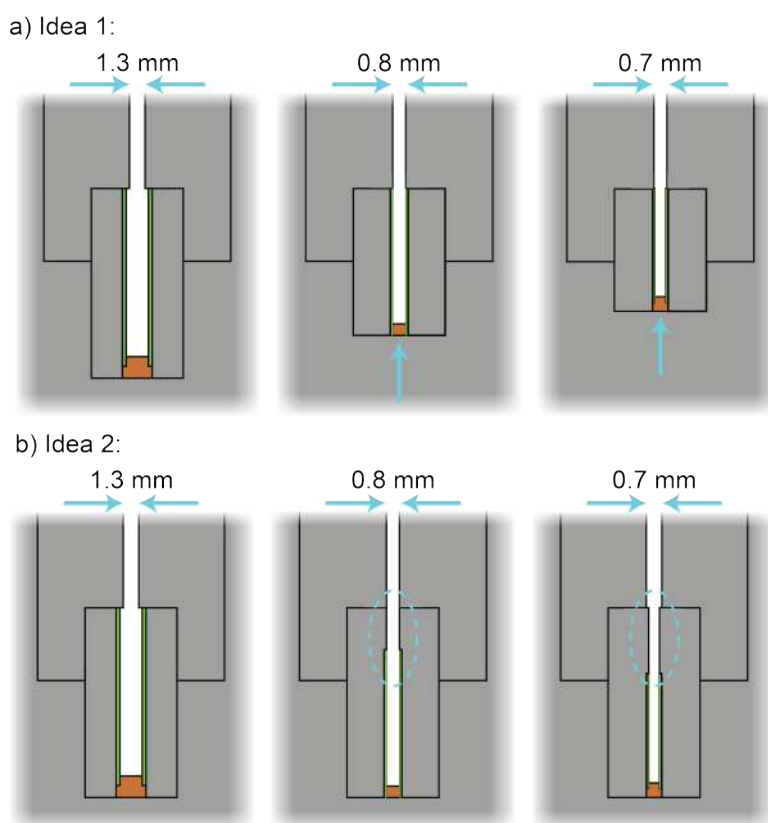


Figure 3.14: Ideas for better adapting the tool for 0.7 and 0.8 mm rotors: a) Reducing the length of the rotor sleeve and b) narrowing the top of the rotor sleeve to 0.5 mm. The SSNMR rotors are highlighted in green and key changes from Figure 3.13 are indicated with either circles or arrows.

| | 0.7 mm Rotor | 0.8 mm Rotor | 1.3 mm Rotor |
|-------|--------------|--------------|--------------|
| 2D | | | |
| 3D | | | |
| Photo | | | |

Figure 3.15: A summary of the differences between the final designs for the rotor sleeves for 0.7 mm, 0.8 mm and 1.3 mm rotors: 2D diagrams showing the internal differences, 3D illustrations of the rotor sleeves (with a quarter cut out to reveal the inside) and the rotors, and finally photographs of the rotor sleeves. (Screw thread not shown on 3D illustrations.)

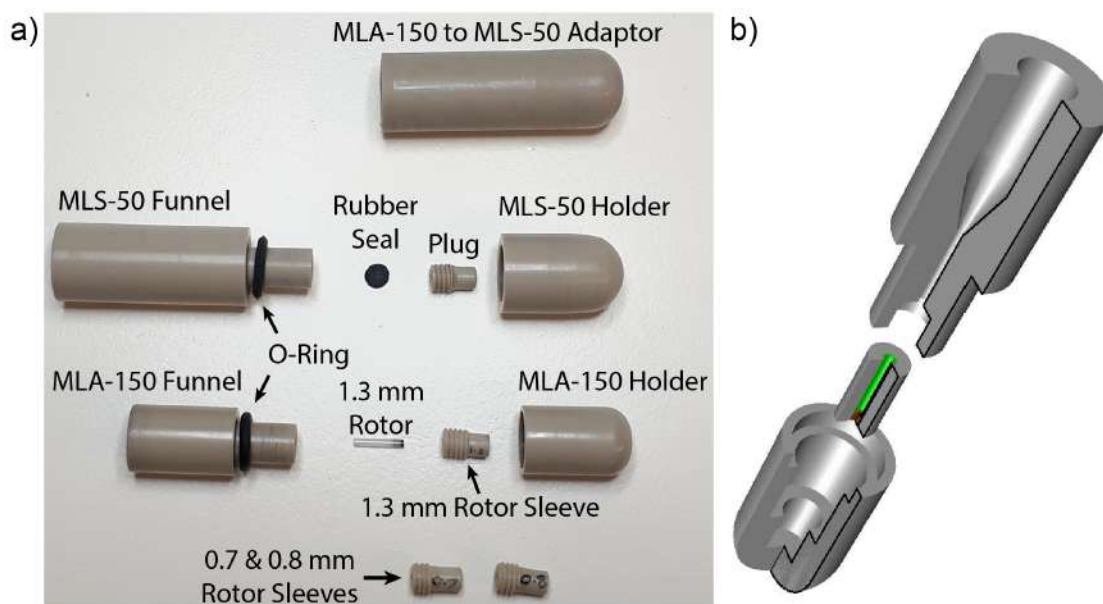


Figure 3.16: a) The tools needed for sedimenting and packing protein into 0.7 mm, 0.8 mm and 1.3 mm SSNMR rotors. The MLS-50 tool fits into both a fixed angle and a swinging bucket rotor. The adaptor holds the MLA-150 assembly so that it fits into the MLS-50 swinging bucket centrifuge rotor. The plugs and rotor sleeves are interchangeable between the two tools. b) A 3D-cutout view to show the internal funnel, sample reservoir, rotor sleeve, and seatings of the device (O-ring not included). The rotor is highlighted in green.

were machined with rounded edges to reduce the point stresses in these areas. A 3D illustration of the tools, with a cut-out to show the internal funnel, sample reservoir and rotor sleeve, is displayed in Figure 3.16b.

In sedimentation mode, a *Polyco chemprotect* rubber seal is glued into the funnel with *Loctite SI 5145* alkoxy silicon adhesive, a threaded plug is screwed into the top and, once the adhesive has cured, placed into the holder. There is usually a gap between the top and bottom caused by the O-ring, but this will be sealed once the centrifuge compresses the pieces together. After sedimentation, the adhesive and rubber plug are quickly and easily removed from the funnel with a needle and generally come out as one piece. The solid plug and rubber seal are replaced with a sleeve containing a rotor, with a bottom cap glued on, when used for packing. The tool, and adaptor if needed, is placed into the swinging bucket ultracentrifuge rotor and, under the conditions stated in Table 3.2, the sedimented protein is centrifuged into the rotor. Finally, the tool is disassembled and the top cap is placed on the rotor.

To pack microcrystalline proteins, a concentrated suspension can be directly transferred into the MLS-50 funnel using a pipette, and packed following the above instructions, skipping the sedimentation steps. The process for packing and/or sedimentation of protein samples is illustrated in Figure 3.17 and a detailed protocol with images of each step is included in Appendix B.1. The tools withstood several weeks spinning at 700,000 x g with no indication of structural deterioration, and are still in active use at

Table 3.2: The tools and ultracentrifuge conditions used to pack crystalline and sedimented protein samples into an SSNMR rotor using the Beckman Coulter Optima MAX-XP ultracentrifuge. Further information on the adaptor is presented in the experimental section.

* The time and force need for protein sedimentation is highly dependent on the nature of the sample, see Section 3.6 for further details.

| Sample | Rotor | Tool | Force | Time |
|------------------------------|---------|------------------------|------------|------------|
| Packing crystalline protein | MLS-50 | Swinging bucket | 60,000 x g | 10 minutes |
| Sedimenting protein solution | MLA-150 | Fixed angle | N/A* | N/A* |
| Packing sedimented protein | MLS-50 | Fixed angle in adaptor | 20,000 x g | 10 minutes |

the time of writing this report.

3.5 Using the Tools to Pack Samples

3.5.1 Packing a Microcrystalline Protein Sample for NMR

Using the tools under the conditions described in Table 3.2, crystalline [$U\text{-}^1\text{H}, ^{13}\text{C}, ^{15}\text{N}$]GB1 protein (see Section 3.8.4 for crystallisation procedure) was successfully packed into both 0.7 mm and 1.3 mm rotors in around 10 minutes, a task which previously took several hours. A 2D $^{13}\text{C}\text{-}^1\text{H}$ SSNMR spectrum of the GB1 crystals packed into the 0.7 mm SSNMR rotor using these tools is presented in Figure 3.18a; the sample gave excellent signal and high resolution showing that the protein was well-hydrated.

For comparison, Figure 3.18b shows a spectrum of microcrystalline protein packed into a 0.8 mm rotor using a spatula. The poor resolution clearly shows that the protein became dehydrated during the lengthy packing process. This demonstrates that using this older packing method can compromise the quality of the final sample.

3.5.2 Sedimentation and Packing of a Protein Sample

These new tools have been used to sediment and pack proteins into 1.3 mm rotors, and additional thorough testing has been conducted for the 0.7 and 0.8 mm components of the MLA-150 tools. Water was used in the initial checks for leaks, after which bovine haemoglobin was used in the sedimentation tests, chosen because it is a relatively large (64.5 kDa), cheap protein. The final version of the MLA-150 tool in sedimentation mode was tested with 200 μl of water at 700,000 x g for 64 hours in a single run, and showed no signs of leaking. This set of tools has been tested at this speed for a cumulative time of > 280 hours. Next, 100 μl of bovine haemoglobin solution (50 mg/ml in pH 5.5, 50 mM phosphate buffer) was ultracentrifuged in the MLA-150 tool for 24 hours at 700,000 x g. Excess supernatant was removed and the plug and glue were replaced with a 1.3 mm rotor and rotor sleeve. This was then placed into the adaptor and ultracentrifuged at 20,000 x g for 10 minutes in the swinging bucket rotor. The sample was successfully packed into the 1.3 mm rotor with relative ease and no leaks.

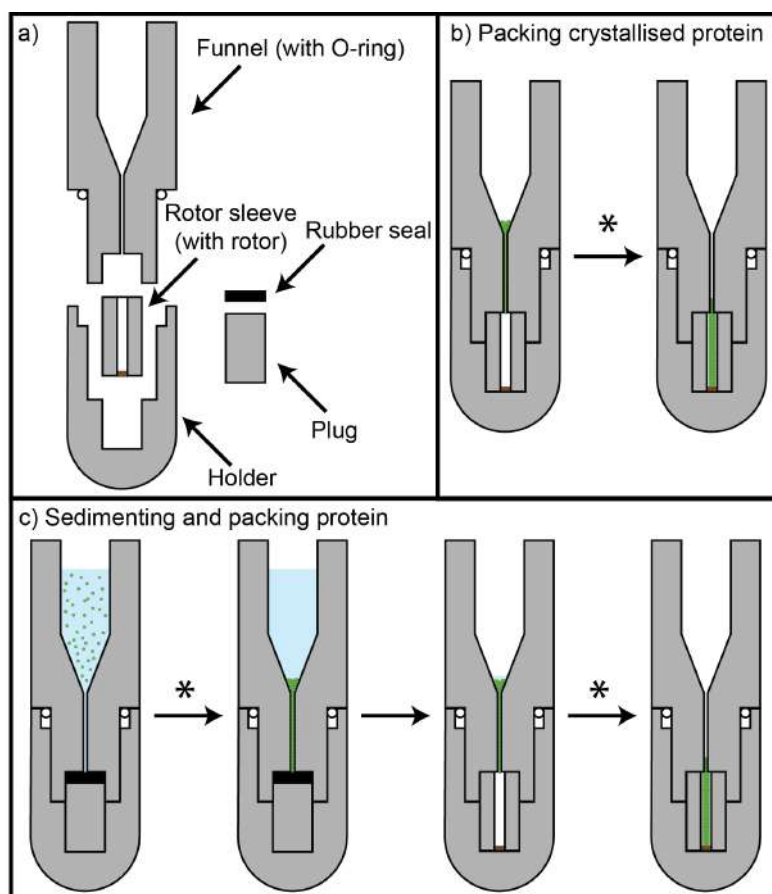


Figure 3.17: a) A cutaway of the centrifuge tools, b) the steps for packing a crystalline protein sample and c) the steps to sediment and pack protein samples into a rotor using the tools. An asterisk represents ultracentrifugation between steps and the protein is represented in green.

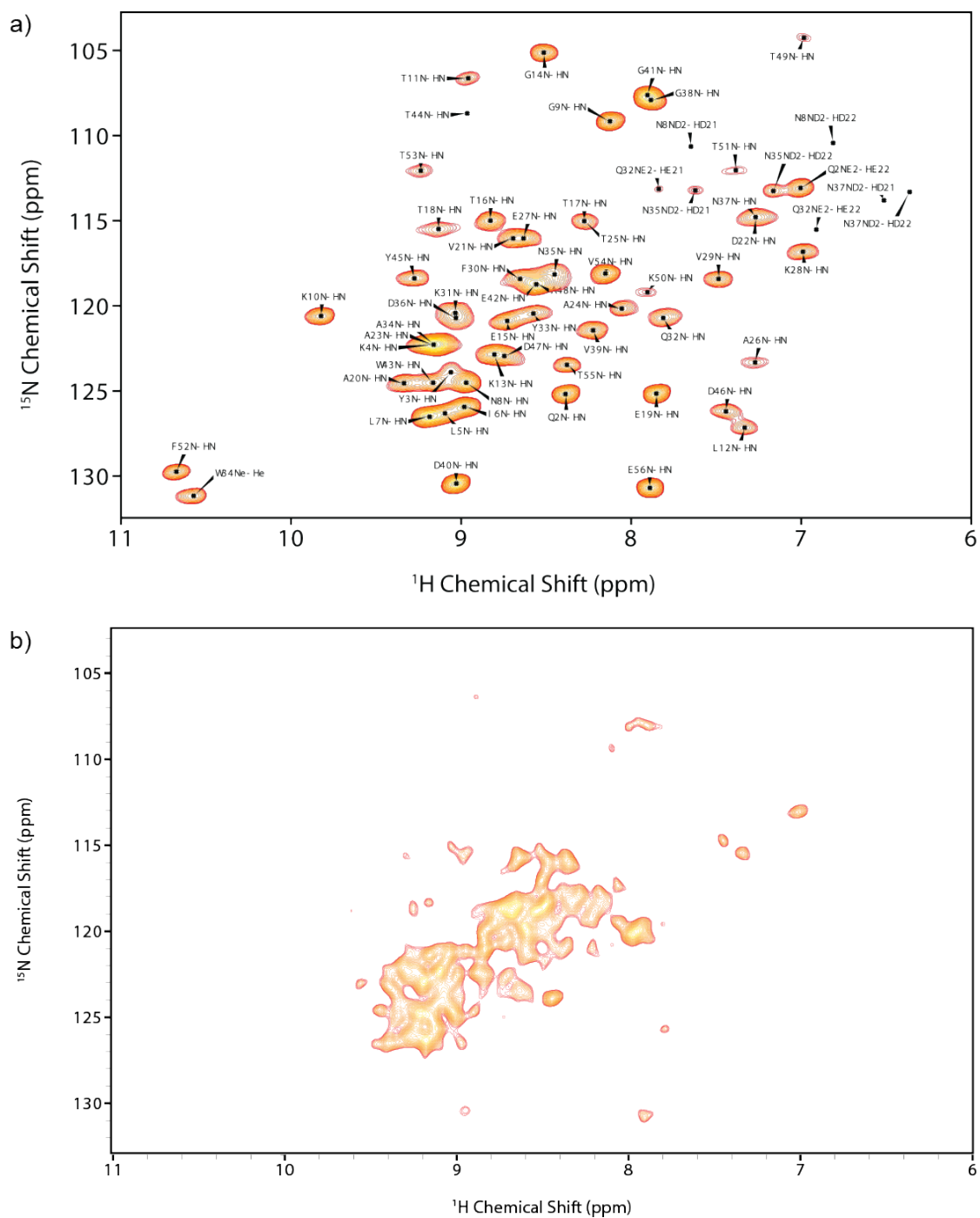


Figure 3.18: a) An assigned 2D ^{15}N - ^1H spectrum of $[\text{U-}^1\text{H}, ^{13}\text{C}, ^{15}\text{N}]$ GB1 crystals packed into a 0.7 mm diameter rotor using the tools presented in this chapter. This spectrum was recorded in 8 scans at 100 kHz MAS and at a ^1H Larmor frequency of 700 MHz. b) A previous 2D ^{15}N - ^1H spectrum of $[\text{U-}^1\text{H}, ^{13}\text{C}, ^{15}\text{N}]$ GB1 crystals packed into a 0.8 mm diameter rotor using a spatula. The protein dehydrated during the lengthy packing process producing a poorly resolved spectrum. This spectrum was recorded in 8 scans at 80 kHz MAS and at a ^1H Larmor frequency of 600 MHz.

As mentioned previously, testing the packing of proteins into the 0.7 or 0.8 mm rotors is significantly more costly than for 1.3 mm rotors. Therefore it was decided that all other aspects of the sedimentation and packing process must be checked thoroughly before attempting to pack a sample into one of these valuable rotors (i.e. the rotors cannot be wasted on test samples). After the initial sedimentation tests and checks for leaks, 100 μ l of the bovine haemoglobin solution was sedimented in the MLA-150 tool at 700,000g for 16.75 hours. Next the 0.7 mm rotor sleeve was swapped in (without a 0.7 mm rotor) and a small piece of parafilm was used to block the bottom of the rotor sleeve, simulating the presence of a 0.7 mm rotor. The tool was then placed into the swinging bucket rotor for 20 minutes at 20,000 x g and the protein was successfully packed into the 0.7 mm rotor sleeve, suggesting that packing the sediment into a 0.7 mm rotor would be equally successful. Furthermore, this final packing step is very similar to the final step for packing microcrystalline samples and therefore is expected to have a comparable result. This test was repeated for the 0.8 mm rotor sleeves with equal success.

The final stage of tests for these MLA-150 tools is to sediment a “real” NMR sample, pack it directly into a rotor using the adaptor and then produce an NMR spectrum of the sedimented protein. Unfortunately this opportunity has not yet arisen because there has been no need to pack this specific type of sample for SSNMR within the Lewandowski lab in the short time since the testing of the tools was completed. The direct transfer of the sediment into 0.7 and 0.8 mm rotors using these tools will make using state-of-the-art MAS technology on large proteins or complexes that are challenging to crystallise far more practical.

3.6 Experimental Considerations for Sedimentation

The success and efficiency of sedimentation is highly dependent on molecular weight, concentration, solvent density and the g-force that the sample is subjected to. Here, these variables are considered in the context of sedimentation of various proteins using the ultracentrifuge tools presented in this chapter.

3.6.1 The Concentration and Molecular Weight Requirements for Successful Protein Sedimentation

First, the effect of protein concentration and molecular weight on the success of sedimentation using the ultracentrifuge tools will be considered. The following equations were published by Bertini *et al.* with regards to their ultracentrifuge device and can also be applied to the tools presented here:¹⁴³

$$c(h) = \frac{c_l}{Ae^{-kh^2} + 1} \quad (3.1)$$

Where $c(h)$ is the concentration of protein (mol dm^{-3}) at h (the distance from the axis of rotation, in metres) and c_l is the limiting concentration of the protein (mol dm^{-3}), experimentally found to be approximately 700 mg ml^{-1} .^{149,150} k and A are given by Equations 3.2 and 3.3.

$$k = \frac{M(1 - \rho_{\text{solvent}}/\rho_{\text{protein}})\omega^2}{2RT} \quad (3.2)$$

Where M is the molecular weight of the protein (kDa), ρ_{solvent} and ρ_{protein} are the densities of the solvent and protein respectively (kg dm^{-3}), ω is the speed of the ultracentrifuge (rad s^{-1}), R is the universal gas constant and T is the temperature (K).

A is an integration constant relating to the total volume of the device (V_{device} , m^3) and the initial concentration of the solution (c_0 , mol dm^{-3}):

$$A = \pi r_1^2 \int_{b_1}^{b_0} c(h) dh + \pi \int_{b_2}^{b_1} \left(\frac{h_p - h + b_1}{h_p} r_1 \right)^2 c(h) dh \\ + \pi r_2^2 \int_{b_3}^{b_2} c(h) dh + \pi r_3^2 \int_{b_4}^{b_3} c(h) dh = c_0 V_{\text{device}} \quad (3.3)$$

Where r_1 , r_2 , r_3 , b_0 , b_1 , b_2 , b_3 , b_4 and h_p refer to various measurements of the device (m), defined in Figure 3.19.

These equations can be used to determine whether the protein can be sedimented straight into the rotor simply by using the MLS-50 ultracentrifuge rotor. This may only be possible for very large proteins, since this rotor can not reach as high speeds as the MLA-150 rotor. The concentration of the protein throughout the device and SSNMR rotor under a range of conditions were calculated using Equations 3.1, 3.2 and 3.3, allowing determination of the fraction of protein in the SSNMR rotor and therefore whether the rotor would be full under these conditions. Figure 3.20 and Table 3.3 show, for a range of molecular weights and proteins, the minimum concentration of protein required for successful sedimentation using both the MLS-50 (black) and MLA-150 (grey) ultracentrifuge tools.

It is clear that high molecular weight proteins (>100 kDa) can be sedimented and packed into a SSNMR rotor using either tool, although the MLA-150 tool may make the process more efficient. On the other hand, it is not possible to sediment

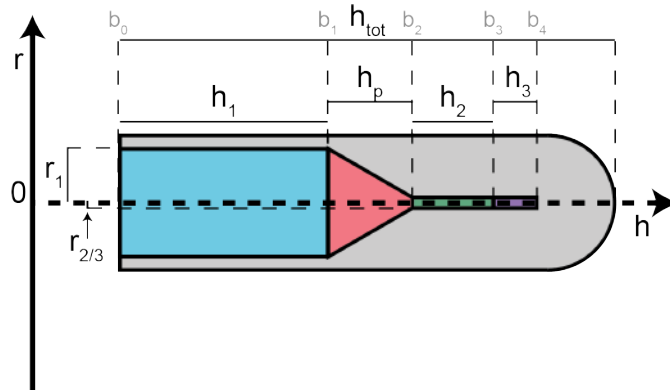


Figure 3.19: A diagram of an ultracentrifuge packing tool highlighting the parameters r_1 , r_2 , r_3 , b_0 , b_1 , b_2 , b_3 , b_4 and h_p for Equation 3.3. Adapted from Bertini *et al.*¹⁴³

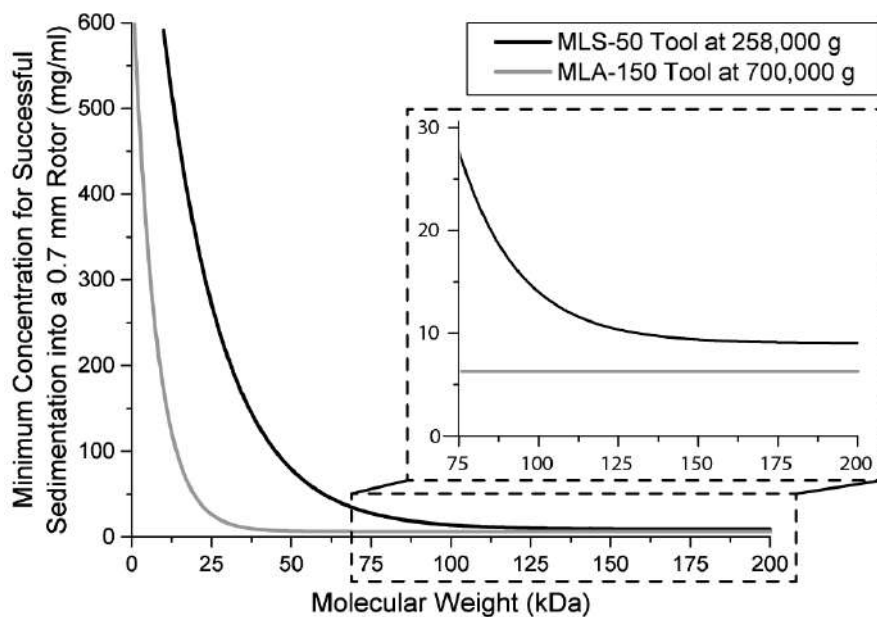


Figure 3.20: Calculated conditions required to fully sediment a protein into a 0.7 mm rotor using the MLS-50 tool at 258,000 x g (black) and the MLA-150 tool at 700,000 x g (grey). The graph indicates the minimum concentration of protein needed for a range of molecular weights.

the lower molecular weight proteins using the MLS-50 tool without unrealistically high concentrations. Therefore the MLA-150 tool is critical for these proteins. For example, sedimentation of a 100 kDa protein requires concentrations of 14.6 and 6.27 mg/ml for the MLS-50 and MLA-150 tools, respectively. Whereas a 25 kDa protein requires 272.70 and 27.51 mg/ml, respectively.

Before deciding which tool to use, these calculations should be performed for the specific protein solution to determine whether the forces produced by the MLS-50 rotor are sufficient to efficiently sediment the sample directly into the rotor or whether the MLA-150 tool is more suitable.

Table 3.3: Examples of proteins with their molecular weights and the minimum concentrations required for successful sedimentation using the MLS-50 and MLA-150 packing tools at 258,000 x g and 700,000g, respectively.

| Protein | MW (kDa) | Minimum Concentration (mg/ml) | |
|--------------------|----------|-------------------------------|--------------|
| | | MLS-50 Tool | MLA-150 Tool |
| Ribonuclease A | 14.0 | 480.46 | 105.45 |
| Chymotrypsinogen A | 25.7 | 263.13 | 25.53 |
| Ovalbumin | 42.9 | 111.66 | 8.00 |
| Albumin | 69.3 | 34.88 | 6.31 |
| Aldolase | 157.4 | 9.86 | 6.27 |
| Catalase | 239.7 | 9.65 | 6.27 |
| Apo-ferritin | 489.3 | 9.65 | 6.27 |

3.6.2 Calculating the Time Required to Sediment a Protein Sample Using the MLS-50 and MLA-150 Packing Tools

Even in cases where it may be possible to sediment directly into an SSNMR rotor using the MLS-50 ultracentrifuge rotor, it can be significantly more efficient to use the MLA-150 rotor and a separate packing step. Furthermore, with either tool it is important to predict the time required for sedimentation. To estimate the sedimentation time, the integrated Svedberg equation can be used:¹⁴³

$$t = 2.533 \times 10^{13} \frac{\ln(b_4/b_0)}{S\omega^2} \quad (3.4)$$

Where t is the time for complete sedimentation (s), ω is the rotation rate of the ultracentrifuge (rad s^{-1}) and S is the sedimentation coefficient of the protein (10^{-13} s). The sedimentation coefficient for proteins is typically in the region of 1-20 Svedberg units (1 Svedberg unit = 10^{-13} s) and can often found in the literature or otherwise determined experimentally. Table 3.4 provides examples of a range of proteins and their sedimentation coefficients.

It is also possible to calculate the maximum sedimentation coefficient (S_{max}) from the molecular weight of the protein:

$$S_{max} = 0.00361 \times M^{2/3} \quad (3.5)$$

Where M is the molecular weight of the protein in Da. This equation is based on the assumption that the protein is a smooth sphere, thus the ratio between S^{max} and S can indicate the shape of a protein.

Figure 3.21 indicates the time required to complete sedimentation using the MLS-50 and MLA-150 tools based on the sedimentation coefficient of the protein. This was calculated using Equation 3.4 and specific examples of sedimentation times can be found in Table 3.4. It is clear that the greater forces achievable using the MLA-150 tool substantially reduce the sedimentation time. Note that this calculation does not take into account whether sedimentation is possible or not, thus Equations 3.1, 3.2 and 3.3 are still crucial for determining the minimum protein concentration for successful sedimentation. The exact parameters used for these calculations are reported in Section B.2.

3.7 Conclusions and Outlook

A set of tools is presented for the sedimentation and packing of biomolecules into 0.7, 0.8 and 1.3 mm rotors, matching the recent developments in MAS SSNMR technology. These tools decrease human error and minimise waste of precious samples whilst also improving sample quality and packing efficiency, reducing the packing time from hours to minutes.

The initial tools (developed by Trent Franks and Georgina Charlton) were tested thoroughly before being used to pack a 1.3 mm rotor with GB1 protein crystals. In order for these tools to be used to both sediment and pack a sample into a 1.3 mm

Table 3.4: Examples of proteins with their molecular weights and sedimentation coefficients (S_{\max} and S). S_{\max} is the theoretical maximum sedimentation coefficient based on the molecular weight of the protein, while S is the experimentally determined coefficient. Both are reported in Svedburg units (10^{-13} s). These values are from Erickson.¹⁵¹ The calculated times for successful sedimentation with the MLS-50 and MLA-150 packing tools at 258,000 x g and 700,000g, respectively, using Equation 3.4 are also reported.

| Protein | MW (kDa) | S_{\max} | S | Sedimentation Time (hours) | |
|--------------------|----------|------------|------|----------------------------|--------------|
| | | | | MLS-50 Tool | MLA-150 Tool |
| Ribonuclease A | 14.0 | 2.1 | 2 | 90.56 | 15.84 |
| Chymotrypsinogen A | 25.7 | 3.15 | 2.6 | 69.66 | 12.19 |
| Ovalbumin | 42.9 | 4.46 | 3.5 | 51.75 | 9.05 |
| Albumin | 69.3 | 6.12 | 4.6 | 39.38 | 6.89 |
| Aldolase | 157.4 | 10.59 | 7.3 | 24.81 | 4.34 |
| Catalase | 239.7 | 13.67 | 11.3 | 16.03 | 2.80 |
| Apo-ferritin | 489.3 | 22.53 | 17.6 | 10.29 | 1.80 |

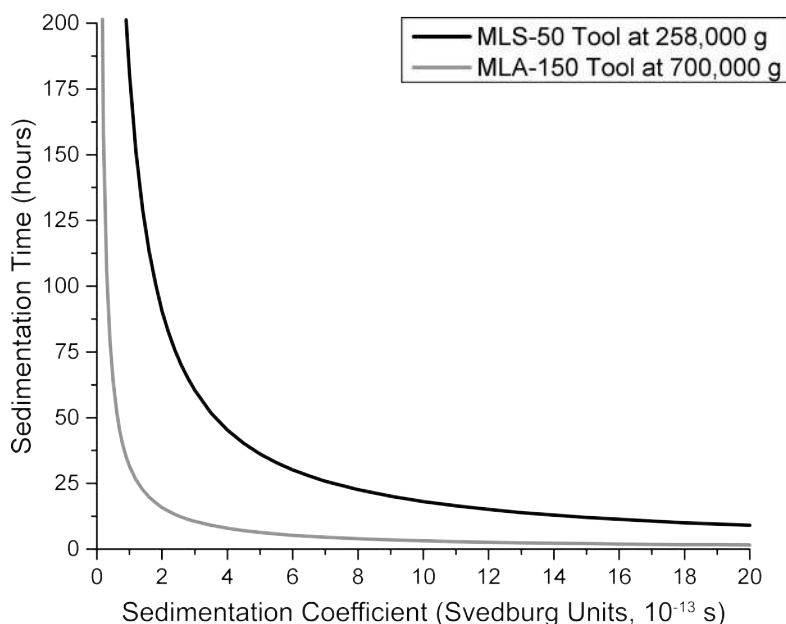


Figure 3.21: The time required for complete sedimentation using the MLS-50 and MLA-150 packing tools at 258,000 x g and 700,000 x g, respectively. These values were calculated using Equation 3.4. For examples of proteins and their sedimentation coefficients in Svedburg units, see Table 3.4.

rotor efficiently, an adaptor was created. The adaptor was functional, however should be shortened slightly to aid with the removal of the MLA-150 tool after packing.

Next, additional tools were created for the smaller (0.7 and 0.8 mm) rotors. A simple design was used, but unfortunately there were leaks and a valuable sample was lost. This leaking was most likely due to the new rotor sleeves not being adapted to the length of each rotor, so new ideas for these rotor sleeves were presented. The second versions of these 0.7 and 0.8 mm rotor sleeves were much improved and the spectrum of a successfully packed crystalline sample is presented in Figure 3.18a. The spectrum had excellent signal and resolution and showed that the protein was well-hydrated. This same sample was then used for the majority of the measurements in Chapter 4.

Sedimentation using the MLA-150 tool followed by packing was tested thoroughly for all rotor sizes. However an NMR spectrum of a sedimented sample packed using these tools is yet to be achieved due to the lack of a suitable protein sample for the smaller rotors, which are effectively one-use and too costly to pack with test samples. A solution of bovine haemoglobin was successfully sedimented and packed into a 1.3 mm rotor using the tools.

The final set of tools presented in this chapter are still in use and have not shown any signs of deterioration, showing that they are able to withstand the extreme conditions essential for the sedimentation and packing of a wide range of proteins. Finally, the equations necessary for predicting the success and efficiency of sedimentation using these tools were presented and discussed.

3.8 Experimental Details

3.8.1 Information on the Ultracentrifuge

The ultracentrifuge used with these tools was the Beckman Coulter Optima MAX-XP ultracentrifuge fitted with either the MLA-150 fixed angle rotor (for sedimentation) or the MLS-50 swinging bucket rotor (for packing). The internal dimensions of the MLA-150 and the MLS-50 are different, so each requires a packing tool of different dimensions. The smaller MLA-150 rotor is used for the sedimentation step, due to the higher forces attainable. For packing the sediment, this smaller packing tool is placed inside an adaptor so that it fits into the larger MLS-50 rotor (see Figure 3.10). The maximum speeds and forces achievable with the different ultracentrifuge rotors are reported in Table 3.5.

3.8.2 Dimensions and Materials of Tools

All parts of the tools were made at the University of Warwick in the Department of Chemistry’s mechanical workshop. *AutoCAD 2017* was used to produce technical drawings of the parts.

The MLS-50 tool (for packing samples) has 3 components; a funnel, a holder and a rotor sleeve, which fits either a 0.7, 0.8 or 1.3 mm rotor inside. The MLA-150 tool (for sedimentation) has 4 components; a funnel, a holder, a rubber seal and a plug. All components, except the O-ring and rubber seal, are made out of PEEK. The rubber seal is made of *Polyco chemprotect* rubber. Technical drawings of all components of the rotor packing tools are provided in Figure 3.22.

3.8.3 Testing of the Tools

Each set of tools was tested as thoroughly as possible in each mode (both sedimentation and packing for each rotor size). Typically, this involved initial tests with water to check the basic functioning of the tool and to test for leaks, followed by using “test” protein samples of either lysozyme crystals for packing or bovine haemoglobin solutions for sedimentation. These proteins were selected due to their low cost, availability and relative simplicity to crystallise or sediment. Finally, once suitable protein samples were ready to be packed into these small rotors for SSNMR, the tools were used to pack these “real” samples.

The maximum forces used in these tests are reported in Tables 3.6 and 3.7, alongside the maximum time the tools were used under these conditions in a single run.

Table 3.5: Maximum speeds of the MLS-50 and MLA-150 ultracentrifuge rotors and the calculated maximum force in each case.

| Rotor | Maximum Speed | Maximum Force |
|---------|---------------|---------------|
| MLS-50 | 50,000 rpm | 258,000 x g |
| MLA-150 | 150,000 rpm | 1,003,000 x g |

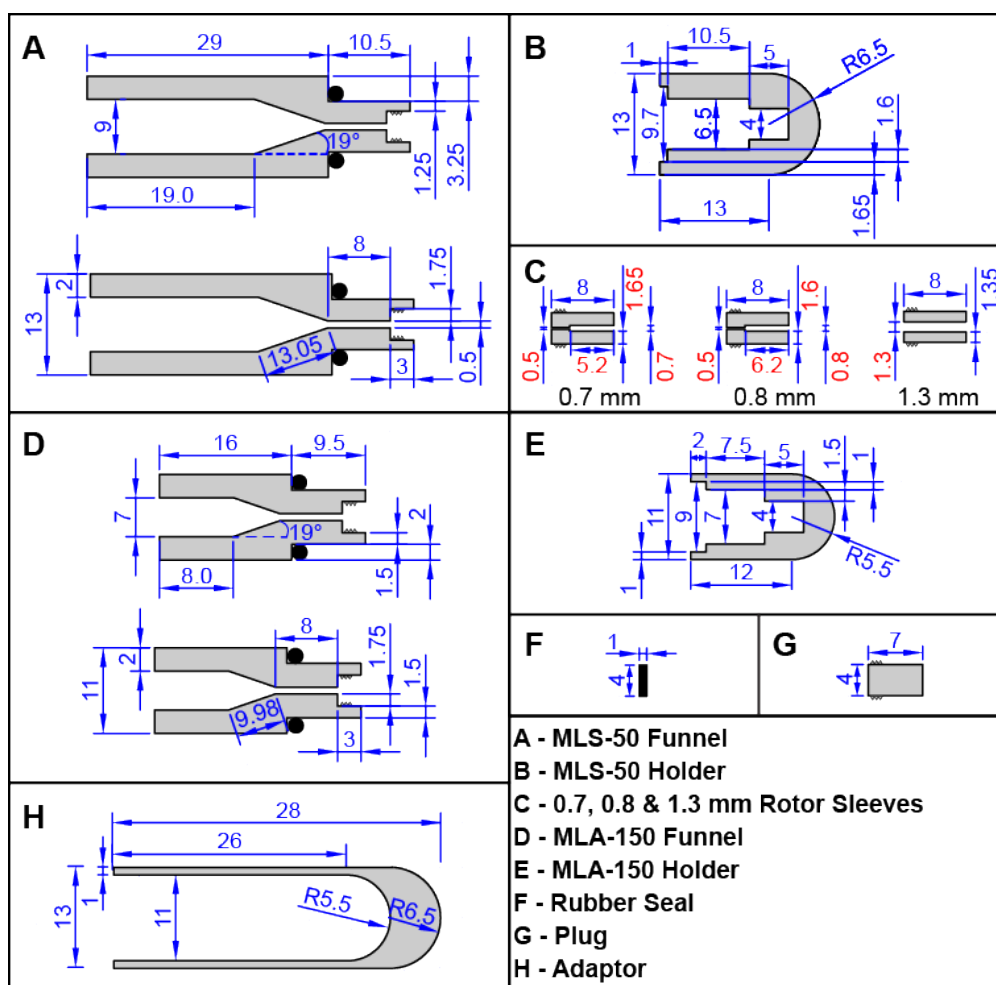


Figure 3.22: Technical drawing of the swinging bucket MLS-50 tool (for packing and sedimentation), fixed angle MLA-150 tool (for sedimentation) and the adaptor. All lengths are in mm. “R” preceding a value denotes the radius of a curve.

The cumulative time that each set of tools has been tested at this force is obviously much longer than stated in the tables, for example the MLA-150 tool in sedimentation mode has been tested at 700,000 x g for over 280 hours in total. Note that it will not always be necessary to use forces as high and times as long as those stated here.

3.8.4 Protein Samples

The [U-¹H, ¹³C, ¹⁵N]GB1 sample was prepared, as described previously,¹³ by expressing the proteins in minimal media with isotopically-labelled with [U-¹³C]glycerol and [U-¹⁵N]-ammonium chloride as the sole sources of carbon and nitrogen. In order to test sedimentation in the tools, 25 mg/ml and 50 mg/ml solutions of bovine haemoglobin in sodium phosphate buffer (pH 5.5m, 50 mM) were produced.

Crystallisation

400 µl sodium phosphate buffer (pH 5.5m, 50 mM) was added to 4.0 mg of [U-¹H, ¹³C, ¹⁵N]GB1, causing the protein to dissolve. 3 x 400 µl aliquots of the precipitant (2:1 2-methyl-2,4-pentanediol (MPD) : isopropanol) were added to the protein solution causing it to become cloudy. The solution was thoroughly mixed and stored in the fridge for at least 48 hours to allow the protein to crystallise.

DSS (4,4-dimethyl-4-silapentane-1-sulphonic acid) was added to the crystallised protein sample as an internal reference. 3.0 mg of [U-¹H, ¹³C, ¹⁵N]GB1 crystals were packed into a 1.3 mm rotor, and 0.5 mg into a 0.7 mm rotor.

3.8.5 NMR Experiment(s)

The NMR experiment was recorded on a Bruker Avance III HD spectrometer, using the software *Topspin 3.5pl7*, operating at 16.4 T ($\omega_{0H}/2\pi = 700$ MHz) with a Bruker 0.7 mm triple-resonance probe. The measurements were performed at 100 kHz spinning frequency at a sample temperature of $13 \pm 1^\circ\text{C}$. The specified sample temperature was achieved by cooling with air (flow of 500 L/h with a target temperature of 15°C) using a Bruker BCU-X cooling unit.

The sample temperature ($^\circ\text{C}$) was measured by the ¹H chemical shift of water with respect to DSS (calibrated to 0 ppm):

$$Temperature = 568.8 - 115.8 \times (\delta_{H_2O} - 0.002 \times (pH - 7.4) - 0.009 \times (salt/100)) \quad (3.6)$$

Where δ_{H_2O} is the chemical shift of water and *salt* is the salt concentration in mM.^{152,153}

Table 3.6: The maximum forces used when testing the **MLA-150** packing tool for each mode. The length of time under these conditions in each case is also reported.

| Mode of MLA-150 Tool | Maximum Force | Time at this Force |
|----------------------|---------------|--------------------|
| Sedimentation | 700,000 x g | 64 hours |
| Packing into 0.7 mm | 20,000 x g | 20 minutes |
| Packing into 0.8 mm | 20,000 x g | 15 minutes |
| Packing into 1.3 mm | 20,000 x g | 10 minutes |

Table 3.7: The maximum forces used when testing the **MLS-50** packing tool for each mode. The length of time under these conditions in each case is also reported.

| Mode of MLS-50 Tool | Maximum Force | Time at this Force |
|----------------------------|----------------------|---------------------------|
| Sedimentation | 200,000 x g | 90 hours |
| Packing into 0.7 mm | 60,000 x g | 10 minutes |
| Packing into 0.8 mm | 60,000 x g | 10 minutes |
| Packing into 1.3 mm | 100,000 x g | 10 minutes |

The measurement was performed using a ^1H -detected ^{13}C - ^1H 2D pulse sequence. The ^1H and ^{13}C $\pi/2$ pulses were of 150 kHz and 83.3 kHz nutation frequency, respectively. Adiabatic double quantum cross-polarization¹⁵⁴ from ^1H to ^{13}C and back to ^1H was used (contact times 0.2 ms and 0.2 ms, $\omega_{1\text{H}}/2\pi \approx 20$ and $\omega_{13\text{C}}/2\pi \approx 80$ kHz). ^1H WALTZ64⁴⁹ ($\omega_{13\text{C}}/2\pi = 10$ kHz) decoupling was applied during t1 evolution (acquisition time of 12 ms). ^{13}C WALTZ64 ($\omega_{13\text{C}}/2\pi = 10$ kHz) decoupling was applied during t2 acquisition (acquisition time of 30 ms). MISSISSIPPI⁵¹ solvent suppression was used with 70 ms of 50 kHz saturation ^1H field on resonance with the solvent. The spectrum in Figure 3.18 was the result of 8 scans and had an experimental time of 40 minutes.

Chapter 4

^1H -Detected NMR Measurements of Aliphatic ^{13}C R_1 in Fully-Protonated Proteins in the Solid State

The SDST measurements presented in this chapter were performed by Dr. Angelo Gallo and the 60 kHz MAS PDSD spectra were recorded with guidance from Dr. Jonathan Lamley (both supervised by Dr. Józef R. Lewandowski, Department of Chemistry, University of Warwick).

4.1 Abstract

It is particularly challenging to suppress the rate-averaging effects of proton-driven spin diffusion during aliphatic ^{13}C R_1 measurements, especially without high levels of deuteration and alternating ^{13}C -labelling of the protein. In this chapter, experiments for the measurement of site-specific $^{13}\text{C}^\alpha$ R_1 relaxation rates in a crystalline, fully-protonated, uniformly ^{13}C -labelled protein at 100 kHz MAS are presented.

Initial spin diffusion control spectra and saturation transfer measurements in the solid state indicated that certain $^{13}\text{C}^\alpha$ nuclei in residues with $^{13}\text{C}^\alpha$ and $^{13}\text{C}^\beta$ close in chemical shift were still undergoing spin diffusion at 100 kHz MAS. However, variable spinning $^{13}\text{C}^\alpha$ R_1 experiments revealed that, at ≥ 90 kHz spinning, this spin diffusion does not have a significant effect on the relaxation rates. The fast spinning enables both effective suppression of the effects of proton-driven spin diffusion for protonated carbons and provides for the high resolution suitable for sensitive proton-detected experiments. These experimental conditions allow for rapid, accurate measurement of $^{13}\text{C}^\alpha$ R_1 on sub-milligram amounts of fully-protonated, uniformly ^{13}C -labelled protein.

4.2 Introduction

Protein dynamics are intimately related to protein function and play a fundamental role in a vast array of biological processes.^{7,9,155} Consequently, detailed characterisation of motions is often a crucial step towards developing a full understanding of these systems at the molecular level. NMR relaxation measurements are particularly valuable in this context because they offer the ability to probe both the amplitudes and correlation times of motions in a quantitative and site-specific manner at physiologically-relevant conditions (relevant temperature, pH and concentration).^{26,156,157} However, further developments are necessary to adequately describe the complex dynamics, especially because in the solid state NMR relaxation rates allow access to motions across a greatly extended range of timescales (ps-ms)^{158–160} compared to in the solution state (ps-ns).²⁶

For R_1 measurements in the solid state, which are particularly sensitive to motions on the ps-ns timescale, the primary challenge is to eliminate proton-driven spin diffusion (PDSD),^{68–70,161,162} whereby polarisation is exchanged between nuclear sites via dipolar couplings.^{163,164} Various techniques can be used to suppress the effects of spin diffusion, such as fast MAS (which reduces dipolar coupling) and substituting nuclei for those of a lower gyromagnetic ratio (e.g. ^1H for ^2H) or with NMR-inactive nuclei (e.g. ^{13}C for ^{12}C) when producing the sample. Often a combination of these techniques is required, especially for nuclei involved in strong dipolar coupling networks such as $^{13}\text{C}^\alpha$ nuclei and other aliphatic ^{13}C nuclei. The literature has shown that, thus far, it has only been possible to accurately measure $^{13}\text{C}^\alpha$ R_1 in proteins with the use of MAS (50 - 60 kHz) combined with both alternating ^{13}C -labelling and high levels of deuteration.¹⁶⁵ Here we investigate the possibility of measuring aliphatic ^{13}C R_1 on a fully-protonated, uniformly ^{13}C -labelled protein using MAS frequencies of up to 100 kHz.

4.3 Literature Review

4.3.1 Spin Diffusion

Spin diffusion (SD) was first described by Bloembergen in 1949 where it was observed that the measured R_1 rates of crystals with paramagnetic impurities were orders of magnitude away from the predicted values for pure crystals.¹⁶² He suggested that there was an exchange of energy between the paramagnetic impurity and the crystal that affects the relaxation rates, and that this exchange was dependent on B_0 , the relaxation rates and concentration of the impurity. Subsequently, spin diffusion has been researched in detail, both theoretically and experimentally.^{22,67,166–168}

Proton driven spin diffusion is the spontaneous exchange of magnetisation between nuclei via terms involving ^1H -X and X-X dipolar couplings, where X = ^{13}C or ^{15}N (see Figure 4.1). Through specific experiments, spin diffusion can be used to calculate distance constraints in proteins, aiding structure determination in the solid state.^{54,120,163,169–173} However, it is critical that spin diffusion is suppressed during relaxation measurements; if the polarisation transfer occurs quickly compared to the measured relaxation rates, these rates will represent an average over a number of sites,

eliminating site-specificity and preventing their use in quantitative analysis.^{68–71} (See Theory Section 2.3.13 for a more detailed explanation of spin diffusion.)

The effects of PDSD can be reduced or completely removed in relaxation measurements through the use of various experimental techniques. PDSD is highly dependent on dipolar couplings, therefore the extent of the spin diffusion is proportional to the gyromagnetic ratios of the nuclei and inversely proportional to the cube of the internuclear distance (see Equation 2.11). Thus the most efficient terms for ^{13}C - ^{13}C PDSD arise from cross-terms involving directly bonded ^1H - ^{13}C and ^{13}C - ^{13}C dipolar couplings (due to their close proximity and relatively high gyromagnetic ratios, see Figure 4.1a), with the terms originating from cross-terms between the ^{13}C - ^{13}C couplings being less important.^{163,164} Because of the geometry of the carbon chain, the most efficient pathway for polarisation transfer involves relayed transfer along the chain. This is especially true for directly bonded ^{13}C sites with similar chemical shifts, meaning that PDSD is particularly prominent in fully-protonated, uniformly ^{13}C -labelled proteins at the aliphatic ^{13}C sites. Therefore it is also very challenging to suppress the effects of PDSD at these nuclei. In contrast, the $^{13}\text{C}'$ sites are much less affected by PDSD due to the lack of directly bonded protons and the large chemical shift difference between $^{13}\text{C}'$ and $^{13}\text{C}^\alpha$ nuclei.

The effects of PDSD on ^{13}C relaxation measurements can, in principle, be mitigated through improved averaging at faster MAS frequencies (Figure 4.1b),^{68,70,158} or by altering the ^1H -X and X-X pathways. The latter can be achieved by substitution of sites with nuclei of a lower gyromagnetic ratio, which reduces the magnitude of dipolar couplings (e.g. ^1H to ^2H substitution),⁷¹ or substituting with NMR-inactive isotopes, which effectively eliminates the dipolar couplings (e.g. ^{13}C to ^{12}C).¹⁶⁵

Fast Magic Angle Spinning

As explained in Section 2.1.3, dipolar couplings can be averaged out through MAS. The faster this spinning, the more complete the removal of dipolar couplings, which will in turn reduce PDSD. For protein SSNMR measurements, it is typical to apply MAS of up to 60 kHz (using a 1.3 mm diameter rotor), however recent advances in NMR equipment now allow for MAS up to 110 kHz (0.7 - 0.8 mm rotors).²³

In a fully-protonated protein, coherent contributions to ^{15}N and ^{13}C $R_{1\rho}$ can be effectively removed in experiments performed at spinning frequencies ≥ 50 kHz and by employing spin-locks with nutation frequencies ≥ 8 kHz.^{158,174} PDSD is generally well-suppressed at spinning frequencies ≥ 20 kHz for ^{15}N R_1 measurements^{68,69,161} and ≥ 60 kHz for $^{13}\text{C}'$ R_1 measurements, due to the different gyromagnetic ratios.⁷⁰ However, even though 60 kHz spinning significantly attenuates PDSD for protonated carbons in uniformly ^{13}C -labelled proteins, it is not negligible under these conditions, especially in the case of $^{13}\text{C}^\alpha$ and ^{13}C sidechain nuclei.^{70,165}

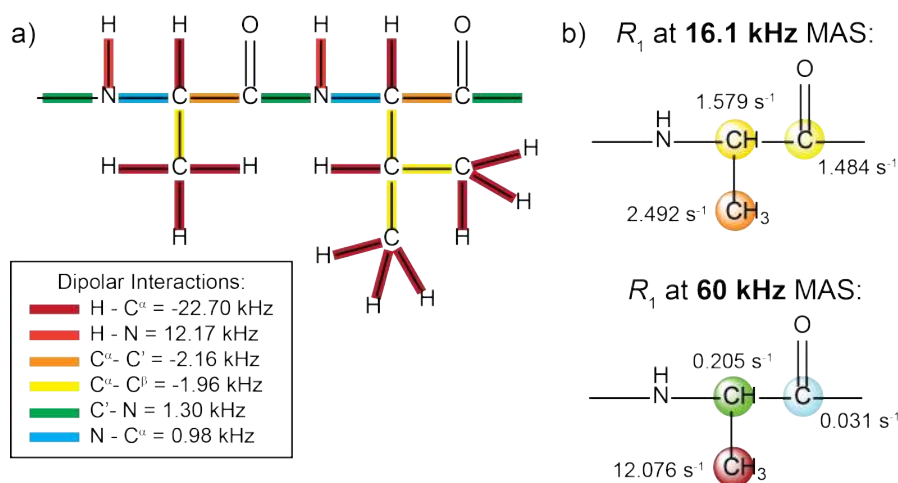


Figure 4.1: a) Examples of dipolar interactions in a section of [U- ^1H , ^{13}C , ^{15}N] protein (alanine-valine) coloured by strength. Spin diffusion originates from these dipolar interactions. b) The measured ^{13}C R_1 values for [U- ^{13}C , ^{15}N] alanine at 16.1 and 60 kHz MAS, highlighting the averaging of the relaxation rates at the slower spinning frequency via PDSD. The rates are from Lewandowski *et al.*⁷⁰ and at ^1H Larmor frequency of 900 MHz.

Substitution of High- γ Sites with Lower- γ Nuclei

The dipolar coupling is proportional to $\frac{\gamma_j \gamma_k}{r_{jk}^3}$, so it is clear that if either of the gyromagnetic ratios are reduced, then the effects of PDSD will be considerably diminished. A common application of this technique is deuteration of the protein sample, which can be achieved with deuterated media during protein production. Note that although the protein may be produced using 100% deuterated media, the amide sites throughout the protein will likely be exchangeable, resulting in a protein with ^2H nuclei at non-exchangeable sites and ^1H nuclei at exchangeable amide sites (see Figure 4.2).^{46,175–178}

Substitution for NMR-Inactive Isotopes

NMR-inactive nuclei, such as ^{12}C , are not involved in dipolar interactions. These are ideal candidates for replacing high- γ nuclei, therefore diluting the spin system and re-

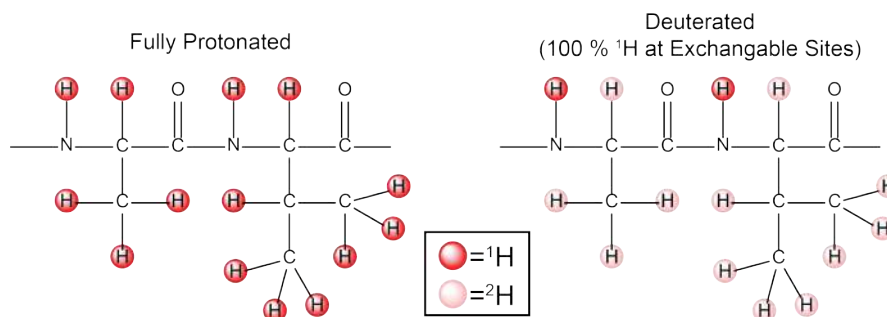


Figure 4.2: The ^1H (red) and ^2H (pink) labelling in an example section of a protein (Ala-Val) for fully-protonated and deuterated samples. Note the ^1H nuclei at the exchangeable sites in the deuterated protein.

ducing spin diffusion.^{54,173} It is common to label protein samples by expressing them in minimal media with partially isotopically labelled ^{13}C or ^{15}N sources, such as [1,3- ^{13}C]-glycerol and [15% ^{15}N]-ammonium chloride, as the sole ^{13}C or ^{15}N source.^{52,54–57} Examples of these labelling schemes are presented in Figures 2.7 and 2.8, a simplified example is shown in Figure 4.3.

Spin Diffusion and Relaxation Measurements

It has been shown that ^{15}N and ^{13}C R_1 and $R_{1\rho}$ relaxation rates can be accurately measured in fully-protonated, uniformly ^{13}C and ^{15}N labelled proteins with just 60 kHz MAS.^{68,158} In fact, an investigation into the contributions of spin diffusion to ^{15}N R_1 at a range of MAS frequencies revealed that 10 kHz spinning is enough to remove most of the effects of PDS due to a combination of the lower gyromagnetic ratio and the sparse spread of the ^{15}N nuclei throughout the protein (compared to ^{13}C sites).^{68,70} However, suppressing spin diffusion in aliphatic ^{13}C R_1 measurements is much more challenging due to the larger size of ^1H - ^{13}C and ^{13}C - ^{13}C dipolar couplings, as well as the density of ^{13}C nuclei throughout the protein. In general, a combination of fast MAS with deuteration and/or partial ^{13}C -labelling is required for reliable measurement of aliphatic ^{13}C R_1 .

Deuteration has been used extensively to aid the measurement of ^{13}C and ^{15}N R_1 and $R_{1\rho}$.^{52,69,71,165,179–181} It is not just a tool for relaxation measurements, deuteration can be highly beneficial in many NMR experiments due to the improvements in resolution, since the strong ^1H - ^1H dipolar couplings that broaden the spectra are removed.^{46,177,178} Unfortunately, not all proteins can be easily produced in large quantities with deuterium labelling, and deuteration is in general expensive. Furthermore, the removal of most of the protons affects sensitivity, which is only partially compensated by the narrowing of ^1H lines. The sensitivity is always an important consideration, but especially for complicated systems, such as sparingly-labelled proteins or large protein complexes.^{5,52}

There are various examples of R_1 and $R_{1\rho}$ measurements on partially ^{13}C - or ^{15}N -labelled proteins in the literature.^{52,57,70,165} Like deuteration, producing large quantities of proteins with these particular labelling schemes can be complex and costly. A further

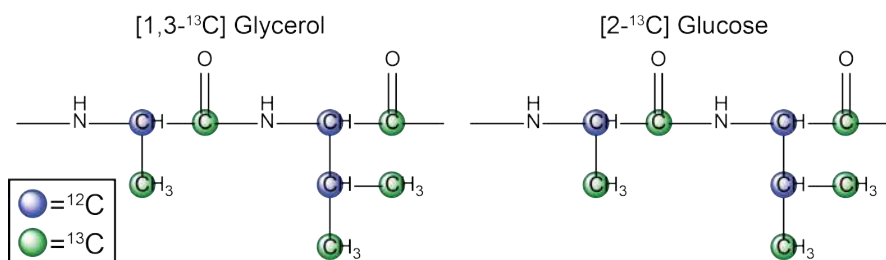


Figure 4.3: The ^{12}C (blue) and ^{13}C (green) labelling in an example section of a protein (Ala-Val) for the [1,3- ^{13}C]glycerol and [2- ^{13}C]glucose labelled samples used in this chapter. For the full [1,3- ^{13}C]glycerol and [2- ^{13}C]glucose labelling schemes see Figures 2.7 and 2.8.

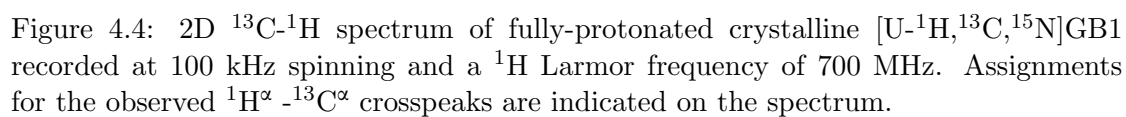
disadvantage of using NMR-inactive nuclei at certain sites, is that these sites cannot be probed with NMR (for example, both C' and C α sites cannot be investigated using a protein labelled with [1,3- ^{13}C]glycerol).

Fast MAS not only mitigates the coherent effects present in relaxation measurements, but also allows one to take advantage of the improved sensitivity of proton-detected experiments (as opposed to ^{13}C and ^{15}N -detected variants).^{43–45,182} Thus allowing high-sensitivity measurements on samples with only limited proton dilution or full protonation.^{23,183–189} In general, the higher the spinning frequency, the larger the fraction of protons that can be retained in the sample, while keeping proton line widths sufficiently narrow for practical applications.^{5,43,184,190} For example, on small, well-behaved, fully-protonated proteins, ^1H - ^{15}N 2D correlations become practical at spinning frequencies > 40-60 kHz^{183,185} and ^1H - ^{13}C 2D correlations at spinning frequencies > 80 kHz.⁵ The latter is illustrated in Figure 4.4, which shows a ^1H - ^{13}C 2D spectrum of fully-protonated, crystalline [U- ^{13}C , ^{15}N]GB1 obtained at 100 kHz MAS and a ^1H Larmor frequency of 700 MHz.

It was previously demonstrated that the $^{13}\text{C}\alpha$ R_1 for [U- ^{13}C , ^{15}N] and [2- ^{13}C] labelled alanine were different at 16.1 kHz MAS, but not significantly different at 60 kHz.⁷⁰ It was thus suggested that spin diffusion is significantly reduced at 60 kHz MAS for a fully-protonated, uniformly-labelled protein, however further improvements are required for quantitative R_1 measurements. Asami *et al.* showed that with extensive deuteration (with 10% H_2O /90% D_2O used in sample production) and partial carbon labelling alongside ≥ 50 kHz spinning it is possible to effectively eliminate PDS for $^{13}\text{C}\alpha$ sites. Therefore enabling accurate, site-specific measurements of the $^{13}\text{C}\alpha$ R_1 rates.¹⁶⁵ The advantage of the latter approach is that it not only eliminates PDS, but that the narrow line widths and improved coherence life times for the remaining protons produce well-resolved ^1H -detected spectra at moderate spinning frequencies. Even though the loss of sensitivity due to removal of most protons is partially compensated by the narrowing of ^1H lines, if narrow ^1H line widths can be achieved with high concentrations of protons this will translate to appropriate gains in sensitivity compared to dilute samples. It is thus desirable to develop approaches that provide access to aliphatic ^{13}C relaxation in fully-protonated systems. This chapter investigates whether it is possible to accurately measure site-specific aliphatic ^{13}C R_1 on a fully-protonated, uniformly-labelled protein using MAS frequencies of up to 100 kHz.

4.4 Results

It is critical to prove that these $^{13}\text{C}\alpha$ R_1 rates at 100 kHz are not affected by PDS, otherwise the R_1 measurements are not meaningful. Here, PDS control spectra are recorded for uniformly and partially ^{13}C -labelled proteins at 60 kHz and 100 kHz MAS, highlighting the effectiveness of fast MAS (and partial ^{13}C -labelling) at suppressing spin diffusion. These are followed by spin diffusion saturation transfer measurements at 100 kHz MAS, which precisely indicate the $^{13}\text{C}\alpha$ sites that are most susceptible to



spin diffusion and also allow predictions of whether PDSD will substantially affect the sidechain ^{13}C nuclei. These data and predictions are then compared to the true effects of SD on aliphatic ^{13}C R_1 , determined experimentally through variable magic angle spinning (VMAS) measurements, which indicate the MAS frequency required for any PDSD effects to become negligible. A final consideration is whether cross-correlated relaxation could be affecting these R_1 measurements under such fast spinning conditions.

4.4.1 Spin Diffusion Control Spectra at 60 and 100 kHz MAS

A PDSD control measurement utilises a mixing time where magnetisation is allowed to exchange. The experiment produces a 2D spectrum with off-diagonal crosspeaks between sites that have exchanged magnetisation. The spin diffusion was compared for $^{13}\text{C}^\alpha$ sites within $[\text{U-}^{13}\text{C}]$ and $[1,3\text{-}^{13}\text{C}]$ glycerol labelled crystalline GB1 samples at 60 kHz MAS (Figure 4.5). The many crosspeaks in the uniformly ^{13}C -labelled spectrum suggest that significant PDSD is occurring under these conditions (60 kHz MAS). However there is a significantly higher level of PDSD suppression for the partially ^{13}C -labelled protein. In fact, the only weak residual crosspeaks that are observed are due to cases where the one-bond ^{13}C - ^{13}C couplings are still retained for a significant fraction of the molecules (due to the specific labelling scheme, see Figure 2.7) and the sites are close in chemical shift, for example $\text{ThrC}^\alpha\text{C}^\beta$ and $\text{AspC}^\alpha\text{C}^\beta$. For cases such as $\text{GlnC}^\alpha\text{C}^\beta$, where both the sites are partially ^{13}C enriched and have significantly different chemical shifts, PDSD is still suppressed. Therefore, if one-bond ^{13}C - ^{13}C dipolar couplings can be eliminated, it is possible to accurately measure $^{13}\text{C}^\alpha$ R_1 in a fully-protonated, partially ^{13}C -labelled sample at 60 kHz MAS. 1D slices extracted from the PDSD spectra for both samples at 22.1, 43.2 and 69.7 ppm highlight just how effective removal of the directly-bonded ^{13}C - ^{13}C dipolar couplings is for suppressing PDSD (Figure 4.5c-e).

Continuing this investigation on the partially ^{13}C -labelled protein, the potential effects of RF-driven spin diffusion (RFSD) and ^{13}C - ^{13}C TOCSY during the spin lock of the ^{13}C $R_{1\rho}$ measurements are also considered. As in the case of PDSD, such effects are not a problem for ^{15}N and ^{13}C relaxation measurements,^{158,174} but might need to be considered for aliphatic ^{13}C sites. The control experiments at 60 kHz spinning, presented in Figure 4.6, demonstrate that the removal of directly bonded ^{13}C - ^{13}C pairs also results in the effective removal of RFSD and ^{13}C - ^{13}C TOCSY for all aliphatic sites.

It is clear that significant PDSD is present at 60 kHz MAS. Similar control spectra were recorded on fully-protonated crystalline $[\text{U-}^1\text{H}, ^{13}\text{C}, ^{15}\text{N}]\text{GB1}$ at 100 kHz MAS to see if PDSD is sufficiently reduced (Figure 4.7). Proton detection was used during these measurements to enhance the sensitivity, resulting in ^1H - ^{13}C spectra (rather than the ^{13}C - ^{13}C in Figure 4.5). In these spectra, evidence of PDSD is monitored through the appearance of additional peaks due to magnetisation transfer in the mixing time (i.e. peaks that are not present in the 0 second mixing time spectrum). The spectra with longer mixing times revealed just six additional $^{13}\text{C}^\alpha$ - $^{13}\text{C}^\beta$ crosspeaks produced by the exchange of magnetisation from neighbouring $^{13}\text{C}^\alpha$ and $^{13}\text{C}^\beta$ sites via spin diffusion (Y3, D22, N37, D40, T51 and T55). Although such crosspeaks are only present for a small

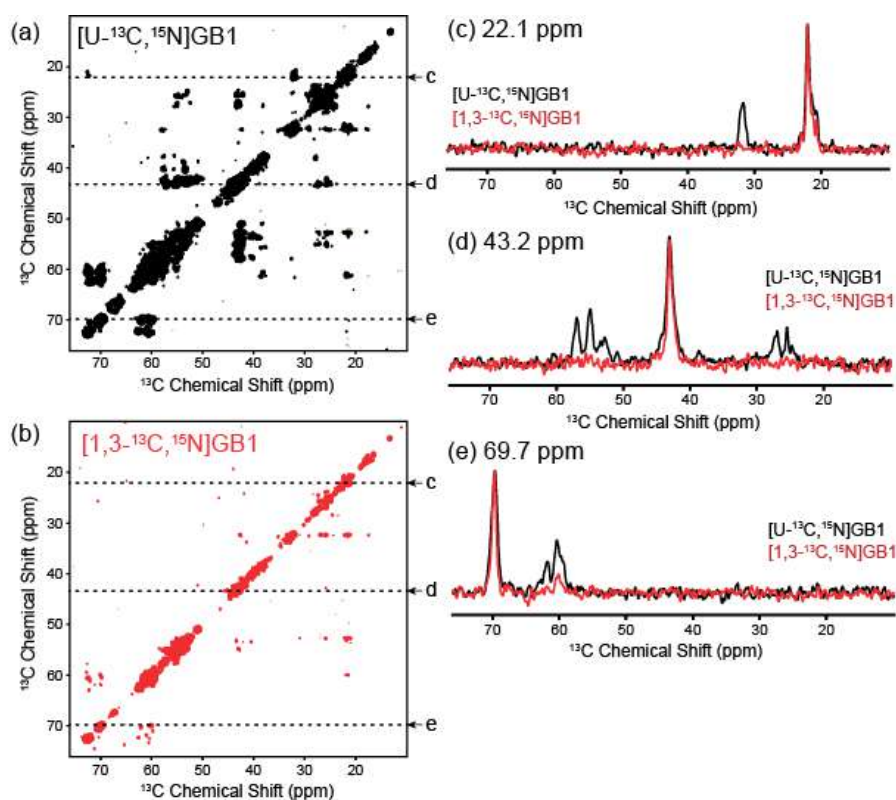
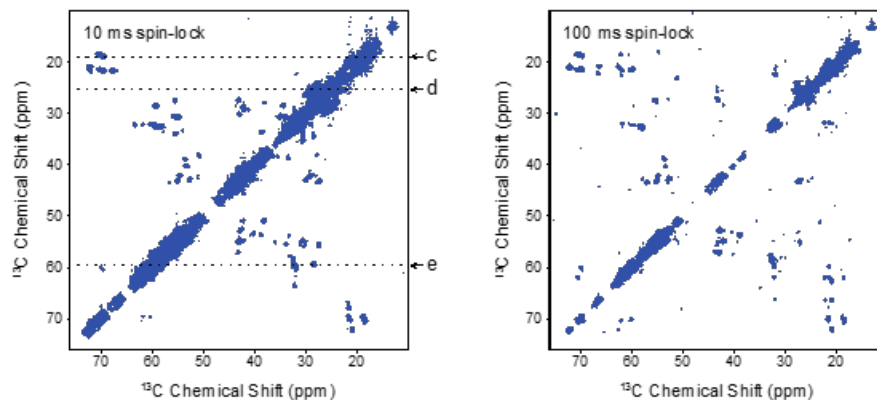
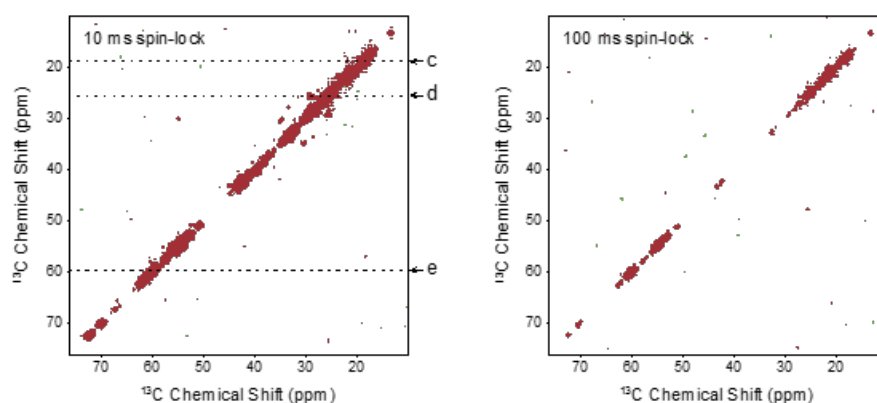


Figure 4.5: Control PDSD spectra recorded on a) $[U-^{13}\text{C}, ^{15}\text{N}]$ GB1 and b) $[1,3-^{13}\text{C}, ^{15}\text{N}]$ GB1 at 60 kHz MAS and 600 MHz ^1H Larmor frequency. The data illustrates that the high level of suppression of PDSD is achieved already at 60 kHz spinning upon removal of one-bond ^{13}C - ^{13}C dipolar couplings (the only weak residual crosspeaks are observed for cases where such couplings are retained for a significant fraction of molecules). Panels (c-e) show 1D slices extracted at frequencies indicated with arrows in panels (a-b). The mixing time is 1 s for both spectra. Note that the absence of peaks in b is partially due to the reduced labelling in addition to the reduced spin diffusion.

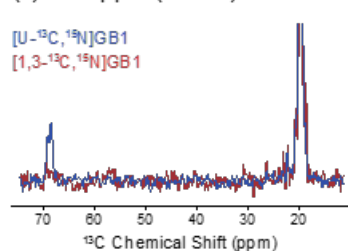
(a) $[U-^{13}C, ^{15}N]GB1$



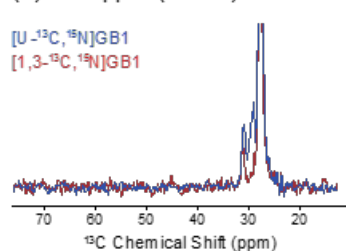
(b) $[1,3-^{13}C, ^{15}N]GB1$



(c) 18.7 ppm (10 ms)



(d) 25.7 ppm (10 ms)



(e) 59.4 ppm (10 ms)

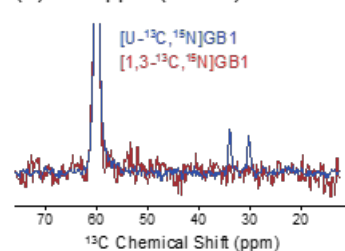


Figure 4.6: Control RFSD spectra with mixing times of 10 and 100 ms recorded on a) $[U-^{13}C, ^{15}N]GB1$ and b) $[1,3-^{13}C, ^{15}N]GB1$ at 60 kHz spinning frequency and 600 MHz 1H Larmor frequency. Panels c-e show 1D slices extracted at frequencies indicated with arrows in panels a and b.

percentage of $^{13}\text{C}^\alpha$ sites, it is clear that spin diffusion is still affecting a handful of the nuclei at 100 kHz MAS, thus further investigation is required.

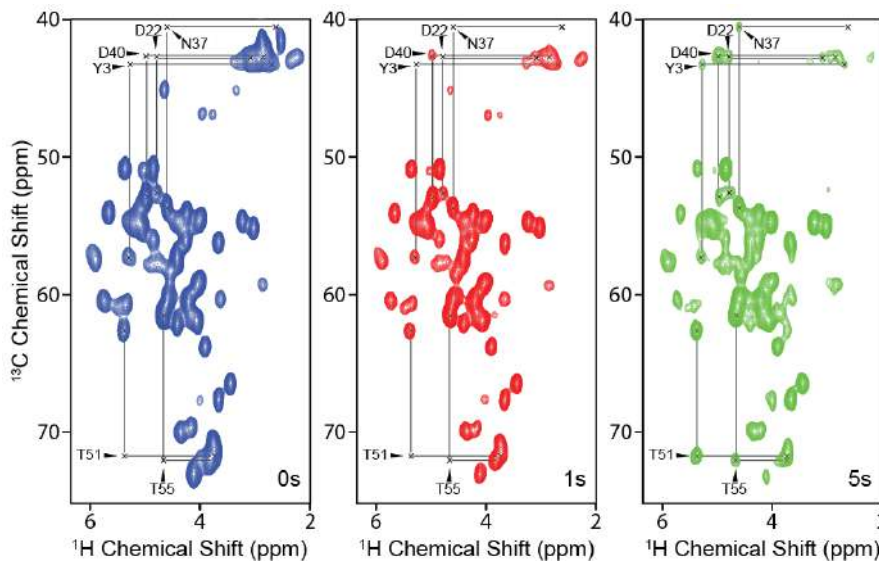


Figure 4.7: Control PDSD spectra recorded on $[\text{U-}^1\text{H}, ^{13}\text{C}, ^{15}\text{N}]\text{GB1}$ at 100 kHz MAS and 700 MHz ^1H Larmor frequency. Mixing times are 0 s (blue), 1 s (red) and 5 s (green). Six additional peaks are observed with a 5 s mixing time that are not present in the 0 s mixing time spectrum, these $^{13}\text{C}^\alpha\text{-}^{13}\text{C}^\beta$ crosspeaks are labelled by residue.

4.4.2 Spin Diffusion Saturation Transfer at 100 kHz MAS

The spin diffusion control spectra have shown that spin diffusion may be affecting six $^{13}\text{C}^\alpha$ sites and that those with a small $^{13}\text{C}^\alpha\text{-}^{13}\text{C}^\beta$ chemical shift difference are most susceptible. Next, the presence of PDSD at each $^{13}\text{C}^\alpha$ site was investigated through spin diffusion saturation transfer (SDST) measurements in the solid state. SDST, like CEST (see Theory Section 2.3.14), utilizes a small, selective field to saturate a small frequency range. In this case, the resulting profiles indicate both magnetisation exchange due to PDSD and, if there were any, chemical exchange. ^{13}C SDST spectra were recorded for $^{13}\text{C}^\alpha$ and some sidechain ^{13}C nuclei throughout fully-protonated crystalline $[\text{U-}^1\text{H}, ^{13}\text{C}, ^{15}\text{N}]\text{GB1}$ at 100 kHz MAS and 700 MHz ^1H Larmor frequency.

The SDST profiles (Figure 4.8) show the relative intensity of the ^{13}C signal plotted against the offset of the saturation pulse. Any spin diffusion affecting the $^{13}\text{C}^\alpha$ nuclei would most likely be from a directly-bonded $^{13}\text{C}^\beta$ nucleus. Therefore a decrease in intensity of the $^{13}\text{C}^\alpha$ peak would be observed when the saturation pulse is at the chemical shift of the $^{13}\text{C}^\beta$ nucleus, due to the exchange of magnetisation between the $^{13}\text{C}^\alpha$ and $^{13}\text{C}^\beta$ sites. For example, the absence of magnetisation exchange due to PDSD for the alanine-34 $^{13}\text{C}^\alpha$ nuclei is indicated by the single decrease in intensity of the $^{13}\text{C}^\alpha$ peak when the saturation pulse is at the frequency of the $^{13}\text{C}^\alpha$ peak (Figure 4.8a). On the other hand, threonine-11 decreases in intensity when saturated at both the $^{13}\text{C}^\alpha$ and $^{13}\text{C}^\beta$ frequencies, indicating spin diffusion between these two sites (Figure 4.8b). The complete $^{13}\text{C}^\alpha$ SDST data is presented in Figures 4.9 and 4.10. In each case the residues

that show evidence of $^{13}\text{C}^\alpha$ - $^{13}\text{C}^\beta$ exchange are boxed in red and the frequency of the $^{13}\text{C}^\beta$ peak is marked. Those that do not show this evidence are boxed in green, and in the cases where it is unclear a black outline is used.

Analysis of the SDST data revealed 17 $^{13}\text{C}^\alpha$ sites that still showed some signs of being affected by PDS at 100 kHz MAS: Y3, N8, T11, K13, T17, T18, D22, N37, D40, T44, D46, D47, T49, T51, F52, T53 and T55. These sites were those in which the $^{13}\text{C}^\alpha$ nuclei and $^{13}\text{C}^\beta$ nuclei are close in chemical shift, for example threonine-53 and aspartic acid-40, which have $^{13}\text{C}^\alpha$ - $^{13}\text{C}^\beta$ chemical shift differences of 11.5 and 11.1 ppm respectively, compared to alanine-34, which has a 38.0 ppm difference. Figure 4.11 highlights how this difference in chemical shift of adjacent aliphatic ^{13}C nuclei correlates with the susceptibility of the nuclei to PDS. Those showing evidence of PDS in the SDST data are shown in red and those not are in green. It becomes clear that the spin diffusion may only be occurring at the sites where the difference in chemical shift is < 15 ppm (black dashed line). These observations agree with the theory presented by Suter and Ernst, which states that the rate of SD is dependent on this difference in chemical shift, alongside other factors such as distance.^{166,191,192} Figure 4.11 highlights that almost all of the sidechain ^{13}C nuclei have a chemical shift difference of < 15 ppm with their neighbouring ^{13}C nuclei. Therefore these sites are predicted to be undergoing PDS at 100 kHz MAS, alongside a handful of the $^{13}\text{C}^\alpha$ nuclei.

4.4.3 Experimental ^{13}C R_1 Measurements at Variable MAS

The SDST profiles and PDS control spectra make it clear that, despite most $^{13}\text{C}^\alpha$ sites being free of spin diffusion at 100 kHz MAS, it is still present at a handful of sites, specifically those with similar $^{13}\text{C}^\alpha$ and $^{13}\text{C}^\beta$ chemical shifts.

Fully-Protonated Crystalline [U- ^{13}C , ^{15}N]GB1

To experimentally establish the extent of the residual SD effects on the measured rates, aliphatic ^{13}C R_1 was measured at MAS frequencies of 60, 70, 80, 90 and 100 kHz on fully-protonated crystalline [U- ^{13}C , ^{15}N]GB1 using proton detection. Lower $^{13}\text{C}^\alpha$ R_1 rates are expected at the lower spinning frequencies, where the effects of PDS are more prominent. Determining the spinning frequency at which the rates become constant will reveal the conditions under which PDS is negligible. The $^{13}\text{C}^\alpha$ R_1 rates were extracted and plotted against MAS frequency. Examples of these are presented in Figure 4.12. The full variable MAS results are in Figures C.2 and C.3, and a 2D ^1H -aliphatic ^{13}C correlation spectrum at each MAS frequency is presented in Figure C.1 (note the improvement in resolution as the spinning frequency is increased) in the appendix.

On average, a 21% decrease in $^{13}\text{C}^\alpha$ R_1 is observed between 60 and 100 kHz. It is clear that at spinning frequencies ≥ 90 kHz significant variation in R_1 is no longer observed. This demonstrates the conditions under which the undesirable effects of PDS are negligible for $^{13}\text{C}^\alpha$ spin-lattice relaxation measurements in a fully-protonated, uniformly ^{13}C -labelled sample, highlighting the effectiveness of very fast MAS. Even the sites close in $^{13}\text{C}^\alpha$ and $^{13}\text{C}^\beta$ chemical shift, which did show some evidence of spin diffusion

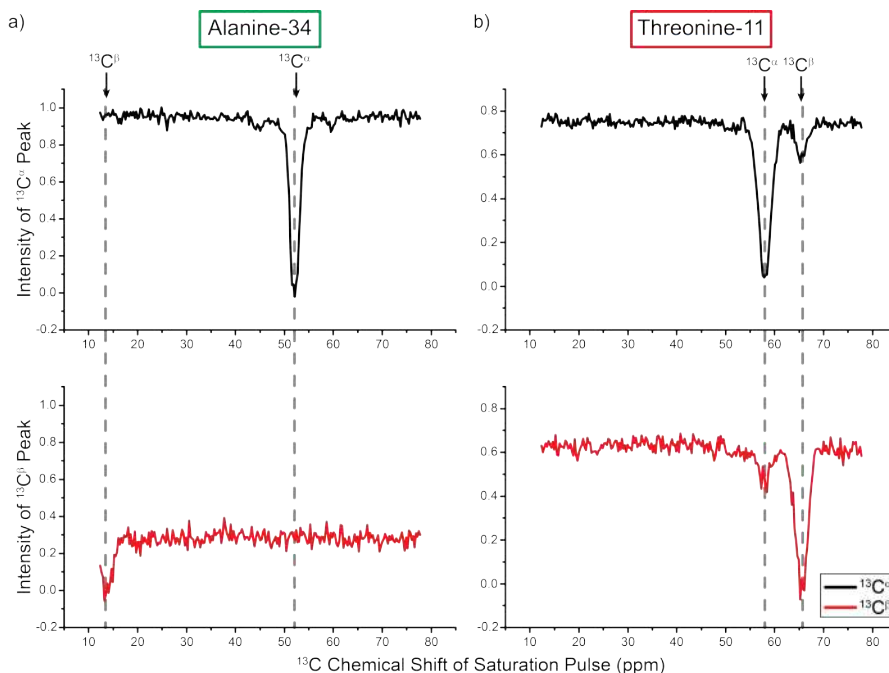


Figure 4.8: SDST profiles of a) alanine-34 and b) threonine-11 $^{13}\text{C}^\alpha$ (black) and $^{13}\text{C}^\beta$ (red) nuclei. The multiple peaks in the threonine-11 spectra are evidence of magnetisation exchange due to PDSD.

in the SDST profiles, have unaffected rates at ≥ 90 kHz MAS within the experimental error. The full data set, showing variation of $^{13}\text{C}^\alpha$ R_1 with MAS frequency throughout the backbone, is displayed in Figure 4.13.

However, the situation is very different for the sidechain ^{13}C nuclei. As predicted from the chemical shift difference calculations, the sidechain ^{13}C nuclei are undergoing considerable spin diffusion, even at 100 kHz MAS, and this does substantially affect the relaxation rates. Examples of sidechain ^{13}C VMAS R_1 are plotted in Figure 4.14 and the full data can be found in Figure C.4 in the appendix. It is immediately obvious that, in comparison to $^{13}\text{C}^\alpha$, the sidechain rates vary a significant amount and have not reached a steady value by 90-100 kHz MAS. This indicates that these nuclei are still undergoing significant PDSD, which will be due to the small chemical shift differences between adjacent ^{13}C nuclei. Thus the R_1 of aliphatic sidechain ^{13}C nuclei cannot be reliably measured under these conditions. In the future, with improvements in MAS technology, even faster spinning may be possible which could help to further reduce the effects of PDSD in the sidechain ^{13}C nuclei. Otherwise methods, such as deuteration, to reduce the ^1H network, and/or alternating ^{13}C -labelling, to remove the ^{13}C - ^{13}C dipolar couplings, should be applied.

Fully-Protonated Crystalline $[2\text{-}^{13}\text{C}(\text{Glucose}), \text{U-}^{15}\text{N}]\text{GB1}$

The $[\text{U-}^{13}\text{C}, ^{15}\text{N}]$ $^{13}\text{C}^\alpha$ R_1 decreases as the MAS frequency increases due to the exchange of magnetisation with the neighbouring $^{13}\text{C}^\beta$ nuclei at low spinning frequencies, which typically have R_1 s of an order of magnitude greater. This investigation into the rela-

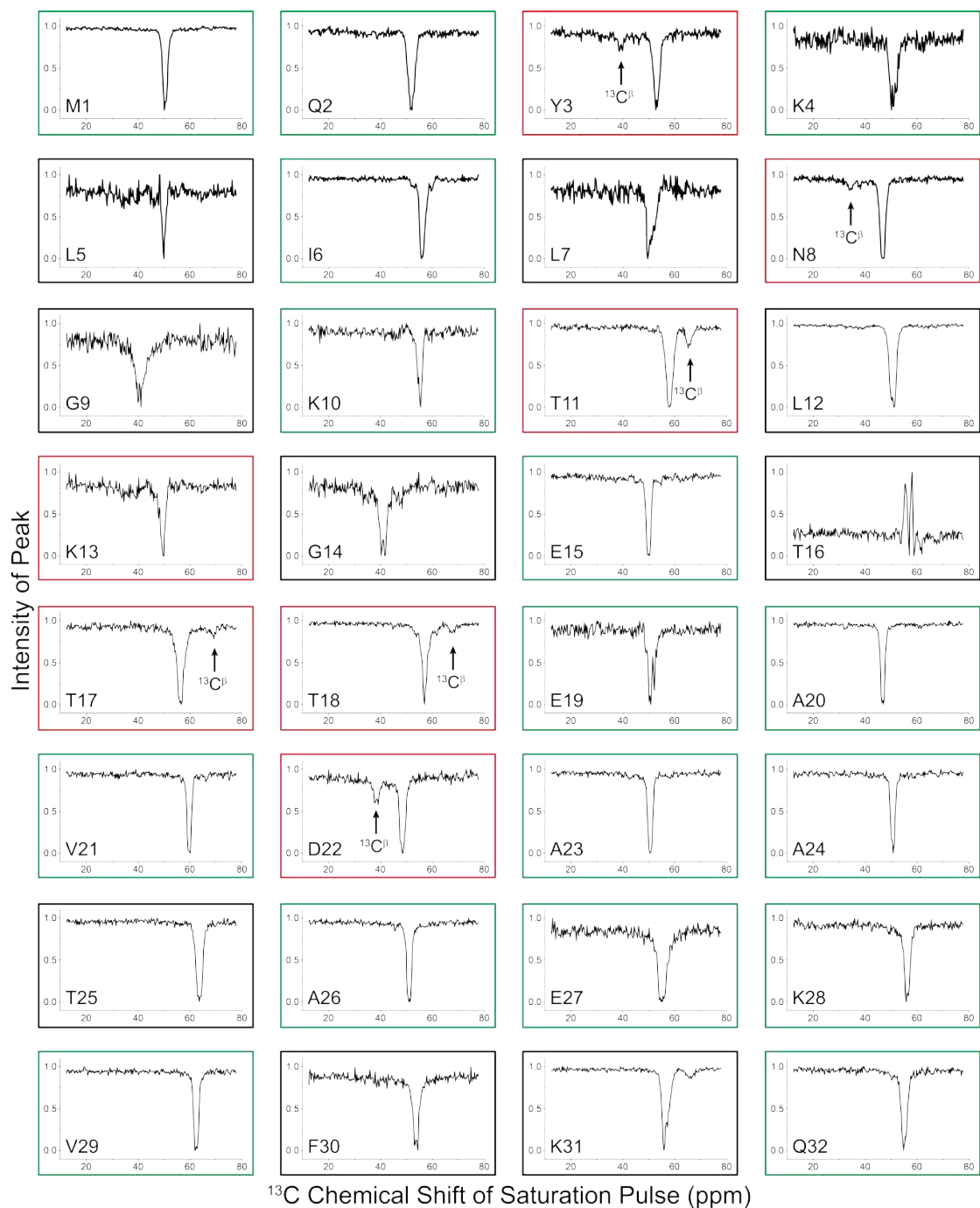


Figure 4.9: $^{13}\text{C}^\alpha$ SDST profiles for residues 1 - 32 in crystalline $[\text{U-}^{13}\text{C}, ^{15}\text{N}]$ GB1 at 100 kHz MAS and 700 MHz ^1H Larmor frequency. The residues that show a decrease in $^{13}\text{C}^\alpha$ intensity at their $^{13}\text{C}^\beta$ frequency are outlined in red (indicating magnetisation exchange due to PDSD), those that clearly do not are outlined in green and in the cases where it is unclear a black outline is used.

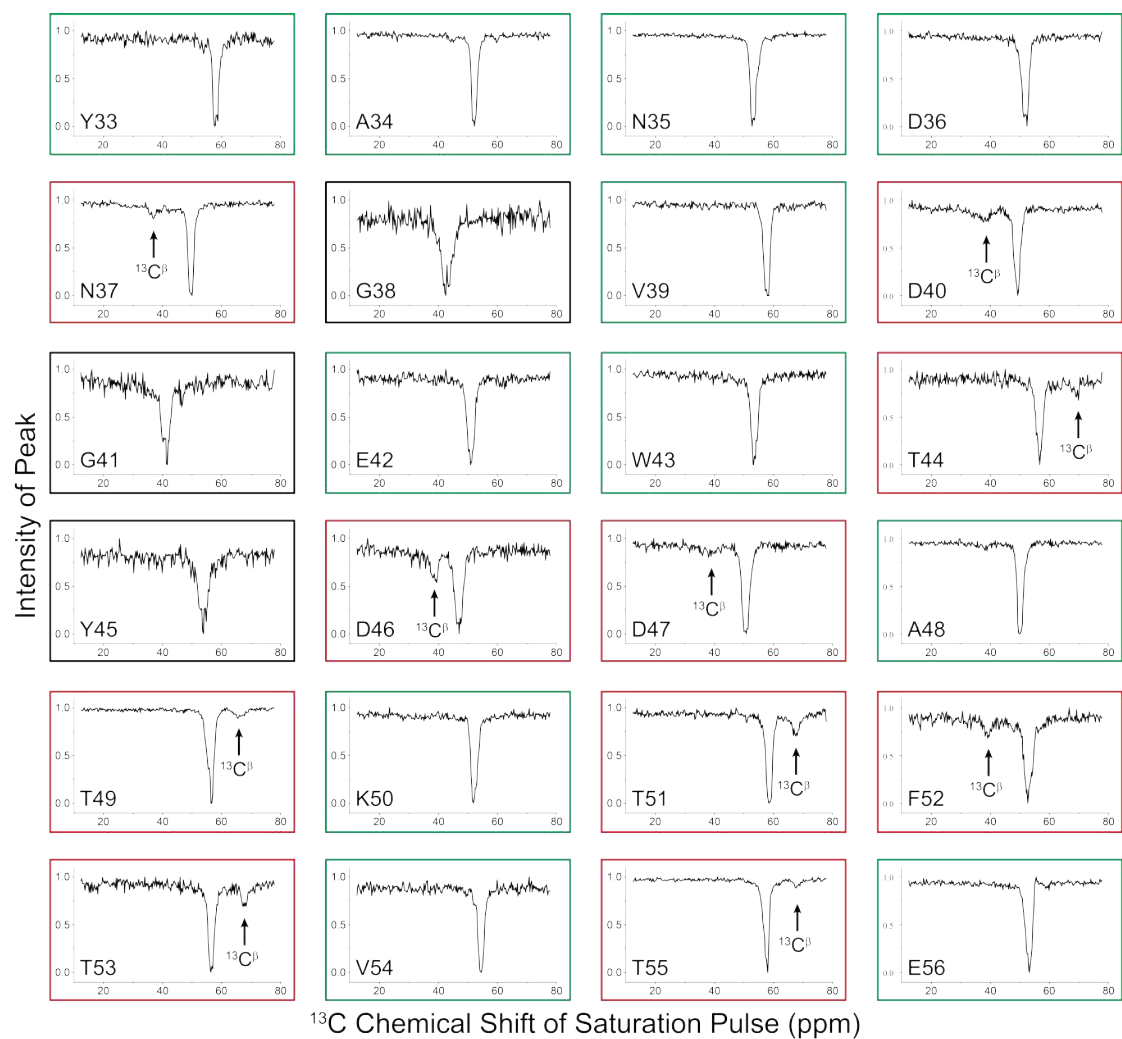


Figure 4.10: The remaining $^{13}\text{C}^\alpha$ SDST profiles for [U- ^1H , ^{13}C , ^{15}N]GB1 (residues 33 - 56).

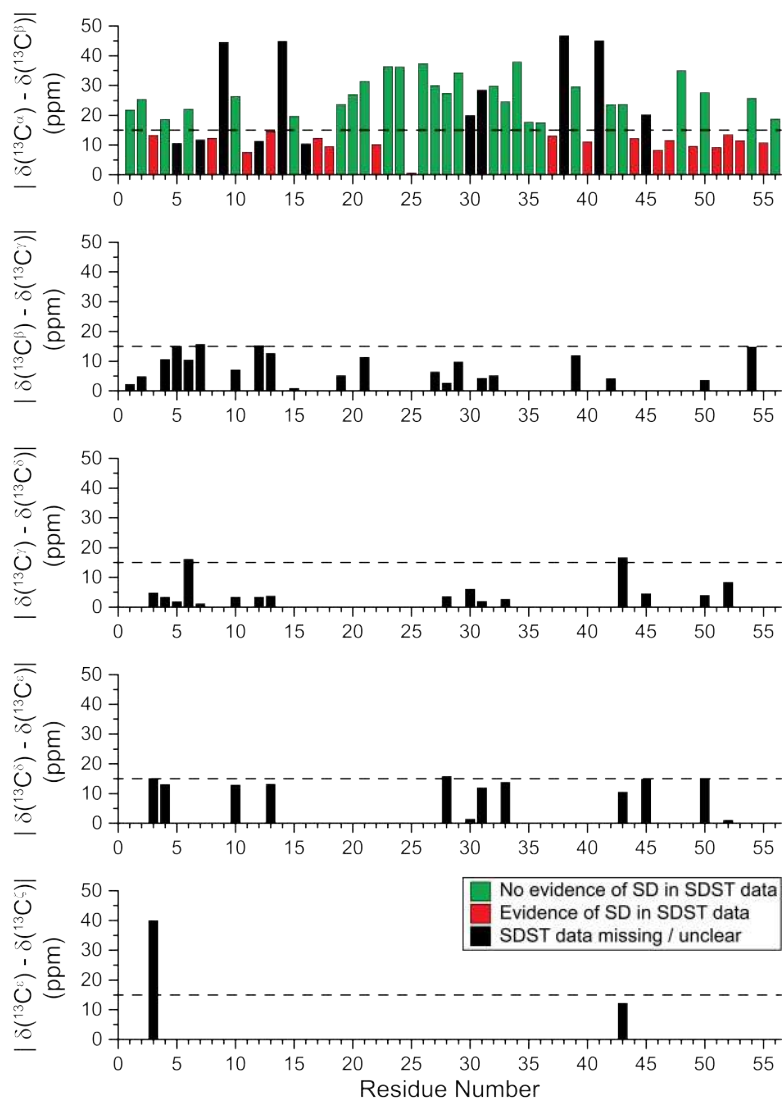


Figure 4.11: The ^{13}C - ^{13}C chemical shift difference between the neighbouring $^{13}\text{C}^\alpha$ and sidechain nuclei plotted against residue number in the protein GB1. Those sites which show evidence of PDSD in the SDST data are shown in red and those which do not are in green. The $^{13}\text{C}^\alpha$ and sidechain ^{13}C nuclei without SDST data are presented, in black, to highlight the chemical shift difference. The black dashed line represents a 15 ppm chemical shift difference, which approximately divides the nuclei which show evidence of PDSD and those which do not.

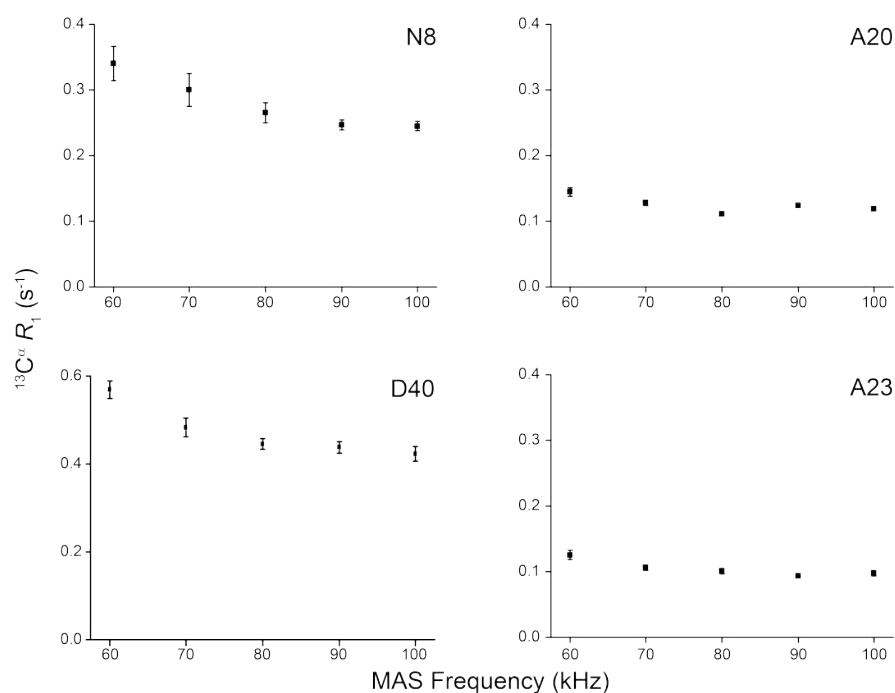


Figure 4.12: Examples of $^{13}\text{C}^\alpha R_1$ plotted against MAS frequency for residues N8, A20, D40 and A23 of fully-protonated crystalline $[\text{U-}^{13}\text{C},^{15}\text{N}]\text{GB1}$ at 700 MHz ^1H Larmor frequency.

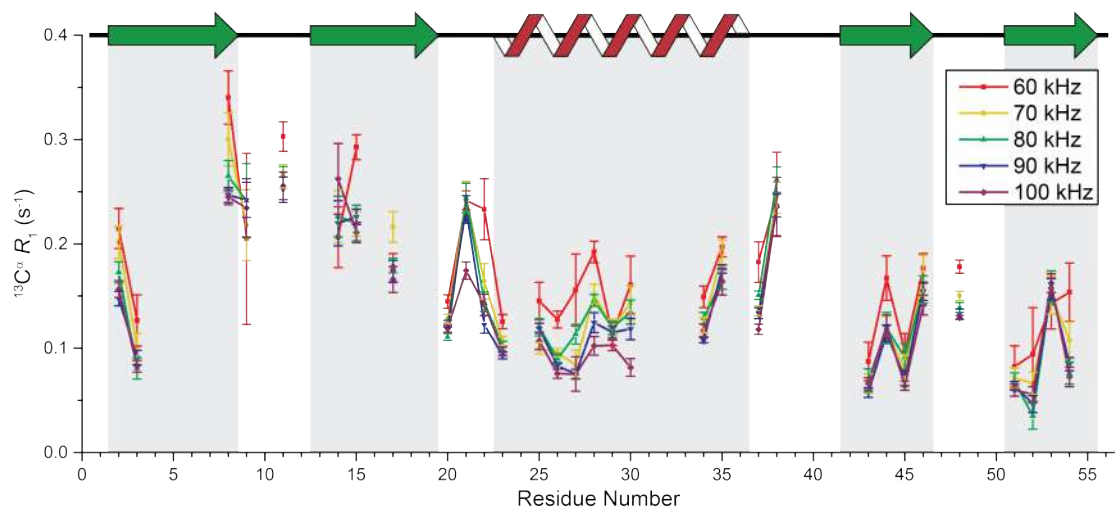


Figure 4.13: $^{13}\text{C}^\alpha R_1$ relaxation rates measured in fully-protonated, crystalline $[\text{U-}^{13}\text{C},^{15}\text{N}]\text{GB1}$ at 60 (red), 70 (yellow), 80 (green), 90 (blue) and 100 kHz MAS (purple) and 700 MHz ^1H Larmor frequency. Values for significantly overlapping peaks were removed.

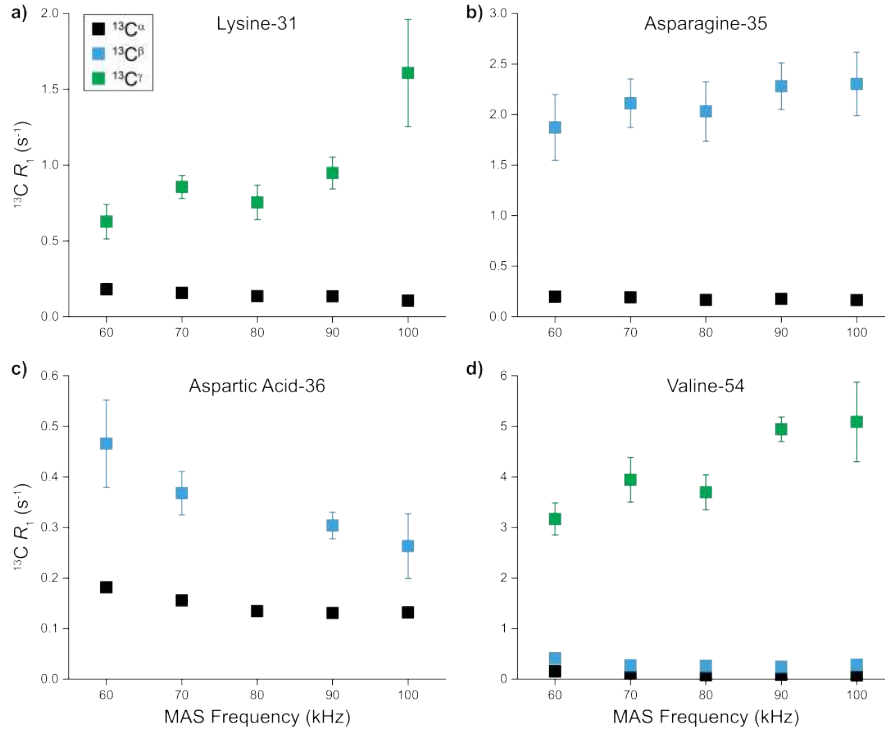


Figure 4.14: ^{13}C R_1 relaxation rates measured in fully-protonated, crystalline $[\text{U-}^{13}\text{C},^{15}\text{N}]\text{GB1}$ plotted against MAS frequency and 700 MHz ^1H Larmor frequency for residues a) lysine-31, b) asparagine-35, c) aspartic acid-36 and d) valine-54. In comparison to the backbone $^{13}\text{C}^\alpha$ R_1 values (black), there is considerably more variation in the sidechain $^{13}\text{C}^\beta$ (blue) and $^{13}\text{C}^\gamma$ (green) rates even at 90-100 kHz MAS. The full set of results is presented in Figure C.4.

tionship between MAS frequency and $^{13}\text{C}^\alpha$ R_1 was continued through further VMAS measurements, this time on $[2\text{-}^{13}\text{C}(\text{Glucose}),\text{U-}^{15}\text{N}]\text{GB1}$ (labelling scheme presented in Figure 2.8). In this partially ^{13}C -labelled protein, the C^β nuclei are not ^{13}C -labelled (except in isoleucine and valine residues), removing the $^{13}\text{C}^\alpha\text{-}^{13}\text{C}^\beta$ dipolar interaction as a potential pathway for PDS.

The full $[2\text{-}^{13}\text{C}(\text{Glucose}),\text{U-}^{15}\text{N}]\text{GB1}$ VMAS $^{13}\text{C}^\alpha$ R_1 results at 600 MHz ^1H Larmor frequency can be found in Figure C.5 in the appendix. These $^{13}\text{C}^\alpha$ R_1 rates do tend to deviate less from the plateau value than in the uniformly, fully ^{13}C -labelled protein and, again, by ≥ 90 kHz MAS there are no significant changes in R_1 indicating that the effects of PDS are negligible under these conditions.

Interestingly, the alanine rates show a unique trend: the $^{13}\text{C}^\alpha$ R_1 rates increase as the MAS frequency increases. This reveals that, now the dominating $^{13}\text{C}^\alpha\text{-}^{13}\text{C}^\beta$ spin diffusion pathway has been effectively eliminated, there is another spin diffusion pathway affecting these alanine $^{13}\text{C}^\alpha$ relaxation rates. Examples of the VMAS $^{13}\text{C}^\alpha$ relaxation rates for residues A23, A26 and A48 in $[2\text{-}^{13}\text{C}(\text{Glucose}),\text{U-}^{15}\text{N}]\text{GB1}$ are presented in Figure 4.15. The corresponding results from the uniformly-labelled protein are also included as a comparison, however it must be noted that the two sets of relaxation rates are measured at different ^1H Larmor frequencies and therefore only the trends can be directly compared between the samples, not the R_1 values themselves.

The increasing alanine $^{13}\text{C}^\alpha$ R_1 indicates that the $^{13}\text{C}^\alpha$ nuclei are exchanging magnetisation with a site of slower R_1 . Although it is unclear why the rates are being affected in this way, it is possible to rule out certain sources of the magnetisation exchange. For example, ^1H R_1 s tend to be far more rapid than $^{13}\text{C}^\alpha$ R_1 and therefore these cannot be the rates the $^{13}\text{C}^\alpha$ nuclei are in exchange with. According to the $2\text{-}^{13}\text{C}(\text{Glucose})$ labelling scheme neither the C^β nor C' sites in alanine should be ^{13}C -labelled. However, when expressing the protein samples in isotopically-labelled minimal media, the incorporation of the isotopic labelling is not always perfect. And so, assuming this could be the case, SD pathways involving the alanine $^{13}\text{C}^\beta$ or $^{13}\text{C}'$ nuclei will be considered. Firstly, the $^{13}\text{C}^\beta$ in alanine is a methyl carbon, which will also be undergoing much faster relaxation than the $^{13}\text{C}^\alpha$, and therefore cannot be causing the effect observed in Figure 4.15. On the other hand the $^{13}\text{C}'$ nuclei will have a significantly slower R_1 s than the $^{13}\text{C}^\alpha$ site and

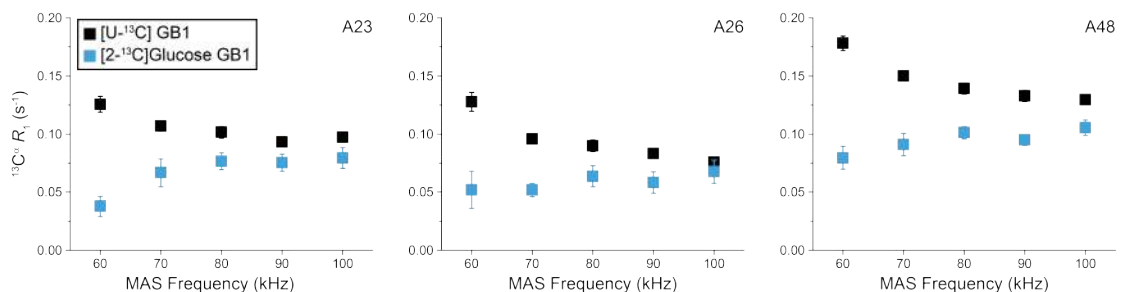


Figure 4.15: Comparison of $^{13}\text{C}^\alpha$ R_1 for fully-protonated $[\text{U-}^{13}\text{C},^{15}\text{N}]\text{GB1}$ (black) and $[2\text{-}^{13}\text{C}(\text{glucose}),\text{U-}^{15}\text{N}]\text{GB1}$ (blue) plotted against MAS frequency for residues A23, A26 and A48. Measured at 700 and 600 MHz ^1H Larmor frequencies, respectively.

thus could be causing averaging of the alanine $^{13}\text{C}^\alpha$ R_1 s to lower values at slower MAS frequencies. It is also possible that this spin diffusion is occurring via backbone ^{15}N sites, but this is unlikely due to the weak $^{13}\text{C}^\alpha$ - ^{15}N dipolar couplings, or via sites in the $i\pm 1$ residues. However, there are no ^{13}C -labelled sites in these neighbouring residues that typically undergo slower relaxation than the $^{13}\text{C}^\alpha$ nuclei, except the $^{13}\text{C}^\alpha$ themselves. It may be possible that these alanine $^{13}\text{C}^\alpha$ nuclei are exchanging magnetisation with $^{13}\text{C}^\alpha$ nuclei on the $i\pm 1$ residues, if these neighbouring sites are undergoing particularly slow relaxation.

These results demonstrate that, although the effects of PDSD are negligible at ≥ 90 kHz MAS for both the uniformly and partially ^{13}C -labelled proteins, there are multiple pathways for polarisation transfer via spin diffusion and the overall effect on relaxation rates is highly specific to the protein and the experimental conditions.

4.4.4 Cross-Correlated Relaxation

A further consideration for these $^{13}\text{C}^\alpha$ R_1 measurements at 100 kHz is the effect of cross-correlated relaxation. Whenever there are multiple mechanisms for relaxation acting simultaneously, for example CSA and dipolar coupling, there can be interference between them (cross-correlation), which will alter the relaxation rates of the nuclei involved.^{97–100,104} Normally, in the solid state, ^1H - ^1H spin diffusion is fast enough to suppress the effects of cross-correlated relaxation. In this situation however, with significant reduction of the ^1H - ^1H SD due to fast MAS, it is important to ensure that the measured relaxation rates are not affected by the cross-correlated relaxation.

In solution-state NMR cross-correlated relaxation tends to be prominent and it is common practice to apply decoupling during the relaxation delay to suppress its effects. In order to refocus the cross-correlated relaxation mechanisms, the decoupling must invert the magnetisation on a timescale substantially faster than the relaxation itself.^{71,97,107,193} To determine whether cross-correlation has affected these R_1 measurements, $^{13}\text{C}^\alpha$ R_1 was measured on the same protein sample under identical conditions with, and without, decoupling during the relaxation delay (^1H 25 kHz π pulses). Figure 4.16 shows that the resulting rates from using the original pulse sequence (red) and the pulse sequence with added decoupling (grey) are the same within error. This suggests that the effects of cross-correlated relaxation are still negligible in these measurements and therefore that the accuracy of these $^{13}\text{C}^\alpha$ R_1 rates at 100 kHz MAS has not been compromised.

4.5 Conclusions and Outlook

This detailed investigation into the effects and significance of spin diffusion in aliphatic ^{13}C R_1 measurements on fully-protonated, uniformly ^{13}C -labelled proteins combined PDSD control spectra, SDST and variable MAS R_1 measurements. Together these techniques revealed that at a few $^{13}\text{C}^\alpha$ sites, those close in $^{13}\text{C}^\alpha$ and $^{13}\text{C}^\beta$ chemical shifts, PDSD may still be present at 100 kHz. However the effects of PDSD on $^{13}\text{C}^\alpha$ R_1 at ≥ 90 kHz MAS are negligible in practice, demonstrating that application of this fast

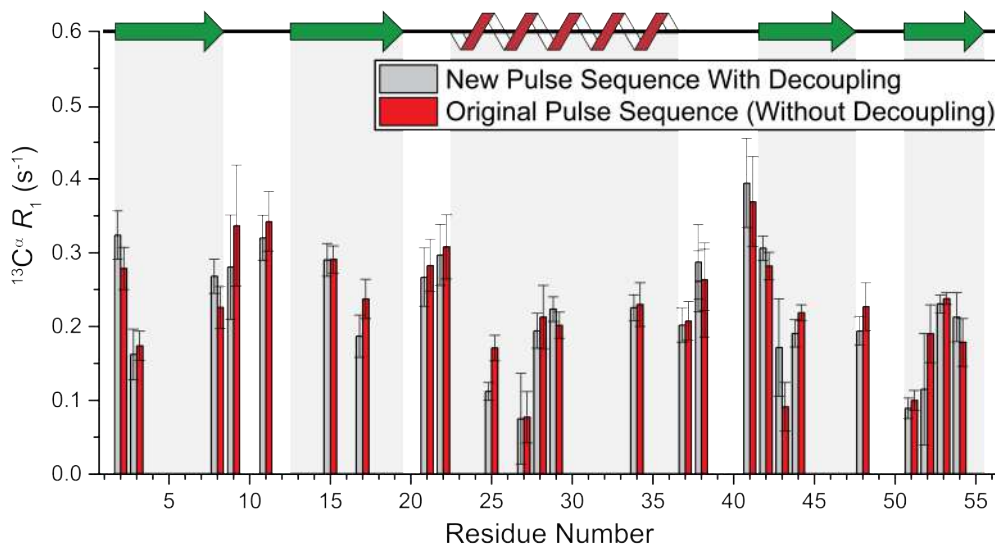


Figure 4.16: $^{13}\text{C}^\alpha$ R_1 measured in fully-protonated, crystalline $[\text{U-}^1\text{H}, ^{13}\text{C}, ^{15}\text{N}]$ GB1 at 100 kHz spinning and 700 MHz ^1H Larmor frequency with (grey) and without (red) ^1H 25 kHz π pulses during the relaxation delay. Values for significantly overlapping peaks were removed.

spinning provides a viable solution for rapid R_1 relaxation measurements for $^{13}\text{C}^\alpha$ nuclei in fully-protonated, uniformly ^{13}C -labelled proteins, free of undesirable coherent effects.

The PDSD spectra at 60 kHz MAS confirmed that spin diffusion is negligible in $^{13}\text{C}^\alpha$ R_1 measurements when all one-bond ^{13}C - ^{13}C dipolar couplings are eliminated, however a substantial number of crosspeaks remained in the uniformly ^{13}C -labelled PDSD spectrum. Similar measurements at 100 kHz on a fully-protonated, uniformly ^{13}C -labelled protein revealed evidence of PDSD at a few remaining sites, even with such fast MAS. Next, $^{13}\text{C}^\alpha$ SDST profiles highlighted that a handful of sites (those close in $^{13}\text{C}^\alpha$ and $^{13}\text{C}^\beta$ chemical shifts) showed evidence of magnetisation exchange via PDSD. This led to the prediction that sites with a chemical shift difference < 15 ppm between adjacent ^{13}C nuclei would be significantly affected by PDSD at 100 kHz MAS, this included all of the sidechain ^{13}C nuclei.

The effects of PDSD on experimental aliphatic ^{13}C R_1 measurements were explored using variable MAS relaxation measurements, revealing that, at spinning speeds ≥ 90 kHz, PDSD is negligible for $^{13}\text{C}^\alpha$ sites. On average, there was a 21% decrease in R_1 when the MAS frequency was increased from 60 to 100 kHz, highlighting the importance of fast MAS for reducing the spin diffusion from the neighbouring $^{13}\text{C}^\beta$ nuclei. However, as predicted, the sidechain ^{13}C rates are still substantially influenced by PDSD, even at 100 kHz MAS. Effective removal of the $^{13}\text{C}^\beta$ nuclei (using $[\text{2-}^{13}\text{C}(\text{Glucose}), \text{U-}^{15}\text{N}]$ labelled protein) reduced the deviation in R_1 from the plateau value at the lower MAS frequencies and, again, there was minimal change in $^{13}\text{C}^\alpha$ R_1 at ≥ 90 kHz MAS.

One last consideration was that, at these extreme MAS conditions, ^1H - ^1H SD may be reduced to a point where it no longer suppresses cross-correlated relaxation. $^{13}\text{C}^\alpha$ R_1 measurements, both with and without decoupling in the relaxation delay revealed that

cross-correlated relaxation is suppressed under these conditions without the need for the additional decoupling.

The above results show that when using proton detection in order to measure $^{13}\text{C}^\alpha$ R_1 on a fully-protonated, uniformly ^{13}C -labelled protein, MAS at ≥ 90 kHz is necessary to ensure that the rates are quantitative and site-specific. Now, it is possible to measure these specific relaxation rates on proteins with confidence. On the other hand, aliphatic ^{13}C sidechain nuclei are still strongly influenced by PDSD under these conditions. Thus other techniques, in addition to fast MAS, must be employed for R_1 measurements at these sites, such as deuteration or alternating ^{13}C -labelling.

With increased availability of ≥ 90 kHz MAS instrumentation, $^{13}\text{C}^\alpha$ relaxation data will enrich the picture of backbone and sidechain motions available from ^{15}N and ^{13}C measurements, especially as C^α nuclei undergo motions distinct from peptide plane fluctuations. These $^{13}\text{C}^\alpha$ relaxation measurements should be valuable in particular for validating the presence of overall motions of protein fragments.^{6, 160, 194}

4.6 Experimental Details

4.6.1 Protein Samples

The $[U-^1H, ^{13}C, ^{15}N]$ GB1, $[1,3-^{13}C(\text{glycerol}), U-^1H, ^{15}N]$ GB1 and $[2-^{13}C(\text{glucose}), U-^1H, ^{15}N]$ GB1 protein samples were expressed in minimal media as described in Section 3.8.4 with $[U-^{13}C]$ -glycerol, $[1,3-^{13}C]$ -glycerol and $[2-^{13}C]$ -glucose as the sole carbon sources, respectively and $[U-^{15}N]$ -ammonium chloride as the sole nitrogen source.

The proteins were crystallised as described in Section 3.8.4 and DSS was added to each crystallised sample as an internal reference. Two 1.3 mm rotors were packed with 3.0 mg of $[U-^1H, ^{13}C, ^{15}N]$ GB1 and $[1,3-^{13}C(\text{glycerol}), U-^1H, ^{15}N]$ GB1, a 0.8 mm rotor was packed with 0.5 mg of $[2-^{13}C(\text{glucose}), U-^1H, ^{15}N]$ GB1 and a 0.7 mm rotor was packed with 0.5 mg of $[U-^1H, ^{13}C, ^{15}N]$ GB1.

The sample temperature (13.0°C) was measured by the 1H chemical shift of water with respect to DSS (calibrated to 0 ppm), see Equation 3.6.^{152,153}

4.6.2 SSNMR Experimental Details

60 kHz MAS PDSD Control Measurements

The ^{13}C -detected control spin diffusion spectra (Figures 4.5 and 4.6) were measured on a Bruker Avance II+ spectrometer operating at 14.1 T ($\omega_{0,H}/2\pi = 600$ MHz) using a Bruker 1.3 mm triple-resonance MAS probe and performed at 60 kHz spinning frequency at a sample temperature of 20.0 ± 1 °C. The mixing times for control PDSD spectra were 1 and 3 s. The mixing times for control RFSD spectra were 10 and 100 ms. A spin-lock pulse with $\omega_{1,C}/2\pi \approx 20$ kHz was employed. The control spectra took between 3-7 h to perform. These sequences were initialised with a 100 kHz $\pi/2$ 1H pulse, followed by CP from 1H to ^{13}C (1.5 ms, $\omega_{1,H}/2\pi \approx 10$ kHz and $\omega_{1,C}/2\pi \approx 50$ kHz). During t_1 evolution and t_2 acquisition, WALTZ16⁴⁹ decoupling was applied at a field strength of $\omega_{1H}/2\pi = 10$ kHz. Total durations of these experiments were ~ 8.0 h for PDSD and ~ 3.0 h for RFSD. The PDSD and RFSD pulse sequences are shown in Figures 4.17a and 4.17b.

100 kHz MAS PDSD Control Measurements

The 1H -detected control spin diffusion spectra (Figure 4.7) were measured on a Bruker Avance III HD spectrometer operating at 16.4 T ($\omega_{0,H}/2\pi = 700$ MHz) using a Bruker 0.7 mm triple-resonance MAS probe and performed at 100 kHz spinning frequency at a sample temperature of 13.0 ± 1 °C. The mixing times for control PDSD spectra were 0, 1 and 5 s. The control spectra took between 1-3 h to perform and each had 8 scans.

These sequences were initialised with a 100 kHz $\pi/2$ 1H pulse, followed by CP from 1H to ^{13}C (200 μs , $\omega_{1,H}/2\pi \approx 80$ kHz and $\omega_{1,C}/2\pi \approx 20$ kHz). During t_1 evolution and t_2 acquisition, WALTZ16⁴⁹ decoupling was applied at a field strength of $\omega_{1H}/2\pi = 10$ kHz and MISSISSIPPI⁵¹ solvent suppression was applied at 50 kHz (70 ms).

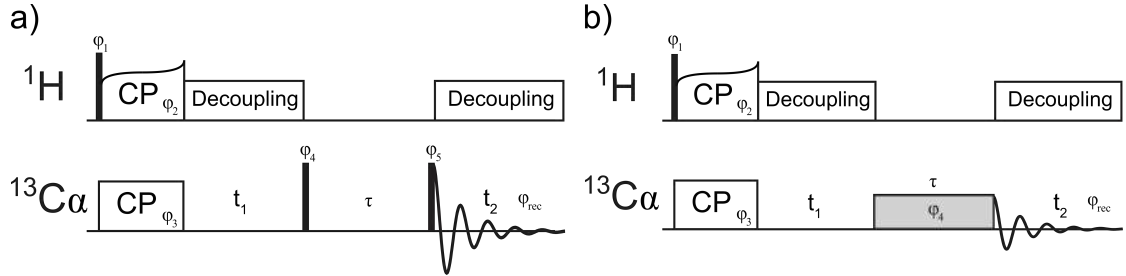


Figure 4.17: The a) PDS and b) RFSD pulse sequences. $\pi/2$ pulses are indicated with a black rectangle. Spinlock pulses are indicated in a light grey rectangle. Indirect and direct acquisition periods are labelled as “ t_1 ” and “ t_2 ” respectively, while phases are shown as “ φ ”. The variable delay or spinlock pulse is labelled τ . Phase cycling: a) $\varphi_1 = (+y\ y)$, $\varphi_2 = (+x)$, $\varphi_3 = (+x\ +x\ -x\ -x\ +y\ +y\ y\ y)$, $\varphi_4 = (+y\ +y\ y\ y\ x\ x\ +x\ +x)$, $\varphi_5 = (-y\ y\ +y\ +y\ +x\ +x\ x\ x)$, and $\varphi_{\text{rec}} = (+y\ y\ x\ +x)$. b) $\varphi_1 = (+y\ y)$, $\varphi_2 = (+x)$, $\varphi_3 = \varphi_4 = (+x\ +x\ +y\ +y\ -x\ -x\ y\ y)$, and $\varphi_{\text{rec}} = (+x\ x\ +y\ y\ x\ +x\ y\ +y)$.

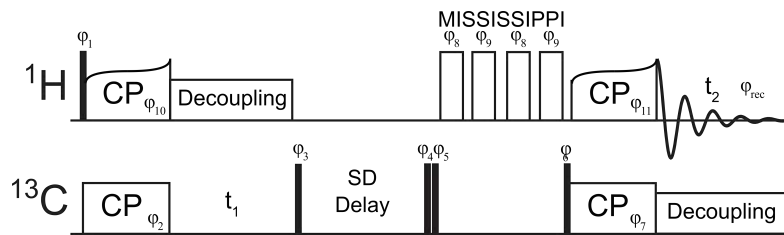


Figure 4.18: A ^1H - ^{13}C - ^1H PDS control pulse sequence. $\pi/2$ pulses are indicated with a black rectangle. Indirect and direct acquisition periods are labelled as “ t_1 ” and “ t_2 ” respectively, while phases are shown as “ φ ”. Phase cycling: $\varphi_0 = \varphi_7 = \varphi_8 = \varphi_{11} = \varphi_{12} = (y)$, $\varphi_1 = (y\ y\ -y\ -y)$, $\varphi_{10} = \varphi_4 = \varphi_5 = \varphi_9 = (x)$, $\varphi_2 = (y\ -y\ y\ -y)$, $\varphi_3 = (-x\ -x\ -x\ -x)$, $\varphi_6 = (-x)$ and $\varphi_{\text{rec}} = (y\ -y\ -y\ y)$.

SDST Measurements

These NMR experiments (Figures 4.9 and 4.10) were measured on a Bruker Avance III HD spectrometer operating at 16.4 T ($\omega_{0,H}/2\pi = 700$ MHz) using a Bruker 0.7 mm triple-resonance MAS probe and performed at 100 kHz spinning frequency at a sample temperature of 27.0 ± 1 °C.

These sequences were initialised with a 100 kHz $\pi/2$ ^1H pulse, followed by CP from ^1H to ^{13}C (200 μs , $\omega_{1,H}/2\pi \approx 80$ kHz and $\omega_{1,C}/2\pi \approx 20$ kHz). Followed by selective saturation achieved with 10 ms 50 kHz ^{13}C pulse, looped 50 times (i.e. 500 ms saturation). During t_1 evolution and t_2 acquisition, WALTZ16⁴⁹ decoupling was applied at a field strength of $\omega_{1,H}/2\pi = 10$ kHz and MISSISSIPPI⁵¹ solvent suppression was applied at 50 kHz (70 ms). This was followed by CP from ^{13}C to ^1H (200 μs , $\omega_{1,H}/2\pi \approx 80$ kHz and $\omega_{1,C}/2\pi \approx 20$ kHz) for acquisition on ^1H . The selective saturation pulse was swept from 7800 Hz-10550 Hz (44 ppm - 60 ppm) every 50 Hz (0.28 ppm). These measurements were recorded using the pulse sequence in Figure 4.19.

Variable MAS Aliphatic ^{13}C R_1 Measurements:

[U- ^1H , ^{13}C , ^{15}N]GB1

All ^{13}C R_1 rates (Figures 4.12, 4.13, 4.14 and C.4) were measured using a ^1H - ^{13}C - ^1H pulse sequence on a Bruker Avance III HD spectrometer operating at 16.4 T ($\omega_{0,H}/2\pi = 700$ MHz) using a Bruker 0.7 mm triple-resonance MAS probe at a sample temperature of 13.0°C.

These sequences were initialised with a 100 kHz $\pi/2$ ^1H pulse, followed by CP from ^1H to ^{13}C and then the variable delay (with 83.33 kHz $\pi/2$ ^{13}C pulse either side). Next t_1 evolved, followed by MISSISSIPPI⁵¹ solvent suppression (70 ms), then a CP from ^{13}C to ^1H and finally acquisition. During the t_1 evolution and t_2 acquisition, WALTZ16⁴⁹ decoupling was applied for 25 μs at field strengths of $\omega_{1,H}/2\pi = 10$ kHz and $\omega_{1,C}/2\pi = 10$ kHz, respectively. The variable delays (τ) were 0.002, 0.005, 0.01, 0.05, 0.2, 0.5, 1, 1.5, 3 and 7 seconds.

These measurements were recorded using the pulse sequence in Figure 4.20a.

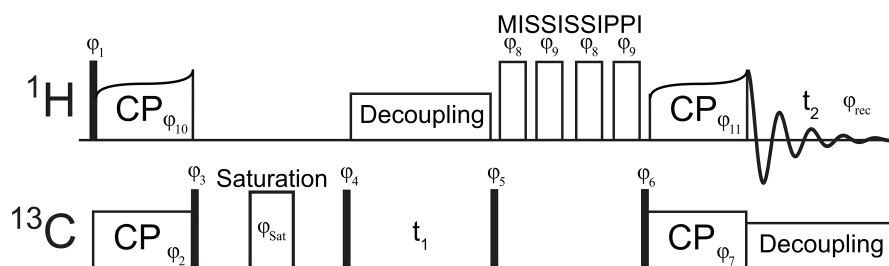


Figure 4.19: The ^{13}C SDST pulse sequence. $\pi/2$ pulses are indicated with a black rectangle. Indirect and direct acquisition periods are labelled as “ t_1 ” and “ t_2 ” respectively, while phases are shown as “ φ ”. Phase cycling: $\varphi_1 = (\text{y y -y -y})$, $\varphi_2 = (\text{y -y y -y})$, $\varphi_3 = \varphi_5 = \varphi_9 = \varphi_{10} = \varphi_{\text{Sat}} = (\text{x})$, $\varphi_4 = \varphi_6 = (\text{-x})$, $\varphi_7 = \varphi_8 = \varphi_{11} = (\text{y})$ and $\varphi_{\text{rec}} = (\text{y -y -y y})$.

Since these experiments were measured at 5 different MAS frequencies the CP and MISSISSIPPI conditions vary between them and therefore are summarised in Table 4.1.

[2-¹³C(glucose),U-¹H,¹⁵N]GB1

All ¹³C R_1 rates (Figures 4.15 and C.5) were measured using a ¹H-¹³C-¹H pulse sequence on a Bruker Avance II+ spectrometer operating at 14.1 T ($\omega_{0,H}/2\pi = 600$ MHz) using a 0.8 mm double-resonance probe developed in the Samoson laboratory at a sample temperature of 17.5°C.

These sequences were initialised with a 100 kHz $\pi/2$ ¹H pulse, followed by CP from ¹H to ¹³C and then the variable delay (with 83.33 kHz $\pi/2$ ¹³C pulse either side). Next t_1 evolved, followed by MISSISSIPPI⁵¹ solvent suppression (70 ms), then a CP from ¹³C to ¹H and finally acquisition. During the t_1 evolution and t_2 acquisition, WALTZ16⁴⁹ decoupling was applied for 25 μ s at field strengths of $\omega_{1,H}/2\pi = 10$ kHz and $\omega_{1,C}/2\pi = 10$ kHz, respectively. The variable delays (τ) were 0.002, 0.01, 0.05, 0.2, 0.5, 1, 1.5, 2, 3, 4 and 7 seconds. These measurements were recorded using the pulse sequence in Figure 4.20a. Since these experiments were measured at 5 different MAS frequencies many of the experimental conditions vary between them and therefore are summarised in Table 4.2.

Determination of Cross-Correlated Relaxation: ¹³C R_1 Measurements With and Without Decoupling

All ¹³C R_1 rates (Figure 4.16) were measured using a ¹H-¹³C-¹H pulse sequence on a Bruker Avance III HD spectrometer operating at 16.4 T ($\omega_{0,H}/2\pi = 700$ MHz) using a Bruker 0.7 mm triple-resonance MAS probe. These sequences were initialised with a 100 kHz $\pi/2$ ¹H pulse, followed by CP from ¹H to ¹³C (175 μ s, $\omega_{1,H}/2\pi \approx 80$ kHz and $\omega_{1,C}/2\pi \approx 20$ kHz) and then the variable delay (with 83.33 kHz $\pi/2$ ¹³C pulse either side). Next t_1 evolved, followed by MISSISSIPPI⁵¹ solvent suppression (70 ms, 50 kHz), then a CP from ¹³C to ¹H (175 μ s, $\omega_{1,H}/2\pi \approx 80$ kHz and $\omega_{1,C}/2\pi \approx 20$ kHz) and finally acquisition. During the t_1 evolution and t_2 acquisition, WALTZ16⁴⁹ decoupling was applied for 25 μ s at field strengths of $\omega_{1,H}/2\pi = 10$ kHz and $\omega_{1,C}/2\pi = 10$ kHz, respectively. The variable delays (τ) were 0, 0.01, 0.05, 0.1, 0.2, 0.5, 0.7, 1, 1.5 and 2 seconds.

The relaxation rates using the “original” pulse sequence and the “new” pulse

Table 4.1: Approximate CP and MISSISSIPPI conditions used in the variable MAS aliphatic ¹³C R_1 measurements on [U-¹H,¹³C,¹⁵N]GB1.

| MAS (kHz) | ¹ H- ¹³ C CP | | | MISSISSIPPI (kHz) |
|-----------|------------------------------------|-----------------------|-----------|-------------------|
| | ¹ H (kHz) | ¹³ C (kHz) | Time (us) | |
| 60 | 42 | 18 | 500 | 30 |
| 70 | 50 | 20 | 500 | 35 |
| 80 | 66 | 14 | 600 | 40 |
| 90 | 72 | 18 | 500 | 45 |
| 100 | 80 | 20 | 200 | 50 |

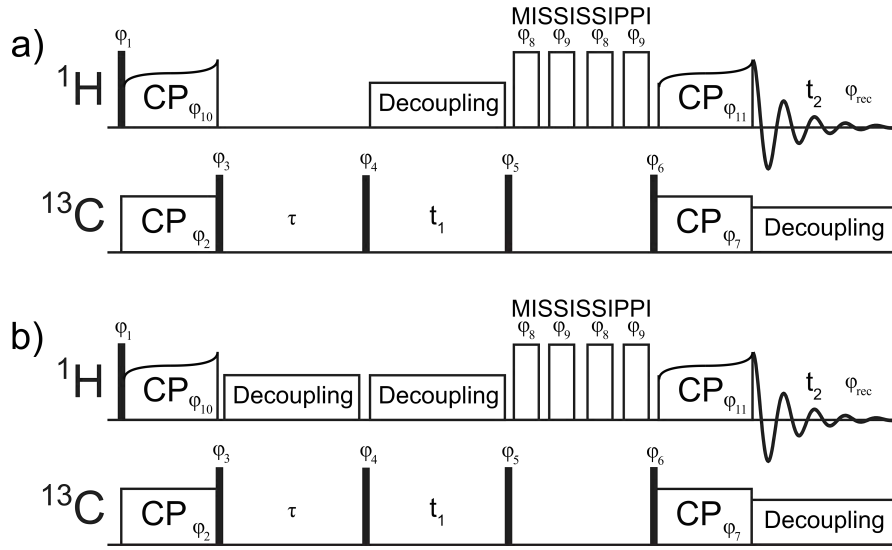


Figure 4.20: ^1H - ^{13}C - ^1H pulse sequence for measuring ^{13}C R^1 a) without and b) with decoupling during the variable relaxation delay (τ). $\pi/2$ pulses are indicated with a black rectangle. Indirect and direct acquisition periods are labelled as “t1” and “t2” respectively, while phases are shown as “ φ ”. Phase cycling: $\varphi_0 = \varphi_7 = \varphi_8 = \varphi_{11} = \varphi_{12} = (y)$, $\varphi_1 = (y \ y \ -y \ -y)$, $\varphi_{10} = \varphi_4 = \varphi_5 = \varphi_9 = (x)$, $\varphi_2 = (y \ -y \ y \ -y)$, $\varphi_3 = (-x \ -x \ -x \ -x)$, $\varphi_6 = (-x)$ and $\varphi_{\text{rec}} = (y \ -y \ -y \ y)$.

Table 4.2: Approximate CP and MISSISSIPPI conditions used in the variable MAS aliphatic ^{13}C R_1 measurements on 2- ^{13}C (glucose),U- ^1H , ^{15}N]GB1.

| MAS (kHz) | ^1H - ^{13}C CP | | | MISSISSIPPI (kHz) |
|-----------|-----------------------------------|-----------------------|-----------|-------------------|
| | ^1H (kHz) | ^{13}C (kHz) | Time (us) | |
| 60 | 50 | 10 | 600 | 30 |
| 70 | 60 | 10 | 400 | 35 |
| 80 | 60 | 20 | 700 | 40 |
| 90 | 70 | 20 | 600 | 45 |
| 100 | 78 | 22 | 600 | 50 |

sequence with the extra decoupling use the pulse sequences in Figures 4.20a and 4.20b, respectively.

4.6.3 Determination of Relaxation Rates

The R_1 rates were calculated from a plot of the peak integral against the variable delay (τ):

$$Integral = Ae^{(-R_1\tau)} \quad (4.1)$$

Chapter 5

Variable-Temperature, Solid-State NMR Measurements to Investigate the Site-Specific Relaxation and Energy Landscape of GB1

5.1 Abstract

Understanding the complex relationship between the thermal motion of a protein and its function at physiological temperature is a major challenge facing physical biologists. A recent investigation on the hierarchy of thermal motions in a hydrated crystalline protein at different temperatures (-168.15°C - 6.85°C) revealed that local motions dominated at the lower temperatures, while larger-amplitude, functionally-relevant motions only became active at higher temperatures.³⁰ In order to expand on this research, similar protein motions were investigated at a higher, more physiologically relevant range of temperatures in a site-specific manner, in the hope of gaining an insight into protein dynamics in their natural conditions. Proton-detected MAS SSNMR was used to investigate the $^{13}\text{C}'$ and ^{15}N relaxation of perdeuterated GB1 protein between -5.15°C and 34.65°C. These measurements showed clear trends in R_1 and $R_{1\rho}$ across the secondary structure elements and revealed significant decreases in $R_{1\rho}$ with increasing temperature. With the aim of accurately modelling the complex peptide plane dynamics, the rates were analysed with the extended model free approach combined with a modified Arrhenius equation, allowing determination of S_s^2 , S_f^2 , $\tau_{c,s}$, $\tau_{c,f}$, $E_{a,s}$ and $E_{a,f}$. The model is still in the development process since the quantity of the data currently available was not sufficient for accurate determination of all six parameters. Measurements at additional B_0 fields are currently underway, which will hopefully lead to a very informative model of the peptide plane dynamics throughout the protein.

5.2 Introduction

Proteins are critical for most biological processes.^{7,9,155,195} These complex macromolecules display an incredibly diverse range of functions. X-ray diffraction studies have discovered many protein structures, but function is also innately linked to the energy landscape of the complex dynamics in the protein. Therefore, to understand the function thoroughly, the probabilities of possible conformations and the energy barriers between them (i.e. the kinetics and thermodynamics) need to be known. Figure 5.1a shows a simplified representation of an energy landscape, highlighting a possible range of motions within a protein and how they relate to one another in terms of frequency and energy. The timescales of the types of motion typically found in proteins are illustrated in Figure 1.1 (Chapter 1), alongside the techniques that are sensitive to these dynamics. Ideally researchers want atomic resolution protein structures across both space and time to reveal their exact dynamics. Obviously this is not currently possible, so instead physical measurements are made from which the dynamics can be interpreted.

The last 40 years have seen huge quantities of research into protein function and dynamics using a wide range of techniques, such as NMR,^{9,66,155,196–198} X-ray diffraction (XRD),^{199,200} cryogenic electron microscopy (cryo-EM),^{201,202} small-angle X-ray scattering (SAXS),^{203,204} fluorescence microscopy,^{195,205,206} IR,^{207,208} circular dichroism (CD),^{209,210} Raman,^{211,212} electron paramagnetic resonance (EPR)^{213–215} and molecular dynamics (MD) simulations.^{9,216,217} The techniques chosen to investigate a specific system are highly dependent on the type of sample and the timescale of the dynamics. For example, μs - ms processes like enzyme catalysis or protein-protein interactions are relatively unlikely to occur and tend to have large amplitudes and very high activation energies. Since these motions are so slow, the stable conformations of these biomolecules can often be directly observed, allowing atomic-resolution snapshots through techniques like XRD or cryo-EM. On the other hand, the conformations of molecules undergoing fast dynamics, such as loop motions (ns timescale), sidechain rotations (ps timescale) and bond vibrations (fs timescale), cannot be directly observed. As is illustrated in Figure 5.1, these motions exist within the energy wells of the slower dynamics and typically have lower amplitudes and activation energies. Variable-temperature SSNMR relaxation measurements are sensitive to a wide range of dynamics and have been crucial for determining the structure and dynamics of biomolecular processes and proteins in a variety of samples.^{111,181,196,218–220}

A single motion can be defined by its timescale, amplitude and direction. The motion can be thought of as a transition between two conformational states, where each transition will have an associated activation energy (i.e. the amount of energy that must be available in the system for the transition to occur). The Arrhenius equation relates the rate of a process at a certain temperature to its activation energy (Equation 5.1).

$$k = Ae^{\frac{-E_a}{RT}} \quad (5.1)$$

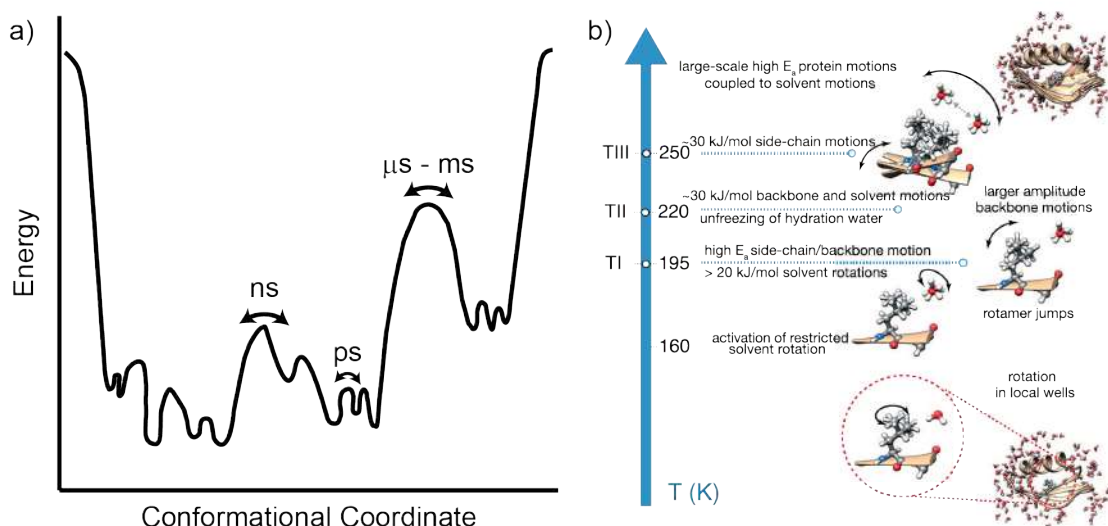


Figure 5.1: a) An example energy landscape within a protein. b) A summary of hierarchical protein dynamics in a protein-solvent system from Lewandowski *et al.* determined through SSNMR in crystalline $[U-^{13}C^{15}N]$ GB1.³⁰ The approximate temperatures for the transitions between different dominant dynamic processes and their activation energies are indicated.

Where k is the rate constant, A is an experimentally-determined constant (relating the k and T), E_a is the activation energy, R is the universal gas constant and T is the absolute temperature.

In this chapter, SSNMR relaxation measurements are used to investigate the site-specific backbone dynamics of protein GB1. The project presented here is a continuation of the work by Lewandowski *et al.* recently published in *Science*.³⁰ In this paper 13 different relaxation rates (R_1 , $R_{1\rho}$ and R_2 for various nuclei in the protein and solvent) were measured between -168.15°C and 6.85°C within crystalline $[U-^{13}C,^{15}N]$ GB1 to determine the hierarchical relationship between the dynamics in the protein-solvent system. At very low temperatures the functionality of the protein was lost, but as the temperature increased the dynamics were activated, producing abrupt changes in the measured relaxation rates at three particular temperatures: -78.15°C , -53.15°C and -23.15°C . Furthermore, these thermally-activated motions dominated different relaxation measurements at different temperatures depending on the type of experiment and nuclei involved.

In general, low temperatures constrain the system to only motions with low energy barriers, such as solvent rotation, and increasing the temperature activates larger-amplitude, higher activation energy motions, such as sidechain motions (Figure 5.1b). A thorough set of SSNMR relaxation measurements across this wide temperature range provided access to these dynamics as they were thermally activated. At the higher temperatures, Lewandowski *et al.* observed correlated motions that traversed the entire β -sheet of GB1 and as well as correlations between high and low activation energy motions, suggesting that fast motions may facilitate the slower motions. In general, there

was strong coupling between backbone, sidechain and solvent motions across extended parts of protein.

Here site-specific, variable-temperature (VT) proton-detected, MAS SSNMR R_1 and $R_{1\rho}$ measurements for both $^{13}\text{C}'$ and ^{15}N throughout the GB1 backbone are presented. In comparison to the bulk measurements made by Lewandowski *et al.*, which are an average of all nuclei of the same type across the protein, the site-specific measurements provide far more detail on the variations in dynamics within the protein. ^1H -detection is used in these experiments to accelerate the acquisition of spectra, thus deuteration of the protein is required. A fully back-exchanged [$\text{U-}^2\text{H}, ^{13}\text{C}, ^{15}\text{N}$] GB1 sample (i.e. perdeuterated $^{13}\text{C}, ^{15}\text{N}$ labelled GB1 where protons were reintroduced at exchangeable sites by recrystallising the sample from water) was used for these measurements. Additionally, deuteration allowed quantitative measurements at just 50 kHz MAS, where a wider range of sample temperatures was available compared to 60 kHz spinning, at which the heating effects of fast MAS are significantly greater. Together the measured, site-specific VT $^{13}\text{C}'$ and ^{15}N R_1 and $R_{1\rho}$ rates provide for an estimation of the amplitudes and timescales of the motion at in the peptide planes and their activation energies.

5.3 Results

5.3.1 Variable Temperature R_1 and $R_{1\rho}$ Measurements

Assignments for the fully back-exchanged [$\text{U-}^2\text{H}, ^{13}\text{C}, ^{15}\text{N}$] GB1 sample were confirmed using HCONH and HCO(C^α)NH 3D spectra (Figure 5.8). $^{13}\text{C}'$ and ^{15}N backbone R_1 and $R_{1\rho}$ measurements were performed on perdeuterated GB1 between -5.15°C and 34.65°C at 50 kHz MAS and 600 MHz ^1H Larmor frequency. The internal sample temperature was determined from the ^1H chemical shift of water with respect to DSS. The use of 50 kHz MAS provided the high resolution required for the measurements, while also allowing access to a wide range of sample temperatures.

Before analysing the variable-temperature data, it is important to discuss the trends throughout the protein and across the different relaxation measurements since these are dominated by different motions. Each type of relaxation rate reports on particular timescales of motion: R_1 is sensitive to ps - ns motions, while $R_{1\rho}$ is dominated by slower, ns - ms motions. It is clear from the y -axis scales in Figure 5.2 that $R_{1\rho}$ is consistently larger than R_1 . This is always the case because the return of the magnetisation to equilibrium (R_1 relaxation) inherently causes loss of the magnetisation in the xy -plane ($R_{1\rho}$ relaxation). In general the $^{13}\text{C}'$ nuclei relax at twice the rate of the ^{15}N nuclei, because the dominating contribution to $^{13}\text{C}'$ relaxation ($^{13}\text{C}'$ CSA) is typically larger than those to ^{15}N relaxation (^{15}N CSA and $^{15}\text{N-}^1\text{H}$ dipolar coupling), due to the higher gyromagnetic ratio of ^{13}C .

It seems intuitive that the $^{13}\text{C}'$ and ^{15}N backbone nuclei will be undergoing similar motions in each residue due to the rigid, planar nature of the peptide bond.^{158,221} Often these sites are treated this way in models and will be throughout the remainder of this chapter. Similarities can be seen between the trends of the different relaxation rates

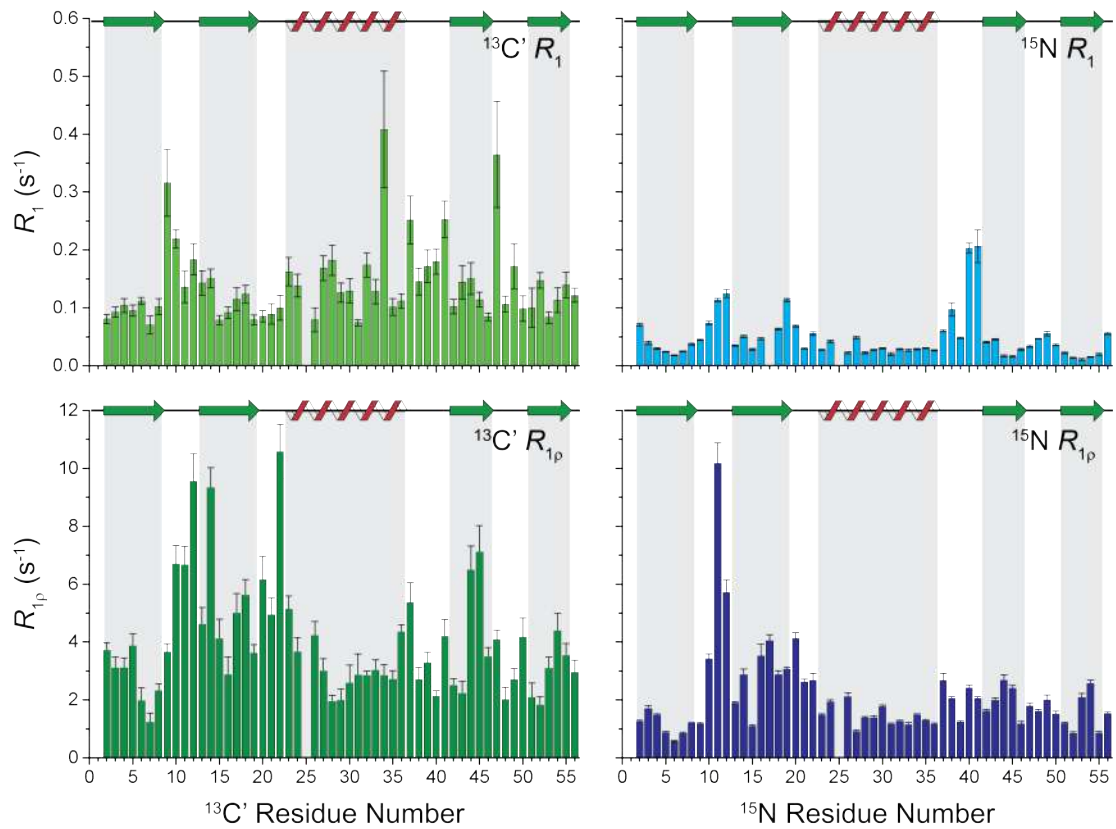


Figure 5.2: The R_1 and $R_{1\rho}$ values for the $^{13}\text{C}'$ and ^{15}N backbone nuclei throughout crystalline perdeuterated $[\text{U-}^{13}\text{C},^{15}\text{N}]$ GB1 at 28.0°C, 600 MHz ^1H Larmor frequency and 50 kHz MAS. The location of the α -helix and β -strands throughout the protein are indicated at the top of each plot. Note the difference in scale between the R_1 and $R_{1\rho}$ plots.

across the backbone, for example all of the rates show significant increases in the β 1- β 2 loop (residues 9 - 12) and moderate increases in the α -helix- β -3 loop (residues 37 - 41). In the ^{15}N R_1 and $R_{1\rho}$ and $^{13}\text{C}'$ $R_{1\rho}$ data, the α -helix (residues 23 -36) displays relatively low rates with minimal variation throughout, indicating that the α -helix is relatively rigid. These low rates suggest that the α -helix is less dynamic than other secondary structure elements of the protein, such as the loops, which show significantly higher motions, both in terms of bond rotations and domain motions. However, there are also some clear differences across the rate measurements, such as the seemingly elevated $^{13}\text{C}'$ R_1 s in the α -helix, residue 34 stands out in particular. Such variations are due to each of the rates being sensitive to different frequencies of motion because of the different spectral density contributions, which are outlined in Section 5.3.2, and also the position of the site in the backbone and its surroundings. A comparison to literature $^{13}\text{C}'$ and ^{15}N R_1 and $R_{1\rho}$ in crystalline GB1 at 27°C shows very good agreement both in the magnitude of rates and the trends throughout.¹⁵⁸ Furthermore, the consistency in these trends across a range of temperatures in Figures 5.3 and 5.4 suggests that these measurements have a high level of accuracy.

The VT R_1 and $R_{1\rho}$ data display rather contrasting trends (Figures 5.3 and 5.4). The $R_{1\rho}$ rates clearly significantly decrease with increasing sample temperature, whereas the R_1 rates display a relatively small decrease. Examples of the relaxation rates for specific residues highlight these trends further. For example, residue E19 shows 13.1% and 11.5% decreases in $^{13}\text{C}'$ and ^{15}N R_1 , respectively, across a temperature increase of approximately 35°C. Whereas for the same sites across a similar temperature range $^{13}\text{C}'$ and ^{15}N $R_{1\rho}$ decrease by 49.3% and 68.8%, respectively. The G41 R_1 plots suggest that there may some sites that do undergo more significant variations in R_1 with temperature. However, calculations of the average change in R_1 across the protein show that there are only very slight decreases with increasing temperature for both $^{13}\text{C}'$ and ^{15}N (0.0042 s^{-1} and 0.0072 s^{-1} , respectively), which are well within the experimental errors (0.033 s^{-1} and 0.075 s^{-1} , respectively). This variation is the equivalent to -0.08%°C⁻¹ for $^{13}\text{C}'$ R_1 and -0.26%°C⁻¹ for ^{15}N R_1 . For comparison, the same calculations for $R_{1\rho}$ data produces average variations of approximately an order of magnitude larger (-1.53%°C⁻¹ for $^{13}\text{C}'$ and -2.33%°C⁻¹ for ^{15}N). Overall, the significant differences in the trends of R_1 and $R_{1\rho}$ with temperature indicate either that the protein dynamics across this temperature range are on the timescales that significantly influence $R_{1\rho}$, but not so much R_1 (i.e. ns - ms dynamics, such as domain motions), or that the R_1 rates are being sampled at their maximum leading to little observed change in rate within this temperature range (see Figure 2.25 in Chapter 2 for the relationship between R_1 and temperature).

The lack of significant variation in the site-specific R_1 rates with temperature is interesting because this is in agreement with the Lewandowski *et al.* variable-temperature measurements by both order of magnitude and temperature trend.³⁰ Both the $^{13}\text{C}'$ and ^{15}N R_1 data recorded by Lewandowski *et al.* reach a maximum at the higher temperatures (> -23°C), suggesting that the lack of variation in the VT R_1 values reported

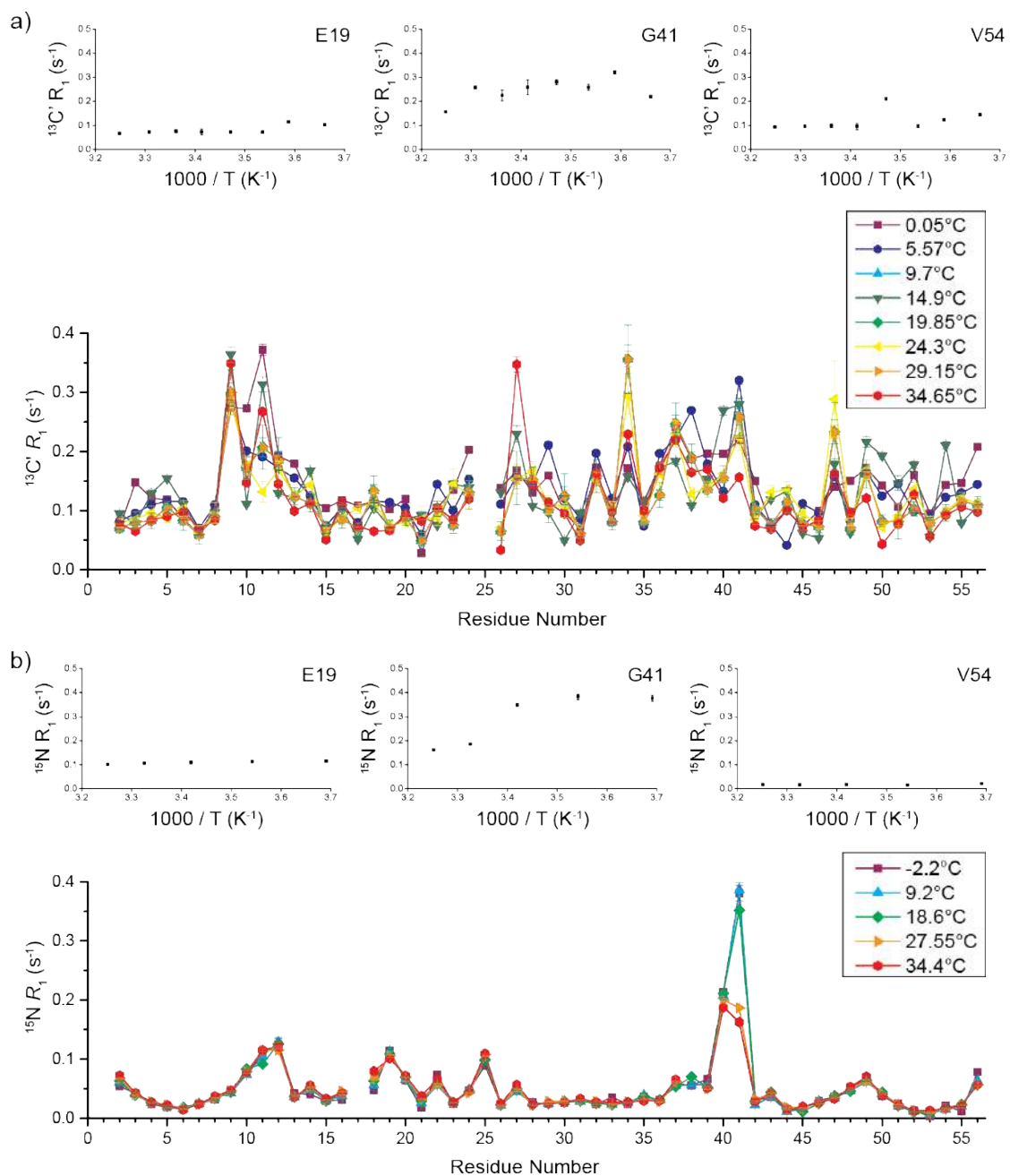


Figure 5.3: a) $^{13}\text{C}'$ and b) $^{15}\text{N} R_1$ plotted against the inverse absolute temperature for residues E19, G41 and V54, plus the complete variable temperature datasets plotted by residue.

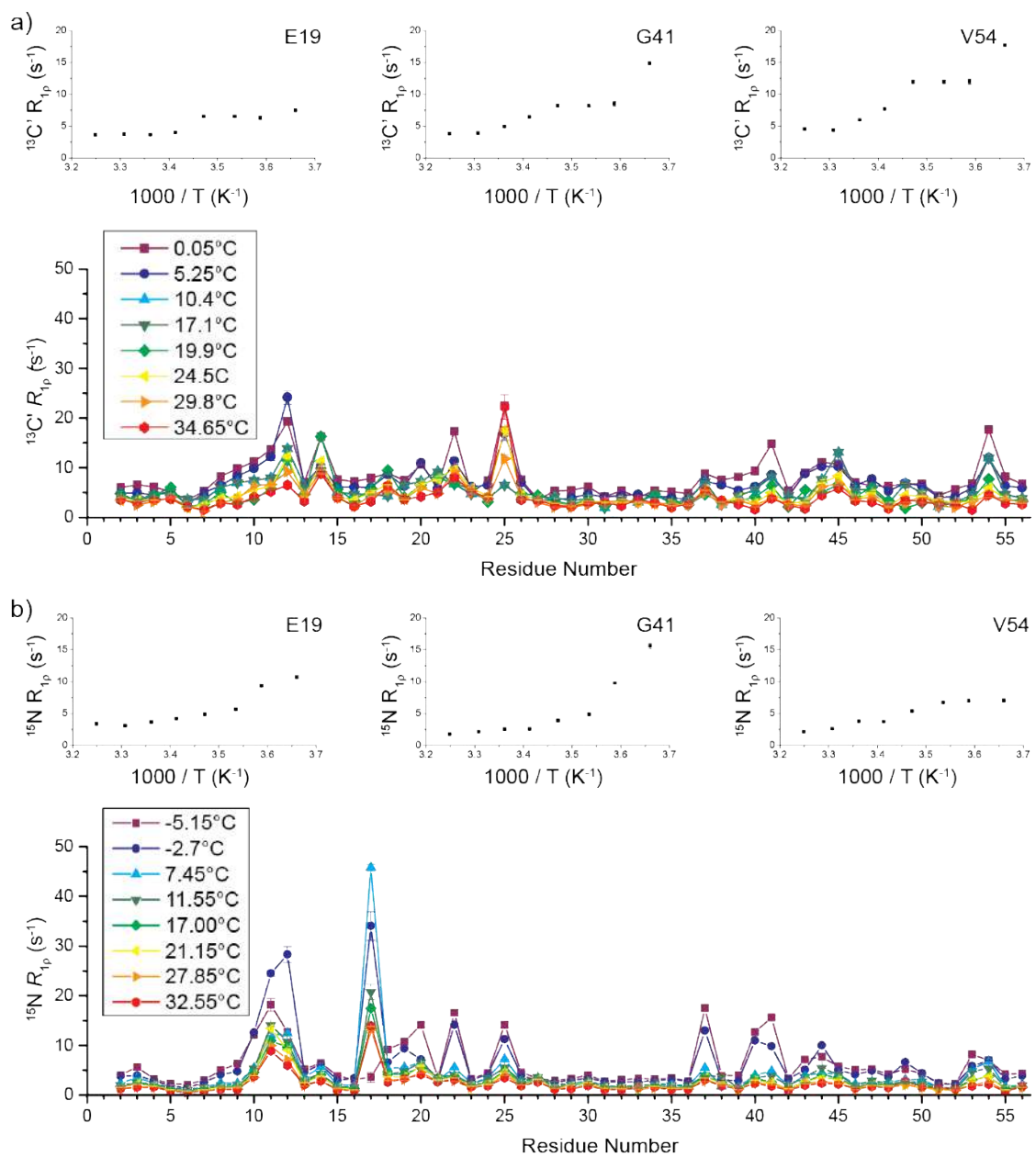


Figure 5.4: a) $^{13}\text{C}'$ and b) $^{15}\text{N} R_{1\rho}$ plotted against the inverse absolute temperature for residues E19, G41 and V54, plus the complete variable temperature datasets plotted by residue.

here may be due to sampling R_1 at the temperatures where it only varies minimally. In this temperature range $^{13}\text{C}'$ and ^{15}N R_1 are dominated by fast backbone dynamics. It is worth stating that the rates presented here were recorded at a different ^1H Larmor frequency to those in the mentioned paper and therefore the data are not expected to be identical. In general, the larger values of R_1 , which suggest areas of increased ps - ns motion, are recorded at sites within the less rigid parts of the protein backbone, such as the loops.

On the other hand, $R_{1\rho}$ clearly decreases as the temperature increases. The $^{13}\text{C}'$ and ^{15}N $R_{1\rho}$ values presented by Lewandowski *et al.* have maxima at approximately -50°C . This trend suggests that continuing to measure these relaxation rates at increasingly warmer temperatures will result in rapidly decreasing rates. This matches the results presented in this chapter, which are about an order of magnitude smaller than those in the paper and continue to decrease with warming, suggesting that slower, ns - ms motions dominate $R_{1\rho}$ at the lower temperatures. The more significant variations in $R_{1\rho}$ with temperature tend to be observed in the flexible loop regions of the protein (e.g. residues 9 - 12). This suggests that the slow μs - ms dynamics of these sites are most influenced by the variation in temperature across this range.

The full results, showing the $^{13}\text{C}'$ and ^{15}N backbone R_1 and $R_{1\rho}$ rates for each residue plotted against temperature, can be found in Figures D.1, D.2, D.3 and D.4.

5.3.2 Use of the Extended Model Free Approach to Determine Order Parameters, Correlation Times and Activation Energies

The $^{13}\text{C}'$ and ^{15}N relaxation rates presented in Figures 5.3 and 5.4 provide an insight into the relative dynamics throughout the protein backbone, however a model is required to quantitatively characterise these motions. The model must be complex enough to provide an realistic representation of the motions, yet straightforward enough that an accurate fitting can be obtained from a reasonable amount of data.

Two types of the “model free” approach^{28,29} are commonly used to fit R_1 and $R_{1\rho}$ rates to order parameters (i.e. effective amplitudes) and correlation times (i.e. effective timescales): the simple model free (SMF) and extended model free (EMF) approaches (Equations 5.2 and 5.3, respectively). The key difference between these models is that the SMF approach is based upon the assumption of a single motion dominating each set of relaxation rates, whereas the EMF approach fits a “fast” and “slow” motion to each. These models relate the order parameters and correlation times to spectral density ($J(\omega)$). Spectral densities at particular frequencies are found within the relaxation rate equations (discussed further on), thus forming a link between relaxation rate and a quantitative measure of motion (S^2 and τ_c).

$$J(\omega) = (1 - S^2) \frac{\tau_c}{1 + (\omega\tau_c)^2} \quad (5.2)$$

Where $J(\omega)$ is the spectral density at the frequency (ω), S^2 is the order parameter and τ_c is the correlation time.

$$J(\omega) = (1 - S_f^2) \frac{\tau_f}{1 + (\omega\tau_f)^2} + S_f^2(1 - S_s^2) \frac{\tau_s}{1 + (\omega\tau_s)^2} \quad (5.3)$$

Where S_s^2 and S_f^2 are the order parameters and τ_s and τ_f are the correlation times for the slow and fast motions, respectively.

Since SSNMR relaxation measurements are sensitive to a wide range of motions, it is possible for different motions to contribute to the same relaxation rate. Alternatively, a single motion may dominate the measured relaxation rate, even if others are present. An investigation into the dynamic contributions to $^{13}\text{C}'$ and ^{15}N R_1 and $R_{1\rho}$ in crystalline GB1 demonstrated that an EMF approach combining all of the data from both nuclei is far more appropriate representation of peptide plane dynamics, than an SMF approach or individual fitting of the $^{13}\text{C}'$ and ^{15}N data.^{158,221} Similar results are found in other protein relaxation studies.^{221,222} Thus currently the optimal approach for determining protein backbone dynamics involves fitting $^{13}\text{C}'$ and ^{15}N R_1 and $R_{1\rho}$ together using the EMF approach.

The $^{13}\text{C}'$ and ^{15}N R_1 and $R_{1\rho}$ data presented in Figures 5.3 and 5.4 is measured at more than one temperature, which creates the possibility of adding a temperature dependence to the model free approach. A modified Arrhenius equation can be used to link correlation time to temperature and an activation energy:³⁵

$$\tau_c = \tau_0 e^{\frac{E_a}{RT}} \quad (5.4)$$

Where τ_0 is an experimentally-determined constant, E_a is the activation energy, R is the gas constant and T is temperature.

It must be noted however that the addition of this Arrhenius equation involves the fitting of an additional parameter (E_a) and so, just like the EMF approach, it should only be used in the cases where ample data is present, otherwise an accurate fit will not be possible. In order to explore whether the data presented in this chapter is sufficient for such a model, the VT relaxation rates will be fitted using the EMF approach with Equation 5.4, before being tested and compared to similar data in the literature.

A variety of $^{13}\text{C}'$ and ^{15}N R_1 and $R_{1\rho}$ measurements on crystalline proteins have been conducted in the solid state, since there has been particular interest in the dynamics at these sites to further understand the peptide plane.^{158,218,221,222} A handful of which have monitored the changes in relaxation rate or order parameters and correlation times across a range of temperatures. These have used models based on the assumption of a single motion (such as the SMF approach) and / or independent analysis of the $^{13}\text{C}'$ and ^{15}N relaxation rates,^{111,218,221} which produce insufficiently simple models of the complex protein dynamics. Here the aim was to directly incorporate the temperature-dependent correlation times into the EMF analysis, producing a more complex representation of the protein dynamics.

Spectral Density Equations for $^{13}\text{C}'$ and ^{15}N R_1 and $R_{1\rho}$

Each relaxation rate measurement is composed of contributions from dynamic processes, such as the random motion of CSA or dipolar couplings. The extent of these contributions depends on the various constants and the spectral densities at specific Larmor frequencies. These spectral densities are crucial for the EMF analysis and, as such, the relevant equations for each contribution to $^{13}\text{C}'$ and ^{15}N R_1 and $R_{1\rho}$ are presented below.

The main contribution to the $^{13}\text{C}'$ R_1 and $R_{1\rho}$ is from the $^{13}\text{C}'$ CSA:

$$R_{1,13\text{C}',\text{CSA}} = \frac{2}{15}\omega_0^2(\sigma_{11}^2 + \sigma_{22}^2 + \sigma_{33}^2 - \sigma_{11}\sigma_{22} - \sigma_{11}\sigma_{33} - \sigma_{22}\sigma_{33})J(\omega_C) \quad (5.5)$$

$$R_{1\rho,13\text{C}',\text{CSA}} = \frac{1}{45}\omega_C^2(\sigma_{11}^2 + \sigma_{22}^2 + \sigma_{33}^2 - \sigma_{11}\sigma_{22} - \sigma_{11}\sigma_{33} - \sigma_{22}\sigma_{33})\{4J(\omega_1) + 3J(\omega_C)\} \quad (5.6)$$

Where ω_C is the Larmor frequency of $^{13}\text{C}'$, ω_1 is the spin-lock frequency, and σ_{11} , σ_{22} and σ_{33} are the principle components of the CSA tensor (where $\sigma_{11} \gg \sigma_{22} \gg \sigma_{33}$) These CSA components were calculated from the $^{13}\text{C}'$ isotropic chemical shifts (σ_{iso}) based on the linear fits of $^{13}\text{C}'$ isotropic chemical shift and each CSA tensor component:²²³

$$\sigma_{11} = 0.24 \times \sigma_{iso} + 200 \quad (5.7)$$

$$\sigma_{22} = 2.82 \times \sigma_{iso} - 305 \quad (5.8)$$

$$\sigma_{33} = 96.5 \quad (5.9)$$

There are also contributions from the $^{13}\text{C}'$ - $^{13}\text{C}^\alpha$, $^{13}\text{C}'$ - ^{15}N and $^{13}\text{C}'$ - ^1H (both from the amide proton and further non-directly bonded protons) dipolar couplings that must be accounted for:

$$R_{1,C'C_a} = \frac{1}{10}\left(\frac{\mu_0}{2\pi}\frac{\gamma_C\gamma_{C_a}}{\hbar r_{C'C_a}^3}\right)^2\{3J(\omega_C) + 6J(\omega_C + \omega_C) + J(\omega_C - \omega_C)\} \quad (5.10)$$

Where μ_0 is the vacuum permeability constant, γ is the gyromagnetic ratio and r is the distance between the nuclei. All bond lengths used in these equations are stated in Table 5.1.

$$R_{1\rho,C'C_a} = \frac{1}{20}\left(\frac{\mu_0}{2\pi}\frac{\gamma_C\gamma_{C_a}}{\hbar r_{C'C_a}^3}\right)^2\{4J(\omega_1) + 3J(\omega_C) + J(\omega_C - \omega_C) + 6J(\omega_C) + 6J(\omega_C + \omega_C)\} \quad (5.11)$$

Table 5.1: The bond lengths used for the relaxation rate equations.

* The effective distance for the contribution of non-directly bonded protons from Allard *et al.*²²⁴

| Bond | Length (Å) |
|---|------------|
| ¹³ C' - ¹³ C ^α | 1.525 |
| ¹³ C' - ¹ H ^N | 2.04 |
| ¹³ C' - ¹ H * | 1.82 |
| ¹³ C' - ¹⁵ N | 1.30 |
| ¹⁵ N - ¹³ C ^α | 1.46 |
| ¹⁵ N - ¹ H ^N | 1.02 |
| ¹⁵ N - ¹ H * | 1.80 |

$$R_{1,C'N} = \frac{1}{10} \left(\frac{\mu_0}{2\pi} \frac{\gamma_C \gamma_N}{\hbar r_{C'N}^3} \right)^2 \{3J(\omega_C) + 6J(\omega_C + \omega_N) + J(\omega_C - \omega_N)\} \quad (5.12)$$

$$R_{1\rho,C'N} = \frac{1}{20} \left(\frac{\mu_0}{2\pi} \frac{\gamma_C \gamma_N}{\hbar r_{C'N}^3} \right)^2 \{4J(\omega_1) + 3J(\omega_C) + J(\omega_C - \omega_N) + 6J(\omega_C) + 6J(\omega_C + \omega_N)\} \quad (5.13)$$

$$R_{1,C'H} = \frac{1}{10} \left(\frac{\mu_0}{2\pi} \frac{\gamma_C \gamma_H}{\hbar r_{C'H}^3} \right)^2 \{3J(\omega_C) + 6J(\omega_C + \omega_H) + J(\omega_C - \omega_H)\} \quad (5.14)$$

$$R_{1\rho,C'H} = \frac{1}{20} \left(\frac{\mu_0}{2\pi} \frac{\gamma_C \gamma_H}{\hbar r_{C'H}^3} \right)^2 \{4J(\omega_1) + 3J(\omega_C) + J(\omega_C - \omega_H) + 6J(\omega_C) + 6J(\omega_C + \omega_H)\} \quad (5.15)$$

The main contributions to the ¹⁵N R_1 and $R_{1\rho}$ are from the ¹⁵N-¹H dipolar coupling with the amide ¹H and ¹⁵N CSA :

$$R_{1,NH} = \frac{1}{10} \left(\frac{\mu_0}{2\pi} \frac{\gamma_N \gamma_H}{\hbar r_{NH}^3} \right)^2 \{3J(\omega_N) + 6J(\omega_N + \omega_H) + J(\omega_N - \omega_H)\} \quad (5.16)$$

$$R_{1\rho,NH} = \frac{1}{20} \left(\frac{\mu_0}{2\pi} \frac{\gamma_N \gamma_H}{\hbar r_{NH}^3} \right)^2 \{4J(\omega_1) + 3J(\omega_N) + J(\omega_N - \omega_H) + 6J(\omega_N) + 6J(\omega_N + \omega_H)\} \quad (5.17)$$

Where ω_H is the Larmor frequency of ¹H and ω_N is the Larmor frequency of ¹⁵N.

$$R_{1,15N,CSA} = \frac{2}{15} \omega_0^2 (\sigma_{11}^2 + \sigma_{22}^2 + \sigma_{33}^2 - \sigma_{11}\sigma_{22} - \sigma_{11}\sigma_{33} - \sigma_{22}\sigma_{33}) J(\omega_N) \quad (5.18)$$

$$R_{1\rho,15N,CSA} = \frac{1}{45}\omega_N^2(\sigma_{11}^2 + \sigma_{22}^2 + \sigma_{33}^2 - \sigma_{11}\sigma_{22} - \sigma_{11}\sigma_{33} - \sigma_{22}\sigma_{33})\{4J(\omega_1) + 3J(\omega_N)\} \quad (5.19)$$

Where σ_{11} , σ_{22} and σ_{33} are the principle components of the CSA tensor (where $\sigma_{11} \gg \sigma_{22} \gg \sigma_{33}$). These CSA components were calculated from the ^{15}N isotropic chemical shifts (σ_{iso}) based on the linear fits of ^{15}N isotropic chemical shift and each CSA tensor component:²²⁵

$$\sigma_{11} = 1.1283 \times \sigma_{iso} + 93.77 \quad (5.20)$$

$$\sigma_{22} = 1.0086 \times \sigma_{iso} - 42.475 \quad (5.21)$$

$$\sigma_{33} = 0.8631 \times \sigma_{iso} - 51.295 \quad (5.22)$$

There are also contributions from the ^{15}N - $^{13}\text{C}^\alpha$, ^{15}N - $^{13}\text{C}'$ and ^{15}N - ^1H (from the non-directly bonded ^1H s) dipolar couplings that must be accounted for:

$$R_{1,NCa} = \frac{1}{10} \left(\frac{\mu_0}{2\pi} \frac{\gamma_N \gamma_C}{\hbar r_{NCa}^3} \right)^2 \{3J(\omega_N) + 6J(\omega_N + \omega_C) + J(\omega_N - \omega_C)\} \quad (5.23)$$

$$R_{1\rho,NCa} = \frac{1}{20} \left(\frac{\mu_0}{2\pi} \frac{\gamma_N \gamma_C}{\hbar r_{NCa}^3} \right)^2 \{4J(\omega_1) + 3J(\omega_N) + J(\omega_N - \omega_C) + 6J(\omega_N) + 6J(\omega_N + \omega_C)\} \quad (5.24)$$

$$R_{1,NC'} = \frac{1}{10} \left(\frac{\mu_0}{2\pi} \frac{\gamma_N \gamma_C}{\hbar r_{NC'}^3} \right)^2 \{3J(\omega_N) + 6J(\omega_N + \omega_C) + J(\omega_N - \omega_C)\} \quad (5.25)$$

$$R_{1\rho,NC'} = \frac{1}{20} \left(\frac{\mu_0}{2\pi} \frac{\gamma_N \gamma_C}{\hbar r_{NC'}^3} \right)^2 \{4J(\omega_1) + 3J(\omega_N) + J(\omega_N - \omega_C) + 6J(\omega_N) + 6J(\omega_N + \omega_C)\} \quad (5.26)$$

$$R_{1,NH} = \frac{1}{10} \left(\frac{\mu_0}{2\pi} \frac{\gamma_N \gamma_H}{\hbar r_{NH}^3} \right)^2 \{3J(\omega_N) + 6J(\omega_N + \omega_H) + J(\omega_N - \omega_H)\} \quad (5.27)$$

$$R_{1\rho,NH} = \frac{1}{20} \left(\frac{\mu_0}{2\pi} \frac{\gamma_N \gamma_H}{\hbar r_{NH}^3} \right)^2 \{4J(\omega_1) + 3J(\omega_N) + J(\omega_N - \omega_H) + 6J(\omega_N) + 6J(\omega_N + \omega_H)\} \quad (5.28)$$

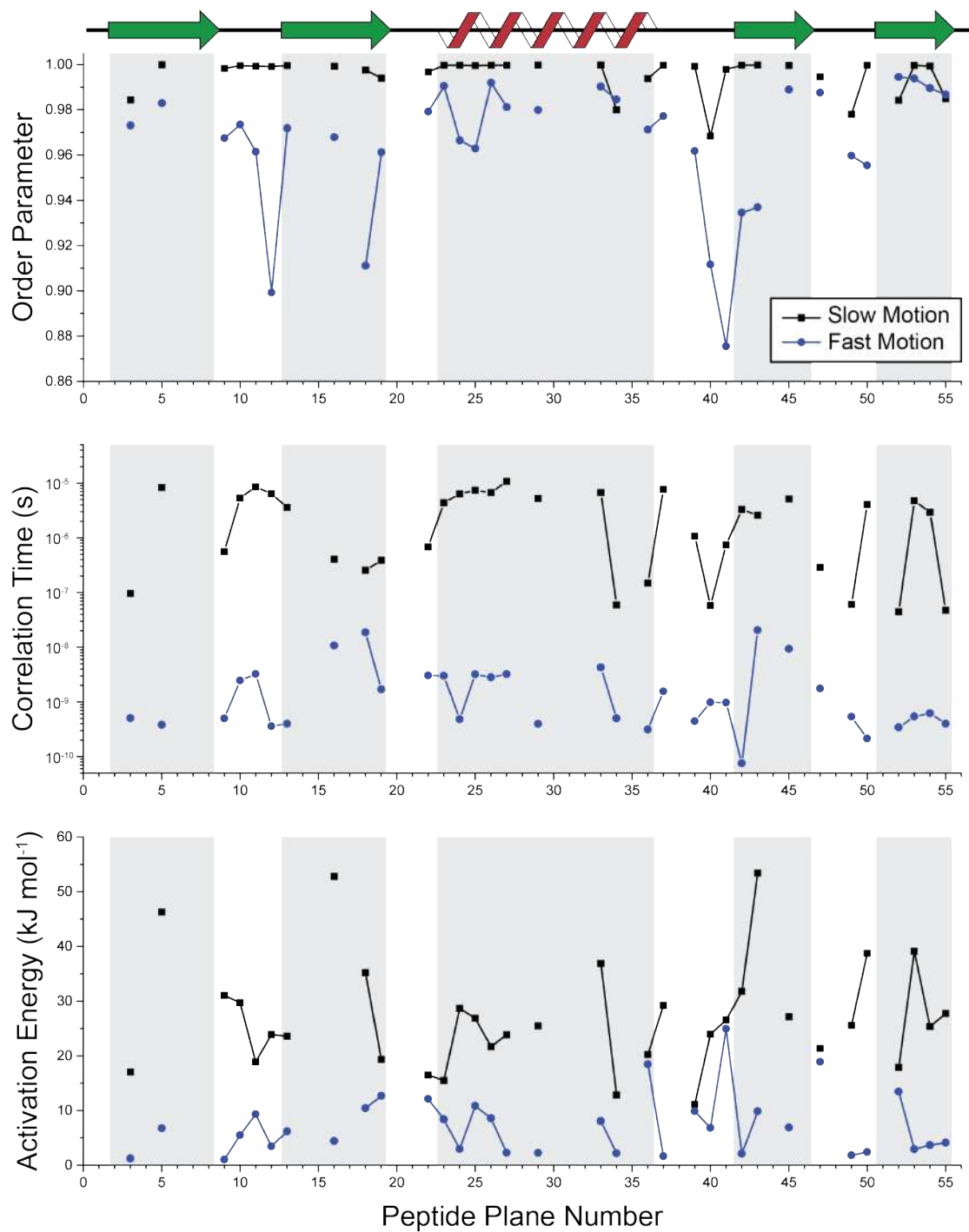


Figure 5.5: The correlation times, order parameters and activation energies (at 25.0°C) for the slow (black) and fast (blue) motions from the EMF analysis on the VT $^{13}\text{C}'$ and ^{15}N R_1 and $R_{1\rho}$ data. Data that did not successfully fit to this model has been removed.

EMF and Arrhenius Analysis of the VT $^{13}\text{C}'$ and ^{15}N R_1 and $R_{1\rho}$ Data

Here the EMF approach with the modified Arrhenius equation (5.4) allows the combined analysis of $^{13}\text{C}'$ and ^{15}N R_1 and $R_{1\rho}$ at 5 temperatures, producing values of S^2 , τ_c and E_a for both a slow and fast motion (Figure 5.5). The *Matlab* scripts used for these calculations can be found in Appendix D.2.

It was clear that some of the peptide planes were not successfully fit from resulting S^2 , τ_c and E_a values (e.g. $E_a = 0$), these have been removed from the figure. The remaining data suggests that these sites can be represented by a slower and a faster motion, the former of which has a higher order parameter, correlation time and activation energy on average.

The calculated order parameters in Figure 5.5 are on a scale of 0 to 1, where 0 is a completely unrestricted motion and 1 is a rigid structure. Thus smaller order parameters are interpreted as larger amplitude motions in this model. S^2 values between 0.8 and 1 are expected for most nuclei in a folded protein, as is seen for all of the peptide plane dynamics investigated here. The EMF analysis produced order parameters that averaged at 0.995 and 0.965 for the slow and fast motions, respectively, and the latter had a much wider range (0.12, compared to 0.032). The slow order parameters are very similar to those of GB1 in the literature (EMF analysis of $^{13}\text{C}'$ and ^{15}N R_1 and $R_{1\rho}$ at 27°C)¹⁵⁸ and they match the significant decreases at peptide planes 41 and 49, both of which are within the flexible loop regions on the C-terminus side of the protein. Whereas the order parameters reported here for the fast motion are approximately 0.1 greater and seem to have little correlation with the previously reported data, except for also having a significant decrease at peptide plane 41.

The EMF-Arrhenius analysis calculates values of τ_0 (a constant related to the correlation time and activation energy) rather than τ_c itself. The values of τ_c in Figure 5.5 have been calculated from τ_0 and E_a at 25.0°C , producing a slow motion on the microsecond timescale (average $\tau_c = 3.39 \times 10^{-6}$ s) and a fast motion on the nanosecond timescale (average $\tau_c = 2.91 \times 10^{-9}$ s). The slower motions are on the same timescale as those reported in the literature, whereas the fast motions presented here are approximately an order of magnitude smaller, implying a faster frequency of motion. The slow and fast correlation times in Figure 5.5 show similar trends across the backbone, for example increases in the middle of the $\beta 1$ - $\beta 2$ loop and $\beta 4$ strand, however these do not particularly correlate well with the literature data.

In general, the fast motions have significantly lower activation energies (average $E_a = 7.26$ kJ mol⁻¹) compared to the slow motions (average $E_a = 27.2$ kJ mol⁻¹). The activation energies of these protein nuclei in the literature indicates that those in Figure 5.5 are mostly within the typical range (< 40 kJ mol⁻¹),^{30,111} however the literature also states that the larger amplitude motions have higher activation energies, which is contrasting to the results here. Lewandowski *et al.* calculated activation energies for a range of protein motions, determining the temperatures at which these become active (see Figure 5.1b).³⁰ A comparison of these to the site-specific energies presented here

suggests that the majority of backbone motions (those ≤ 30 kJ mol⁻¹) are active at -50°C and therefore it is assumed that all backbone motions are active by the higher temperature range used in these measurements (-5°C - 30°C). Furthermore, it is logical that all of the protein dynamics should be active at these physiologically-relevant temperatures.

For all of the parameters calculated using this EMF-Arrhenius model, there seems to be a relatively large amount of variation throughout the protein backbone, which does not necessarily correlate with the literature, despite high levels of agreement with the relaxation rates. This leads one to question the accuracy of the fitting procedure and suggest that substantially more data is required for this fit.

Testing of the EMF-Arrhenius Analysis

As a simple check to determine the accuracy of the S^2 , τ_c and E_a values, they were used firstly, to reproduce the relaxation rates at 34.85°C (which were used as part of the EMF-Arrhenius analysis), and secondly, to reproduce a partial set of VT relaxation data that had not been used in the fitting process. A comparison of the measured relaxation rates at 34.85°C and those reproduced using the calculated S^2 , τ_c and E_a values (Figure 5.6) immediately highlights that the model used does not fully account for the ¹³C' R_1 and $R_{1\rho}$ rates, largely underestimating them. The calculated ¹³C' rates are heavily skewed towards those of the ¹⁵N nuclei, suggesting that the ¹⁵N rates dominate this model. On the other hand, the calculated ¹⁵N R_1 and $R_{1\rho}$ values match the experimental data to a high degree of accuracy. One possible reason for the weighting of fits towards the ¹⁵N rates might be that they have lower errors on average (compared to for ¹³C') and this error is involved in the fitting procedure.

Due to the lack of a complete ¹³C' and ¹⁵N R_1 and $R_{1\rho}$ dataset at certain temperatures, some of the measured relaxation rates were not used in the EMF analysis. Three of these datasets are used to test the ability of the calculated order parameters, correlation times and activation energies to reproduce the site-specific ¹³C' R_1 at 5.75°C, ¹³C' $R_{1\rho}$ at 5.25°C and ¹⁵N $R_{1\rho}$ at 7.45°C (Figure 5.7). Here a similar trend is observed, there is poor correlation between the calculated and experimental fits for ¹³C'. In particular, the ¹³C' R_1 values within the α -helix show the most deviation, which is most likely due to the significant variation between ¹³C' and ¹⁵N R_1 s in these peptide planes. Although the ¹⁵N relaxation rates seem to dominate the model, the reproduced ¹⁵N R_1 s still tend to underestimate a few of the larger rates.

These quick tests make it sufficiently clear that this EMF-Arrhenius model is currently too complex for the quantity of data presented in this chapter and the ¹³C' rates are not being fully accounted for. Although the calculated order parameters, correlation times and activation energies seem to be within the expected ranges, these parameters lack the required accuracy for further analysis and discussion.

5.4 Conclusions and Outlook

Variable-temperature SSNMR relaxation measurements are a great tool for investigating the complex dynamics within proteins, as shown by the hierarchy of motions determined

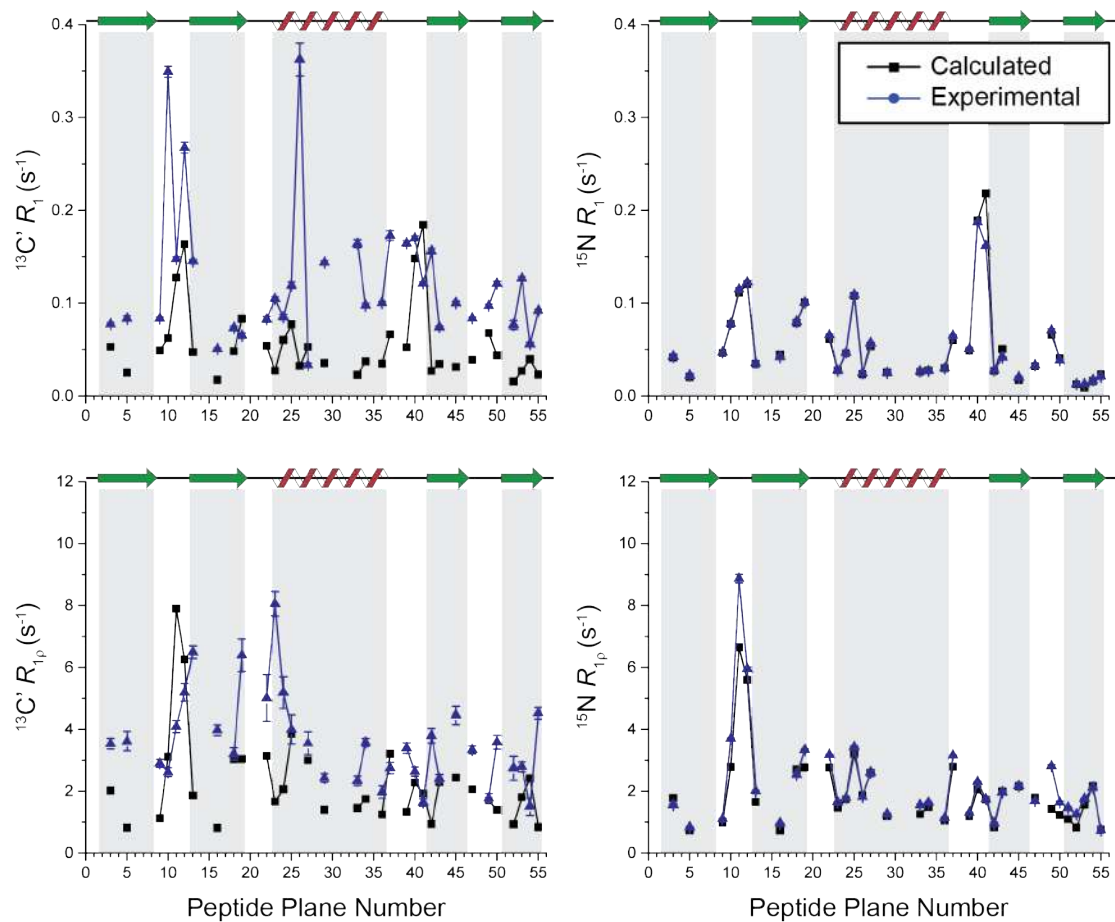


Figure 5.6: The original $^{13}\text{C}'$ and ^{15}N R_1 and $R_{1\rho}$ rates at 34.85°C (blue) plotted alongside the rates reproduced using the EMF-Arrhenius model.

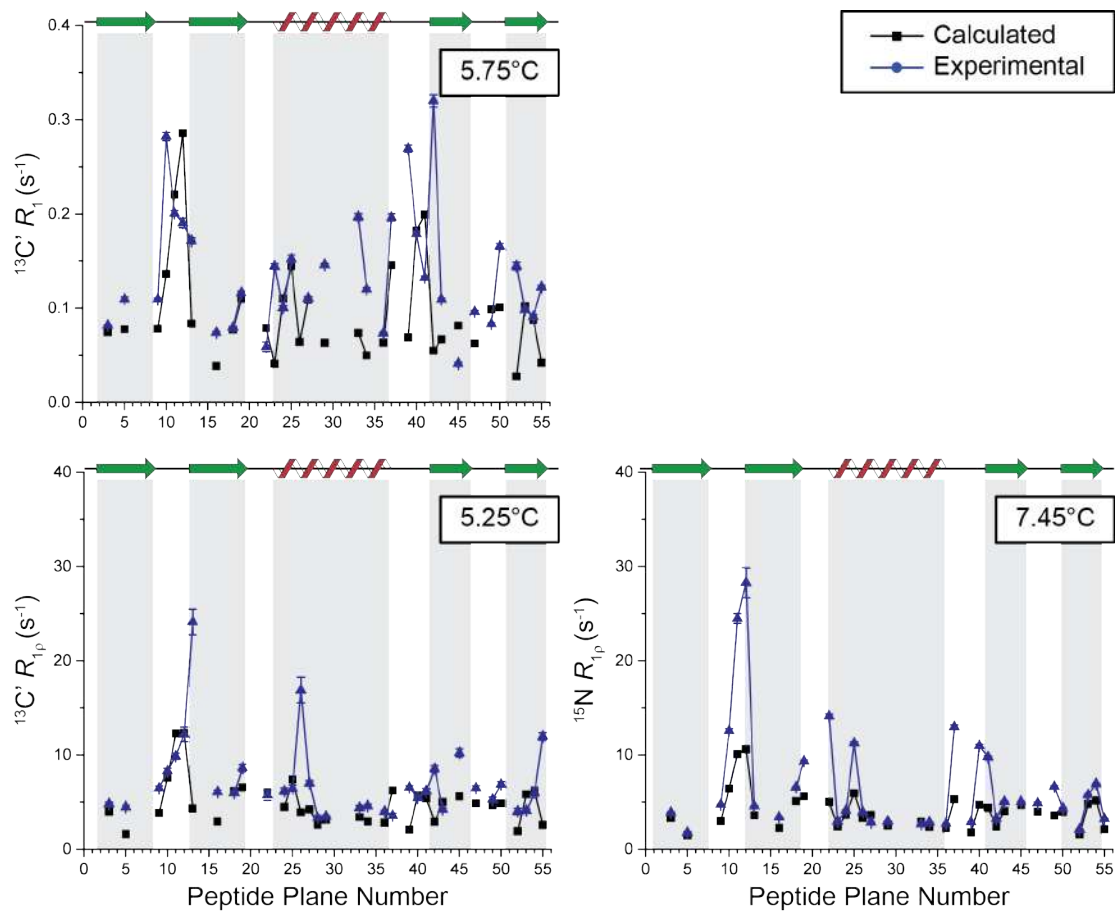


Figure 5.7: The original $^{13}\text{C}' R_1$ and $R_{1\rho}$, and $^{15}\text{N} R_{1\rho}$ rates at 5.75°C, 5.25°C and 7.45°C (blue) plotted alongside the same rates reproduced using the EMF-Arrhenius model. These relaxation rates were not used in the initial EMF-Arrhenius analysis to produce the model.

through low temperature measurements by Lewandowski *et al.*³⁰ Similar measurements are presented here, but with two key differences, the measured relaxation rates are site specific and the chosen temperature range is physiologically relevant. These experiments aimed to reveal the precise $^{13}\text{C}'$ and ^{15}N dynamics throughout the backbone of crystalline $[\text{U-}^2\text{H}, ^{13}\text{C}, ^{15}\text{N}]\text{GB1}$, a model protein.

Analysis of the measured $^{13}\text{C}'$ and ^{15}N R_1 and $R_{1\rho}$ rates at 28.0°C revealed higher rates within the loops on the outside of the protein and very consistent, relatively low rates within the α -helix. This suggests that the flexible loops are more dynamic than the rigid, hydrogen-bonded α -helix and β -strands. The range of dynamics throughout the protein presented here clearly highlights the need for site-specific relaxation measurements when investigating protein motions and that simply measuring average $^{13}\text{C}'$ and ^{15}N rates to represent all of these sites throughout the backbone, as done in the discussed paper,³⁰ does not do them justice.

Overall, the R_1 rates showed minimal variation with temperature, whereas the $R_{1\rho}$ values clearly decreased with increasing temperature (on average 53% over 34.6°C for $^{13}\text{C}'$ and 64% over 32.6°C for ^{15}N). These trends can be explained through comparison with the bulk rate measurements at lower temperatures by Lewandowski *et al.*³⁰ For $R_{1\rho}$, the maximum rate is at temperatures just below those sampled in this chapter, thus further warming of the sample moves the rates away from the maximum, producing dramatic decreases in $R_{1\rho}$. Although these significant decreases in $R_{1\rho}$ are observed at all sites, the largest changes are at sites within the loops of the protein. In contrast, the R_1 maxima are at slightly higher temperatures and it is assumed that the minimal change observed in these R_1 rates is because they are at the maximum. Therefore to see significant change, these measurements need to be recorded at either much higher or lower temperatures.

In the future, measuring R_1 at a wider range of temperatures would clarify where these rates are within the overall hierarchy of dynamics. Alternatively, since the temperature range is limited by the cooling ability of the equipment and the robustness of the protein, repeating these measurements at a different ^1H Larmor frequency may shift the relaxation rates a suitable amount, revealing this information too. It would also be interesting to measure similar relaxation rates on the $^{13}\text{C}^\alpha$ nuclei, which undergo motions distinct from the peptide plane, in contrast to the $^{13}\text{C}'$ and ^{15}N nuclei.

There are various models and methods available for extracting further information from these variable-temperature relaxation rates. Previous studies indicate that SMF analysis of this data would be inappropriate due to multiple motions occurring within the peptide plane, and therefore EMF analysis (that uses both the $^{13}\text{C}'$ and ^{15}N rates within the same fit) is deemed best.^{158, 221} Furthermore, here the use of EMF-Arrhenius analysis allows for combination of the relaxation rates at 5 different temperatures, providing site-specific activation energies for both the fast and slow motions.

It was clear from attempts to reproduce experimental relaxation data from the calculated S^2 , τ_c and E_a values, that this EMF-Arrhenius model is too complex for the

quantity of VT relaxation data used and, although the parameters are all within the expected range for this protein, their accuracy can not be relied upon. It is possible to fit this VT data with simpler models, such as the SMF approach, however this would result in parameters that are unable to realistically represent the complex dynamics.^{158,221} Despite this EMF-Arrhenius model being too ambitious for the quantity of data presented in this chapter, in the future measurements at additional B_0 fields and additional temperatures could lead to it becoming a very informative model on the peptide plane motions. Alternatively, dipolar order parameters could be used as constraints when fitting the relaxation data to the model,^{225–228} aiding the estimation of the internal protein dynamics. The process of measuring these VT relaxation rates at additional B_0 fields is underway with the aim of combining these datasets with the work presented here for an improved fitting and an in-depth analysis of the resulting dynamic parameters.

5.5 Experimental Details

5.5.1 Protein Samples

The fully back-exchanged $[U-^2H, ^{13}C, ^{15}N]$ GB1 protein sample was expressed in minimal media as described in Section 3.8.4 with $[U-^{13}C]$ -glycerol, $U-^{15}N$ -ammonium chloride and D_2O as the sole carbon, nitrogen and hydrogen sources. The proteins were crystallised as described in Section 3.8.4 and DSS was added to each crystallised sample as an internal reference. A 1.3 mm rotor was packed with 3.0 mg of $[U-^2H, ^{13}C, ^{15}N]$ GB1.

5.5.2 Assignment

Firstly, the fully back-exchanged $[U-^2H, ^{13}C, ^{15}N]$ GB1 sample was assigned using HCONH and HCO(C^α)NH 3D pulse sequences. The 1H - ^{15}N assignments are displayed in Figure 5.8. It was not possible to assign four of the $^{13}C^\alpha$ chemical shifts (residues 9, 14, 25 and 38) due to an incorrect setting of the spectral width in the ^{13}C dimension; this caused these peaks to fold back into the spectrum, so the $^{13}C^\alpha$ chemical shift information was lost.

5.5.3 SSNMR Experimental Details

All of the SSNMR experiments in this chapter were measured on a Bruker Avance II+ spectrometer operating at 14.1 T ($\omega_{0,H}/2\pi = 600$ MHz) using a Bruker 1.3 mm triple-resonance MAS probe and performed at 50 kHz spinning frequency.

The ^{13}C pulse sequences were initialised with a 100 kHz $\pi/2$ 1H pulse, followed by CP from 1H to ^{15}N (1.5 ms, $\omega_{1,H}/2\pi \approx 40$ kHz and $\omega_{1,N}/2\pi \approx 10$ kHz), followed by t1 evolution and CP from ^{15}N to ^{13}C (10 ms, $\omega_{1,N}/2\pi \approx 10$ kHz and $\omega_{1,C}/2\pi \approx 40$ kHz). Next a variable delay or variable length spin-lock pulse are applied for R_1 and $R_{1\rho}$, respectively, followed by acquisition. A spin-lock pulse with $\omega_{1,C}/2\pi \approx 7.8$ kHz was employed.

The ^{15}N pulse sequences were initialised with a 100 kHz $\pi/2$ 1H pulse, followed by CP from 1H to ^{15}N (1.5 ms, $\omega_{1,H}/2\pi \approx 40$ kHz and $\omega_{1,N}/2\pi \approx 10$ kHz). Next a variable delay or variable length spin-lock pulse are applied for R_1 and $R_{1\rho}$, respectively, followed by t1 evolution and solvent suppression. Finally there is CP from ^{15}N to 1H (1.0 ms, $\omega_{1,N}/2\pi \approx 10$ kHz and $\omega_{1,H}/2\pi \approx 40$ kHz) and acquisition. A spin-lock pulse with $\omega_{1,N}/2\pi \approx 7.8$ kHz was employed.

In all pulse sequences, during t1 evolution and t2 acquisition, WALTZ16 decoupling was applied at a field strength of $\omega_{1H}/2\pi = 10$ kHz. The variable length delays and spin-lock pulses were: 0.002, 0.1, 0.5, 1, 2.5, 5, 8, 12 and 0.5 s for $^{13}C'$ R_1 . 0.002, 0.007, 0.015, 0.03, 0.06, 0.1, 0.15, 0.2 and 0.015 s for $^{13}C'$ $R_{1\rho}$. 0.001, 0.2, 0.5, 0.8, 1.2, 2.2, 4.0, 8.0, 12.0 and 18 for ^{15}N R_1 . 0.002, 0.012, 0.024, 0.035, 0.05, 0.1, 0.2, 0.3, 0.4 and 0.5 s for ^{15}N $R_{1\rho}$.

Each of these relaxation measurements were recorded across the range of temperatures: $^{13}C'$ R_1 at 0.005, 5.75, 24.30, 9.70, 14.90, 19.85, 29.15 and 34.65 °C, $^{13}C'$ $R_{1\rho}$ at 0.05, 5.25, 10.4, 17.1, 19.8, 24.5, 29.8 and 34.65 °C, ^{15}N R_1 at -2.2, 9.25, 18.6, 27.55 and

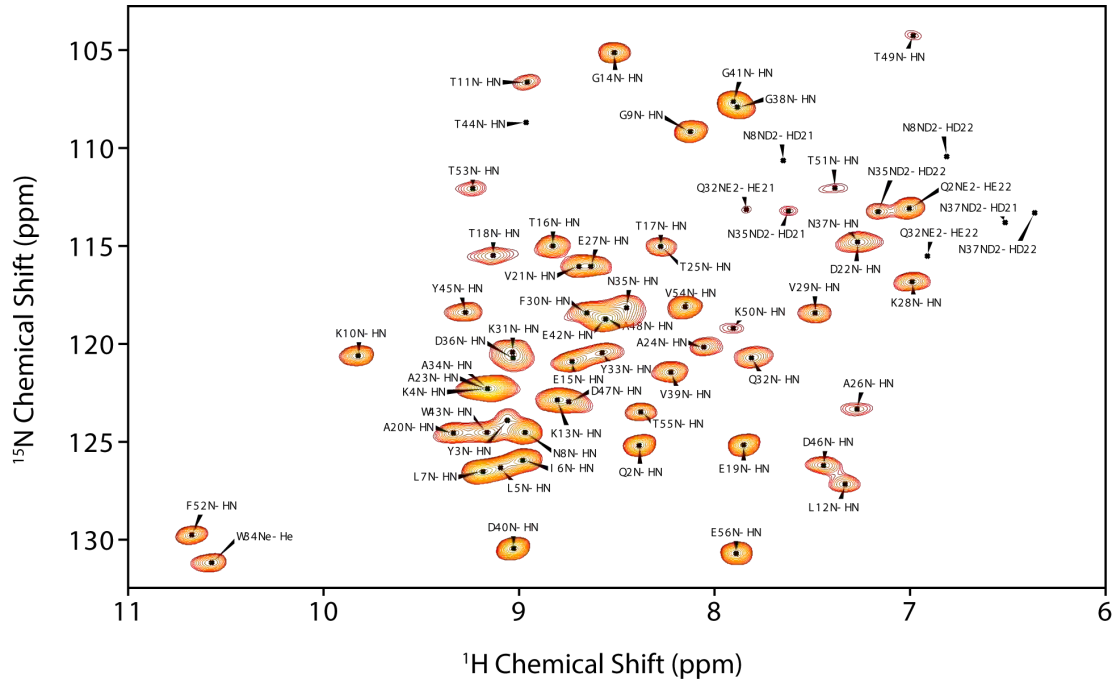


Figure 5.8: The ^1H - ^{15}N assignments for fully back-exchanged $[\text{U-}^2\text{H}, ^{13}\text{C}, ^{15}\text{N}]$ GB1. Recorded at 600 MHz ^1H Larmor frequency and 50 kHz MAS.

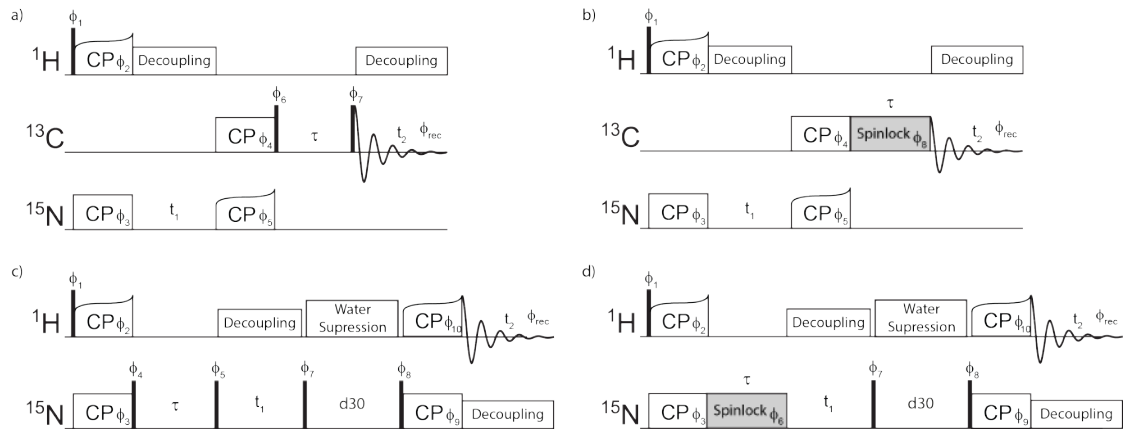


Figure 5.9: a) The ^1H - ^{13}C - ^{15}N pulse sequences used for $^{13}\text{C}'$ R_1 and b) $R_{1\rho}$ and c) the ^1H - ^{15}N - ^1H pulse sequences used for ^{15}N R_1 and d) $R_{1\rho}$.

34.4 °C and ^{15}N $R_{1\rho}$ at -5.15, -2.70, 7.45, 11.55, 17.00, 21.15, 27.85 and 32.55 °C. The sample temperature (°C) was measured by the ^1H chemical shift of water with respect to DSS (calibrated to 0 ppm), see Equation 3.6.^{152,153}

5.5.4 Determination of Relaxation Rates

The R_1 rates were calculated from a plot of the peak integral against the variable delay (τ):

$$Integral = Ae^{(-R_1\tau)} \quad (5.29)$$

The $R_{1\rho}$ rates were calculated from a plot of the peak integral against the variable spin-lock length (τ):

$$Integral = Ae^{(-R_{1\rho}\tau)} \quad (5.30)$$

5.5.5 EMF-Arrhenius Analysis of the $^{13}\text{C}'$ and ^{15}N R_1 and $R_{1\rho}$

Data were fitted using the extended model free approach and modified Arrhenius equation in *Matlab R2017a* using the *fminsearch* algorithm to minimise the χ^2 value:

$$\chi^2 = \sum_i \frac{(R_i^{exp} - R_i^{calc})^2}{\sigma_i^2} \quad (5.31)$$

Where i is the number of data points (i.e. temperatures), (R_i^{exp} is the measured relaxation rate, (R_i^{calc} is the calculated relaxation rate and σ_i is the error in the measured relaxation rate.

The temperature dependence of the correlation time can be defined as:

$$\tau_c = \tau_0 e^{\frac{E_a}{RT}} \quad (5.32)$$

Where τ_0 is an experimentally-determined constant, E_a is the activation energy, R is the gas constant and T is temperature. Since the sample temperature varied slightly between the different datasets, the mean temperature was used (Table 5.2).

The EMF approach uses the expressions for relaxation rates and spectral density given in Section 2.3. These particular expression are noted below:

Table 5.2: The sample temperature across the VT $^{13}\text{C}'$ and ^{15}N R_1 and $R_{1\rho}$ measurements and the mean temperatures, which were used for the fitting.

| $^{13}\text{C}'$ R_1 (K) | $^{13}\text{C}'$ $R_{1\rho}$ (K) | ^{15}N R_1 (K) | ^{15}N $R_{1\rho}$ (K) | Mean (K) |
|----------------------------|----------------------------------|---------------------------|---------------------------------|----------|
| 273.2 | 273.2 | 270.95 | 270.45 | 271.95 |
| 282.85 | 283.55 | 282.4 | 284.7 | 283.375 |
| 288.05 | 290.25 | 291.75 | 290.15 | 290.05 |
| 302.3 | 302.95 | 300.7 | 301 | 301.7375 |
| 307.8 | 307.8 | 307.55 | 305.7 | 307.2125 |

$$J(\omega) = (1 - S_f^2) \frac{\tau_f}{1 + (\omega\tau_f)^2} + S_f^2(1 - S_s^2) \frac{\tau_s}{1 + (\omega\tau_s)^2} \quad (5.33)$$

Where S_s^2 and S_f^2 are the order parameters and τ_s and τ_f are the correlation times for the slow and fast motions, respectively.

$$R_{1,DD} = \frac{1}{10} b^2 \{J(\omega_j - \omega_k) + 3J(\omega_j) + 6J(\omega_j + \omega_k)\} \quad (5.34)$$

$$R_{1,CSA} = \frac{2}{15} \omega_0^2 (\sigma_{11}^2 + \sigma_{22}^2 + \sigma_{33}^2 - \sigma_{11}\sigma_{22} - \sigma_{11}\sigma_{33} - \sigma_{22}\sigma_{33}) J(\omega_j) \quad (5.35)$$

$$R_{1\rho,DD} = \frac{1}{20} b^2 \{4J(\omega_1) + 3J(\omega_j) + J(\omega_j - \omega_k) + 6J(\omega_j) + 6J(\omega_j + \omega_k)\} \quad (5.36)$$

$$R_{1\rho,CSA} = \frac{1}{45} \omega_j^2 (\sigma_{11}^2 + \sigma_{22}^2 + \sigma_{33}^2 - \sigma_{11}\sigma_{22} - \sigma_{11}\sigma_{33} - \sigma_{22}\sigma_{33}) \{ (4J\omega_1) + (3J\omega_j) \} \quad (5.37)$$

5.5.6 Monte Carlo Error Analysis

Monte Carlo error analysis was performed on all of the relaxation rates in this chapter using *Matlab R2017a* in order to determine the errors with improved accuracy.

The relaxation rate and y -intercept of each measurement was used to re-plot the relaxation decay curve. Additional random error (calculated from the average noise in the spectra) was added to each data point in the decay. Based on the new data points (with the random error) a new relaxation rate was calculated from the exponential decay of the graph. This process was repeated 1000 times. The standard deviation of these 1000 rates is the error.

Chapter 6

Investigating the Effects of “Antifreeze” Molecules on Ice Growth Using Solid-State NMR

All of the work presented in this chapter is in collaboration with Alice Fayter, supervised by Professor Matthew I. Gibson (Department of Chemistry, University of Warwick). The PVA samples were synthesised by Christopher Stubbs and the AFPs by Alice Fayter and Dr Muhammad Hasan (also supervised by Professor Gibson).

6.1 Abstract

Antifreeze (glyco)proteins facilitate the survival of a diverse range of organisms. These proteins and their synthetic mimics have many vital applications throughout science and engineering, but their mechanism of action is still unknown. Antifreeze molecules cause changes to the freezing point and structure of water that are reflected in the motion of the water molecules. In this chapter, solid-state NMR relaxation measurements are used to investigate the proton dynamics and exchange within ice in the presence of antifreeze (glyco)proteins and their synthetic mimics. The measured relaxation rates clearly show that the addition of small amounts of antifreeze to water (0.1 % w/w) have a dramatic influence on both the slow (ms - ns) and fast (ns - ps) ice dynamics. Together, 2D EXSY spectra and relaxation measurements revealed that both AFGP and AFP I bind to ice reversibly, whereas AFP III binds irreversibly. Furthermore, the measurements presented here indicate that the two synthetic antifreezes, PVA and safranin, reversibly bind to ice and may be undergoing a similar mechanism to that of the AFGP. These relaxation measurements were conducted on PVA samples of different chain lengths; the polymers with < 20 repeat units did not change the ice dynamics, supporting the current literature on the effect of PVA chain length on antifreeze activity.²²⁹

6.2 Introduction

If a substance exhibits antifreeze activity it changes the properties of water in such a way as to alter and, under particular conditions, prevent ice crystal growth. These

“antifreezes” can be divided into two categories: colligative, the antifreeze effect occurs because of the sheer concentration of solute, and non-colligative, the antifreeze effect is caused by some physical or chemical property of the solute. Antifreezes have many applications in everyday life and across science and technology, such as preventing ice formation on roads and improving the cryopreservation of tissue and cells.^{230,231}

Most well-known antifreezes are colligative, such as NaCl or glycerol. Despite their considerable ability to suppress the freezing point of water, colligative antifreezes are often unsuitable for many systems. Critically, they are most effective when highly concentrated (see Table 6.1), making them unsuitable for biological systems due to the osmotic shock on cells. Additionally, some of these antifreezes can be toxic, for example, ethylene glycol, or corrosive, for example, high concentrations of NaCl(aq).²³² For these reasons there is an increasing interest in non-colligative antifreezes, in particular, for use in biological systems.

Despite the many antifreeze proteins (AFPs) and antifreeze glycoproteins (AFGPs) found in nature, little is known about the mechanism of these non-colligative antifreezes. In fact, there is currently no unified hypothesis for their mechanism of action. These proteins are highly effective antifreezes at very low concentrations, however producing large quantities of them is extremely challenging and costly. Thus the development of synthetic analogues is very valuable. Currently only a handful of synthetic mimics of AFPs and AFGPs have been found: a polymer (polyvinyl alcohol),^{229,237,238} a dye molecule (safranin chloride),²³⁹ two metallic salts (zirconium acetate and zirconium acetate hydroxide),^{240–243} particular metalloheliices²⁴⁴ and, most recently, monomolecular sheets of graphene oxide.²⁴⁵

In this chapter, SSNMR relaxation measurements are used to determine the dynamics of the water molecules in frozen solutions of AF(G)Ps, polyvinyl alcohol and safranin chloride with the aim of enhancing the understanding of non-colligative antifreeze effects and shedding light on a possible mechanism.

6.3 Terminology

Before discussing potential mechanisms of non-colligative antifreezes and how SSNMR relaxation measurements can aid this investigation, several terms, concepts and laws

Table 6.1: Examples of common colligative antifreezes, their ability to suppress the freezing point of water, the concentration required to achieve this suppression and examples of their uses.

| Colligative Antifreeze | Maximum Suppression of Freezing Point (°C) | Concentration (% w/w) | Example Application |
|---------------------------------|---|------------------------------|------------------------------------|
| NaCl ²³³ | -21.2 | 23.2 | Roads |
| Glycerol ²³⁴ | -46.5 | 66.7 | Enzymatic Cryoprotectant |
| Ethylene Glycol ²³⁵ | -49.0 | 58.0 | De-Icing Aircraft & Windscreens |
| Propylene Glycol ²³⁶ | -60.0 | 60.0 | Radiators |

must be defined.

Hexagonal Ice (I_h): The phase of ice is dependent on temperature and pressure. Under the conditions in the following experiments water will form hexagonal ice (structure presented in Figure 6.1).²⁴⁶

All further mentions of “ice” in this chapter are specifically referring to hexagonal ice.

Ice Planes: Hexagonal ice has various planes that antifreezes may interact with, the most commonly mentioned planes in this chapter (basal, primary prism, secondary prism and pyramidal) are illustrated in Figure 6.2.

Blagden’s Law: This law states that freezing point depression in dilute solutions is proportional to the concentration and thus can be used to calculate the kinetic (i.e. colligative) effects of a solute on the freezing point.²⁴⁹

$$\Delta T_F = K_F \cdot b \cdot i \quad (6.1)$$

Where ΔT_F is the change in freezing point due to the presence of colligative antifreeze in the solution, b is the molarity, i is the Van ’t Hoff factor and K_F is the cryoscopic constant of the solvent:

$$K_F = R \cdot T_F^2 \cdot \frac{M}{\Delta H_F} \quad (6.2)$$

Where R is the gas constant, M is molar mass of the solvent and ΔH_F is the heat of fusion per mole of water.

Colligative Antifreeze: An antifreeze that lowers the freezing (and melting) point of water according to Blagden’s law (Equation 6.1), i.e. in proportion to the concentration of solute particles.

Non-Colligative Antifreeze: An antifreeze that depresses the freezing point of water significantly more than predicted by Blagden’s Law at very low concentrations.

From this point onwards “antifreeze” is used to mean “non-colligative antifreeze”, the focus of this project.

Thermal Hysteresis (TH): A kinetic effect that causes a difference between the melting and freezing points of water, known as the thermal hysteresis gap. If a solution is held at a temperature within this TH gap, any nucleated ice crystals will neither grow nor melt. TH is only seen in some non-colligative antifreeze solutions.

Ostwald Ripening: A thermodynamically driven process whereby smaller crystals melt into the bulk water at the expense of the growth of larger, more energetically favourable, crystals (see Figure 6.3).

Ice Recrystallisation Inhibition (IRI): The ability of an antifreeze to slow or stop the growth of an ice crystal, first demonstrated by Knight *et al.* in 1988.^{250,251} (Note that this is different to inhibiting ice crystal nucleation or reducing the freezing point of

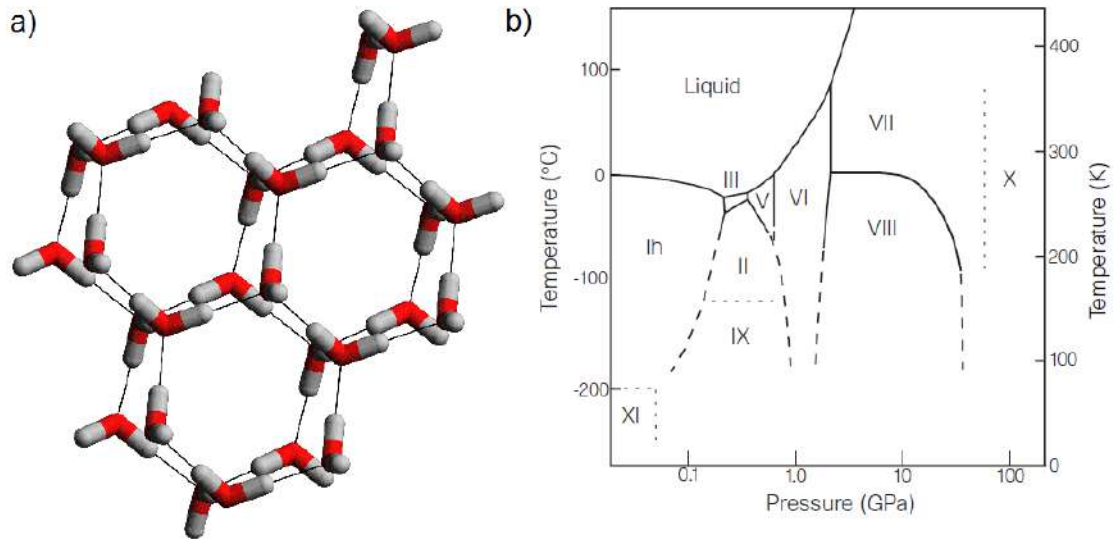


Figure 6.1: a) The structure of hexagonal ice. b) The temperatures and pressures required for some of the phases of ice from Lobban *et al.*²⁴⁷

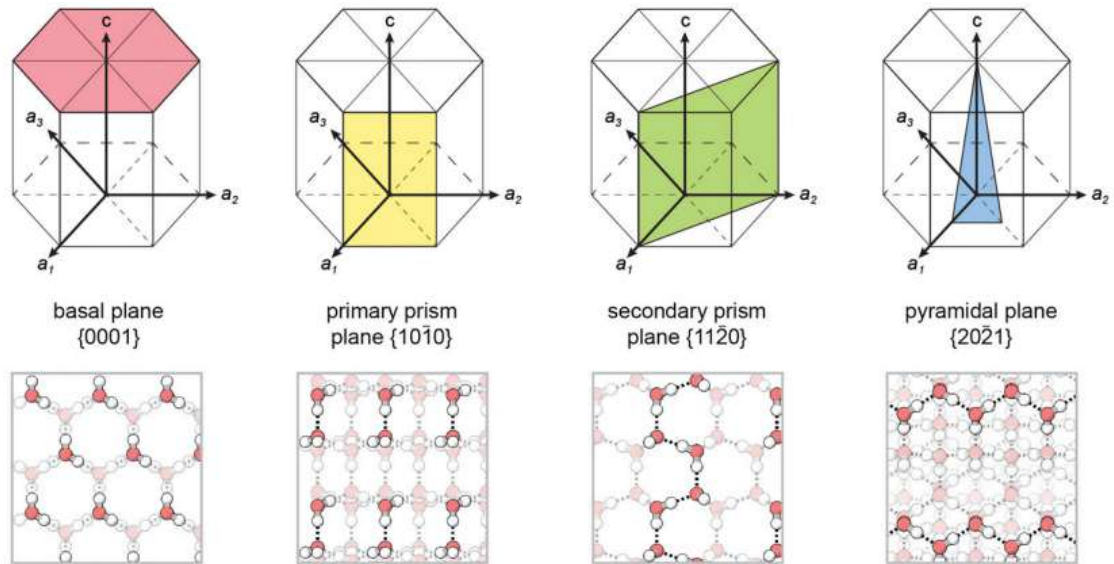


Figure 6.2: Planes of hexagonal ice that antifreezes commonly interact with. Adapted from Olijve *et al.*²⁴⁸

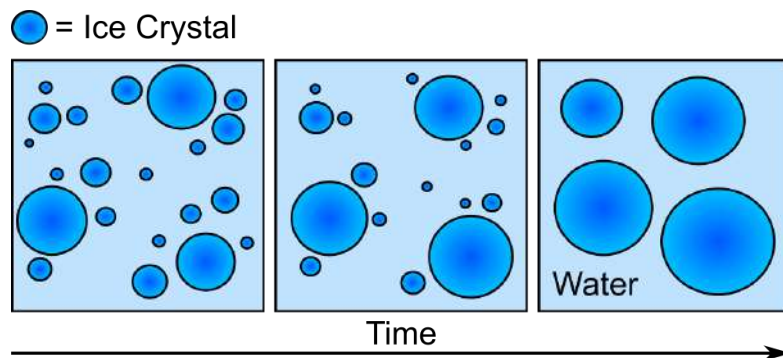


Figure 6.3: The process of Ostwald ripening, which minimises the energy of the system.

the solution.) IRI is important for biological applications because ice recrystallisation is associated with structural damage of cells and dehydration of tissues surrounding the ice.

Dynamic Ice Shaping (DIS): The ability of an antifreeze to influence the shape of an ice crystal, due to it interacting with, and therefore inhibiting ice growth at, specific ice planes (see Figure 6.4 for examples). This usually happens close to the freezing point and only below the TH gap. In certain cases DIS can be problematic; for example, growth of needle-like ice crystals can puncture and damage cells.

Quasi-Liquid Layer (QLL): It is proposed that instead of an abrupt water-ice interface, there is a 10 - 15 Å wide region between the ice surface and bulk liquid in which the ice structure gradually decreases until it becomes bulk water (Figure 6.5). In this region, known as the quasi-liquid layer, molecules are neither part of the rigid ice layer nor the bulk water.²⁵³⁻²⁵⁶

6.4 Literature Review

The study of how polar fish survive in water at temperatures as low as -1.9°C revealed that their ability to cope could not solely be explained by the high levels of dissolved solutes in their blood. DeVries and Wohlschlag determined that AFPGs were responsible for the remaining freezing point depression, despite their relatively low concentration.²⁵⁷ Since this initial discovery, similar AFPs and AFPGs have been discovered in a wide range of fish, insects, plants and bacteria that rely on these proteins to survive in extremely cold habitats.^{230,232,258-262} Interestingly, many of these AF(G)Ps have evolved convergently,²⁶³⁻²⁶⁵ for example there is evidence of AFPs evolving independently at least four times in fish.²⁶²

Although the exact protein differs between organisms, there is little structural variation in AFPGs; all AFPGs are based on an alanine-alanine-threonine repeat unit with a disaccharide (galactose-*N*-acetylgalactosamine) replacing the hydroxyl group of each threonine (Figure 6.6). AFPGs can contain 4 to 50 repeats of this tripeptide, so are divided into 8 classes by mass from the heavier AFGP1s (up to 34 kDa) to the much smaller AFGP8s (down to 2.6 kDa).²³⁰ Normally, these proteins are found at concentrations of 4 - 50 mg/ml *in vivo*.²³⁰

AFPs were discovered shortly after AFPGs. They display similar antifreeze activ-

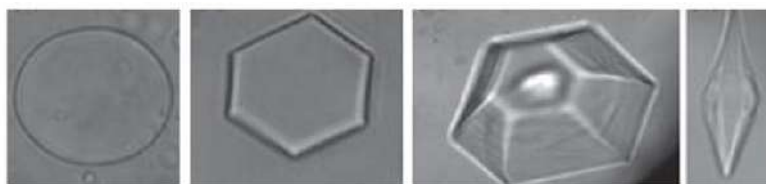


Figure 6.4: The image on the left is an ice crystal formed in pure water. The remaining images are all in the presence of an antifreeze protein and show evidence of dynamic ice shaping. Adapted from Gibson.²⁵²

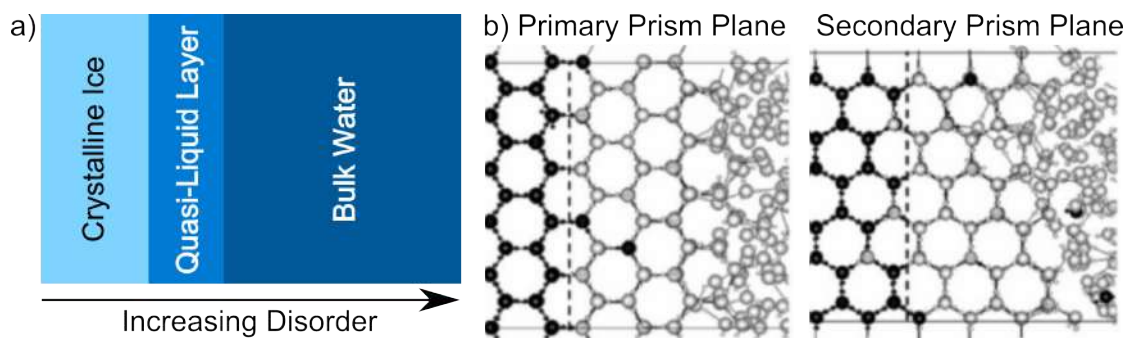


Figure 6.5: a) The semi-order quasi-liquid layer between the ice surface and bulk water. b) Snapshots from MD simulations of the ice/water interface at the primary and secondary prism planes, highlighting the presence of a QLL, adapted from Nada *et al.*²⁵⁶ The black and grey molecules show those that originated in ice and liquid water, respectively, at the start of the simulation.

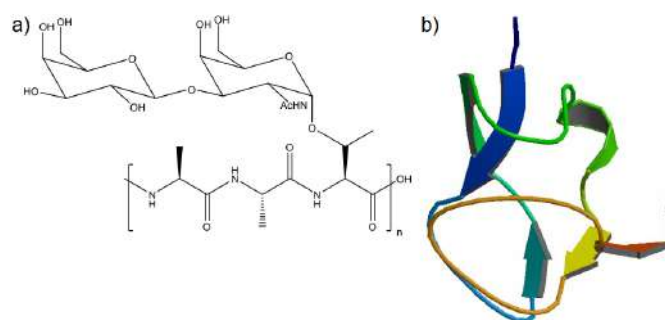


Figure 6.6: a) The general AFGP structure showing the Ala-Ala-Thr repeat unit with the disaccharide galactose-*N*-acetylgalactosamine attached to each Thr. b) An example of an AFGP (from the ocean pout). (Structure “1MSI” from the protein data bank).

ity, however are found in a much wider range of organisms and the variation in structure is rather more extensive (see Figure 6.7). AFPs are divided into six classes based on their secondary structure: AFP I-IV, plant AFP and insect AFP. These can vary from a 3 kDa single stranded α -helix type structure to small globular proteins with molecular weights of up to 24 kDa. The primary structure of all AFPs largely consists of many alanines alongside threonines, asparagines and glutamates.

6.4.1 Binding Sites of AF(G)Ps

Despite a lack of agreement on a unified “antifreeze mechanism” for AF(G)Ps, it is generally well accepted that an ice-binding site (IBS) is critical. Mutagenesis studies in various species of AF(G)P have identified that the IBS will typically consist of many aligned threonine or polar residues on one side of the protein. These regularly-spaced residues are organised in such a way that they align with the crystal structure of ice or can organise water molecules so that they replicate the structure of ice. Due to the huge variation in AF(G)P structure, it is unsurprising that the size of the IBS and the specific residues involved, as well as the particular plane of ice that the protein binds to do vary between proteins. Examples of AFPs and their ice-binding plane(s) are provided in Table 6.2.

It is proposed that an effective IBS must have relatively rigid sidechains, required for the ice-binding, and a reasonably flat surface to maximise the ice-IBS contact. Examples of such AFP IBSs are illustrated in Figure 6.8 from Oude Vrielink *et al.*²⁶⁰ and Davies *et al.*²⁷³

The regularly ordered threonine sites on these AFPs form a lattice of repeating units with similar dimensions to planes of hexagonal ice. Initially it was believed that hydrogen bonding, between the hydroxyl groups of the threonines and ice, was critical for the AF(G)P-ice interactions,^{274,275} yet this has been disputed more recently.^{276–278} Modelling experiments have shown that the number of hydrogen bonds present in these systems are insufficient to bind the protein to the ice surface as tightly as it actually

Table 6.2: Examples of AFPs with their structures and the ice planes they bind to.

| AFP | Type | Size (kDa) | Structure | Bound Ice Plane | PDB | Reference(s) |
|-----------------|---------------|------------|--------------------------------------|---------------------------|------|--------------|
| Winter Flounder | AFP I | 6.5 | α -helical | Pyramidal | 1WFA | 250, 266–269 |
| Alaskan Plaice | AFP I | 7.0 | β -strands & α -helices | Pyramidal | 2MSI | 266 |
| Sculpin | AFP I | 3.0 | α -helical | Secondary Prism | 1Y03 | 266 |
| Herring | AFP II | 14.0 | β -strands & α -helices | Non-Basal | 2PY2 | 258 |
| Ocean Pout | AFP III | 7.0 | β -strands & α -helix | Primary Prism & Pyramidal | 1AME | 270 |
| Snow Flea | <i>sf</i> AFP | 6.5 | Polyproline type II | Primary Prism & Basal | 2PNE | 271 |
| Spruce Budworm | <i>cf</i> AFP | 12.0 | β -solenoid | Primary Prism & Basal | 1M8N | 272 |

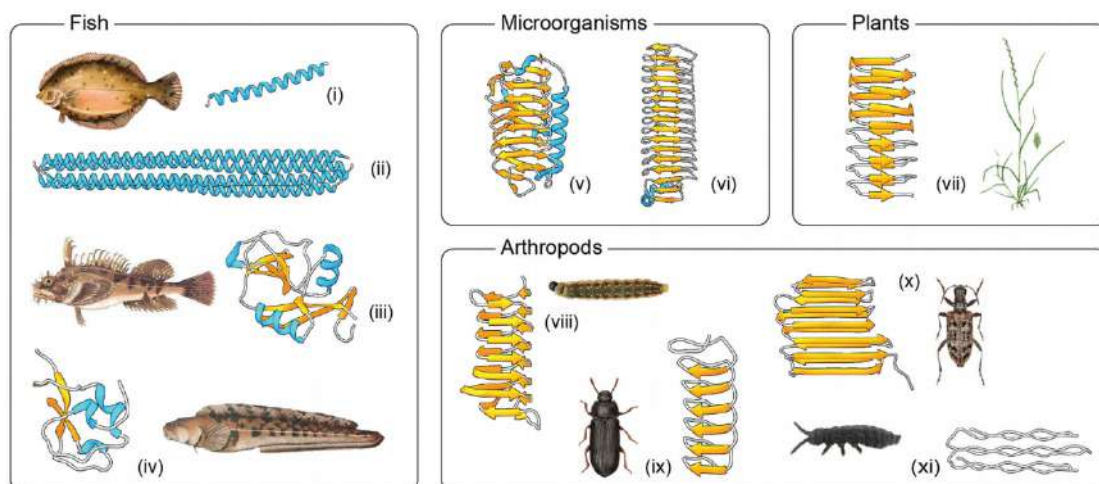


Figure 6.7: Examples of AFPs from a range of organisms highlighting the diversity in size and structure of the proteins from Oude Vrielink *et al.*²⁶⁰ (i) Type I wfAFP from winter flounder, (ii) type I hypAFP1 from winter flounder, (iii) type II hAFP from herring, (iv) type III opAFP (HPLC12) from ocean pout, (v) TisAFP6 from gray snow mold fungus, (vi) MpAFP from an Antarctic bacterium, (vii) LpAFP from winter ryegrass, (viii) sbwAFP from spruce budworm, (ix) TmAFP from mealworm beetle, (x) RiAFP from ribbed pine borer, and (xi) sfAFP from snow flea. α -helices are indicated in cyan, β -sheets in orange and coils in grey.

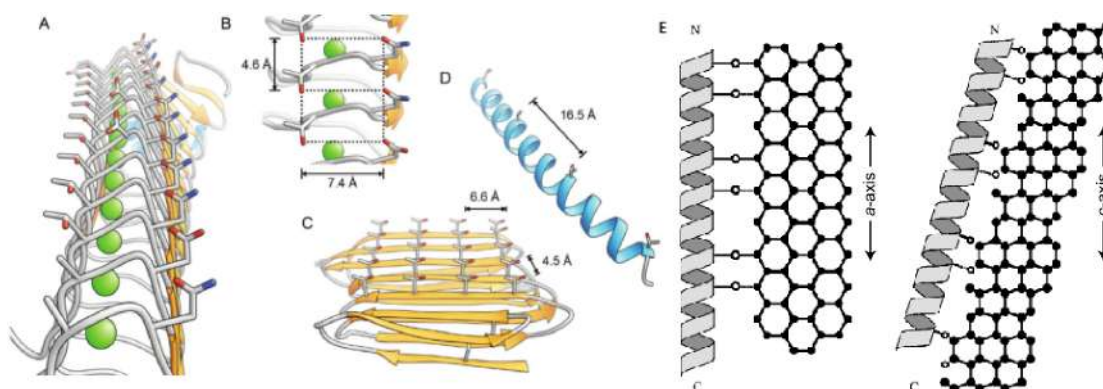


Figure 6.8: a) and b) show the IBS of *marinomas primoryensis* AFP (bacterium), c) the IBS of *rhagium inquisitor* AFP (beetle) and d) the IBS of winter flounder AFP. In each case the distances between the regularly ordered threonine, asparagine or aspartic acid residues are noted. Adapted from Oude Vrielink *et al.*²⁶⁰ e) Possible methods of the winter flounder AFP binding to the primary prism or the pyramidal plane of ice. Adapted from from Davies *et al.*²⁷³

is, suggesting that non-polar interactions were equally important.²⁷⁶ Further research found that the sidechain flexibility also plays an important role.^{276,279,280} Interestingly, mutagenesis studies show that replacement of a threonine (on the IBS of winter flounder AFP) with a serine causes a significant decrease in TH activity, while mutating the threonine to valine had a minimal effect.^{276,281} This shows that the hydrophobic group is critical for the function of this AFP, whereas the hydroxyl group isn't as important as initially thought.

Since AFGPs have a different structure to AFPs, typically a 3-fold helix with a disaccharide attached to every third residue (see Figure 6.6),²⁸² it is reasonable to believe that these proteins may have considerably different ice-binding sites and antifreeze mechanisms. The disaccharides are aligned along one face of the protein providing potential hydrophilic interactions with the ice surface. On the other side of the protein, the alanine residues form a hydrophobic surface which may block access to the ice surface for growth. NMR relaxation measurements revealed that the hydrophobic side of the disaccharide has a preferential interaction with the protein backbone, leaving the hydrophilic sites facing out from the protein and able to interact with ice.²⁸²

Over the years a range of structural modifications on the disaccharide groups of AFGP have been tested for TH activity.²⁸³ Key findings show that particular hydroxyl groups are critical for TH activity while others are not.^{284,285} The same studies proved that an AFGP dimer (MW = 1.2 kDa) will display antifreeze activity, but that AFGPs of above 5 tripeptide repeat units gave was no further increase in TH activity.²⁸⁵ Rao *et al.* suggested that the differences seen in the activities of AFGP types 1-4 were not due to conformation, but instead dependent on the length of the protein.²⁸⁶ Many potentially critical aspects of AFGPs still remain unknown, such as the number of hydroxyl groups and their stereochemistry required for IRI activity.²⁸³

AF(G)Ps Binding to Particular Ice Planes

Dynamic ice shaping is a by-product of an AF(G)P binding to ice. The affinity of different proteins for particular ice planes leads to variations in this DIS. Optical or fluorescence microscopy is often used to view the DIS and aid the determination of the ice plane(s) that the protein has bound to. In pure water (or in the presence of colligative antifreezes) flat disks of ice will form, whereas the presence of an AF(G)P can cause the growth of hexagonal or bipyramidal structures.^{84,232,258,269,283} For example, bipyramidal shaped ice crystals show that the protein binds to the prism planes foremost. This allows ice growth to continue on the basal planes, producing a new prism plane. As this process repeats, the surface area of the basal plane is reduced at each step and the crystals slowly narrow into bipyramidal needles (illustrated in Figure 6.9).^{252,274,287}

Ice growth and etching experiments are used to clearly indicate the ice plane(s) that a particular AF(G)P is bound to: Ice hemispheres are grown in the presence of the protein, this is followed by partial sublimation which leaves "etches" where the protein has bound to the ice. An example of such an experiment for the *sbw*AFP is presented in Figure 6.10a, it is clear that the protein is binding to both the prism and basal ice

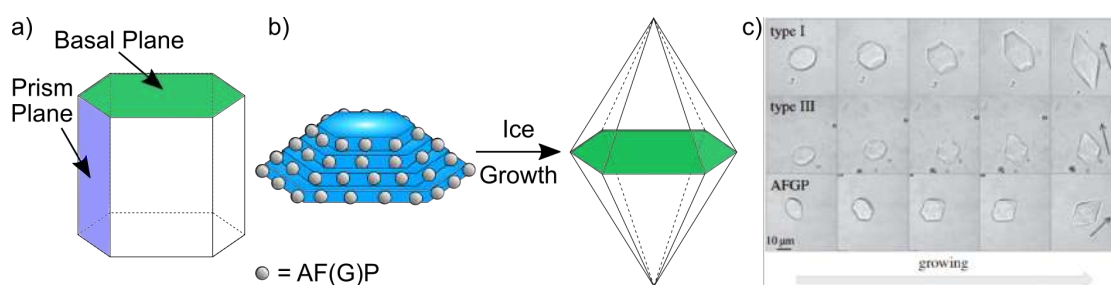


Figure 6.9: a) Illustration of the basal and prism planes in hexagonal ice. b) AF(G)P can bind to the prism plane allowing ice growth to continue on the basal plane. This process repeats causing the ice crystal to adopt a bipyramidal shape. c) Images of the DIS caused by the binding of various types of AF(G)P within the TH gap adapted from Bar-Dolev *et al.*²⁵⁹ the images were taken starting at T_m (left) and decreasing to 0.01 - 0.1°C below it. The arrow indicates the direction of the c-axis.

plane. Further analysis revealed that the prism and basal planes of ice in fact have a very similar arrangement of oxygen atoms (see Figure 6.10b).²⁷² This introduces the concept that an AF(G)P can bind to more than one plane.

Initial studies on AFP III (from Antarctic eel pout) suggested that this protein binds solely to the primary prism plane,^{250,288} however more recently fluorescence tagging, etching and mutagenesis studies have revealed that it also binds to the pyramidal plane.^{270,289} Results like these start to suggest that many AF(G)Ps which have been shown to bind to a single ice plane could in fact bind to multiple ice planes.

6.4.2 Is AF(G)P-Ice Binding Reversible?

This is an extremely important and largely unanswered question, the solution to which would provide many clues towards an ice-AF(G)P mechanism. The initial model for the antifreeze effect of ice, the adsorption-inhibition model, assumes that the protein irreversibly adsorbs onto the ice surface (see Section 6.3).²⁸⁷ Over the years, various pieces of evidence for both reversible and irreversible binding on a range of AF(G)Ps have been reported, leading to the proposal of new mechanisms involving irreversible binding. The possible mechanisms are discussed in Section 6.4.3, but first the evidence for reversible and irreversible binding will be reviewed.

Irreversible Ice Binding

At first glance it seems logical that the binding must be irreversible to prevent ice growth: The ice crystals are surrounded by a huge excess of super-cooled water molecules, thus desorption of a protein molecule from the ice surface would expose this site and allow the water to instantly join the ice lattice, thus the ice growth would continue.²⁹⁰ Various research groups provide evidence for AFPs irreversibly binding to ice, such as the incorporation of the protein molecules into the growing ice front.^{261,287,291-293} Fluorescence microscopy combined with microfluidics has revealed that AFP III and (high and low molecular weight) AFGPs bind irreversibly to ice and do not return to the solution.^{290,294-296}

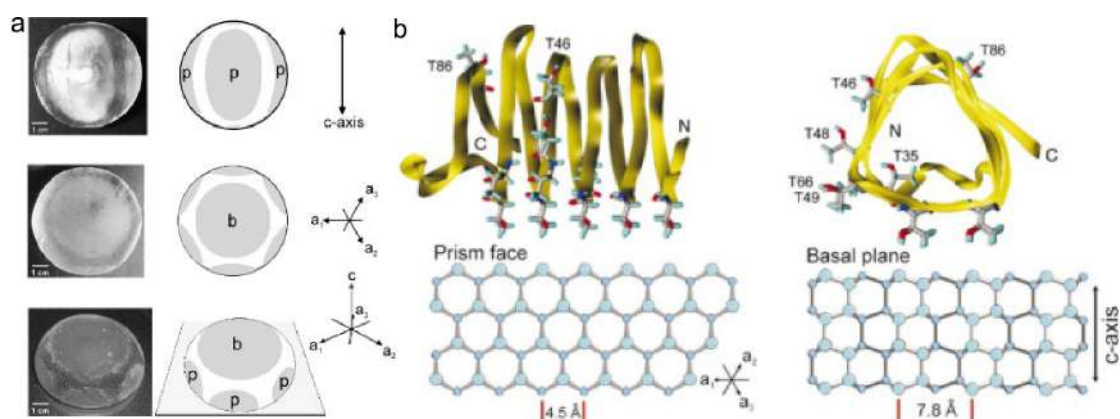


Figure 6.10: a) Photographs and illustrations of ice etching experiments by Graether *et al.* showing that the spruce budworm AFP binds to both the prism and basal planes of ice.²⁷² b) Illustration of how the *sbw*AFP can bind to both of these planes of ice due to the regularly spaced threonines aligning with the oxygens in the ice. Adapted from Graether *et al.*²⁷² The threonines are indicated on the protein structures and the ice structures are represented as a lattice of oxygen atoms.

Reversible Ice Binding

In 2008, Zepeda *et al.* presented imaging and protein distribution calculations that showed no evidence of AFGP within the ice crystals, supporting reversible adsorption. Furthermore they presented images showing the desorption of AFGP from an ice plane and continued ice growth in that direction (Figure 6.11).²⁹⁷ Evidence of an AFP reversibly adsorbing comes from SSNMR measurements showing exchange of *wf*AFP between solution and the ice surface.^{298,299}

6.4.3 Proposed Mechanisms for the Antifreeze Effect(s) of AF(G)Ps on Ice

Over the last 50 years various mechanisms have been proposed for the effect of AF(G)Ps on ice, but no single mechanism has been agreed upon to date. Of course, it is possible that there might be a variety of mechanisms at work for the different proteins. A selection of the more popular mechanisms are reviewed below.

The Adsorption-Inhibition Mechanism:

For a long time the adsorption-inhibition mechanism, published by Raymond and DeVries in 1977,²⁸⁷ was generally accepted,^{278,299–302} but more recently this mechanism has been criticised due to new evidence of irreversible ice binding. This model states that after the antifreeze has bound to the ice surface, the ice continues to grow between the protein molecules with a high surface curvature. There is now a high energetic cost of adding a water molecule to this convex ice surface (due to the Gibbs-Thomson or Kelvin effect), causing non-equilibrium freezing point depression (Figure 6.12).^{230,287,303,304} Ice growth will only resume if the temperature decreases further.

Early static models for ice growth in the presence of AF(G)Ps based on this mechanism are the “mattress model”^{230,266} and the “step pinning model”^{230,266,303,306,307}

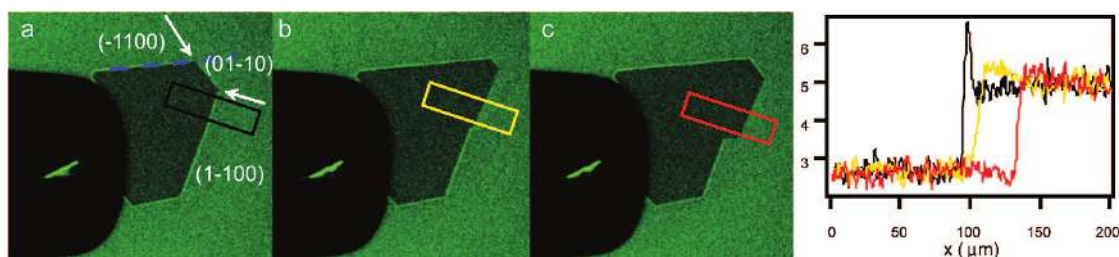


Figure 6.11: Evidence of reversible ice binding adapted from Zepeda *et al.*²⁹⁷ showing confocal images of an ice crystal with AFGP adsorbed onto particular planes. Images b and c were taken 4 and 9.6 seconds after image a. The arrows in image a indicate an ice plane where a new surface of AFGP has just formed (01-10). Image b and c show ice growth in a new direction (1-100) after desorption of the protein. The plot shows the AFGP intensity in the rectangles highlighted in the images. The black line indicates the significantly higher concentration of protein on the ice plane before it desorbs (b, yellow line) and the ice growth continues (c, red line).

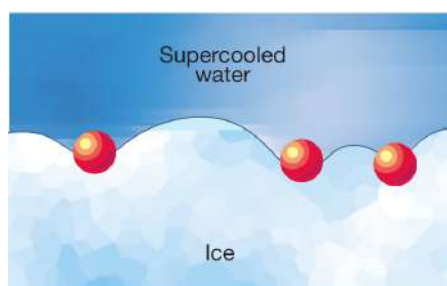


Figure 6.12: The adsorption-inhibition mechanism from Knight.³⁰⁵ After AF molecules have bound to the ice surface, ice growth continues in the gaps between the protein molecules for a short while until the curvature of the ice surface makes it energetically unfavourable for water molecules to join the ice lattice.

(see Figure 6.13). The mattress model is a 2D model whereby the AF molecules inhibit ice growth perpendicular to the surface, whereas the step pinning model is a 3D model where the AF molecules are adsorbed in a mono-step layer blocking the growth of that step. Kuiper and co-workers produced dynamics simulations of an insect AFP solution in the presence of ice that clearly showed the adsorption-inhibition mechanism in action, confirming that this species of AFP binds irreversibly to ice.²⁹³ However, these models are by no means perfect, mainly due to the growing evidence of reversible ice binding.^{230, 252, 297–301, 308}

The Two-Step Reversible Adsorption Mechanism:

Figure 6.11 shows that AFGP adsorption is not instant, in fact it takes several seconds to reach maximum coverage. Interestingly, after just a small portion of the protein molecules have adsorbed onto ice the surface there is no further ice growth, showing that maximum coverage is not required to halt the growth. Zepeda and co-workers proposed, based on their observations of the interactions between AFGPs (types 4-6) and ice, that initially a number of protein molecules strongly bind to the ice surface, halting the ice growth, after which further proteins continue to bind weakly.²⁹⁷

The reversible binding reported here shows that some of the proteins must be adsorbed weakly enough that the addition of water molecules to the ice plane can eject the protein molecules, allowing ice growth to continue where it was previously halted. This indicates that the AFGP-ice interactions are much weaker and more dynamic than originally predicted.^{297, 309}

The two-step reversible adsorption mechanism also considers the role of protein solvation and the QLL; AFGPs are highly flexible³¹⁰ and ice surfaces are highly dynamic, so a rigid match between these, such as the adsorption-inhibition mechanism, is a poor description of the antifreeze mechanism. A much more fitting mechanism is that the protein molecules disrupt the quasi-ordering of the surface liquid at the interface by purely kinetic effects.²⁹⁷ Measurements show that the solvation entropy can dominate the whole process³¹¹ and that both AGFP and AFP III reduce the surface free energy of the water which can be attributed to a significant increase in the thickness of the

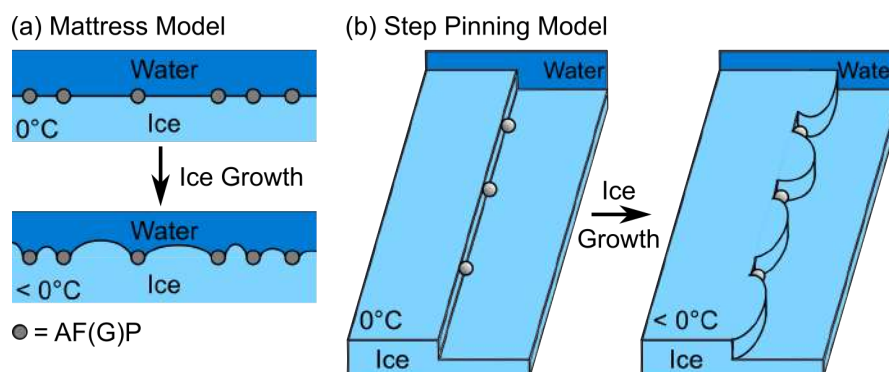


Figure 6.13: The (a) “mattress model” and (b) “step pinning model”, examples of adsorption-inhibition models for ice growth in the presence of AF(G)P.

QLL.^{297,312–314} This research acts as a reminder that it is critical to consider the protein solvation and QLL dynamics in an antifreeze mechanism, in addition to the structure of the protein and ice lattice.^{254,297,304,315}

The Anchored Clathrate Water Mechanism:

In 2008, the anchored clathrate water mechanism was proposed by Nutt and Smith to explain the interaction between ice, AF(G)Ps and their neighbouring water molecules.³¹⁶ In an AF(G)P solution, when the temperature becomes low enough, the water molecules in the solvation shell become more structured and less dynamic at the ice-binding site (Figure 6.14a). This ordered, ice-like region of water at the IBS now has a lower energy barrier for ice formation. When the protein approaches the ice and comes into contact with the QLL, the ordered waters at the IBS merge with the QLL (Figure 6.14b) facilitating local ice growth. If the growing ice surface is the correct plane and the protein is orientated favourably, then the ice growth will incorporate the IBS of the protein into the ice lattice (Figure 6.14c).^{258,316} The hydrophilic surface of the non-IBS disrupts the solvent shells in order to prevent the protein being fully surrounded by ice,^{316,317} highlighting that the non-IBS could play a crucial role in the antifreeze effect of AF(G)Ps.^{258,261}

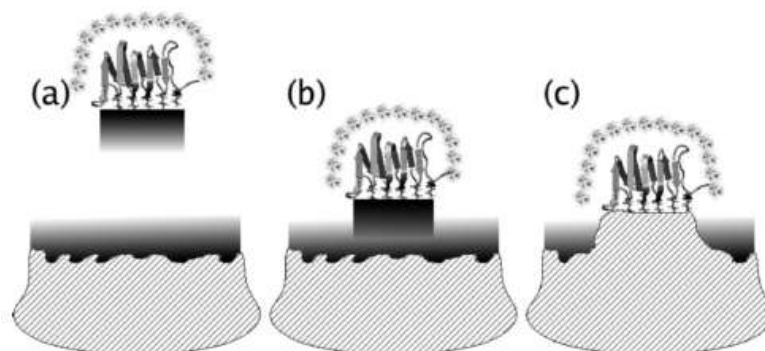


Figure 6.14: The anchored clathrate water mechanism from Nutt and Smith.³¹⁶ Ordering at the ice-water and protein-water interfaces is indicated by shading (black represents more structured water and white less structured water). The figure shows, a) the protein with ordered ice-like water molecules at the ice-binding site, b) the protein approaching the ice surface causing the ordered regions of water to overlap and c) the local ice growth incorporating the IBS of the protein into the ice plane.

Several studies, using a combination of x-ray diffraction (XRD) and computational simulations, have revealed clathrate waters at the ice-binding sites of AFPs.^{268,318,319} These studies also revealed that the “maxi” AFP has at least 400 intramolecular ice-like water molecules that are critical for stabilisation and has ice-binding residues within the protein core, strongly supporting the anchored clathrate water mechanism.²⁶⁸

6.4.4 Research into Antifreeze Proteins and Ice by Solid-State NMR

Over the last 50 years, vast amounts of research have significantly broadened the understanding of AF(G)Ps and synthetic AFs. However there are still many unanswered

questions, mainly concerning a specific or general mechanism for how the AF-ice binding actually alters ice formation or growth. In the last 15 years a few research groups have used SSNMR as a tool to help answer some of these questions. Unlike many other analytical techniques, SSNMR can independently provide direct data on both the ice and the antifreeze bound to the ice. This provides great potential for characterisation of the ice-binding interface and furthers the understanding of the ice-binding mechanism.

Most of the SSNMR research into non-colligative antifreezes in the literature focuses on AFP III. McDermott and co-workers determined that the protons of AFP III are in exchange with the surrounding proton bath of ice through ^1H R_1 SSNMR measurements on this protein and ubiquitin (a negative control).³²⁰ Furthermore, cross-saturation experiments and R_2 measurements show that this protein establishes direct contact with ice and a partially-intact hydration shell (Figure 6.15 illustrates this proposed interaction).^{320,321} Finally, the ice-binding site of AFP III was confirmed by calculating the differences in ^{13}C chemical shift of the protein while in solution and while frozen.³²²

Exchange SSNMR measurements combined with specific ^2H labelling were used to investigate the ice-binding of a type I AFP revealing that this process is reversible.²⁹⁸ Lastly, a comparison of the type I AFP ^{13}C R_1 while frozen in either H_2O or D_2O showed that the energy barrier for reorientation of frozen water molecules neighbouring the active site was only 17.1 kJmol^{-1} compared to 55.8 kJmol^{-1} for pure hexagonal ice. This indicates that water molecules in the protein-ice interface are far more dynamic than in the bulk ice.³²³

6.4.5 AFGP8, North Atlantic Pout AFP and Barfin Plaice AFP

Three different AF(G)Ps are investigated in this chapter alongside various synthetic mimics: AFGP8, North Atlantic Pout AFP (a type III AFP) and Barfin Plaice AFP (a type 1 AFP). From this point onwards these proteins will be referred to as AFGP, AFP III and AFP I, respectively. This AFGP is the smallest of the AFGPs, it is a 14 residue long alanine-rich protein. The AFP III is a 7.5 kDa protein that contains three β -strands and the AFP I is a 40 residue ($< 30 \text{ kDa}$) protein. The structures of the AFGP and AFP III are displayed in Figure 6.16 (the structure of the AFP I has not yet been

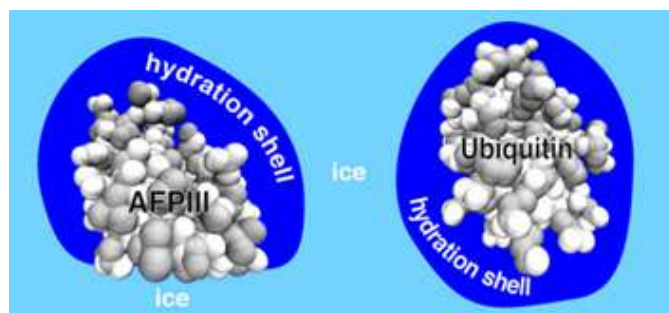


Figure 6.15: The interaction of AFP III with its hydration shell and ice (compared to ubiquitin) proposed by McDermott and co-workers.³²⁰

published).

6.4.6 Synthetic Antifreezes

AFPs and AFGPs are highly effective antifreezes at very low concentrations, however producing large quantities of these proteins is challenging, inefficient and costly (initially the proteins are exacted from fish, for example, and then replicated on a larger scale using genetically modified yeast), thus the development of synthetic analogues is extremely desirable. Currently only a handful of synthetic mimics of AF(G)Ps have been discovered and the research on these tends to be rather limited due to their recent discovery, for example, the first paper on graphene oxide as an antifreeze was published in 2017.²⁴⁵

Polyvinyl Alcohol (PVA)

In 2000, the antifreeze activity of polyvinyl alcohol (Figure 6.17), which has similar structural features to AFPs (hydrophobic and hydrophilic sides),¹³⁹ was first reported as a potential additive for use in ice-slurry cold-storage systems.²³⁷ Subsequently, the antifreeze effects of PVA have been thoroughly researched; it works effectively at concentrations as low as 0.005 mg/ml^{229,238} and shows some thermal hysteresis activity,³²⁴ but the link between its structure and antifreeze activity is still unknown. It has been demonstrated that PVA does enhance recovery in the cryopreservation of various cells, including human blood cells, and critically, PVA shows no signs of cytotoxicity at concentrations as high as 20 mg/ml.^{325–327}

Images of ice crystals grown in the presence of PVA clearly show that PVA can bind to the primary and secondary prism planes of ice, see Figures 6.18 e and f, respectively. Budke and co-workers suggested possible mechanisms for the PVA binding to these planes, based upon aligning every third hydroxyl group of PVA (7.56 Å) with every second oxygen atom in the ice lattice (7.36 Å), see Figures 6.18 i and j.²³⁸ Various research groups have shown that when the concentration of PVA is increased, the ice recrystallisation inhibition activity increases too (Figure 6.19).^{238,324,328,329}

Significant research has demonstrated that the PVA chain length (degree of polymerisation, DP) has a strong influence on the antifreeze activity; PVA with a DP ≥ 19 is required for an effective antifreeze (Figure 6.19b) and a higher DP reduces the concentration required for antifreeze activity.^{229,328,329} Vail and co-workers showed that a

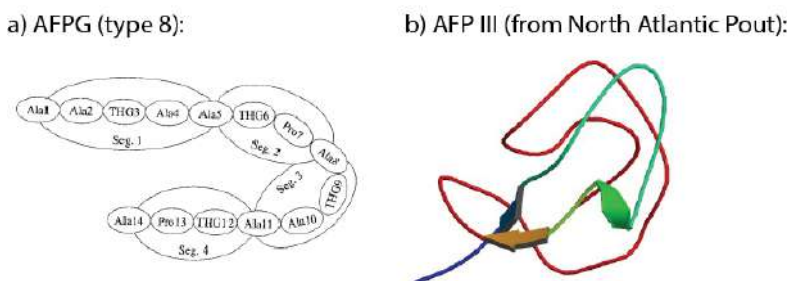


Figure 6.16: The structures of a) AFGP8 and b) AFP III (North Atlantic Pout) from the Protein Data Bank (PDB ID: 1KDF).

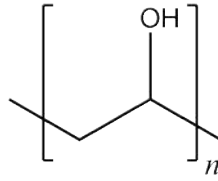


Figure 6.17: The structure of polyvinyl alcohol, where n is the number of repeat units.

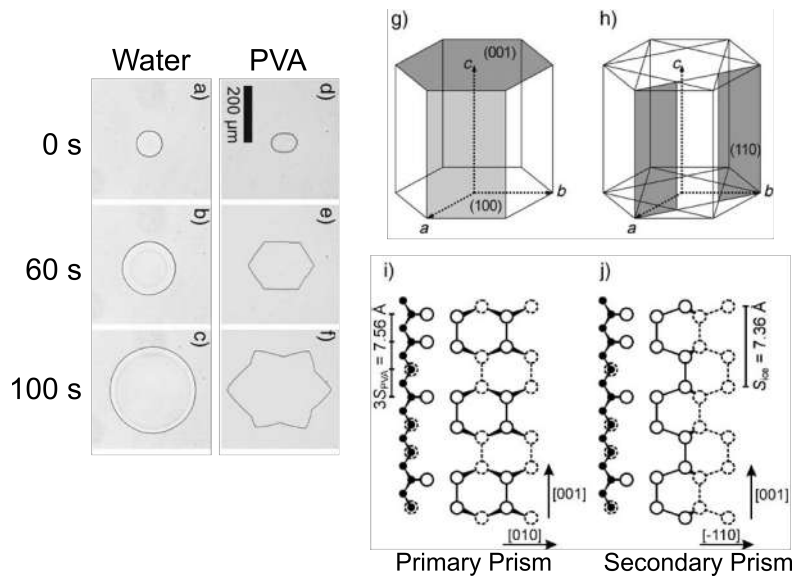


Figure 6.18: Images of ice crystals grown in pure water (a-c) and 10 mg/ml DP27 PVA (d-f), the primary (g) and secondary prism (h) planes of ice and the suggested mechanism of binding to these planes (i and j, respectively), where solid lines indicate oxygen atoms in the paper plane and dashed lines are 0.92 \AA behind. e) and f) demonstrate the effects of PVA binding to the primary and secondary prism planes, respectively. Adapted from Budke *et al.*²³⁸

PVA sample with the same DP but a lower dispersity can be significantly less active,³³⁰ hence it is also critical to take the polydispersity of the polymer into account.

Hydrophobicity is known to play a crucial role in IRI.^{332,333} Considering that acetate groups are more hydrophobic than hydroxyls, Gibson and co-workers investigated the antifreeze activity of copolymers of PVA and poly vinyl acetate;²²⁹ less than 20% acetylation was tolerated by the PVA and more than 25% produced an inactive polymer. Since additional hydrophobic groups reduced the IRI activity, the same measurements were conducted with the addition of hydrophilic groups (*N*-vinyl pyrrolidone), but these additions could also only be tolerated at low percentages. The results demonstrate that the antifreeze activity of PVA is not just due to the presence of hydrophobic or hydrophilic groups, but that the structure and orientation of the functional groups as well.

Safranin Chloride

In 2016 Drori *et al.* discovered that safranin chloride (referred to as “safranin” from here on) inhibited ice growth in a non-colligative manner.²³⁹ Safranin is a small dye molecule that aggregates in solution to form supramolecular stacks (see Figure 6.20a). In addition to this aggregation, the methyl groups, amine groups and the chloride ion all play an important role in the inhibition of ice growth.²³⁹ Drori *et al.* showed that safranin binds reversibly to ice crystals, which form hexagonal plates at lower concentrations (0.49 mg/ml) and bipyramidal needles at higher concentrations (9.82 mg/ml).

When safranin aggregates, the π - π interactions in the aromatic regions cause the molecules to form stacks with the phenyl groups on alternating sides (see Figure 6.20a). This results in rows of methyl and amine groups along two sides of the supramolecular stacks which seem to mimic the ice-binding sites found in AFPs. Crystal structures show that the gap between each molecule in the stack is 3.7 Å and, due to the alternating pattern in the stack, the distance between two amino groups is 7.4 Å, a good match with every second oxygen atom in the ice lattice (7.36 Å). This suggests that the pre-organisation of safranin molecules allows the amino groups in safranin to form hydrogen bonds along the primary or secondary prism planes of hexagonal ice, creating a crystal-ice interface.

Phenosafranin chloride (Figure 6.20b), which has the same structure as safranin minus the two methyl groups, exhibits no antifreeze activity demonstrating that the methyl groups are critical for the antifreeze activity of safranin. A comparison of the safranin and phenosafranin chloride crystal structures confirms that the latter does not form supramolecular stacks, which seem to be key for antifreeze activity. Next, the importance of the chloride ion was investigated through a comparison of safranin chloride and safranin nitrate (Figure 6.20c). Safranin nitrate showed no signs of antifreeze activity however, once sodium chloride was added to a safranin nitrate solution, antifreeze activity was observed due to the formation of safranin chloride. Again, a comparison of the crystal structures shows that, although some order is retained, the supramolecular stacks are no longer formed in the case of safranin nitrate, most likely due to the change

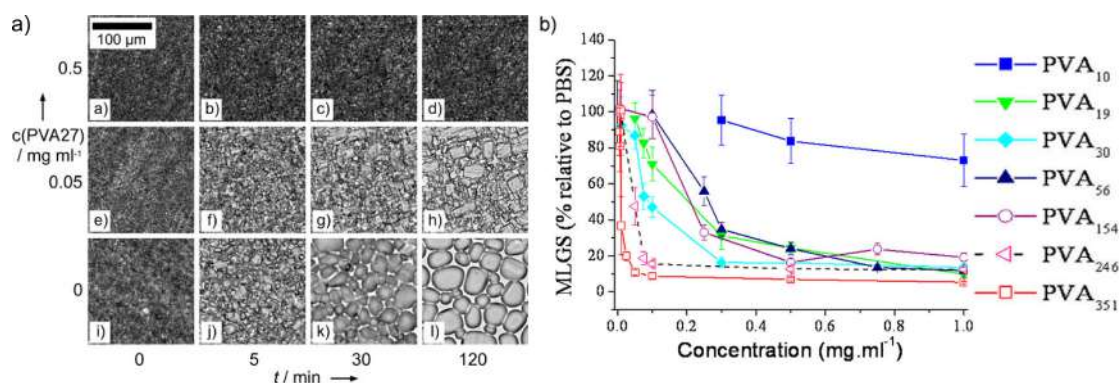


Figure 6.19: a) Splat images³³¹ compare the IRI activity of 0.05 and 0.5 mg/ml DP27 PVA with pure water by observing the size of the ice crystals over time. Adapted from Budke *et al.*²³⁸ b) The mean largest grain size (MLGS) of PVA of a range of DPs (10, 19, 30, 56, 154, 246 and 351) and concentrations (0 - 1 mg/ml) relative to a phosphate-buffered saline (PBS) control, highlighting that DP < 19 is relatively ineffective. Adapted from Congdon *et al.*²²⁹

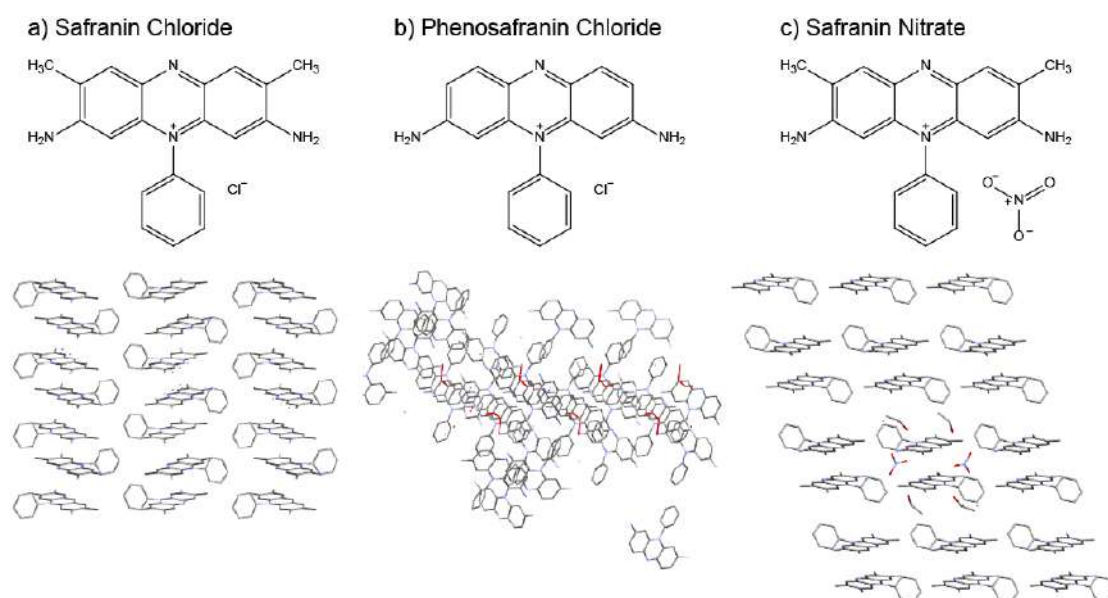


Figure 6.20: Chemical structures and crystal structures of a) safranin chloride, b) phenosafranin chloride and c) safranin nitrate. The crystal structures were obtained from the Cambridge Structural Database under the identifiers “YAGTOS”, “YAGTEI” and “YAGTIM” respectively.

in anion size.

Zirconium Acetate and Zirconium Acetate Hydroxide

Zirconium acetate and zirconium acetate hydroxide are two metallic salts which have IRI and DIS activity.^{240–243} Two ice-structuring mechanisms of these salts have been suggested, both involving the salt forming a hydroxy-bridged polymer-like structure with hydroxyl groups on one side and acetate groups on the other. Even though the exact mechanism is unknown, once again it is clear that there are important similarities between these synthetic analogues and the AF(G)Ps found in nature.

Graphene Oxide

Recently, graphene oxide (GO) has shown evidence of suppressing ice growth and restricting recrystallisation of ice crystals due to its hexagonal scaffold.²⁴⁵ In solution, GO forms monomolecular sheets with large oxidised regions containing hydroxyl and epoxy groups on the basal plane and carboxyl groups at the periphery of the structure. The repeating hexagonal carbon rings in the GO sheet cause any surface hydroxy groups to follow this honeycomb-like pattern which matches the structure of hexagonal ice (note the similarities to the IBSs of the antifreezes previously discussed).

Studies have shown that GO acts as an effective non-colligative antifreeze from concentrations of 0.1 - 5.0 mg/ml and that smaller sheets (10 nm) of GO were more effective than larger sheets (500 nm or 5000 nm). Molecular dynamics studies show that GO has a preference for binding to ice crystals rather than the surrounding liquid water and that a combination of hydrogen bonding and hydrophobic interactions are critical for the antifreeze activity displayed by GO.²⁴⁵ Furthermore, the viability of GO as a cryoprotectant was validated; 0.025 mg/ml GO gave similar results to that of 0.1 mg/ml PVA.²⁴⁵ Within the last year, several studies have shown that GO and carbon nanomaterials actually show evidence of ice nucleation activity which can be tuned by doping the surfaces.^{231,334–336} These are the first synthetic materials found to nucleate ice.³³⁷

Metallohelices

In 2017, Gibson and co-workers determined that various amphipathic, metallohelices inhibited ice growth at extremely low concentrations (20 μ M).²⁴⁴ Since AF(G)Ps and the other synthetic antifreezes discussed so far have a similar amphipathic structure, these results confirm that amphipathicity might be the key for antifreeze behaviour.

6.4.7 Negative Controls

Throughout this study, various negative controls are used to ascertain that results are due to the non-colligative effects of the antifreezes, and are not caused by simply adding a solute to the water (colligative effects). In particular, three negative controls are used to compare to the three different types of antifreezes that are being investigated in this study: phenosafranin chloride, polyethylene glycol (PEG) and lysozyme (Figure 6.21).

As already discussed, phenosafranin chloride (referred to as “phenosafranin” from

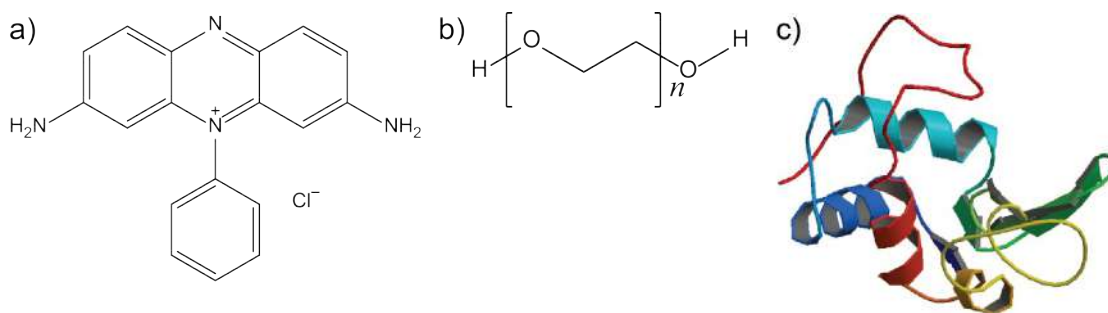


Figure 6.21: Structures of a) phenosafranin chloride, b) polyethylene glycol (PEG) and c) lysozyme, which are used as controls for safranin, PVA and the AF(G)Ps, respectively.

here on) has an extremely similar structure to safranin, however the literature shows that it affects neither ice crystal growth nor the morphology of the crystals.^{239,328} Lysozyme does not display any antifreeze behaviour and so will be used as a negative control for AF(G)Ps, and PEG has been used extensively as a negative control for PVA in the literature.^{238,238,239,329} In addition to checking the literature, splat assays³³¹ were conducted on the three negative controls to check for any non-colligative antifreeze activity.

6.4.8 Applications of AFPs, AFGPs and Synthetic Antifreezes

Non-colligative antifreezes have many applications across science and technology.^{230,232,258} Below, the importance of current and future uses is highlighted through examples in biomedical science, the agriculture and food industries and engineering.

Biomedical Applications

It is well known that there are thousands of people in the UK alone waiting for an organ transplant to change, and potentially save, their life. When a donor is found, currently an organ can only be stored for a handful of hours before the transplant must take place. Non-colligative antifreezes have the potential to decrease the storage temperature and therefore increase this storage time and improve the chances of a successful transplant.^{252,338,339}

This is just one of the many critical applications of research into the use of non-colligative antifreezes for the cryopreservation and hypothermic storage of cells,^{340–342} tissues,^{340,342–344} embryos^{345,346} and organs.^{340,343,347,348} Freezing can cause cellular damage by intracellular ice formation,^{345,349} ice recrystallisation,^{349,350} freeze-dehydration³⁴³ and mechanical stress,³⁴³ all of which can lead to cell death by apoptosis,^{344,351} cell rupture³⁵² or necrosis.³⁴⁷ Some common biomedical cryoprotectants that penetrate the cells, such as glycerol and DMSO, are effective, however they are far from ideal. These cryoprotectants do not fully protect the cells from damage, and in some cases they are toxic and therefore must be thoroughly removed from the cells before use.³⁴³ These problems have driven research into non-penetrating cryoprotectants, such as AFPs, AFGPs and their synthetic analogues.^{340,345,351}

Applications in the Agricultural and Food Industries

Foods can significantly deteriorate in quality throughout the process of freezing, thawing and any temperature fluctuations, thus non-colligative antifreezes have huge potential in the frozen food industry.^{258,353} One well-known example is the addition of AFPs to ice cream to reduce ice crystal size, helping to retain the creamy texture desired by consumers.^{354–356} Another example is the use of type I AFPs to treat thawed dough, improving the fermentation capacity.³⁵⁷ Additionally, AFGPs and AFPs have demonstrated the ability to reduce drip loss after thawing lamb meat and improve the nutritional value and texture of frozen meat and fish.^{354,358–360} In the future, antifreezes may allow the freezing of various foods, such as some berries, that cannot currently be frozen without significant deterioration in quality.²⁵⁸

Some species of crops have been genetically engineered to express AFGPs with the aim of improving cold hardiness. Freezing resistance in crops down to temperatures of -5°C or -6°C would provide significant protection during minor freezes in the spring or autumn, but so far freezing depression of a only few degrees has been managed.^{361–363}

Other Applications

Antifreezes can effect the growth and morphology of crystals (other than ice), which has led to their use as a gas hydrate inhibitor, a critical consideration for the petroleum industry.^{364,365} Interestingly, macroporous alumina ceramics have been fabricated through freezing with AFP to produce uniform pores.³⁶⁶ Finally, these proteins have been used in research on the icing of aircraft wings and the resulting aerodynamic performance.²³¹

6.5 Results

Antifreeze molecules alter the freezing point, structure and growth of ice, all of which are reflected in the dynamics of the water molecules. A high proportion of the literature is centred around the antifreeze molecules themselves, whereas this research focuses on the surrounding water molecules, aiming to bridge the gap between structure and mechanism. Here, variable temperature SSNMR relaxation measurements (R_1 , R_2 , $R_{1\rho}$ relaxation dispersion and 2D EXSY) are used to directly probe changes in the dynamics of the bulk water protons due to the addition of small quantities of non-colligative antifreezes.

It is likely that, rather than an abrupt antifreeze-ice interface, there are different regions of water or ice present, such as a QLL (see Figure 6.5). The water molecules may be exchanging between these regions, which will have different structures and dynamics, as well as binding and possibly unbinding to and from the additives. SSNMR relaxation measurements on the bulk water protons provide a population-weighted average of the molecules across these different regions of water and/or ice. A variety of pulse sequences under a range of conditions are used to extract as much information as possible on these motions and any exchange within the ice-antifreeze systems.

6.5.1 Variable Temperature ^1H R_1 of Ice in the Presence of Antifreezes

Spin-lattice relaxation (R_1) originates from local motions, such as rotations, which modulate anisotropic interactions (for example, chemical shift anisotropy and dipolar couplings). Motions on the nanosecond - picosecond timescale are most effective at modulating such interactions and therefore dominate the R_1 rates. Moreover, these rates have a negative quadratic relationship with the correlation time (see Figure 2.25), assuming a single motion dominates the relaxation process.

In order to access these relatively fast dynamics within the bulk ice of the frozen antifreeze solutions, variable temperature ^1H R_1 measurements were conducted using the saturation recovery method (Figure 6.22). Under these conditions there is most likely substantial ^1H - ^1H spin diffusion throughout the sample due to the dense ^1H network. This will result in averaging of ^1H R_1 across different sites. However it will not significantly affect these rate measurements since only the bulk water peak is observable, which is already a population-weighted average of all the water protons. Varying the temperature will slightly alter the correlation time, changing the measured R_1 . Ideally the chosen temperature range will include the maximum R_1 and the rates will show a clear quadratic relationship with temperature. Unfortunately, this is neither particularly predictable nor always possible. For example in these measurements on ice the temperature range is limited by the melting point of the sample and the cooling ability of the equipment. Nevertheless, a maximum was identified in the majority of the VT R_1 measurements presented here.

Firstly, the VT R_1 plots of ice in the presence of the polymers are considered, all of which display a reasonably clear maximum and fall into one of two categories (Figure 6.22a). Three of the samples (1.0 mg/ml DP8 PVA, 5.0 mg/ml DP8 PVA and 5.0 mg/ml DP9 PVA) show similar maxima at approximately -20.0°C , the magnitude of these rates is also very consistent. The PEG sample has a slightly shifted (-17.5°C) and marginally greater maximum. These maxima that are at relatively low temperatures indicate a higher correlation time for the motion dominating R_1 . On the other hand, the 5.0 mg/ml DP20 PVA and DP230 PVA show a significantly different trend; their R_1 maxima are considerably shifted to the left (-31.0°C and -33.5°C , respectively). Even without further analysis it is evident that the addition of high DP PVAs ($\text{DP} \geq 20$) to water leads to significantly different ns - ps dynamics in the ice compared to the control (PEG) and lower DP PVAs (8 and 9). It is worth noting that two of the solutions have a concentration of 1.0 mg/ml, whereas the remainder are 5.0 mg/ml. This slight discrepancy could be affecting the results, however a comparison of the 1.0 and 5.0 mg/ml DP8 PVA R_1 plots suggests that this change in concentration has minimal effect (at least in the case of low DP PVAs).

Next, these VT relaxation measurements were conducted on the bulk ice protons in frozen 1.0 and 5.0 mg/ml safranin and phenosafranin solutions (Figure 6.22b). In this case the variation in concentration did have a considerable effect on the rates of both samples. Unfortunately, only three of the four plots showed an obvious R_1 maximum

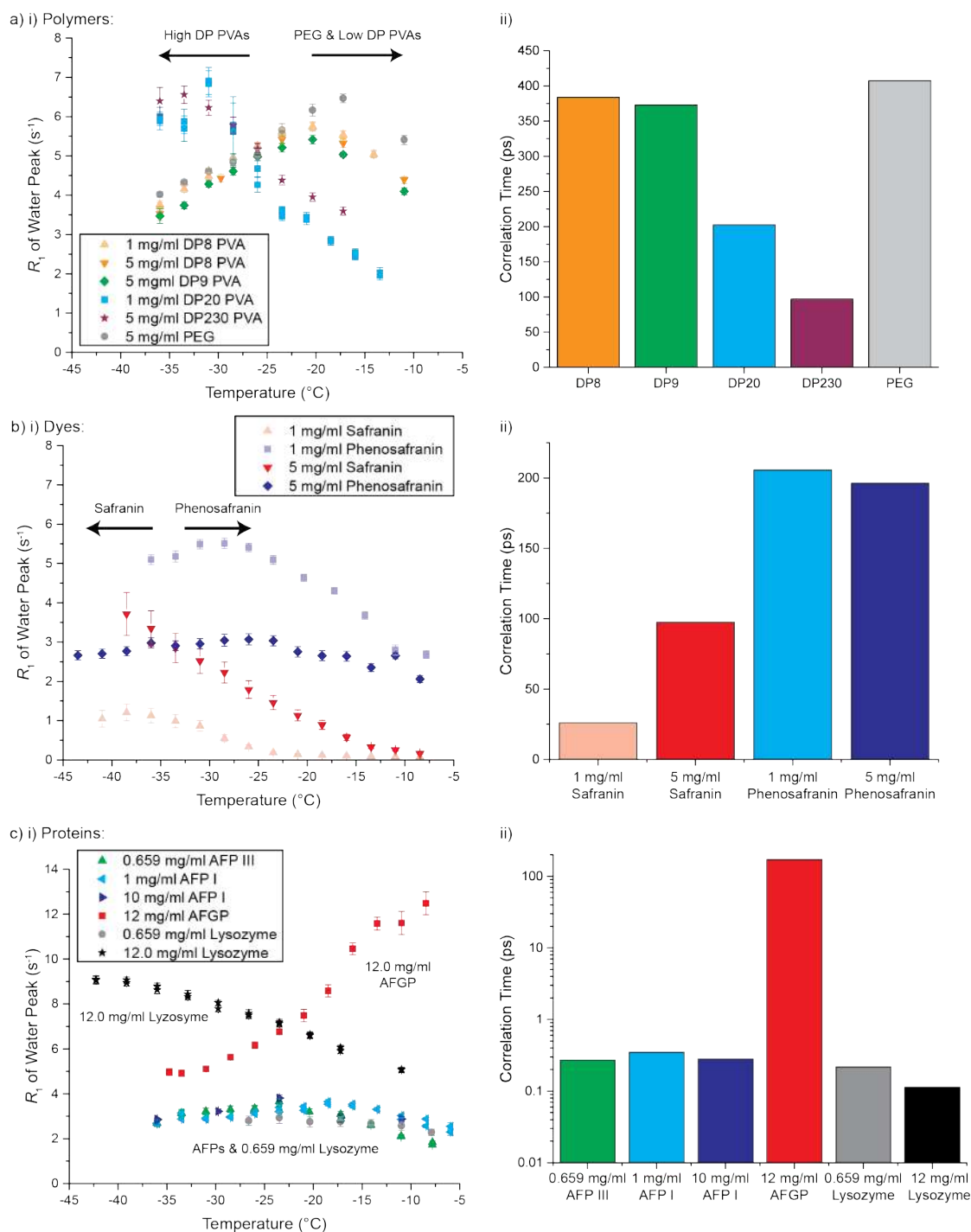


Figure 6.22: VT 1H R_1 of ice in the presence of different additives: a)i) 1 mg/ml DP8 and DP20 PVA, 5 mg/ml DP8, DP9 and DP230 PVA and 5.0 mg/ml PEG. b)i) 1.0 mg/ml and 5.0 mg/ml safranin and phenosafranin. c)i) 0.659 mg/ml AFP III, 1.0 mg/ml and 10.0 mg/ml AFP I, 12.0 mg/ml AFGP and 0.659 mg/ml 12.0 mg/ml lysozyme. Note the different R_1 scales between the plots. The arrows and labels on the plots highlight the observed trends in R_1 maxima. ii) The calculated correlation times for the ice protons in these samples at $-30^{\circ}C$ using Equations 6.3 - 6.5. For the 5.0 mg/ml safranin and 12.0 mg/ml AFGP rates, the fits were less accurate due to the lack of an R_1 maximum, so the resulting correlation times should only be analysed in a qualitative manner.

which limits the accuracy of any quantitative analysis, but qualitative discussion on the trends observed is still possible. As far as it is possible to tell, ice in the presence of the dyes seems to follow a similar trend to the polymer samples; the higher R_1 values of the antifreeze (safranin) are shifted to the left of the plot and, although the maxima are not visible within this temperature range for one of the samples, it is clear that they will be at a much lower temperature than for the control (phenosafranin) samples. Interestingly, the relaxation rates for 5.0 mg/ml phenosafranin do not vary much within this temperature range and the rates are significantly lower than the others mentioned so far.

Finally, R_1 values are recorded for the protein samples (0.659 mg/ml AFP III, 1.0 mg/ml AFP I, 12.0 mg/ml AFGP and 12.0 mg/ml lysozyme) between -6°C and -43°C, which had a very different effect on the fast ice dynamics (Figure 6.22c). Firstly, the 12.0 mg/ml AFGP and 12.0 mg/ml lysozyme display the opposite trend to the dye and polymer samples; although it is not possible to see either of these maxima, the trends clearly suggest that the antifreeze will have a maximum at a vastly higher temperature than the negative control. These two samples also have relaxation rates considerably greater than any of the others mentioned so far (note the difference in scale), although this could be due to the significantly higher concentration of these samples. The remaining three protein samples, 0.659 mg/ml AFP III, 1.0 mg/ml AFP I and 0.659 mg/ml lysozyme, are different yet again. The ice dynamics they produce have relatively low rates and show little variation, producing rather flat curves (like those seen in the frozen 5.0 mg/ml phenosafranin solution).

If a clear R_1 maximum is present and enough data is available, it is possible to calculate the correlation time of the ice motion in each sample using Equations 6.3 - 6.5. These equations are based on the assumption of a single fast motion dominating these relaxation measurements. Since these samples produce quadratic plots with a single maximum it can be assumed that this is the case.

$$R_1 = \Sigma C[J(\omega_0) + 4J(2\omega_0)] \quad (6.3)$$

$$J(\omega) = \frac{\tau_c}{1 + \omega^2 \tau_c^2} \quad (6.4)$$

$$\tau_c = \tau_0 e^{\left(\frac{E_a}{RT}\right)} \quad (6.5)$$

Where $J(\omega)$ and $J(2\omega)$ are the spectral densities evaluated at the Larmor frequency (ω_0) and twice the Larmor frequency ($2\omega_0$), respectively, C represents various constants in addition to the magnitude of the motion, τ_c is the correlation time, τ_0 is an experimentally-determined constant relating to the correlation time and E_a is the activation energy.

These calculations were conducted for the VT R_1 rates. The resulting correlation times at -30.0°C are displayed in Figure 6.22ii. For most of the samples a good fit was obtained. However in the cases of the 5.0 mg/ml safranin and 12.0 mg/ml AFGP

samples, the fits were not as accurate due to the lack of an R_1 maximum. Although these correlation times are not suitable for quantitative analysis, they still help to indicate the overall trends across the samples qualitatively.

As expected from the VT R_1 data, the correlation times for the safranin, DP20 PVA and DP230 PVA are significantly shorter than for the controls and low-DP PVA samples. This indicates that the picosecond ^1H ice motions in the former samples are far more rapid than those in the latter samples. Contrastingly, the AFP samples have relatively similar correlation times to the lysozyme samples. This suggests that the AFPs are not causing any significant changes to the fast ice dynamics. On the other hand, 12.0 mg/ml AFGP has a correlation time that is approximately three orders of magnitude larger than the other proteins, showing that this protein is significantly altering the fast dynamics of the ice protons. It is also interesting that the AFGP has a larger correlation time than the controls, this is the reverse of the relationship between the antifreezes and controls for the dye and polymer samples.

These ^1H R_1 rates and correlation times are discussed in the context of antifreeze mechanisms in Section 6.5.5.

6.5.2 Variable Temperature ^1H R_2 of Ice in the Presence of Antifreezes

Like R_1 , spin-spin relaxation (R_2) is induced by local motions, however this relaxation is dominated by relatively slow dynamics (millisecond - nanosecond). As the temperature increases (or correlation time decreases), R_2 will decrease (see Figure 2.25). Besides these motions, other factors may contribute to the measured R_2 value, such as exchange and coherent contributions.⁶⁶

Under these conditions, R_2 will contain coherent contributions, such as dipolar dephasing, originating from incomplete averaging of anisotropic interactions. It is not possible to quantify the extent of these contributions, however it can be assumed that simply changing the temperature should not significantly affect the quantity of the coherent contributions. Therefore, any variations in the measured rates across different temperatures are due to changes in the contributions from random molecular motions or exchange.

Chemical exchange will contribute to R_2 differently depending on whether it is “slow” ($k \ll |\Delta\omega|$) or “fast” ($k \gg |\Delta\omega|$). In the case of slow exchange, it will simply add to the relaxation rate:

$$R_2^{Obs} = R_2^0 + k \quad (6.6)$$

Where R_2^{Obs} is the observed relaxation rate, R_2^0 is relaxation in the absence of exchange and k is the rate of the exchange. As temperature increases, so will the exchange rate. Thus the contribution of slow exchange to R_2 will increase with temperature.

Fast exchange also increases the observed R_2 :

$$R_2^{Obs} = R_2^0 + \frac{p_a p_b \Delta\omega^2}{k} \quad (6.7)$$

Where p_a and p_b are the populations of states a and b , and $\Delta\omega^2$ is the chemical shift difference between the two states.

Increasing the fast exchange rate decreases its contribution to R_2 . Therefore as the exchange rate increases with increasing temperature, its contribution to R_2 will tend towards zero.

Here, VT ^1H R_2 is recorded using a CPMG pulse sequence on the bulk ice in the presence of the antifreezes and negative controls (Figures 6.23 and 6.25). The huge variations recorded in the R_2 of bulk ice due to the addition of very small quantities of antifreeze demonstrate just how significantly these additives alter the ice system and ms - ns dynamics within. Immediately, it is clear that most of the samples do not have a simple decaying relaxation rate as the temperature increases, suggesting that the reorientational motions are not always the sole contributor to R_2 in these systems.

The primary observation is that, although these samples present vastly different trends in the ice ^1H R_2 , the negative controls all produce relatively low R_2 values ($<1500\text{ s}^{-1}$) that do decrease with sample heating, i.e. they are in line with the theoretical relationship mentioned above. This suggests that the reorientation of water molecules dominates these relaxation rates (rather than exchange) and the correlation time of this motion decreases as the temperature increases.

The frozen solutions of 1.0 mg/ml DP5 PVA, DP8 PVA, DP9 PVA and 0.659 mg/ml AFP III show very similar rates to the control samples, indicating that these rates are also dominated by reorientational motions. This is expected for the low DP PVA samples (which have been shown to be ineffective as an antifreeze).²²⁹ However, AFP III is an effective antifreeze at concentrations down to 0.05 mg/ml and so it is unexpected that its rates are much more like the control solutions rather than the other antifreeze solutions.

The safranin R_2 values seem to be dominated by reorientational motions at very low temperatures ($<-30^\circ\text{C}$), but as the temperature is increased past this point, R_2 starts to increase. This increasing R_2 with temperature must be due to a contribution from slow exchange (Figure 6.24b). Similar trends are seen in the 1.0 mg/ml DP20 PVA and AFGP relaxation rates, indicating that these also have a significant contribution from slow exchange. The higher concentration AFGP (12.0 mg/ml) and higher DP PVA (1.0 mg/ml DP150 and DP230) showed a third set of trends. These samples produced very high R_2 values that decreased as temperature increased, suggesting that, once again, the reorientational dynamics are dominating the measurements. The higher concentration or DP of these solutions increases their viscosity,³⁶⁷⁻³⁶⁹ which slows motions and therefore increases the reorientational contribution to R_2 . This concept is illustrated in Figure 6.24b.

At this point it is worth noting that the PEG used in these measurements has an average DP of 90 and it seems that for PEG this is not high enough to cause significant increases in viscosity, since the R_2 values are very low. It is very clear that the PEG solution does not have any contributions from slow exchange, compared to the DP20 and

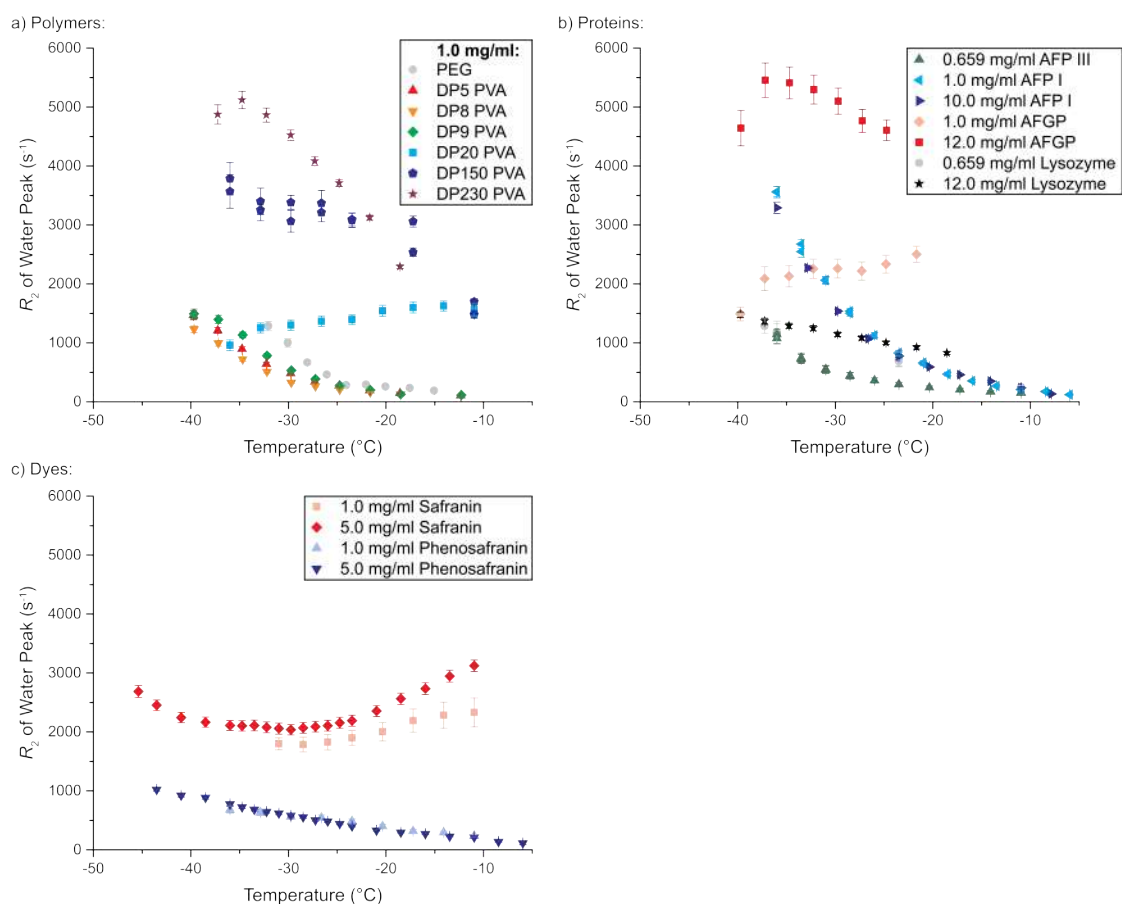


Figure 6.23: VT ^1H R_2 of the bulk ice in the presence of antifreezes and controls. a) 1.0 mg/ml DP5, DP8, DP9, DP20, DP150 and DP230 PVA and PEG (additional concentrations are presented in Figure 6.25). b) 0.659 mg/ml AFP III, 1.0 and 10.0 mg/ml AFP I, 1.0 and 12.0 mg/ml AFGP and 0.659 and 12.0 mg/ml lysozyme. c) 1.0 mg/ml and 5.0 mg/ml safranin and phenosafranin.

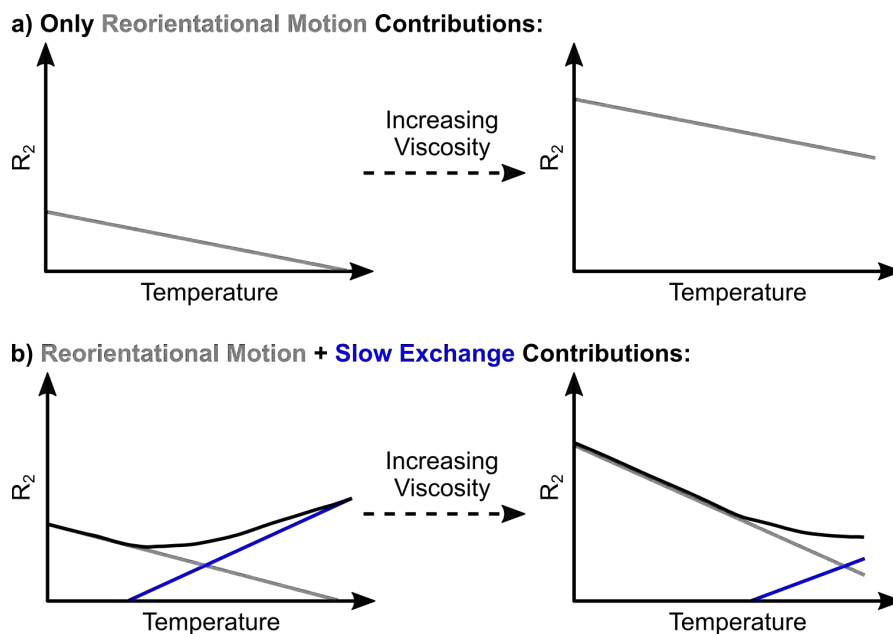


Figure 6.24: An approximate guide to the relationships between temperature, concentration and the contributions to R_2 from a) reorientational motions and b) both reorientational motions and slow exchange. The reorientational motion, slow exchange and total contributions are represented by grey, blue and black solid lines, respectively.

DP150 PVAs. Additionally, the dyes do not seem to be as affected by changes in concentration compared to the proteins and polymers, most likely because these molecules are far smaller.

The final trend observed in these R_2 measurements on ice is of the 1.0 mg/ml and 10.0 mg/ml AFP I solutions. These samples show rather high R_2 values at low temperatures that rapidly decay to extremely low values as the temperature increases. It is clear that there is no slow exchange contribution to these relaxation rates, which means the variation in relaxation rate must be due to reorientational contributions and/or fast exchange. Furthermore, there is no substantial change in rate across the two concentrations of AFP I, which suggests that this protein is not significantly affecting the viscosity of these system. This is very different from the other protein solutions and is potentially due to the compact, α -helical structure of AFP I compared to the much more flexible, varied structures of AFP III, AFGP and lysozyme.

Additional measurements on the polymer samples at a range of concentrations are presented in Figure 6.25. All of these plots are on the same scale, highlighting the dramatic changes in the ice R_2 as a result of relatively minute variations in the concentration or DP of the polymer. The frozen solutions of PEG and the low DP PVAs continue to show comparably low relaxation rates that decrease slightly with warming due to the reorientational motions. A comparison of the DP20 PVA rates shows that at 1.0 mg/ml R_2 is dominated by contributions from a slow exchange process, but at 5.0 mg/ml reorientational motions dominate the rates again due to the increased viscosity. Comparing the DP230 PVA rates produces a similar result: the effects of slow exchange

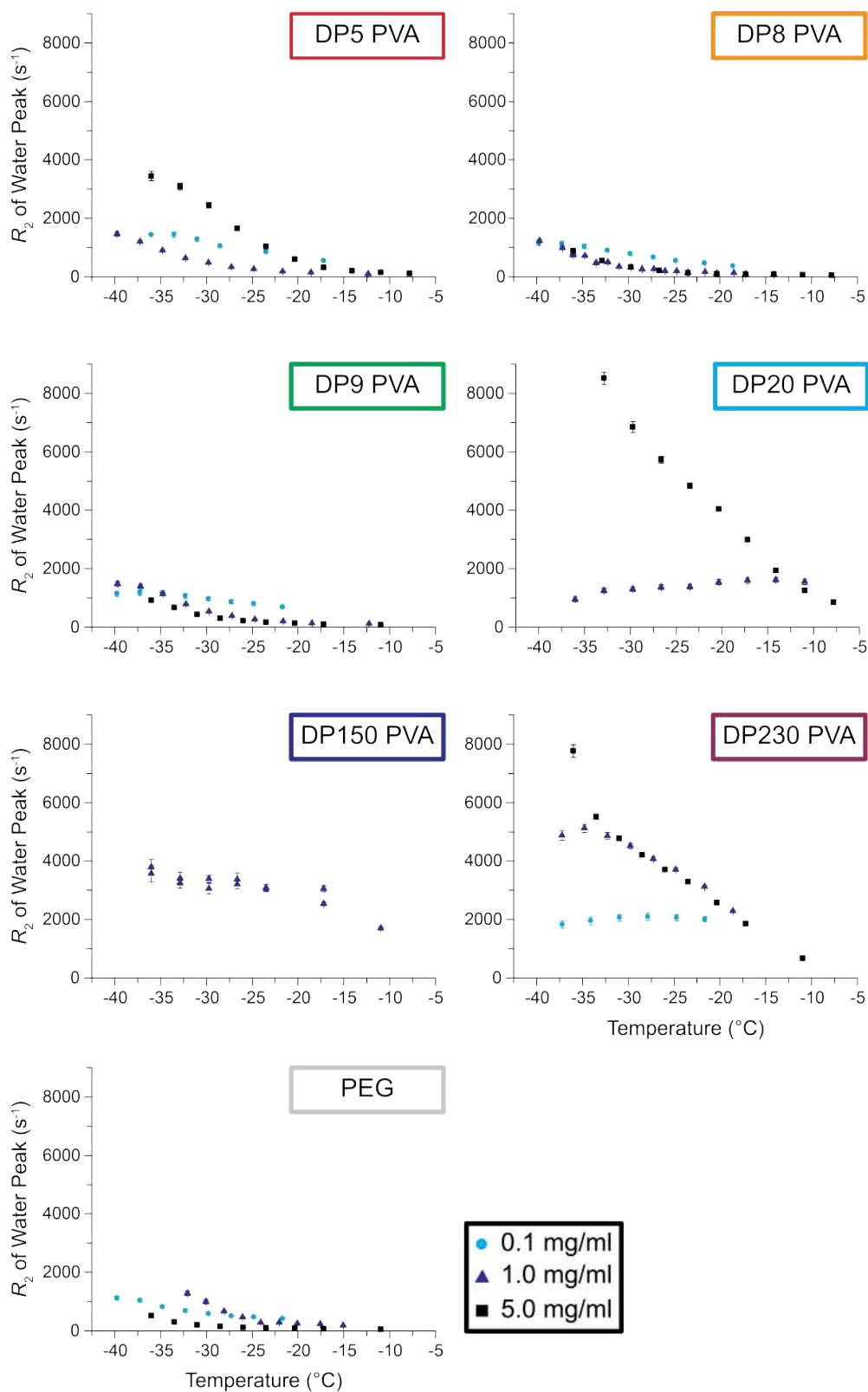


Figure 6.25: Additional VT R_2 of ice in the presence of different concentrations (0.1 mg/ml (cyan circles), 1.0 mg/ml (blue triangles) and 5.0 mg/ml (black squares)) of PVA (DP5, DP8, DP9, DP20, DP150 and DP230) and PEG.

are observable in the 0.1 mg/ml DP230 PVA rates, but the 1.0 mg/ml DP230 PVA rates are dominated by the reorientational motions.

This variety of complex relationships between temperature and the ice ^1H R_2 acts as evidence that, in the majority of cases (safranin, high DP PVAs and AFGP), there is a substantial contribution to the relaxation rates of the frozen antifreeze solutions from a slow chemical exchange process involving water molecules. The significant trends observed provide clues to the interactions between ice and the different antifreezes.

6.5.3 Variable Temperature ^1H Relaxation Dispersion of Ice in the Presence of Antifreezes

In order to access just the microsecond motions that may be present in the frozen antifreeze solutions, $R_{1\rho}$ relaxation dispersion (RD) measurements were conducted. These experiments involve measuring $R_{1\rho}$ using a range of spin-lock frequencies. (For further details refer to Sections 2.3.6, 2.3.8 and 2.3.9).

$R_{1\rho}$ measurements are sensitive to millisecond and nanosecond motions, since the microsecond motions are decoupled by the spin-lock pulse. This spin-lock pulse reduces the relaxation due exchange processes on the microsecond timescale by refocusing exchange broadening. Significant refocusing is typically achieved when the spin-lock pulse exceeds half the exchange rate. Therefore monitoring the change in $R_{1\rho}$ as a function of the spin-lock frequency provides a measure of the microsecond motions.

The relationship between the observed $R_{1\rho}$, exchange rate and spin-lock frequency is described by the equation below in the case of two-site fast exchange:

$$R_{1\rho}^{obs} = R_{1\rho}^0 + \frac{p_a p_b \Delta\omega^2 k}{\omega_{eff}^2 + k^2} \quad (6.8)$$

Where $R_{1\rho}^{obs}$ is the observed $R_{1\rho}$, $R_{1\rho}^0$ is the $R_{1\rho}$ in the absence of any microsecond exchange contributions, k is the exchange rate, ω_{eff} is the spin-lock frequency, p_a and p_b are the populations of the exchanging sites (a and b , respectively) and $\Delta\omega$ is chemical shift difference of these sites.

In the absence of exchange, $R_{1\rho}$ is independent of the spin-lock frequency, producing flat RD profiles that only reflect the ms and ns ^1H dynamics. In the presence of exchange occurring on the microsecond timescale, the exchange contribution to the measured $R_{1\rho}$ will be increasingly decoupled as the spin-lock frequency increases, producing significant dispersion. Under the conditions used here, there will be some coherent contributions to the measured rates, which may lead to “pseudodispersion”. In order to gain further information about the dynamics, and potentially exchange, these ^1H RD measurements were recorded at various temperatures, since motion and temperature are intrinsically related.

The results of measuring VT ^1H RD on the ice peaks in the presence of 0.659 mg/ml AFP III, 1.0 mg/ml AFP I, 12.0 mg/ml AFGP and 12.0 mg/ml lysozyme at a range of temperatures between -4.7°C and -42.3°C are presented in Figure 6.26. It is immediately

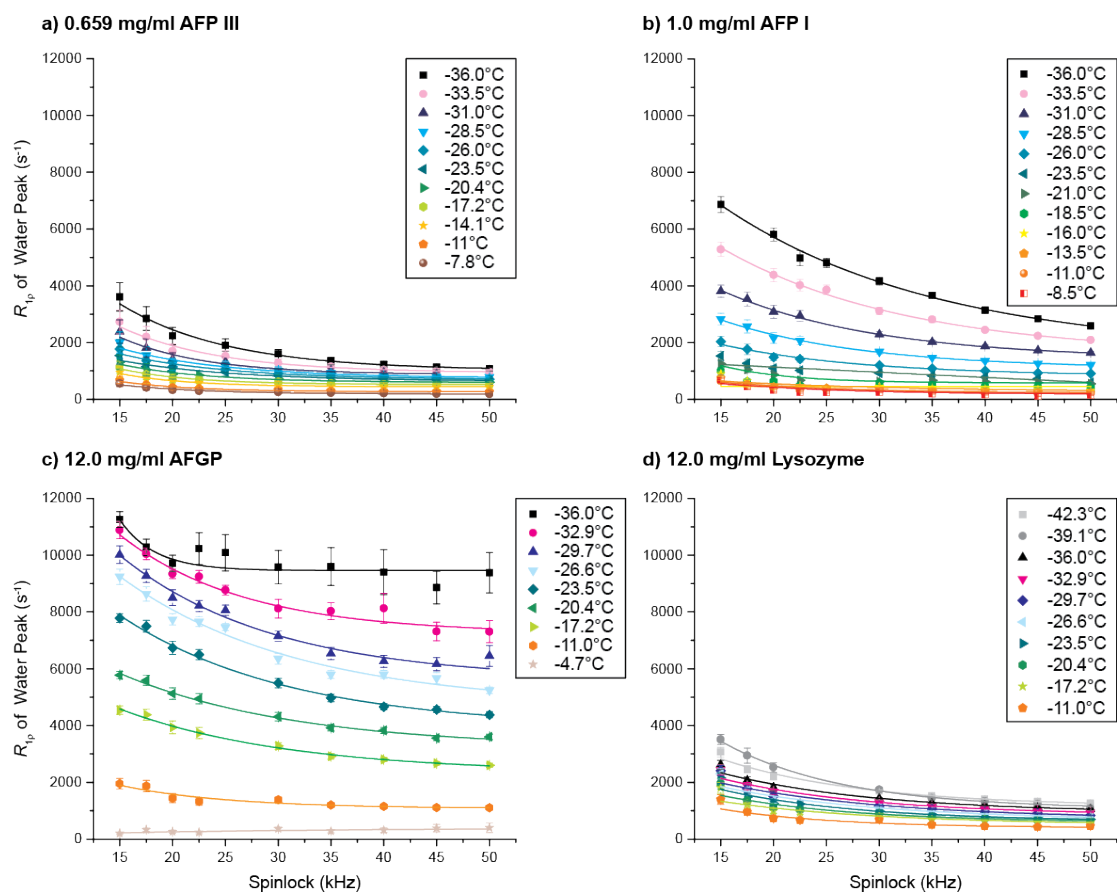


Figure 6.26: VT ^1H RD of ice in the presence of a) 0.659 mg/ml AFP III, b) 1.0 mg/ml AFP I, c) 12.0 mg/ml AFGP and d) 12.0 mg/ml lysozyme. The solid lines are fitted to Equation 6.8.

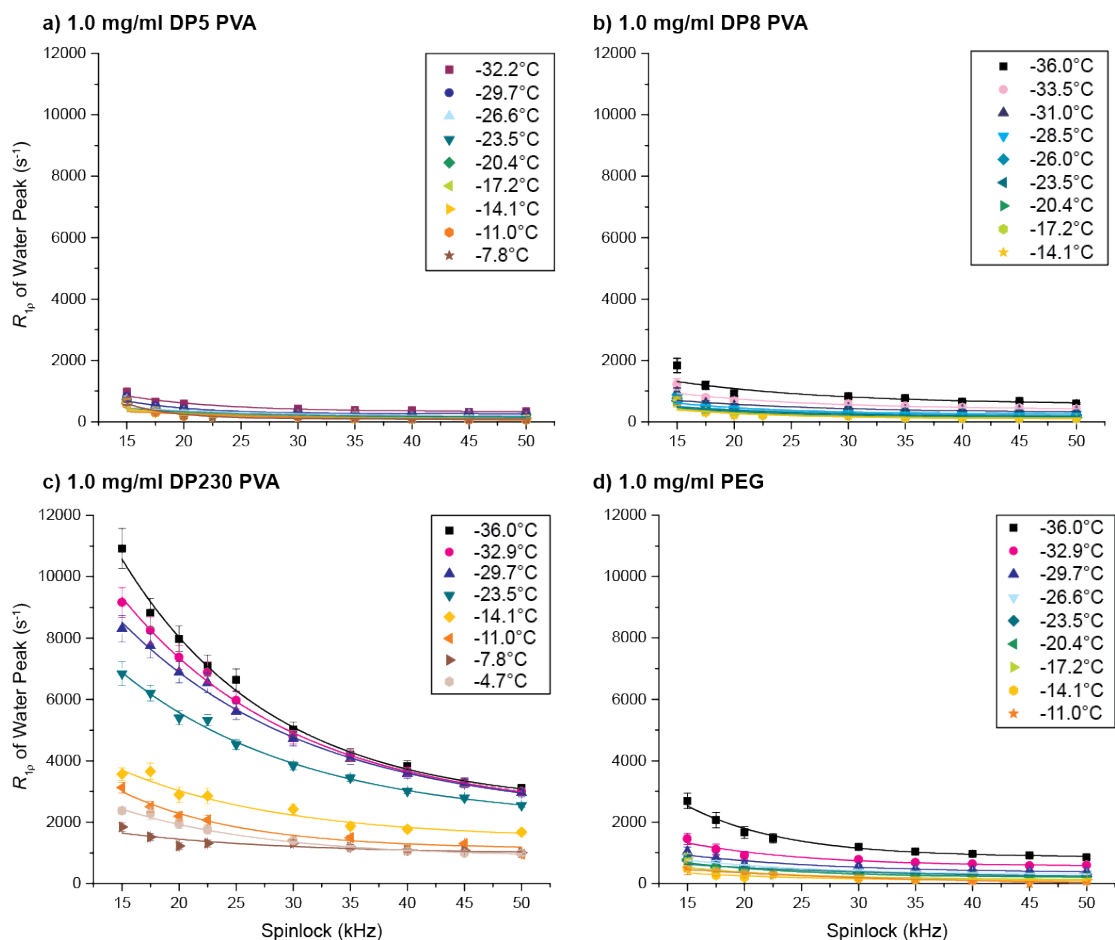


Figure 6.27: VT ^1H RD of ice in the presence of 1.0 mg/ml a) DP5 PVA, b) DP8 PVA, c) DP230 PVA and d) PEG. The solid lines are fitted to Equation 6.8.

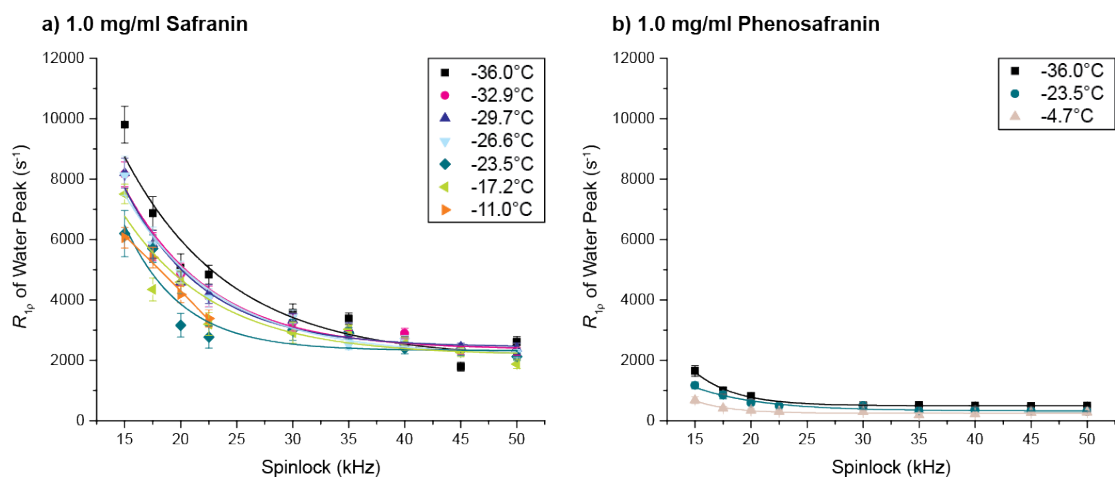


Figure 6.28: VT ^1H RD of ice in the presence of 1.0 mg/ml a) safranin and b) phenosafranin. The solid lines are fitted to Equation 6.8.

clear that the ice in the 12.0 mg/ml AFGP sample behaves very differently to that in the other protein samples; the large changes in the base $R_{1\rho}$ without much change in dispersion suggests that the exchange here may be in the slower microsecond regime. In AFP I there also seems to be a significant contribution from exchange, the greater dispersion indicates that this may be faster microsecond exchange. The AFP III and lysozyme profiles show minimal variation in $R_{1\rho}$ and the slight variation in rate can be attributed to pseudodispersion from coherent contributions i.e. in these cases there is no significant contribution from exchange.

Figure 6.27 presents the rates from the RD measurements conducted for 1.0 mg/ml polymer antifreeze solutions (PEG and DP5, DP8 and DP230 PVA) between -4.7°C and -36.0°C. Here it is very clear that DP230 PVA is experiencing significant exchange on the microsecond timescale, but there is no evidence of this exchange in the DP5 PVA, DP8 PVA and PEG profiles, which are relatively flat.

Once again, VT ^1H RD was measured on ice, this time in the presence of 1.0 mg/ml safranin and phenosafranin (Figure 6.28). Similar trends are seen to those in the polymer data; the safranin sample shows significant dispersion indicating exchange in microsecond regime and phenosafranin does not.

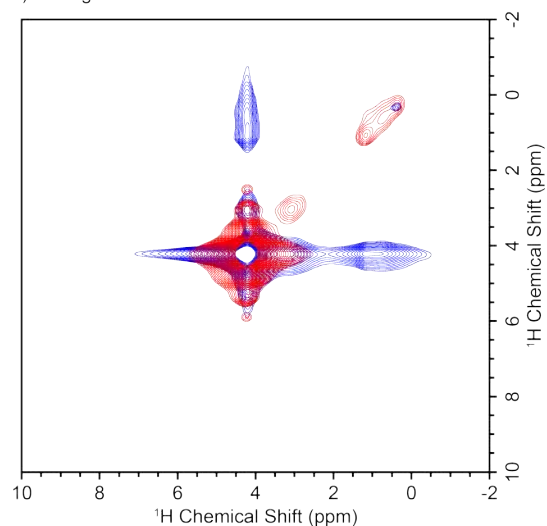
6.5.4 2D ^1H - ^1H EXSY Spectra

The relaxation data has shown that the AFGP, AFP I and the synthetic antifreezes are undergoing an exchange process on the microsecond timescale. Whereas AFP III and the control samples have not shown any evidence of chemical exchange. Here 2D ^1H - ^1H exchange spectroscopy (EXSY) measurements⁶⁷ are used to determine which antifreeze and control molecules bind to water molecules.

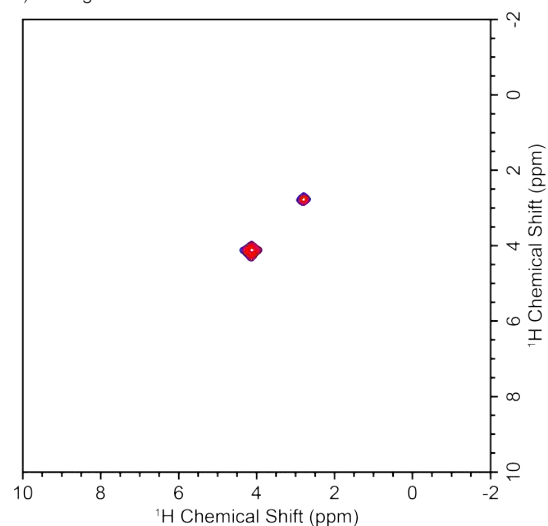
In the EXSY measurements, after the initial 90° pulse and the indirect acquisition period, there is a mixing period. During this mixing period magnetisation can exchange due to either slow chemical exchange or the nuclear Overhauser effect (NOE). After this mixing time there is a direct acquisition period recording the nuclei at their new frequency. This results in a spectrum with off-diagonal crosspeaks between nuclei that are close in space or are slowly exchanging magnetisation. 2D ^1H - ^1H EXSY measurements for a range of the frozen antifreeze and control solutions are presented in Figure 6.29. In each case the pulse sequence was recorded with mixing times of 0 ms (red) and 100 ms (blue), these are overlaid to make any off-diagonal crosspeaks clearer. The dominating diagonal crosspeak in each spectrum (at 4 - 5 ppm) is due to the water protons. All additional peaks are due to the additive and water-additive interactions.

It is clear that, when frozen, the DP230 PVA, AFGP and AFP III are all binding to water molecules. In the DP230 PVA spectrum there are crosspeaks between the bulk water and the aliphatic protons (and possibly the hydroxyl protons), in the AFGP spectrum the crosspeaks are between the water and aliphatic protons and in the AFP III spectrum the crosspeaks are between the water and amine protons. The PEG and lysozyme spectra lack any off-diagonal crosspeaks indicating that these control molecules are not interacting with the water in this way. Due to experimental time limitations

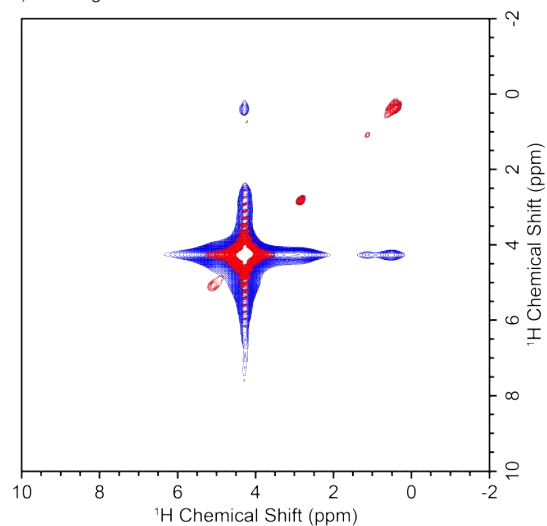
a) 5.0 mg/ml DP230 PVA in Water:



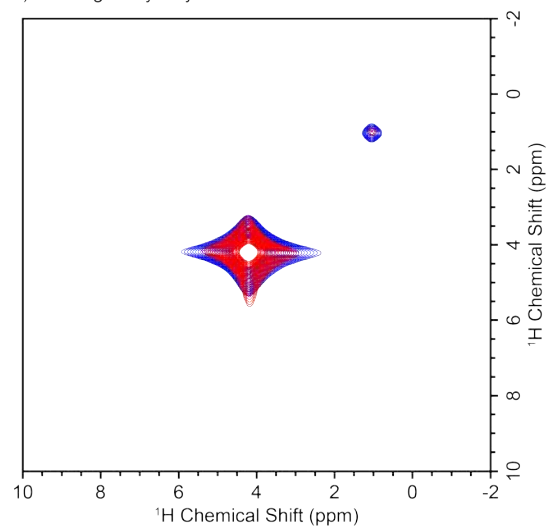
b) 5.0 mg/ml PEG in Water



c) 12.0 mg/ml AFGP in Water:



d) 25.0 mg/ml Lysozyme in Water



e) 0.659 mg/ml AFP III in Water

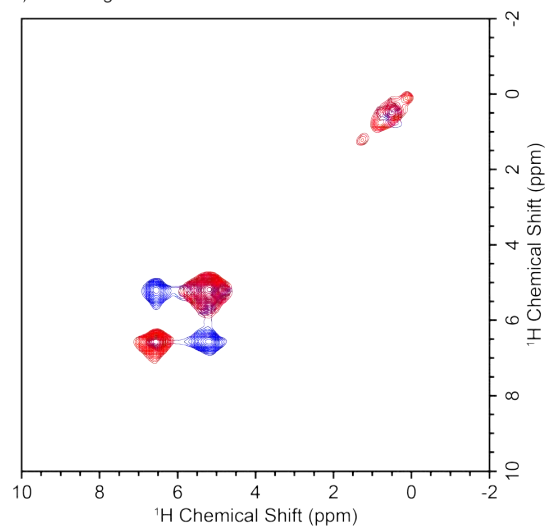


Figure 6.29: 2D ^1H - ^1H EXSY measurements at -10.0°C for a) 5.0 mg/ml DP230 PVA, b) 5.0 mg/ml PEG, c) 12.0 mg/ml AFGP, d) 25.0 mg/ml lysozyme and e) 0.659 mg/ml AFP III. The mixing times for the red and blue spectra were 0 ms and 100 ms, respectively.

it was not possible to record the EXSY spectra on all of the antifreeze and control solutions, and in the future these measurements should be made on safranin, AFP I and phenosafranin. However, based on the trends observed so far, it can be assumed that the safranin and AFP I are binding to water molecules in a similar way to the other antifreezes, whereas the phenosafranin is not. Thus, these results combined with those from the relaxation measurements suggest that the AFGP, AFP I and the synthetic antifreezes reversibly bind to the water molecules, whereas the AFP III binds irreversibly (due to the lack of evidence of an exchange process in the RD measurements for this sample).

It is not possible to tell from these spectra whether the observed antifreeze-water interactions involve ice or liquid water, since only a bulk water peak is observable. In order to determine whether or not the antifreezes are binding to liquid water, these 2D EXSY measurements were repeated at a temperature where the samples were liquid, but close to the freezing point. The EXSY spectra for liquid 1.0 mg/ml DP230 PVA and 1.0 mg/ml PEG (Figure 6.30) only have diagonal crosspeaks, indicating that these antifreeze molecules are not binding to liquid water. Therefore the off-diagonal crosspeaks in Figure 6.29 show that the antifreeze molecules are binding to ice.

6.5.5 Discussion

A key conclusion of these relaxation measurements is that, although only very small quantities of antifreeze are added to the solutions, large changes (typically increases) are observed in the ^1H relaxation rates of the bulk ice, compared to the rates of the relevant negative controls, which rule out any colligative antifreeze effects. This supports the hypothesis that antifreeze activity significantly changes the ice dynamics. These changes could either be a critical part of the antifreeze mechanism itself or a side effect of altering the ice structure and freezing point. The key observations from each set of SSNMR measurements are summarised in Figure 6.31.

Clear trends were observed in the variable temperature R_1 data, and therefore it was possible to extract the correlation times for the ps - ns motions. These correlation times, alongside the temperatures of the R_1 maxima in the VT R_1 plots, provide a guide to the fast bulk ^1H ice dynamics in each of these systems. The frozen safranin and high-DP PVA ($\text{DP} \geq 20$) solutions clearly reduce the correlation time of the ice dynamics, indicating more rapid motions (in comparison to their controls). Interestingly, the opposite relationship is seen between AFGP and lysozyme, suggesting that the addition of AFGP actually reduces the rate of the fast dynamics. Neither the AFP I nor AFP III proteins cause any significant change to the relaxation rates or correlation times, they are very similar to those of lysozyme, indicating that the AFPs are not affecting the fast ice dynamics at all. The significant changes in dynamics caused by the synthetic antifreezes and AFGP, suggest that these molecules may have similar antifreeze mechanisms, which are significantly different to the mechanism of the AFPs.

The VT R_2 measurements show that there are substantial contributions from reorientational motion in all of the frozen solutions. However, under certain conditions,

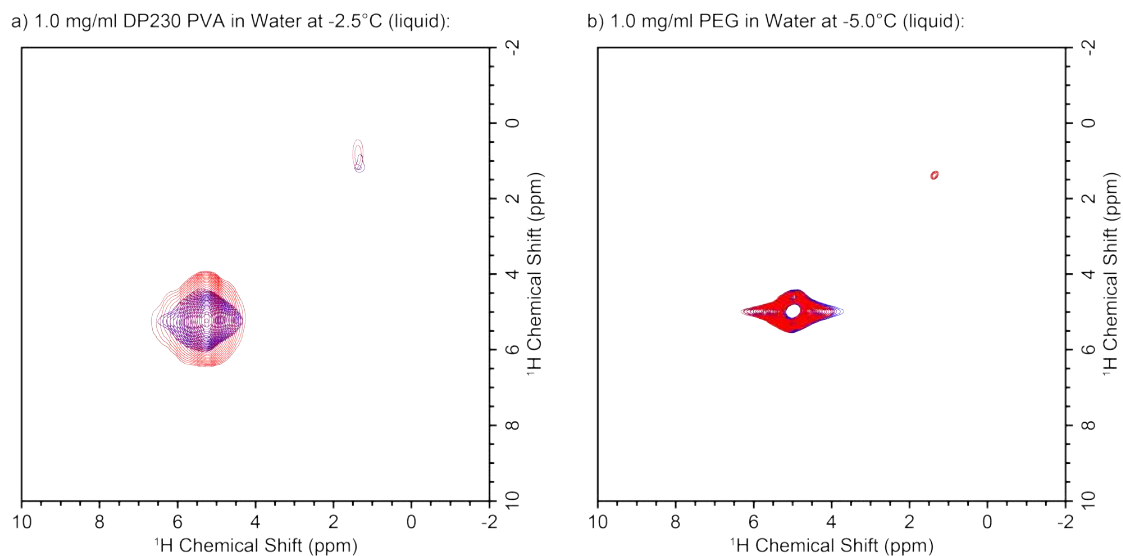


Figure 6.30: 2D ^1H - ^1H EXSY measurements on liquid a) 1.0 mg/ml DP230 PVA at -2.5°C and b) 1.0 mg/ml PEG at -5.0°C. The mixing times for the red and blue spectra were 0 ms and 100 ms, respectively.

| SSNMR Measurement | VT R_1 Change in τ_c ? | VT R_2 Slow exchange? | VT RD μs exchange? | 2D Exchange Spectra Binds to ice? | Conclusion |
|-------------------|----------------------------------|----------------------------|----------------------------------|--------------------------------------|--------------------|
| Safranin | Decrease | ✓ | ✓ | — | Binds reversibly |
| Phenosafranin | — | ✗ | ✗ | — | No binding |
| DP < 20 PVA | No change | ✗ | ✗ | — | No binding |
| DP \geq 20 PVA | Decrease | ✓ | ✓ | ✓ | Binds reversibly |
| PEG | — | ✗ | ✗ | ✗ | No binding |
| AFP I | No change | ✗ | ✓ | — | Binds reversibly |
| AFP III | No change | ✗ | ✗ | ✓ | Binds irreversibly |
| AFGP | Increase | ✓ | ✓ | ✓ | Binds reversibly |
| Lysozyme | — | ✗ | ✗ | ✗ | No binding |

Figure 6.31: Summary of the key observations from SSNMR measurements on ice ^1H s in the presence of various antifreezes and negative controls.

contributions from slow exchange started to dominate the measured R_2 values for the safranin, high DP PVA and AFGP samples. Changes in the concentration or DP of the AFGP and PVA solutions seemed to have significant effects on the viscosity of the samples, leading to larger contributions from reorientational motions. In comparison to these samples, the AFP I solutions produced considerably different trends, which can only result from reorientational dynamics and / or fast exchange. Finally, AFP III showed almost identical R_2 rates to lysozyme, indicating that it is not undergoing any exchange processes.

The VT $R_{1\rho}$ relaxation dispersion measurements produced relatively flat profiles for all of the control samples and AFP III, demonstrating that there is no exchange on the microsecond timescale in these cases (although often a small amount of pseudodispersion can be seen, which originates from incomplete averaging of anisotropic interactions). Throughout these measurements the DP230 PVA, safranin, AFGP and AFP I showed evidence of microsecond exchange. It was noted that AFP I had slightly faster exchange and AFGP had significantly slower exchange based on the dispersion profiles. The contrasting results between AFP I and AFP III suggest that they are undergoing rather different mechanisms, probably due to their very different structures; the AFP I (2.5 kDa) has a monomeric α -helical structure, whereas the AFP III consists of a sheet of β -strands and is much larger (> 6 kDa).

Together the VT R_2 and $R_{1\rho}$ RD measurements indicate that the safranin, high DP PVAs and AFGP are undergoing a slow exchange process with water, and that AFP I may be undergoing a slightly faster exchange process. 2D EXSY spectra were used to confirm that all of the antifreezes bind to ice and the controls do not. Thus, the 2D EXSY spectra alongside these relaxation measurements show that safranin, high DP PVAs, AFGP and AFP I reversibly bind to ice, whereas AFP III irreversibly binds to ice. This supports the general consensus in the literature that these different types of proteins interact with ice in dramatically different ways and introduces the idea that the synthetic antifreezes investigated here reversibly bind to ice, potentially with a similar mechanism as AFGPs. Furthermore, the evidence presented here of AFP III molecules irreversibly binding to ice suggests that this antifreeze could have an adsorption-inhibition-like mechanism. Whereas the other antifreeze molecules, which presented evidence of reversible binding to ice, cannot be undergoing the adsorption-inhibition mechanism, but instead could have a mechanism like the two-step reversible adsorption mechanism.

6.6 Conclusions and Outlook

The SSNMR relaxation measurements confirmed that the ^1H dynamics of bulk ice are dramatically altered by the addition of a small amount of non-colligative antifreeze (in comparison to the dynamics of ice in control solutions, which remove any colligative contributions). Overall, the results support the current literature in two key ways. Firstly, PVAs with a DP < 19 have been reported as ineffective;²²⁹ here the ice dynamics observed in frozen solutions of the DP5, DP8 and DP9 PVAs are very similar to PEG, the control. Secondly, the general consensus in the literature is that AFGPs and AFPs are

very different proteins and they are not expected to have similar antifreeze mechanisms, for example most of the literature points towards AFGPs binding to ice reversibly and AFPs binding to ice irreversibly.^{290,294,297} Throughout the relaxation measurements reported here, the AFGP samples produced contrasting results to the AFPs. In fact the combination of 2D EXSY spectra and relaxation measurements indicate that both AFGP and AFP I bind to ice reversibly, but seem to do so at different rates, whereas AFP III binds irreversibly. There is relatively little research on synthetic antifreezes; it is not known whether they act in a similar way to the natural antifreezes or not. However, the SSNMR measurements presented here strongly suggest that high DP PVAs and safranin reversibly bind to ice, and that these may undergo a similar mechanism to AFGPs.

In order to improve the accuracy of the conclusions on the protein samples, AFGP and lysozyme relaxation measurements should be repeated at the same concentration as the AFPs, allowing a fairer comparison. Furthermore, there are a few samples on which 2D EXSY and /or $R_{1\rho}$ RD measurements have not been run due to experimental time restraints and it would also be interesting to compare all of the results to those of pure water. These experiments should be conducted to complete the data set.

In addition to the relaxation measurements mentioned above, this project can progress in multiple directions using SSNMR. For example, 2D exchange spectra of ^{13}C -labelled antifreezes could be used to identify the IBS of each antifreeze either through correlations with water or by observing the change in ^{13}C chemical shift between liquid and frozen solutions. This may require faster MAS to achieve the necessary resolution. Alternatively, ^2H or ^{13}C relaxation measurements could help to enhance the current picture of ice and antifreeze dynamics. Finally, there is potential to simulate the relaxation rates measured here with molecular dynamics. This would produce a completely new insight into the antifreeze-water interaction as the solution freezes.

6.7 Experimental Details

6.7.1 Antifreeze Samples

The specific antifreeze (glyco)proteins used were AFGP8, North Atlantic Pout AFP (AFP III) and BpAFP (AFP I).

The PVA samples (except DP230) were produced by Christopher Stubbs (Gibson Group, Department of Chemistry, University of Warwick) through RAFT polymerisation (see Table 6.3).^{229,370} The DP230 PVA, PEG and lysozyme samples were purchased from Sigma-Aldrich. The safranin and phenosafranin were purchased from ACROS Organics. The proteins were produced by Alice Fayter and Dr Muhammad Hasan (Gibson Group, Department of Chemistry, University of Warwick). The AFP III protein had to be buffer exchanged so that it was in an aqueous solution for the NMR experiments. It is unknown how long this protein stays active for under these conditions. The 0.659 mg/ml AFP III sample was checked for antifreeze activity before and half way through experiments.

All solutions in this chapter are made with “Milli-Q ultrapure” water

6.7.2 Temperature Calibration

Throughout these measurements a variable temperature unit (VTU) was used to control and monitor the sample temperature. However the temperature that the VTU senses (“target temperature”) will not always be accurate due to the location of the sensor and the friction caused by MAS. Fortunately, the sample temperature can easily be calibrated by monitoring the difference between hydroxyl and methyl ^1H chemical shifts in methanol and using the equation below:

$$\text{Temperature} = 403 - (0.059 \times \Delta\delta) - (0.953 \times 10^{-4}) \times (\Delta\delta^2) \quad (6.9)$$

Where the resulting temperature is in Kelvin and $\Delta\delta$ is the difference between the methyl and hydroxyl ^1H chemical shifts of methanol

This calibration was conducted between the target temperatures of -34.0°C and -2.0°C for a 4 mm rotor spinning at 10 kHz (the same conditions used in all experiments in this chapter), see Figure 6.32.

A linear fit revealed that the following relationship between the target tempera-

Table 6.3: The molecular weights and PDIs of the PVA samples produced at this university. Data provided by Chris Stubbs (Gibson Group, Department of Chemistry, University of Warwick.)

| DP | MW (g/mol) | PDI |
|----|------------|----------|
| 5 | 445 | 1.05997 |
| 8 | 712 | 1.330377 |
| 9 | 801 | 1.129683 |
| 20 | 1780 | 1.24635 |

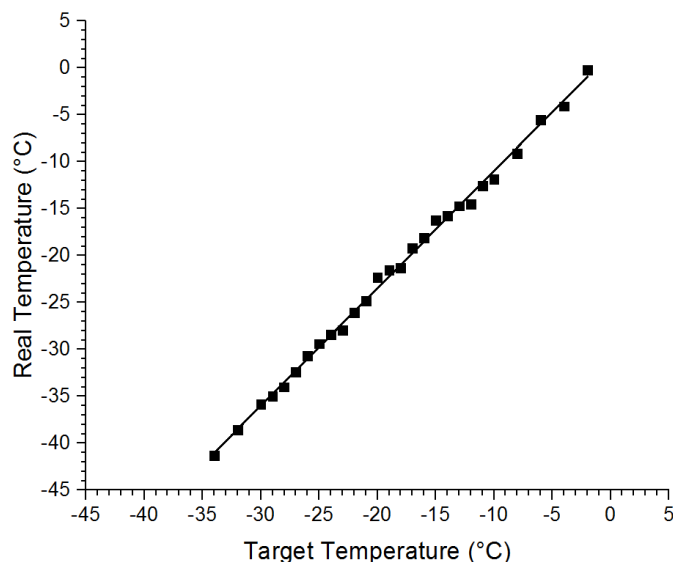


Figure 6.32: A plot of the target temperature versus the calculated real sample temperature using Equation 6.9. The data fits the linear equation 6.10 (solid line).

ture and the real temperature (in °C):

$$T_{Real} = 1.252 \times T_{Target} + 1.550 \quad (6.10)$$

Where T_{Real} is the real sample temperature and T_{Target} is the target sample temperature.

6.7.3 NMR Experimental Details

All NMR experiments in this chapter were measured on a Bruker Avance III spectrometer operating at 11.75 T ($\omega_{0,H}/2\pi = 500$ MHz) using a Bruker 4.0 mm triple-resonance MAS probe and performed at 10 kHz spinning frequency. In each case the rotor was packed by pipetting 60 μ l of solution into the rotor and sealing with the top cap. In all experiments the rotor was undergoing MAS before the sample was frozen. The sample was cooled to -36 °C to ensure it was frozen throughout before being gently warmed to the temperature required for the measurement. All measurements were recorded at a range of temperatures, this range was often limited by the sample melting point and the capability of the VTU. TTMSS was used as a ^1H reference ($\delta = 0.20$ ppm).

It is not possible to probe a particular region of the complex system using SSNMR, since the chemical shift of all water and ice protons are very similar causing the spectra to consist of a single peak. However, liquid water produces a peak orders of magnitude more intense and narrow than ice, so the point at which the water freezes is easily observable in the spectra as a broad peak with low intensity. Although the proportions of liquid and solid water cannot be determined in the sample, the presence of this low, broad peak suggests that there is little or no liquid water present, since a liquid water peak would completely dominate the spectrum. For examples of the 1D ^1H spectra of the liquid and frozen solutions see Section E.1.

Variable Temperature ^1H R_1 of Ice in the Presence of Antifreezes

These ^1H R_1 measurements were initialised by saturating the spins using a series of non-selective 90° pulses ($2.5\ \mu\text{s}$, $\omega_{1,\text{H}}/2\pi \approx 100\ \text{kHz}$, followed by a $20\ \mu\text{s}$ delay). Next there is the variable delay (τ), before a 90° pulse ($2.5\ \mu\text{s}$, $\omega_{1,\text{H}}/2\pi \approx 100\ \text{kHz}$) and acquisition. The variable delay times in these experiments ranged from 0.01 to 5.0 s. The pulse sequence for these ^1H R_1 measurements is illustrated in Figure 6.33.

Variable Temperature ^1H R_2 of Ice in the Presence of Antifreezes

These ^1H R_2 measurements were initialised with a $100\ \text{kHz}$ $\pi/2$ ^1H pulse ($2.5\ \mu\text{s}$), followed by n spinechoes before acquisition. The pulse sequence is repeated, varying the value of n . In these measurements n was varied between 2 and 400, which corresponds to total spinecho times of 0.026 and 5.2 ms. The pulse sequence for these ^1H R_2 measurements is illustrated in Figure 6.34.

Under the conditions for these R_2 measurements and the $R_{1\rho}$ measurements (below), the recorded rates contain coherent contributions (mostly dipolar dephasing, which originates from incomplete averaging of anisotropic interactions by MAS and radio-frequency pulses) in addition to the incoherent contributions (i.e. from random molecular motions). These unwanted dipolar dephasing contributions will vary if the averaging conditions (i.e. MAS frequency and RF amplitudes) are altered. However, if these conditions are kept the same throughout all measurements, then this coherent contribution should be approximately constant across the measurements and therefore any significant changes observed in the relaxation rates as a function of temperature can be attributed to variations in the system dynamics.

Variable Temperature ^1H Relaxation Dispersion of Ice in the Presence of Antifreezes

These ^1H $R_{1\rho}$ measurements were initialised with a $100\ \text{kHz}$ $\pi/2$ ^1H pulse ($2.5\ \mu\text{s}$), followed by a variable-length, variable-power spin-lock pulse ($\omega_{1,\text{H}}/2\pi \approx 15, 17.5, 20, 25, 30, 35, 40, 45$ and $50\ \text{kHz}$) and acquisition. The spin-lock pulse was varied between

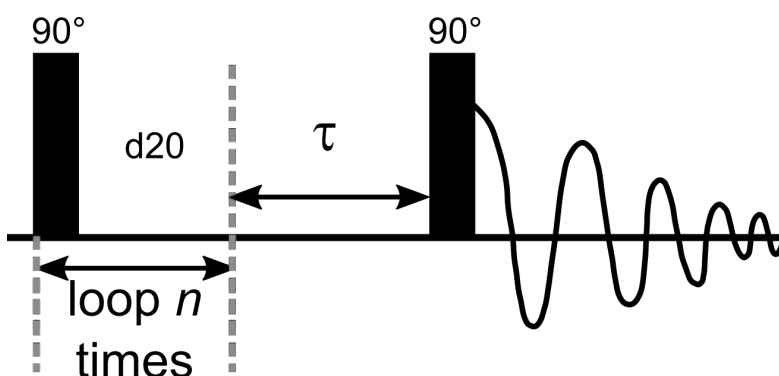


Figure 6.33: The pulse sequence for measurement of ^1H R_1 . The variable delay is labelled τ . The phase cycling of all pulses is (x), except during acquisition in which case it is (y, -y).

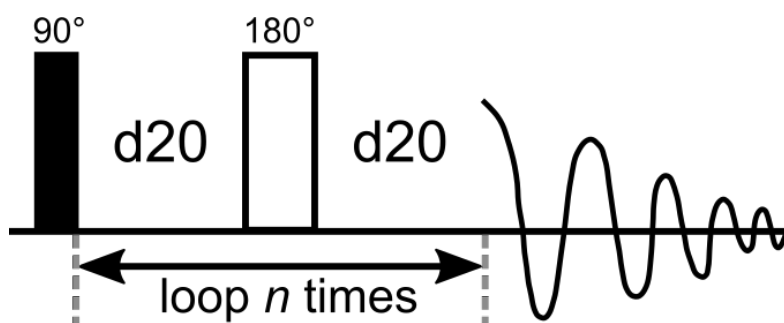


Figure 6.34: The pulse sequence for measurement of $^1\text{H } R_2$. The spin-echo part of the pulse sequence is repeated n times, where n varies. Phase cycling: 90° pulse = (x, x, -x, -x, y, y, -y, -y), 180° pulse = (y, -y, y, -y, x, -x, x, -x) and during acquisition = (x, x, -x, -x, y, y, -y, -y).

0.001 and 1.5 ms. The pulse sequence for these $^1\text{H } R_{1\rho}$ measurements is illustrated in Figure 6.35.

2D ^1H EXSY Measurements

The 2D ^1H EXSY measurements were initialised with a 100 kHz $\pi/2$ ^1H pulse (2.5 μs), followed by the indirect evolution time (t_1). Then there is a 100 kHz $\pi/2$ ^1H pulse (2.5 μs), a mixing time ($\tau_{\text{mix}} = 0$ or 100 ms) and another a 100 kHz $\pi/2$ ^1H pulse (2.5 μs), followed by acquisition. The pulse sequence for these 2D ^1H EXSY measurements is illustrated in Figure 6.36.

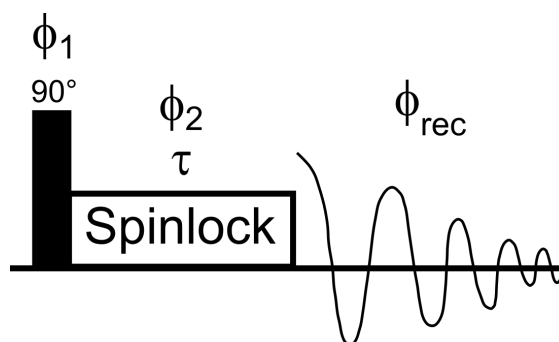


Figure 6.35: The pulse sequence for measurement of $^1\text{H } R_{1\rho}$. The length of the spin-lock pulse is τ . Phase cycling: $\phi_1 = \phi_{\text{rec}} = (\text{x}, \text{x}, \text{y}, \text{y}, -\text{x}, -\text{x}, -\text{y}, -\text{y})$ and $\phi_2 = (\text{y}, -\text{y}, \text{x}, -\text{x})$.

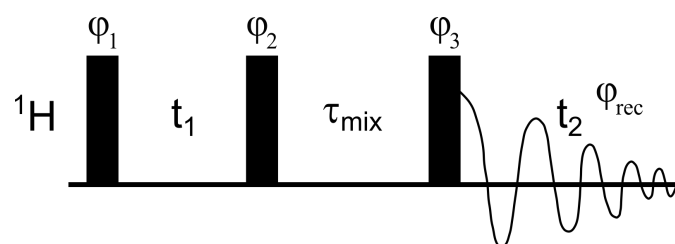


Figure 6.36: The pulse sequence for measurement of 2D ^1H EXSY spectra. The length of the mixing times (τ_{mix}) were 0 and 100 ms. Phase cycling: $\phi_1 = (\text{x}, -\text{x})$, $\phi_2 = (\text{x}, \text{x}, -\text{x}, -\text{x})$, $\phi_3 = (\text{x}, \text{x}, \text{x}, \text{x}, -\text{x}, -\text{x}, -\text{x}, -\text{x})$ and $\phi_{\text{rec}} = (\text{x}, -\text{x}, -\text{x}, \text{x}, -\text{x}, \text{x}, \text{x}, -\text{x})$.

Chapter 7

Summary and Outlook

SSNMR is a very powerful technique for the determination of quantitative, site-specific information from a vast range of samples, such as proteins, pharmaceuticals, polymers and batteries. The application of SSNMR to dynamic systems, as demonstrated in this thesis, provides opportunities to probe motions on timescales from picoseconds to milliseconds.

SSNMR is particularly adept at elucidating the structure and dynamics of proteins, including those that are difficult to study using other techniques, such as membrane proteins, large protein-protein complexes and amyloid fibrils.^{1,3,4} The use of cutting-edge SSNMR technology, such as 100 kHz MAS, enables high-resolution, high-sensitivity spectra of these complicated biomolecules. Increasingly faster MAS requires increasing smaller rotors. Protein samples prepared for SSNMR are sticky semi-solids that are fiddly to pack, and this only becomes more challenging with smaller rotors. Moreover, slow packing increases the risk of sample dehydration, which would render the costly, potentially isotopically-labelled, protein unsuitable for SSNMR. A handful SSNMR research groups have developed ultracentrifuge tools to pack proteins into 1.3 - 4 mm rotors,^{108,138,142–145} but there are currently none in the literature for smaller rotors. **Chapter 3** presented the design, development and application of ultracentrifuge tools for packing or sedimenting proteins into 0.7, 0.8 and 1.3 mm SSNMR rotors. These tools, which were initially designed for just 1.3 mm rotors, progressed through several stages of development so that the same set could be used for the 0.7 and 0.8 mm rotors as well. Additionally, an adaptor was created to allow a protein to be sedimented exploiting the high g-forces of the MLA-150 rotor, and then evenly packed using the MLA-50 rotor, within the same tool. Although the adaptor was functional, in the future it should be shortened slightly to aid with the removal of the MLA-150 tool after packing. These ultracentrifuge tools considerably minimise the waste of expensive protein samples and significantly reduce the packing time. The final set of tools presented in this chapter are still in use and have not shown any signs of deterioration, showing that they are able to withstand the extreme conditions essential for the sedimentation and packing of a wide range of proteins.

These ultracentrifuge tools were used to pack crystalline [U-¹H,¹³C,¹⁵N]GB1 into

a 0.7 mm rotor, which was used for the majority of measurements in **Chapter 4**. The small rotor and cutting-edge MAS were critical for the effective removal of proton-driven spin diffusion in the site-specific $^{13}\text{C}^\alpha$ R_1 measurements on the fully-protonated, uniformly ^{13}C labelled protein. In this chapter, spin diffusion control spectra and spin diffusion saturation transfer measurements revealed that, at 100 kHz MAS, most $^{13}\text{C}^\alpha$ sites were free of the effects of PDSD and therefore relaxation measurements at these sites would be quantitative and site-specific. The nuclei that were still affected by PDSD were close in chemical shift with their neighbouring $^{13}\text{C}^\beta$ nuclei (< 15 ppm). It was concluded that the vast majority of sidechain ^{13}C sites would also be affected by PDSD at 100 kHz MAS, because these ^{13}C sites also have small chemical shift differences with their neighbouring ^{13}C nuclei. Variable MAS ^{13}C R_1 measurements indicated that for all $^{13}\text{C}^\alpha$ sites, even those which had shown some evidence of PDSD, the effects of PDSD are negligible on R_1 if $\text{MAS} \geq 90$ kHz. However, this is definitely not the case for the sidechain ^{13}C nuclei, which show substantial variation in R_1 between 90 and 100 kHz MAS. Finally, $^{13}\text{C}^\alpha$ R_1 measurements, both with and without decoupling in the relaxation delay, revealed that cross-correlated relaxation is suppressed under these conditions without the need for the additional decoupling.

$^{13}\text{C}^\alpha$ R_1 measurements on fully-protonated, uniformly-labelled proteins can be made with confidence at ≥ 90 kHz MAS, without the requirement of complex labelling schemes or expensive deuteration. A further benefit of these measurements is the increased sensitivity, due to all hydrogen and carbon sites in the sample being ^1H or ^{13}C labelled. Maximising sensitivity is always a high priority in SSNMR since it is such an inherently insensitive technique.

In **Chapter 5**, we present some of the first extensive site-specific variable temperature measurements of $^{13}\text{C}'$ and ^{15}N R_1 and $R_{1\rho}$ relaxation rates in a crystalline protein as a way to explore its conformational energy landscape. The measured rates showed strong agreement with those in the literature and similar trends across the protein backbone were observed. For example, the loops and termini of the protein had larger rates in general, which suggests increased mobility at these sites. There was a clear trend of decreasing $R_{1\rho}$ as the temperature increased from -5.15°C to 34.65°C , and although the R_1 rates seemed to subtly decrease in the same way, the changes in R_1 were within the experimental error. A rigid peptide bond joins the $^{13}\text{C}'$ and ^{15}N nuclei between each residue, therefore it is assumed that these sites within an individual peptide plane will be undergoing the same dynamics. Variation is observed between the relaxation rates of $^{13}\text{C}'$ and ^{15}N within the same peptide plane, this is because different timescales of motion contribute to each, as can be seen by the relevant spectral density equations. It is these equations that, along with the model free approach and Arrhenius equation, allow the calculation of order parameters, correlation times and activation energies for each peptide plane. In multiple studies, the simple model free approach has been deemed unsuitable for analysis of this kind of data, because it is unable to sufficiently represent the peptide plane motions.^{158,221,222} Thus the extended model free approach with the

Arrhenius equation was used to analyse the VT ^{13}C and ^{15}N R_1 and $R_{1\rho}$ relaxation rates for each peptide plane. Unfortunately, although the resulting values seemed to be within the correct range, quick testing of the order parameters, correlation times and activation energies revealed that they did not represent the measured relaxation rates accurately enough. It is thought that this analysis was too ambitious for the quantity of data available. However, the measurement of these relaxation rates at different B_0 fields is currently underway, with the aim of combining these datasets with the work presented in this chapter for an improved fitting. This should produce a very informative model of the peptide plane dynamics and energy landscape of the protein.

So far this thesis has provided detailed examples of developments in SSNMR dynamics measurements for proteins. But these SSNMR techniques are extremely versatile, as is demonstrated in **Chapter 6**, where similar relaxation measurements are applied to ice-antifreeze systems. AF(G)Ps are very effective non-colligative antifreezes, but are not particularly suitable for other applications and can be expensive and challenging to produce. Thus the discovery and development of synthetic mimics of AF(G)Ps is of particular interest to researchers. Despite decades of research into AF(G)Ps, no antifreeze mechanism has been agreed upon to date, but it is often suggested that AFGPs and AFPs have different mechanisms of action.^{232,283} The synthetic antifreezes investigated here, PVA¹³⁹ and safranin,²³⁹ were discovered relatively recently (2000 and 2016, respectively), so it is unsurprising that their antifreeze mechanisms are also unknown. In this chapter, SSNMR VT R_1 , R_2 , relaxation dispersion and 2D exchange measurements are used to explore the ^1H dynamics of ice in the presence of non-colligative antifreezes. It was immediately clear, across all measurements, that these low concentrations of antifreeze molecules were having large effects on the ice dynamics (in comparison to the relevant controls). The 2D exchange spectra indicated that all of the antifreezes were binding to ice, and that this was definitely ice, rather than liquid water. The relaxation measurements demonstrated that the AFGP, safranin and PVA were all undergoing a similar slow exchange process and the AFP I was undergoing a different, slightly faster exchange process. The AFP III and control samples showed no signs of chemical exchange. This led to the conclusion that the AFGP, AFP I, PVA and safranin reversibly bind to ice, whereas the AFP III binds irreversibly. This supports the general consensus in the literature that these different types of proteins interact with ice in dramatically different ways, and introduces the idea that PVA and safranin reversibly bind to ice, potentially with a similar mechanism to that of AFGP.

Throughout this investigation, a variety of PVA samples are measured with varying degrees of polymerisation, because the literature states that PVA with a DP < 19 does not act as an effective antifreeze.²²⁹ In all cases, the DP5, DP8 and DP9 PVA samples measured here produce similar results to PEG (the negative control), and these were significantly different to those from DP20, DP150 and DP230 PVA, supporting this hypothesis.

This investigation is the first comprehensive use of a wide selection of SSNMR

relaxation and exchange measurements to study ^1H ice dynamics in the presence of antifreezes. The results presented here significantly enhance the subject area, especially for the synthetic antifreezes, where research into the antifreeze mechanisms is very limited. It is clear that SSNMR can reveal detailed information on these dynamic ice-antifreeze systems. In the future, these SSNMR measurements should be continued on a wider range of proteins, since these results cannot yet be generalised across all types of AFGP, for example. Additionally, SSNMR measurements, such as ^2H and ^{13}C relaxation measurements or 2D exchange spectra of ^{13}C -labelled antifreezes, could help to reveal more about the ice and antifreeze dynamics. Hopefully these measurements, alongside other techniques, will ultimately lead to the determination of antifreeze mechanisms and improve their viability for many applications across science and technology.^{230, 232, 258}

Overall, this thesis has demonstrated that SSNMR relaxation measurements are a powerful technique for investigating dynamic systems and although these measurements are extremely well-developed for proteins, they can be applied to a much wider range of samples, as is explored in **Chapter 6**. The significant advances in SSNMR technology, methodology and applications across the past few decades have moulded it into a unique and increasingly vital tool for the study of these complicated samples, and there is great potential for this rapid development to continue.

Appendices

Appendix A

Theory

A.1 Assignments of Protein GB1

Table A.1: The ^1H , ^{13}C and ^{15}N assignments for crystalline GB1.

| Residue | $^1\text{H}^{\text{N}}$ | $^1\text{H}^{\alpha}$ | $^{13}\text{C}^{\gamma}$ | $^{13}\text{C}^{\alpha}$ | $^{13}\text{C}^{\beta}$ | $^{13}\text{C}^{\gamma}$ | $^{13}\text{C}^{\delta}$ | $^{13}\text{C}^{\epsilon}$ | $^{13}\text{C}^{\zeta}$ | ^{15}N | $^{15}\text{N}^{\delta}$ | $^{15}\text{N}^{\epsilon}$ | $^{15}\text{N}^{\zeta}$ |
|---------|-------------------------|-----------------------|--------------------------|--------------------------|-------------------------|--------------------------|--------------------------|----------------------------|-------------------------|-----------------|--------------------------|----------------------------|-------------------------|
| M1 | 8.6 | | 171.4 | 54.3 | 32.5 | 30.3 | | 15.9 | | 40.0 | | | |
| Q2 | 8.4 | 4.8 | 175.1 | 55.9 | 30.5 | 35.3 | 180.4 | | | 125.2 | | 113.2 | |
| Y3 | 9.4 | 5.4 | 175.0 | 57.0 | 43.7 | 128.5 | 134.7 | 118.3 | 158.3 | 123.3 | | | |
| | | | | | | | 132 | 118.3 | | | | | |
| K4 | 9.5 | 5.1 | 173.3 | 54.9 | 36.3 | 25.7 | 29.1 | 42.2 | | 122.7 | | | 33.1 |
| L5 | 9.5 | 4.8 | 174.8 | 53.0 | 42.5 | 27.4 | 26.0 | | | 127.0 | | | |
| | | | | | | | 25.1 | | | | | | |
| I6 | 9.4 | 4.5 | 175.3 | 60.0 | 37.9 | 27.5 | 12.8 | | | 126.3 | | | |
| | | | | | | 17.6 | | | | | | | |
| L7 | 9.5 | 4.5 | 175.1 | 54.7 | 42.9 | 27.2 | 26.9 | | | 127.1 | | | |
| | | | | | | | 25.1 | | | | | | |
| N8 | 9.2 | 5.5 | 176.4 | 50.7 | 38.4 | 176.6 | | | | 125.1 | 110.9 | | |
| G9 | 8.3 | 4.9 | 173.2 | 44.6 | | | | | | 109.6 | | | |
| | | 3.3 | | | | | | | | | | | |
| K10 | 10.1 | 4.1 | 179.2 | 59.3 | 32.9 | 25.8 | 29.2 | 42.1 | | 121.1 | | | 33.1 |
| T11 | 9 | 4.5 | 173.4 | 61.9 | 69.5 | 22.6 | | | | 106.4 | | | |
| L12 | 7.3 | 4.8 | 173.9 | 54.4 | 43.1 | 27.9 | 26.1 | | | 127.8 | | | |
| | | | | | | | 23 | | | | | | |
| K13 | 9.2 | 5.2 | 175.8 | 53.3 | 38.8 | 26.1 | 29.8 | 43.0 | | 123.3 | | | 33.3 |
| G14 | 8.7 | 5.5 | 171.4 | 44.9 | | | | | | 105.6 | | | |
| | | 3.3 | | | | | | | | | | | |
| E15 | 8.9 | 5.7 | 174.1 | 53.9 | 34.2 | 35.1 | 181.9 | | | 121.1 | | | |
| T16 | 9 | 4.6 | 172.0 | 60.1 | 70.5 | 20.1 | | | | 115.2 | | | |
| T17 | 8.4 | 5.8 | 174.3 | 60.3 | 72.6 | 21.8 | | | | 116.1 | | | |
| T18 | 9.5 | 4.7 | 171.3 | 61.3 | 70.8 | 18.9 | | | | 116.3 | | | |
| E19 | 7.9 | 5.2 | 175.9 | 54.3 | 30.6 | 35.8 | 182.2 | | | 125.4 | | | |
| A20 | 9.5 | 4.8 | 177.8 | 50.7 | 23.7 | | | | | 125.9 | | | |
| V21 | 8.7 | 3.9 | 175.1 | 63.5 | 32.0 | 20.2 | | | | 116.3 | | | |
| | | | | | | 21.2 | | | | | | | |
| D22 | 7.3 | 4.7 | 175.1 | 52.5 | 42.3 | 179.9 | | | | 115.5 | | | |
| A23 | 9.4 | 3.2 | 179.7 | 54.6 | 18.2 | | | | | 122.8 | | | |
| A24 | 8 | 4.1 | 181.5 | 54.5 | 18.2 | | | | | 120.8 | | | |
| T25 | 8.7 | 3.7 | 175.9 | 67.2 | 67.8 | 21.4 | | | | 117.4 | | | |
| A26 | 7.3 | 3.1 | 177.3 | 55.0 | 17.6 | | | | | 124.0 | | | |
| E27 | 9 | 2.7 | 177.8 | 59.1 | 29.1 | 35.5 | 181.7 | | | 116.4 | | | |
| K28 | 7 | 3.7 | 179.2 | 60.2 | 32.8 | 30.1 | 26.5 | 42.3 | | 117.4 | | | 32.6 |
| V29 | 7.6 | 3.5 | 179.0 | 66.3 | 32.0 | 22.2 | | | | 119.3 | | | |
| F30 | 8.7 | 4.8 | 179.1 | 57.5 | 37.5 | 138.4 | 132.3 | 130.9 | | 118.7 | | | |
| K31 | 9.2 | 4.1 | 179.6 | 60.1 | 31.6 | 27.3 | 29.3 | 41.2 | | 120.8 | | | 32.2 |
| Q32 | 7.9 | 4.1 | 177.6 | 58.9 | 29.0 | 34.2 | 180.0 | | | 121.3 | | 115.6 | |
| Y33 | 9 | 4.2 | 178.8 | 61.6 | 37.0 | 129.8 | 132.5 | 118.7 | 159.4 | 121.0 | | | |
| A34 | 9.3 | 3.7 | 179.6 | 56.1 | 18.1 | | | | | 122.7 | | | |
| N35 | 8.5 | 4.4 | 179.6 | 57.0 | 39.3 | 176.1 | | | | 118.2 | 113.2 | | |
| D36 | 9.2 | 4.2 | 176.2 | 55.9 | 38.3 | 177.8 | | | | 121.1 | | | |
| N37 | 7.2 | 4.6 | 174.3 | 53.5 | 40.4 | 176.9 | | | | 115.0 | 114.6 | | |
| G38 | 8 | 4.9 | 174.0 | 46.8 | | | | | | 108.4 | | | |
| | | 2.8 | | | | | | | | | | | |
| V39 | 8.3 | 4.1 | 175.2 | 61.7 | 32.0 | 22.0 | | | | 121.8 | | | |
| | | | | | | 18.2 | | | | | | | |
| D40 | 9.1 | 5.1 | 174.9 | 52.8 | 41.7 | 180.7 | | | | 131.1 | | | |
| G41 | 7.8 | 4.7 | 172.8 | 45.1 | | | | | | 108.1 | | | |
| | | 2.9 | | | | | | | | | | | |
| E42 | 8.7 | 4.8 | 177.9 | 55.1 | 31.5 | 35.7 | 181.8 | | | 119.0 | | | |
| W43 | 9.4 | 5.9 | 177.4 | 57.5 | 33.8 | 111.8 | 127.2 | 138.5 | 114.7 | 125.0 | | 131.7 | |
| | | | | | | | 129.7 | 119.9 | 120.6 | | | | |
| T44 | 9.2 | 5.3 | 174.0 | 60.9 | 73.1 | 21.1 | | | | 109.2 | | | |
| Y45 | 9.5 | 4.6 | 171.9 | 57.8 | 37.6 | 127.8 | 132.5 | 118.8 | 157.5 | 118.6 | | | |
| | | | | | | | 132.2 | 116.2 | | | | | |
| D46 | 7.9 | 4.8 | 176.3 | 50.9 | 42.6 | 180.2 | | | | 126.3 | | | |
| D47 | 8.9 | 4.2 | 177.5 | 54.6 | 43.0 | 179.8 | | | | 123.4 | | | |
| A48 | 8.6 | 4.2 | 179.7 | 54.0 | 19.0 | | | | | 119.0 | | | |
| T49 | 6.9 | 4.2 | 175.8 | 60.3 | 69.9 | 21.6 | | | | 104.2 | | | |
| K50 | 8.3 | 5.1 | 175.5 | 55.6 | 28.0 | 24.4 | 28.3 | 43.3 | | 119.7 | | | 33.9 |
| T51 | 7.4 | 5.4 | 174.4 | 62.5 | 71.7 | 21.3 | | | | 112.0 | | | |
| F52 | 11 | 5.9 | 175.8 | 56.6 | 43.1 | 140.0 | 131.6 | 130.5 | | 130.3 | | | |
| T53 | 9.7 | 5.4 | 172.3 | 60.4 | 71.9 | 21.1 | | | | 112.2 | | | |
| V54 | 8.3 | 4.6 | 172.6 | 58.5 | 32.7 | 21.9 | | | | 118.4 | | | |
| | | | | | | 19.8 | | | | | | | |
| T55 | 8.5 | 4.7 | 174.2 | 61.3 | 72.1 | 21.5 | | | | 124.1 | | | |
| E56 | 8 | 4.6 | 180.5 | 57.6 | 38.8 | 183.2 | | | | 131.1 | | | |

A.2 Calculating the Effect of Spin Diffusion on PDSD

The solution to equations 2.81 and 2.82, which describe the evolution of a two-spin system coupled by spin diffusion, is:

$$\begin{aligned}
 I(t,1) = & \exp(-(t*(RI + RS + 2*\sigma + (RI^2 - 2*RI*RS + RS^2 + 4*\sigma^2)^{1/2}))/2) * ((2*M0*RS^2 + RI^2*S0 - RS^2*S0 + 4*I0*\sigma^2 - S0*(RI^2 - \\
 & 2*RI*RS + RS^2 + 4*\sigma^2) - 2*M0*RI*RS + 2*M0*RS*(RI^2 - 2*RI*RS + RS^2 \\
 & + 4*\sigma^2)^{1/2} - 2*RS*S0*(RI^2 - 2*RI*RS + RS^2 + 4*\sigma^2)^{1/2} \\
 & + 2*I0*RI*\sigma + 2*I0*RS*\sigma - 4*M0*RI*\sigma + 2*I0*\sigma*(RI^2 - \\
 & 2*RI*RS + RS^2 + 4*\sigma^2)^{1/2} + 2*RI*S0*\sigma - 2*RS*S0*\sigma - \\
 & 2*S0*\sigma*(RI^2 - 2*RI*RS + RS^2 + 4*\sigma^2)^{1/2}))/((2*(RI + RS + \\
 & 2*\sigma + (RI^2 - 2*RI*RS + RS^2 + 4*\sigma^2)^{1/2})*(RI^2 - 2*RI*RS + \\
 & RS^2 + 4*\sigma^2)^{1/2}) + (\exp((RI*t)/2 + (RS*t)/2 + (t*(RI^2 - 2*RI*RS \\
 & + RS^2 + 4*\sigma^2)^{1/2}))/2 + \sigma*t)*((2*M0*RI*RS - 2*M0*RS^2 + \\
 & 4*M0*RI*\sigma + 2*M0*RS*(RI + RS + 2*\sigma))/(RI + RS + 2*\sigma \\
 & + (RI^2 - 2*RI*RS + RS^2 + 4*\sigma^2)^{1/2}) - 2*M0*RS))/((2*(RI^2 - \\
 & 2*RI*RS + RS^2 + 4*\sigma^2)^{1/2}))*((RI/2 + RS/2 + \sigma + (RI^2 \\
 & - 2*RI*RS + RS^2 + 4*\sigma^2)^{1/2})/2)/\sigma - (RS + \sigma)/\sigma) \\
 & - \exp(-(t*(RI + RS + 2*\sigma - (RI^2 - 2*RI*RS + RS^2 + 4*\sigma^2)^{1/2}))/2) * ((\exp((RI*t)/2 + (RS*t)/2 - (t*(RI^2 - 2*RI*RS + RS^2 + 4*\sigma^2)^{1/2}))/2 + \sigma*t)*((2*M0*RI*RS - 2*M0*RS^2 + 4*M0*RI*\sigma + 2*M0*RS*(RI + RS + 2*\sigma))/(RI + RS + 2*\sigma - (RI^2 - 2*RI*RS + RS^2 + 4*\sigma^2)^{1/2}) - 2*M0*RS))/((2*(RI^2 - 2*RI*RS + RS^2 + 4*\sigma^2)^{1/2}) + (2*M0*RS^2 + RI^2*S0 - RS^2*S0 + 4*I0*\sigma^2 - S0*(RI^2 - 2*RI*RS + RS^2 + 4*\sigma^2) - 2*M0*RI*RS - 2*M0*RS*(RI^2 - 2*RI*RS + RS^2 + 4*\sigma^2)^{1/2} + 2*RS*S0*(RI^2 - 2*RI*RS + RS^2 + 4*\sigma^2)^{1/2} + 2*I0*RI*\sigma + 2*I0*RS*\sigma - 4*M0*RI*\sigma - 2*I0*\sigma*(RI^2 - 2*RI*RS + RS^2 + 4*\sigma^2)^{1/2} + 2*RI*S0*\sigma - 2*RS*S0*\sigma + 2*S0*\sigma*(RI^2 - 2*RI*RS + RS^2 + 4*\sigma^2)^{1/2}))/((2*(RI + RS + 2*\sigma - (RI^2 - 2*RI*RS + RS^2 + 4*\sigma^2)^{1/2})*(RI^2 - 2*RI*RS + RS^2 + 4*\sigma^2)^{1/2}))*((RI/2 + RS/2 + \sigma - (RI^2 - 2*RI*RS + RS^2 + 4*\sigma^2)^{1/2})/2)/\sigma - (RS + \sigma)/\sigma)
 \end{aligned}$$

Where t is time, RI and RS are the R_1 rates of spins I and S, $I0$ and $S0$ are the magnetisations of the spins at $t = 0$ and σ is the exchange rate of the PDSD.

Appendix B

Development of Tools to Aid the Packing of Proteins into Solid-State NMR Rotors

B.1 Detailed Protocol for the Ultracentrifuge Packing Tools

B.1.1 Sedimenting Samples:

Sample: Concentrated solution.

Tools needed:



Put a small amount of glue onto the rubber seal:



Place inside the funnel (glue side first):



Screw the plug tightly on top and leave to set (for at least 24 hours):



Place the holder over the protruding plug:



Transfer your sample into the top of the funnel:



Assemble another tool in the same way and fill with water so that they have the same mass (to act as a counter balance):



Place the tools in opposite holes in the MLA-150 rotor and screw on the top:



Place the MLA-150 rotor in the ultracentrifuge and then slide the cover back over:



Turn on vacuum and wait for it to get below 100.

Check that the MLA-150 rotor is selected, set to the required speed and time.
(These tools have been tested up to 700,000 g.)

Press go!

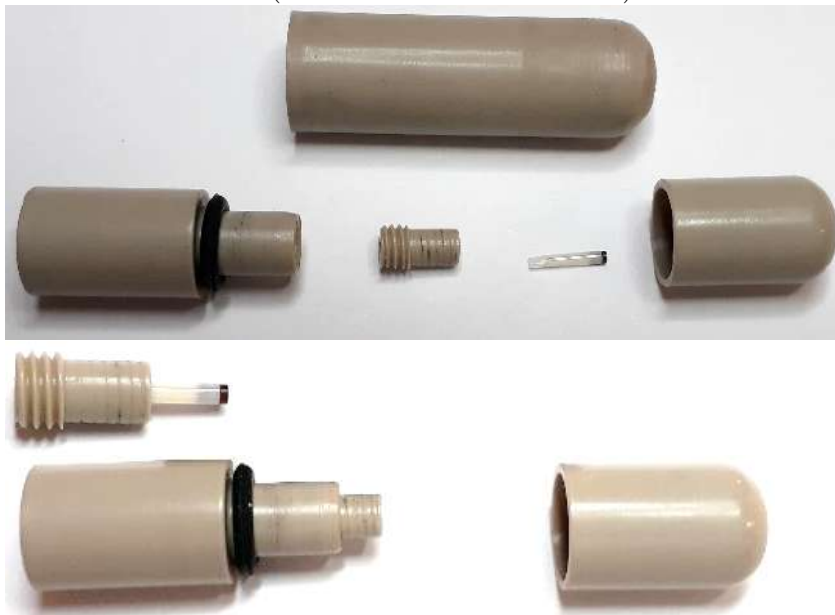
After sedimentation disassemble the rotor and remove excess supernatant from your sample:



Disassemble the tool, replacing the rubber seal and bung with the rotor sleeve and rotor:



Reassemble the tool (with rotor sleeve and rotor):



Place in the adaptor:



Then pack the same using the “Packing Crystalline Sample” instructions and the MLS-50 swinging bucket rotor.

B.1.2 Packing a Crystalline Sample into a Rotor:

Sample: Crystallised and made into a concentrated suspension.

Tools needed:



Place bottom cap on 0.7/0.8/1.3 mm rotor.

Place rotor into rotor sleeve (select the correct size for your rotor):



Screw rotor sleeve into funnel:



Place holder over the protruding rotor sleeve:



The tool is now assembled.

Transfer your sample into the funnel (remember to add the reference if necessary).

Assemble the other tool as above to act as a counter balance (use the rubber seal and plug instead of the rotor sleeve to reducing leaking).

Add the exact amount of water required to the second tool so that the tools have equal mass:



Place the tools into the MLS-50 swinging buckets:



Slot them into the ultracentrifuge rotor (make sure the numbers of the swinging buckets match the numbers of the slots and that the tools are in buckets opposite each other):



Place MLS-50 rotor in the ultracentrifuge and slide the cover back over:



Turn on vacuum and wait for it to get below 100.

Check that the MLS-50 rotor is selected, set the speed to 20,000 g and the timer to 10 minutes.

Press go!

Once 10 minutes has passed and the ultracentrifuge has stopped, release the vacuum.

Remove the tool from the swinging bucket:



Remove the rotor from the tool.

Put top cap on rotor and draw on black mark.

Check rotor under microscope.

B.2 Sedimentation Calculations

Below are the details and parameters required to calculate the possibility and efficiency of sedimentation as has been done in Section 3.6. these values were used with the webtool at py-enmr.cerm.unifi.it/access/index/sednmr. The parameters required for calculating

sedimentation into a 0.7 mm SSNMR rotor using the MLS-50 and MLA-150 tools based on concentration and molecular weight are displayed in Table B.1. In the case of the MLA-150 rotor it was assumed that the rotor was horizontal (keeping b_4 constant) for these calculations, since the effect of gravity should be negligible when the tool is subjected to 700,000 g.

Table B.1: Parameters required for calculating sedimentation into a 0.7 mm SSNMR rotor using the MLS-50 and MLA-150 tools (cm).

| Parameter | MLS-50 Tool (cm) | MLA-150 Tool (cm) |
|------------------|-------------------------|--------------------------|
| r_1 | 0.45 | 0.35 |
| r_2 | 0.05 | 0.05 |
| r_3 | 0.05 | 0.05 |
| h_1 | 1.9 | 0.8 |
| h_2 | 0 | 0 |
| h_3 | 1.6 | 1.6 |
| h_{Max} | 9.58 | 3.99 |
| h_{Tot} | 4.85 | 3.35 |
| h_{Fun} | 2.85 | 1.45 |

Once it has been determined that the protein solution is suitable for sedimentation (dependent on molecular weight and concentration), Equation 3.4 can be used to estimate the sedimentation time (s). Values of b_0 , b_4 , f (rotation rate of the ultracentrifuge in rad s^{-1}) and S (sedimentation coefficient of the protein in 10^{-13} s) are required. The first three parameters are defined in Table B.2 for each tools. The sedimentation coefficient of the protein can often found in the literature or otherwise determined experimentally.

Table B.2: Parameters required for calculating the time for sedimentation into a 0.7 mm SSNMR rotor using the MLS-50 and MLA-150 tools (cm).

| | MLS-50 Tool | MLA-150 Tool |
|-----------------------------|--------------------|---------------------|
| b_0 (cm) | 47.3 | 6.4 |
| b_4 (cm) | 85.6 | 30.7 |
| f (rad s^{-1}) | 314159 | 659734 |

Appendix C

¹H-Detected NMR Measurements of Aliphatic ¹³C R_1 in Fully-Protonated Proteins in the Solid State

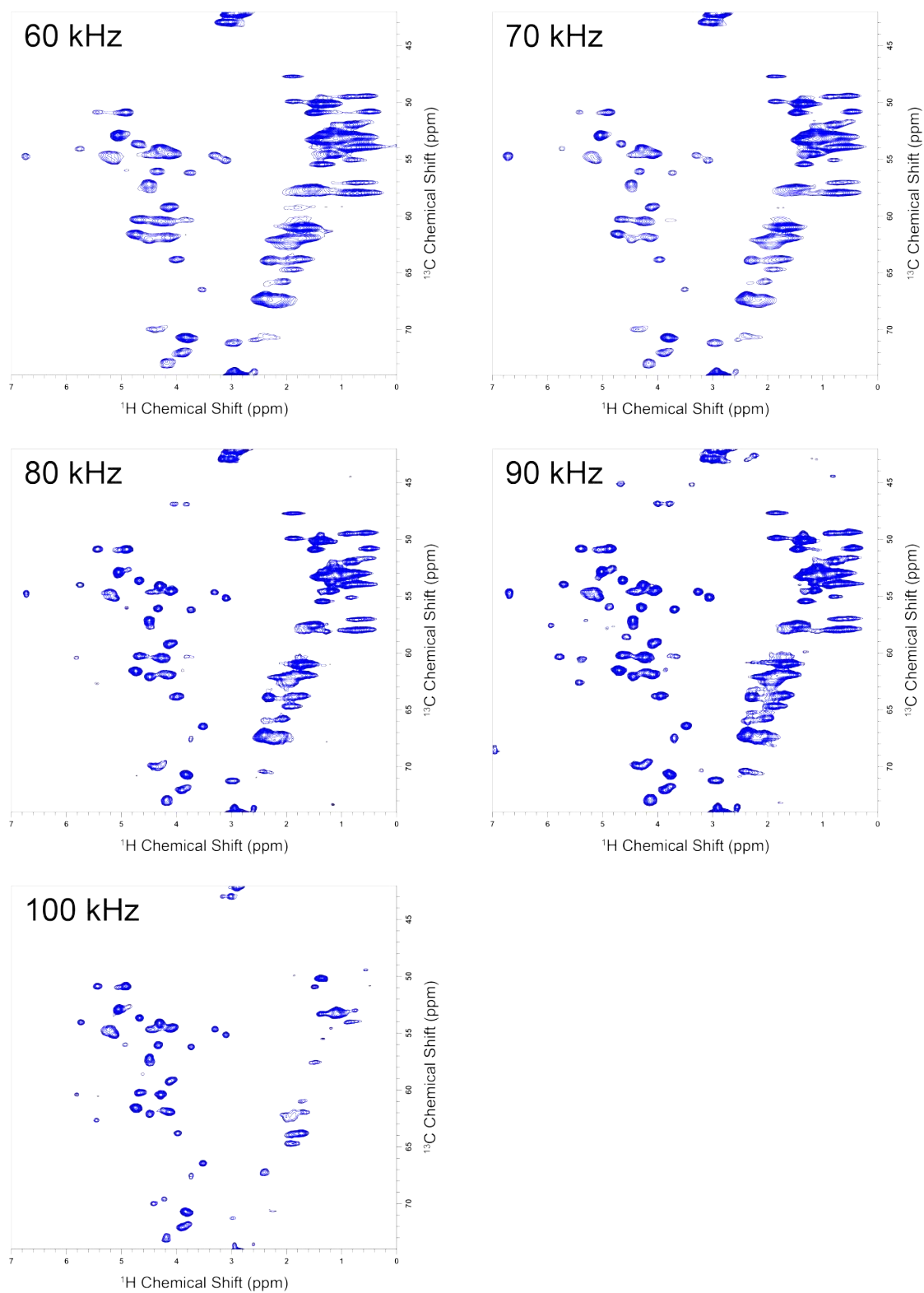


Figure C.1: Aliphatic ^{13}C - ^1H spectra at 60 kHz, 70 kHz, 80 kHz, 90 kHz and 100 kHz MAS and 700 MHz ^1H Larmor frequency for crystalline $[\text{U-}^{13}\text{C},^{15}\text{N}]\text{GB1}$. The improvement in resolution with increasing MAS is evident.

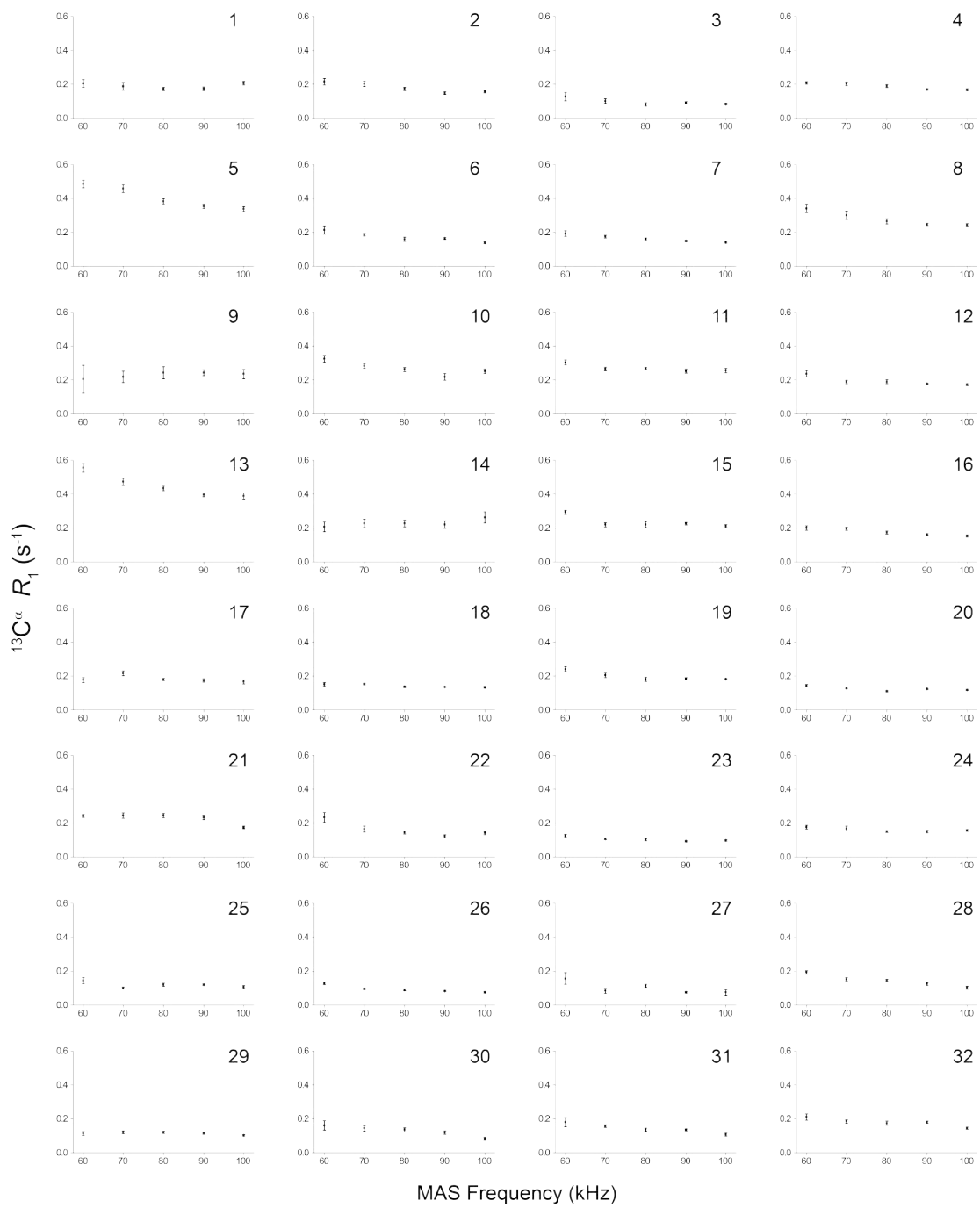


Figure C.2: $^{13}\text{C}^\alpha R_1$ plotted against MAS frequency for residues 1 - 32 of fully protonated crystalline [U- ^{13}C , ^{15}N]GB1 at 700 MHz ^1H Larmor frequency.

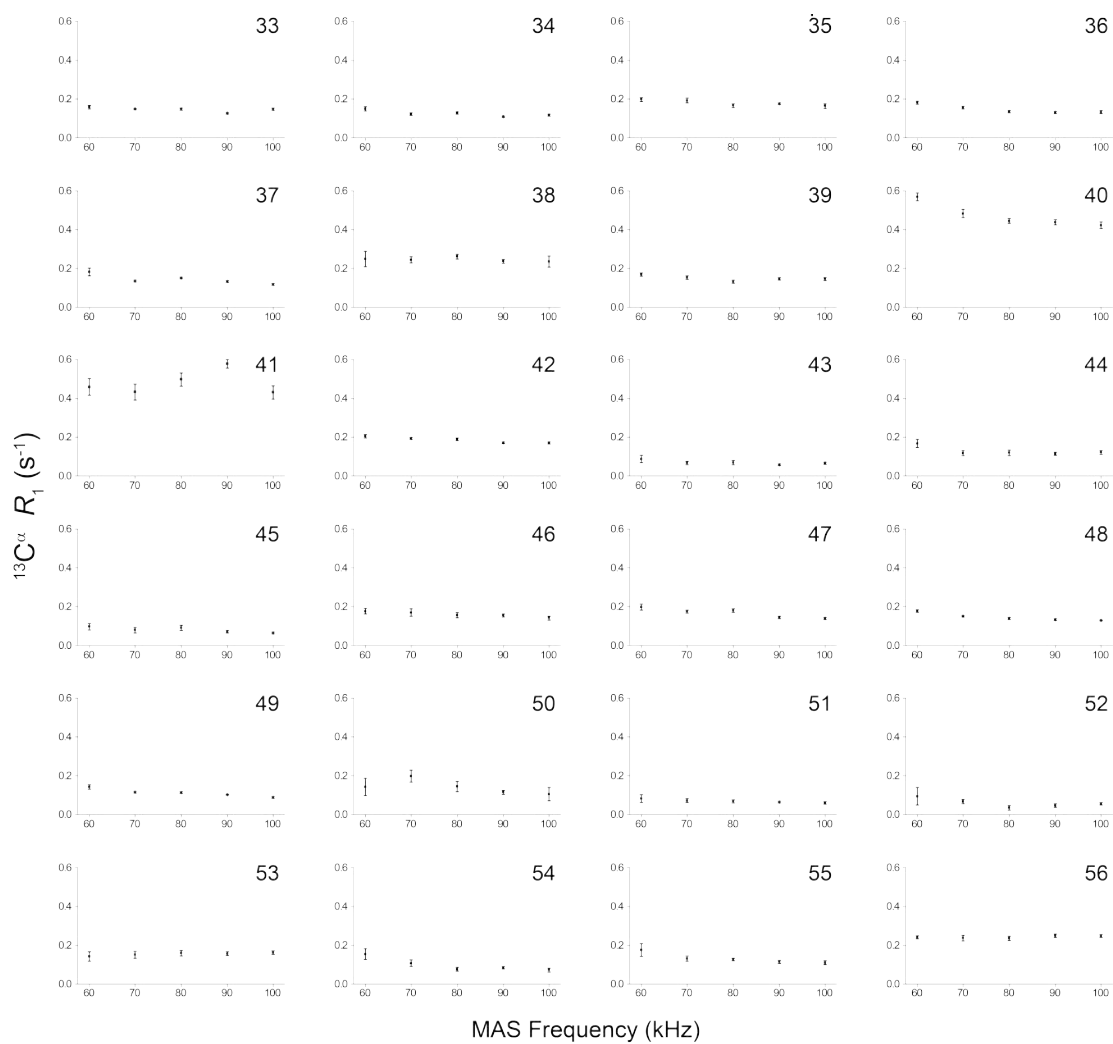


Figure C.3: $^{13}\text{C}_\alpha$ R_1 plotted against MAS frequency for residues 33 - 56 of fully protonated crystalline [U- ^{13}C , ^{15}N]GB1 at 700 MHz ^1H Larmor frequency.

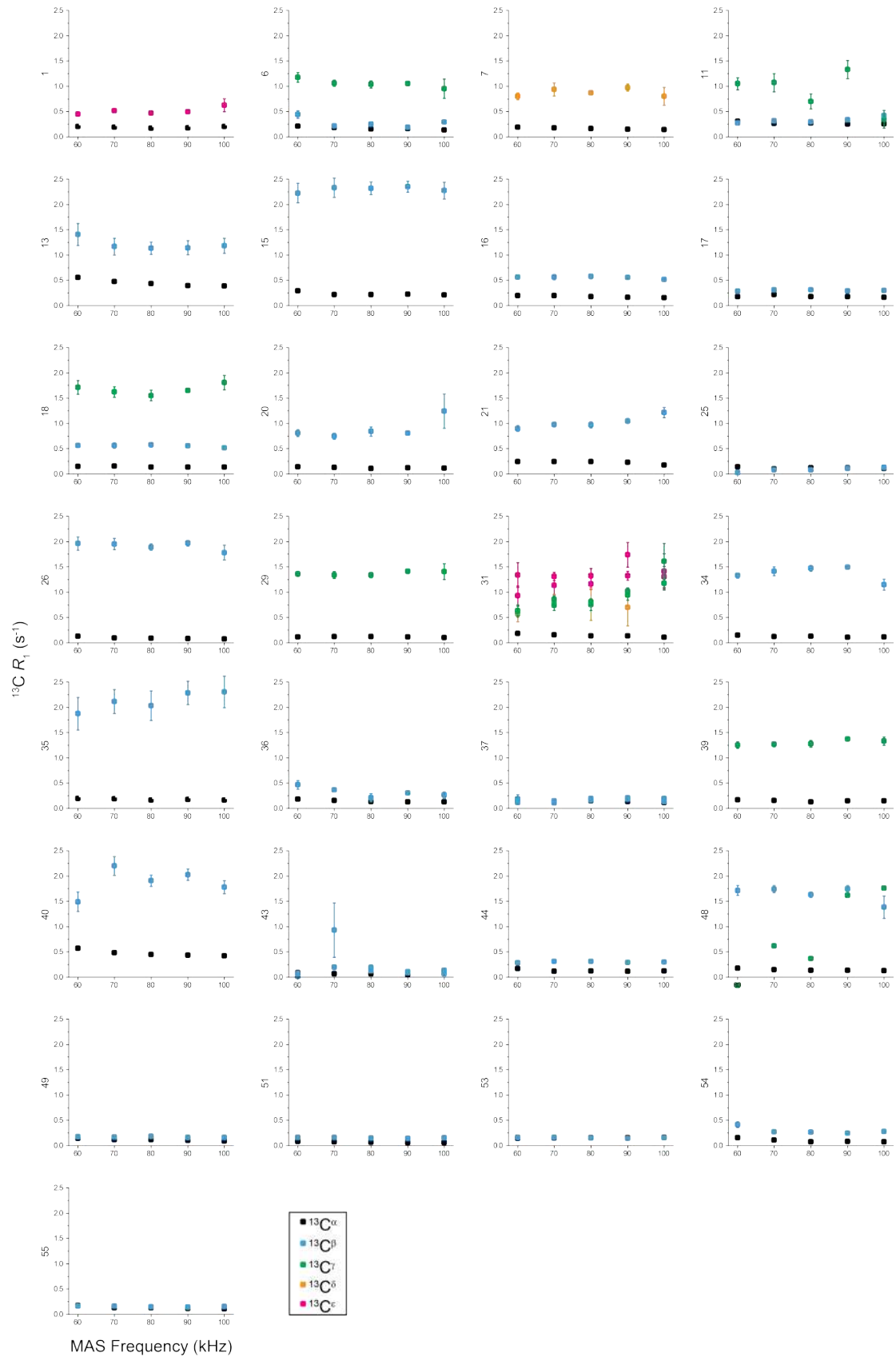


Figure C.4: Sidechain ^{13}C R_1 plotted against MAS frequency for fully protonated crystalline [U- ^{13}C , ^{15}N]GB1 at 700 MHz ^1H Larmor frequency.

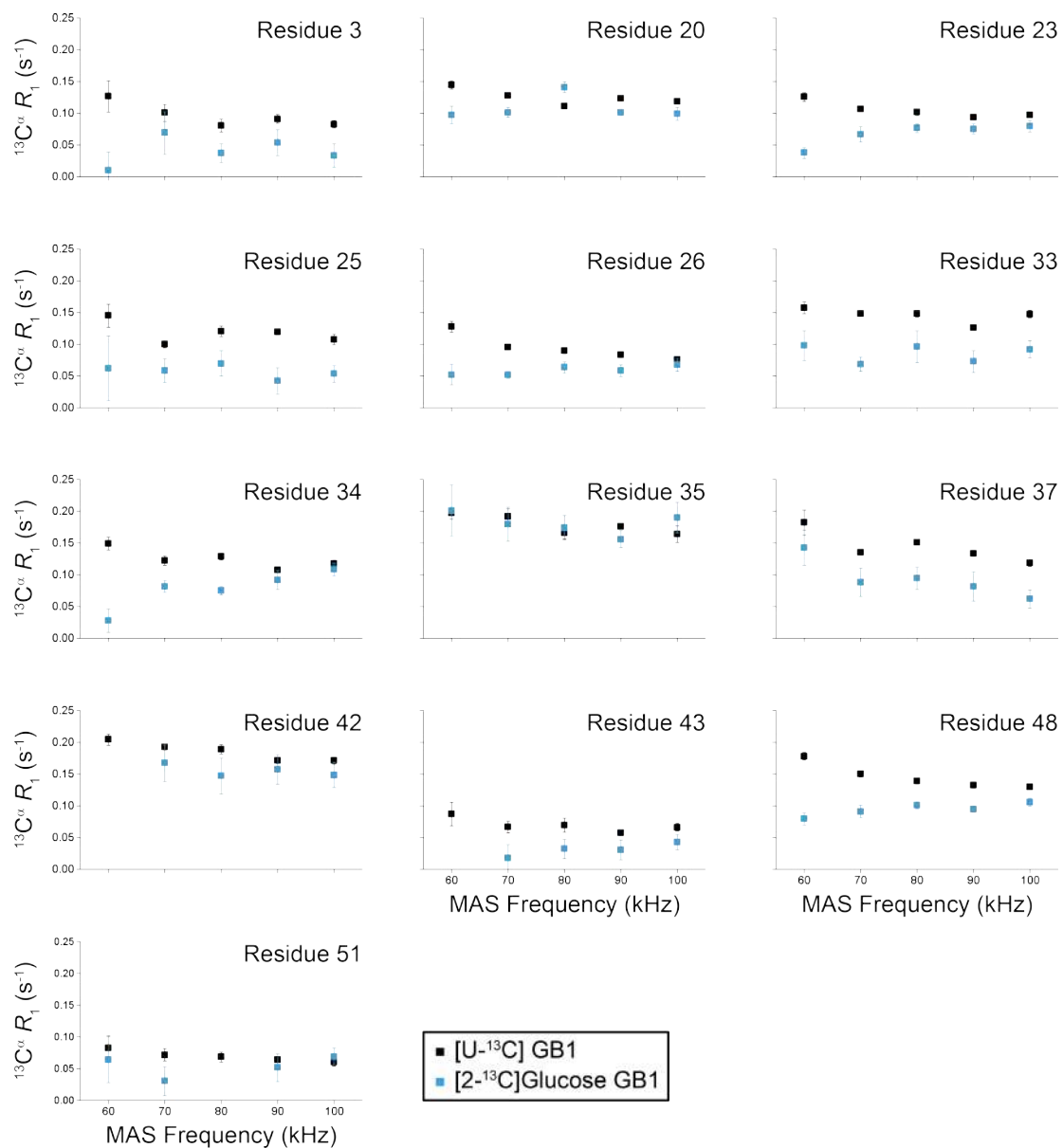


Figure C.5: $^{13}\text{C}^\alpha R_1$ plotted against MAS frequency of fully protonated crystalline [2- ^{13}C (Glucose),U- ^{15}N]GB1 at 600 MHz ^1H Larmor frequency (blue). The relaxation rates for the same $^{13}\text{C}^\alpha$ sites in the uniformly ^{13}C -labelled protein are included as a comparison.

Appendix D

Variable-Temperature, Solid-State NMR Measurements to Investigate the Site-Specific Relaxation and Energy Landscape of GB1

D.1 ^{13}C and ^{15}N R_1 and $R_{1\rho}$ Plotted Against the Inverse Absolute Temperature

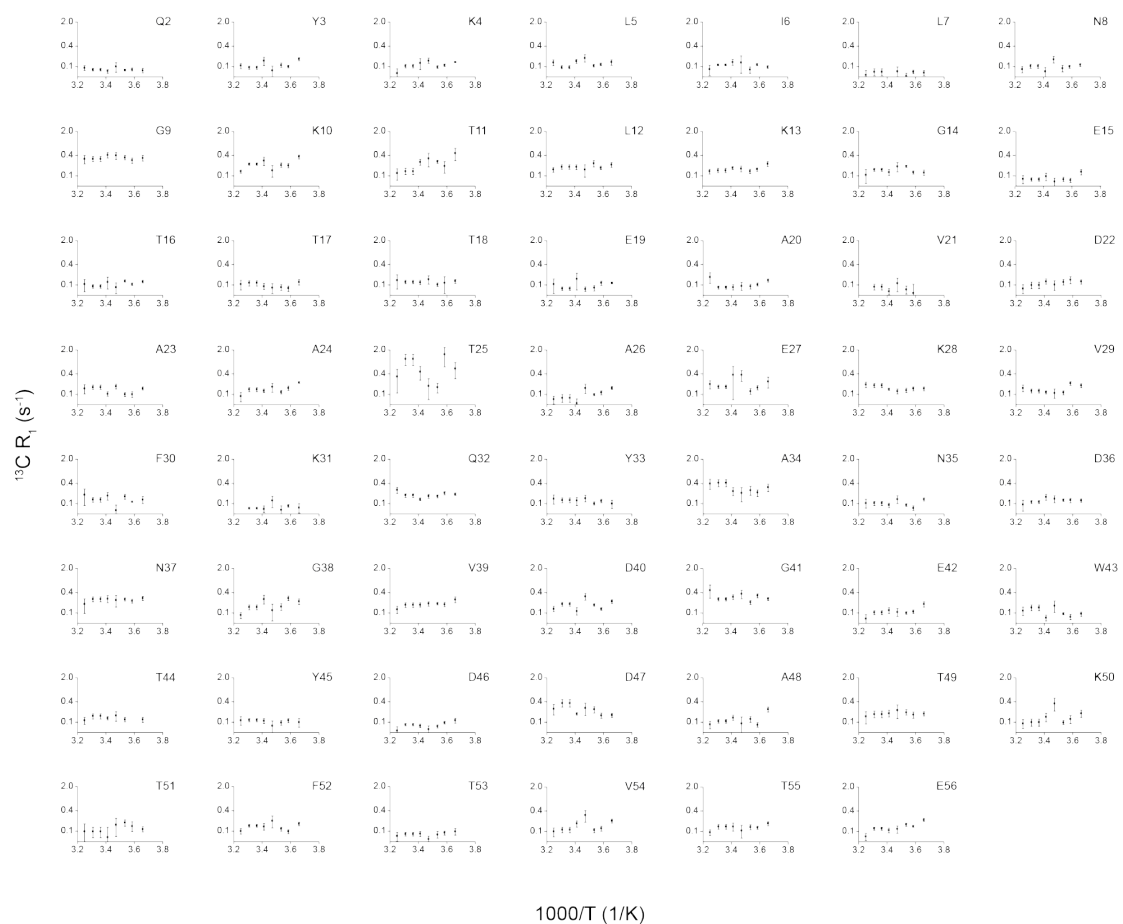


Figure D.1: $^{13}\text{C}' R_1$ plotted against the inverse absolute temperature for each backbone residue in fully back exchanged $[\text{U-}^2\text{H}, ^{13}\text{C}, ^{15}\text{N}]$ GB1 at 600 MHz ^1H Larmor frequency and 50 kHz MAS.

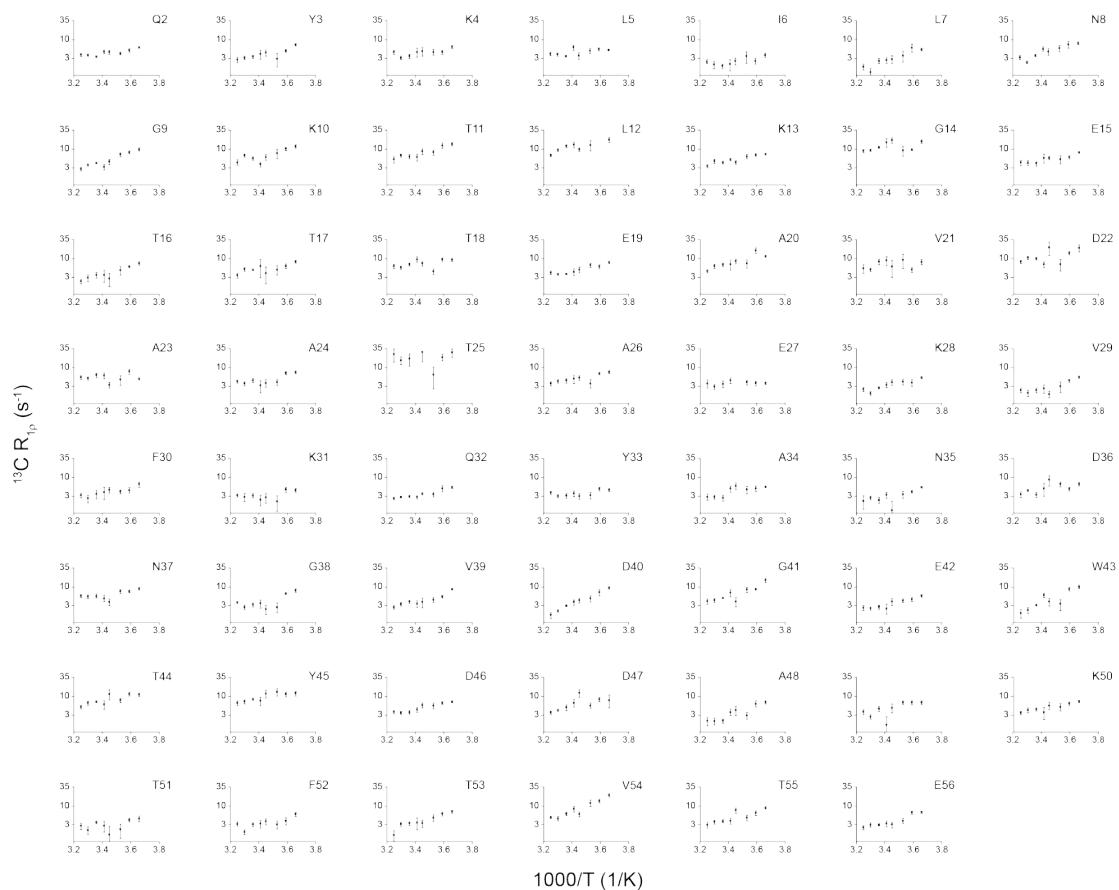


Figure D.2: $^{13}\text{C}' R_{1\rho}$ plotted against the inverse absolute temperature for each backbone residue in fully back exchanged $[\text{U-}^2\text{H}, ^{13}\text{C}, ^{15}\text{N}]$ GB1 at 600 MHz ^1H Larmor frequency and 50 kHz MAS.

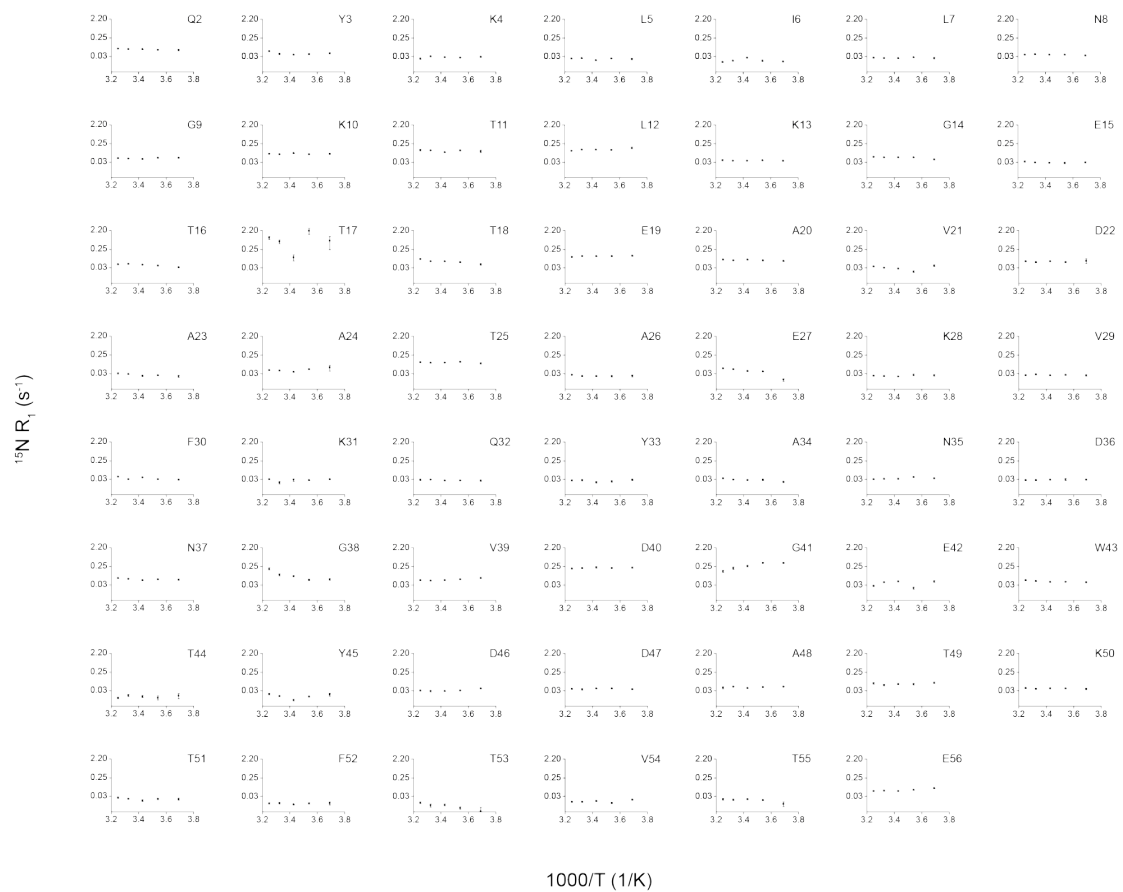


Figure D.3: ^{15}N R_1 plotted against the inverse absolute temperature for each backbone residue in fully back exchanged $[\text{U-}^2\text{H}, ^{13}\text{C}, ^{15}\text{N}]$ GB1 at 600 MHz ^1H Larmor frequency and 50 kHz MAS.

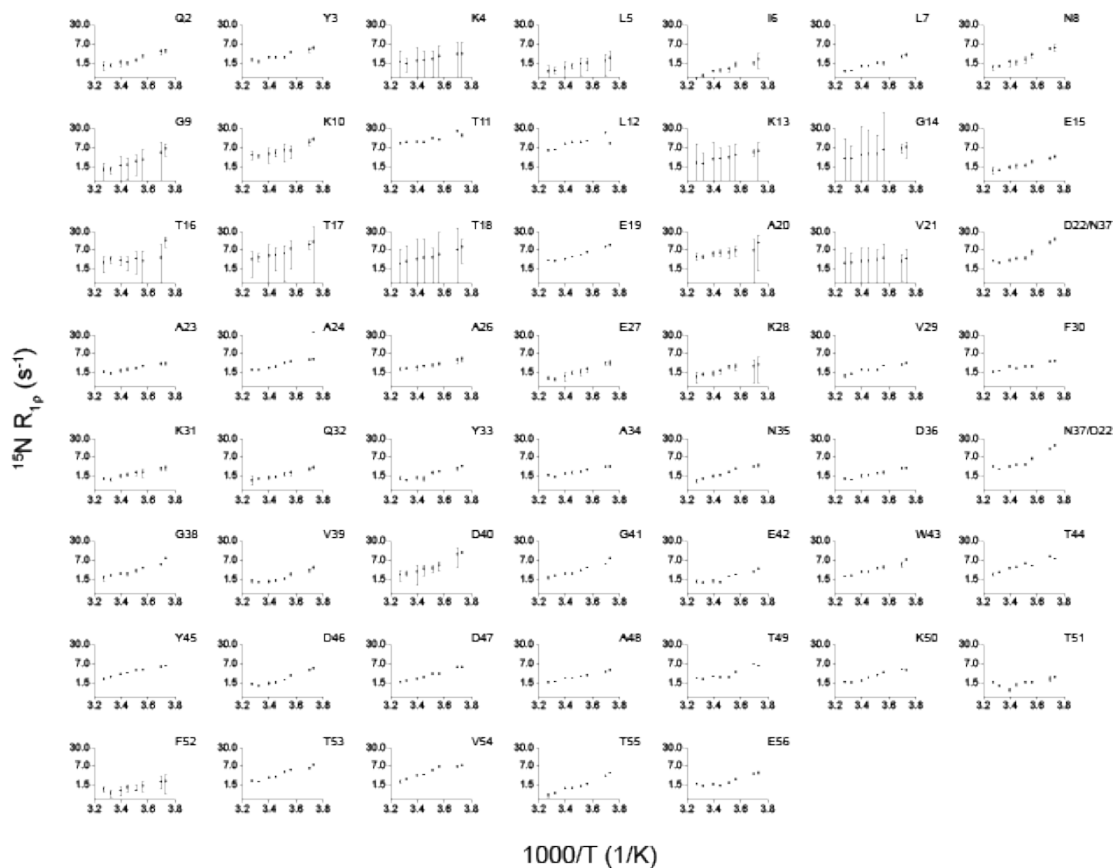


Figure D.4: ^{15}N $R_{1\rho}$ plotted against the inverse absolute temperature for each backbone residue in fully back exchanged $[\text{U-}^2\text{H}, ^{13}\text{C}, ^{15}\text{N}]$ GB1 at 600 MHz ^1H Larmor frequency and 50 kHz MAS.

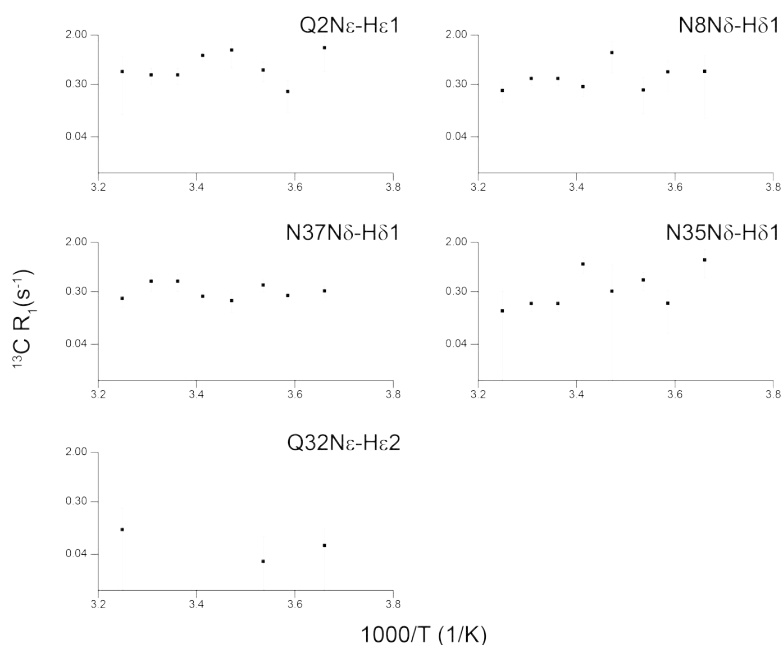


Figure D.5: Sidechain ^{13}C R_1 plotted against the inverse absolute temperature for each residue in fully back exchanged $[\text{U-}^2\text{H}, ^{13}\text{C}, ^{15}\text{N}]$ GB1 at 600 MHz ^1H Larmor frequency and 50 kHz MAS.

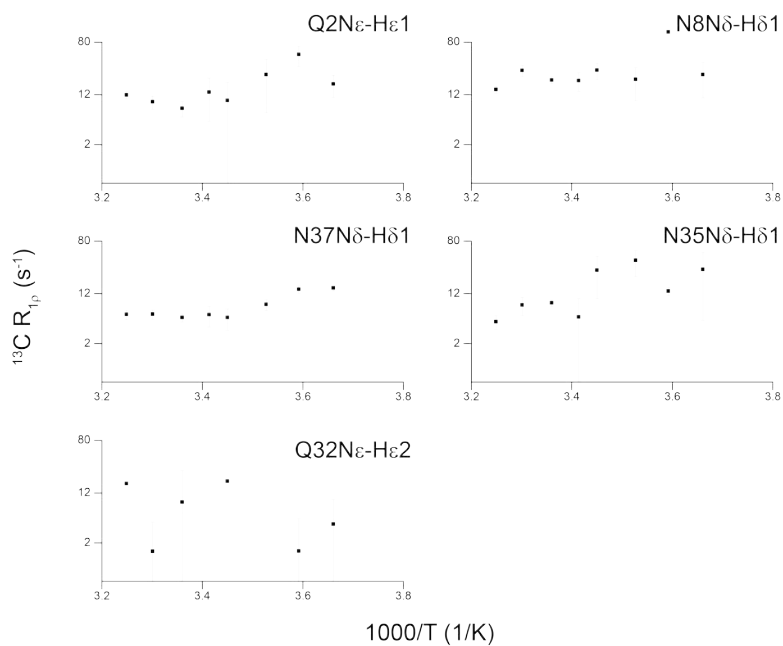


Figure D.6: Sidechain ^{13}C $R_{1\rho}$ plotted against the inverse absolute temperature for each residue in fully back exchanged $[\text{U-}^2\text{H}, ^{13}\text{C}, ^{15}\text{N}]$ GB1 at 600 MHz ^1H Larmor frequency and 50 kHz MAS.

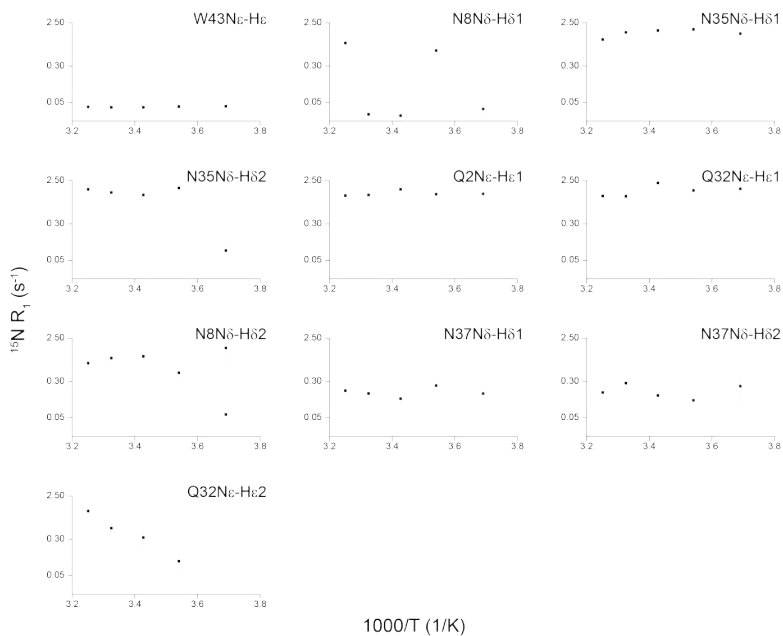


Figure D.7: Sidechain ^{15}N R_1 plotted against the inverse absolute temperature for each residue in fully back exchanged $[\text{U-}^2\text{H}, ^{13}\text{C}, ^{15}\text{N}]$ GB1 at 600 MHz ^1H Larmor frequency and 50 kHz MAS.

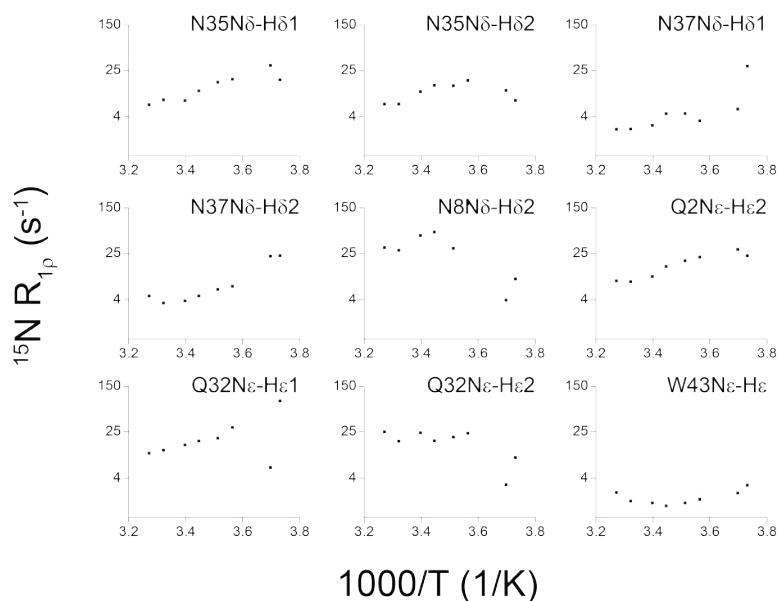


Figure D.8: Sidechain ^{15}N $R_{1\rho}$ plotted against the inverse absolute temperature for each residue in fully back exchanged $[\text{U-}^2\text{H}, ^{13}\text{C}, ^{15}\text{N}]$ GB1 at 600 MHz ^1H Larmor frequency and 50 kHz MAS.

D.2 Calculation of the Correlation Times, Order Parameters and Activation Energies from $^{13}\text{C}'$ and ^{15}N R_1 and $R_{1\rho}$

The *Matlab* scripts used in this chapter are presented below.

Calculation of $^{13}\text{C}'$ and ^{15}N R_1 and $R_{1\rho}$ from the Correlation Times, Order Parameters and Activation Energies

```
function [CR1,CR1rho,NR1,NR1rho]=EMF_13C_15N_R1_R1rho(field,S2s,S2f,tau0s,tau0f,Eas,Eaf,T,Csi,Nsi)

%general constants
h=6.626*10^(-34); %Planck's constant
R=8.314462175; %Ideal gas constant

%Larmor frequencies
gamma_1H=26.75*10^7;
gamma_13C=6.73*10^7;
gamma_15N=2.71*10^7;
field2=field*10^6;
omega_1H=2*pi*field2;
omega_15N=2*pi*(field2/9.869683408806043);
omega_13C=2*pi*(field2/3.976489314034722);

r_CaCprime=1.525*10^(-10);%
r_CprimeH_rest=1.82*10^(-10);%
r_CprimeHn=2.04*10^(-10);%
r_CprimeN=1.3*10^(-10);%
r_CaN=1.46*10^(-10); %
r_NH=1.02*10^(-10); %
r_NH_rest=1.8*10^(-10);%
```

```

dCaCprime=10^(-7)*(gamma_13C*gamma_13C)*(h/(2*pi))/(r_CaCprime^3);
dCprimeH_rest=10^(-7)*(gamma_13C*gamma_1H)*(h/(2*pi))/(r_CprimeH_rest^3);
dCprimeHn=10^(-7)*(gamma_13C*gamma_1H)*(h/(2*pi))/(r_CprimeHn^3);
dCprimeN=10^(-7)*(gamma_13C*gamma_15N)*(h/(2*pi))/(r_CprimeN^3);
dCaN=10^(-7)*(gamma_13C*gamma_15N)*(h/(2*pi))/(r_CaN^3);
dNH=10^(-7)*(gamma_15N*gamma_1H)*(h/(2*pi))/(r_NH^3);
dNH_rest=10^(-7)*(gamma_15N*gamma_1H)*(h/(2*pi))/(r_NH_rest^3);

%15N:
s11N=1.1283*Nsi+93.77;
s22N=1.00086*Nsi-42.475;
s33N=0.8631*Nsi-51.295;

%13C':
s11C=0.24*Csi+200;
s22C=2.82*Csi-305;
s33C=96.5;

d22totN=(s33N^2+s22N^2+s11N^2-s22N*s33N-s22N*s11N-s33N*s11N)*(10^(-6))^2*(omega_15N)^2 ;
d22totC=(s33C^2+s22C^2+s11C^2-s22C*s33C-s22C*s11C-s33C*s11C)*(10^(-6))^2*(omega_13C)^2 ;

%extra sampling frequencies
tauCs = tauOs * (exp (Eas/(R*T)));
tauCf = tauOf * (exp (Eaf/(R*T)));

w1=8000; %spinlock frequency for R1rho
wr=50000; % MAS frequency

omega=0;
J0=(real(1-S2f)* (tauCf/(1+((omega*tauCf).^2))) + S2f*(1-S2s)* (tauCs/(1+((omega*tauCs).^2)) ) );

omega=2*pi*w1;
J01=(real(1-S2f)* (tauCf/(1+((omega*tauCf).^2))) + S2f*(1-S2s)* (tauCs/(1+((omega*tauCs).^2)) ) );

omega=omega_13C;
J1C=(real(1-S2f)* (tauCf/(1+((omega*tauCf).^2))) + S2f*(1-S2s)* (tauCs/(1+((omega*tauCs).^2)) ) );

omega=2*omega_13C;
J2C=(real(1-S2f)* (tauCf/(1+((omega*tauCf).^2))) + S2f*(1-S2s)* (tauCs/(1+((omega*tauCs).^2)) ) );

omega=omega_1H-omega_13C;
J0HC=(real(1-S2f)* (tauCf/(1+((omega*tauCf).^2))) + S2f*(1-S2s)* (tauCs/(1+((omega*tauCs).^2)) ) );

omega= omega_1H+omega_13C;
J2HC=(real(1-S2f)* (tauCf/(1+((omega*tauCf).^2))) + S2f*(1-S2s)* (tauCs/(1+((omega*tauCs).^2)) ) );

omega= omega_1H;
J1H=(real(1-S2f)* (tauCf/(1+((omega*tauCf).^2))) + S2f*(1-S2s)* (tauCs/(1+((omega*tauCs).^2)) ) );

omega=omega_15N+omega_13C;
J2NC=(real(1-S2f)* (tauCf/(1+((omega*tauCf).^2))) + S2f*(1-S2s)* (tauCs/(1+((omega*tauCs).^2)) ) );

omega=-omega_15N+omega_13C;
J0NC=(real(1-S2f)* (tauCf/(1+((omega*tauCf).^2))) + S2f*(1-S2s)* (tauCs/(1+((omega*tauCs).^2)) ) );

omega= omega_15N;
J1N=(real(1-S2f)* (tauCf/(1+((omega*tauCf).^2))) + S2f*(1-S2s)* (tauCs/(1+((omega*tauCs).^2)) ) );

```

```

omega=omega_15N-omega_1H;
JONH=(real(1-S2f)* (tauCf/(1+((omega*tauCf).^2))) + S2f*(1-S2s)* (tauCs/(1+((omega*tauCs).^2)) ) );

omega=omega_15N+omega_1H;
J2NH=(real(1-S2f)* (tauCf/(1+((omega*tauCf).^2))) + S2f*(1-S2s)* (tauCs/(1+((omega*tauCs).^2)) ) );

% 13C CSA autorelaxation
R1rho13CprimeCSA=(1/45)*(d22totC*(4*J01+3*J1C));
R1_13CprimeCSA=(2/15)*(d22totC*(J1C));

% Ca-C' DD autorelaxation
R1rhoCaCprime=(1/5)*(1/4)*dCaCprime*dCaCprime*(4*J01+J0+9*J1C+6*J2C);
R1CaCprime=(1/10)*dCaCprime*dCaCprime*(J0+3*J1C+6*J2C);

% Ca-N DD autorelaxation
R1rhoCaN=(1/5)*(1/4)*(dCaN^2)*(4*J01+3*J1C+J0NC+6*J1C+6*J2NC);
R1CaN=(1/10)*(dCaN^2)*(J0NC+3*J1C+6*J2NC);

% C'-H rest autorelaxation
R1rhoCprimeH_rest=(1/5)*(1/4)*(dCprimeH_rest^2)*(4*J01+3*J1C+J0HC+6*J1H+6*J2HC);
R1CprimeH_rest=(2/5)*(1/4)*(dCprimeH_rest^2)*(J0HC+3*J1C+6*J2HC);

% C'-Hn autorelaxation
R1rhoCprimeHn=(1/5)*(1/4)*(dCprimeHn^2)*(4*J01+3*J1C+J0HC+6*J1H+6*J2HC);
R1CprimeHn=(2/5)*(1/4)*(dCprimeHn^2)*(J0HC+3*J1C+6*J2HC);

% 15N CSA:
R1rho15NCSA=(1/45)*d22totN*(4*J01+3*J1N);
R1_15NCSA=(2/15)*d22totN*(J1N);

% N-H:
R1rhoNH=(1/5)*(1/4)*(dNH^2)*(4*J01+3*J1N+J0NH+6*J1H+6*J2NH);
R1NH=(1/10)*(dNH^2)*(J0NH+3*J1N+6*J2NH);

% N-H rest:
R1rhoNH_rest=(1/5)*(1/4)*(dNH_rest^2)*(4*J01+3*J1N+J0NH+6*J1H+6*J2NH);
R1NH_rest=(1/10)*(dNH_rest^2)*(J0NH+3*J1N+6*J2NH);

%N-C':
R1rhoNCprime=(1/20)*((dCprimeN)^2)*(4*J01+3*J1N+J0NC+6*J1C+6*J2NC);
R1NCprime=(1/20)*((dCprimeN)^2)*(J0NC+3*J1N+6*J2NC);

%C'-N:
R1rhoCprimeN=(1/20)*((dCprimeN)^2)*(4*J01+3*J1C+J0NC+6*J1N+6*J2NC);
R1CprimeN=(1/20)*((dCprimeN)^2)*(J0NC+3*J1C+6*J2NC);

CR1 = R1_13CprimeCSA + R1CaCprime + R1CprimeH_rest + R1CprimeHn + R1CprimeN
CR1rho = R1rho13CprimeCSA + R1rhoCaCprime + R1rhoCprimeH_rest + R1rhoCprimeHn + R1rhoCprimeN
NR1 = R1_15NCSA + R1CaN + R1NH + R1NH_rest + R1NCprime
NR1rho = R1rho15NCSA + R1rhoCaN + R1rhoNH + R1rhoNH_rest + R1rhoNCprime
end

```

Fitting of the $^{13}\text{C}'$ and ^{15}N R_1 and $R_{1\rho}$ to Correlation Times, Order Parameters and Activation Energies

```

function [estimates, model,chi] = FITMIN_EMF_13C_15N_R1_R1rho(field,Temp,iS2s,iS2f,
itau0s,itau0f,iEas,iEaf,a,CR1_INPUT,CR1rho_INPUT,NR1_INPUT,NR1rho_INPUT,C_shifts,N_shifts);

```

```

global Output
start_point = [iS2s,iS2f,ita0s,ita0f,iEas,iEaf];

model = @R1rocking;
[estimates,chi] = fminsearchbnd(model,start_point,[0.2,0.2,1e-20,1e-20,0,0],[1,1,1e-2,1e-2,100000,100000],
optimset('Display','off','MaxFunEvals',200000,'MaxIter',200000,'TolFun',1e-20,'TolX',1e-20));
function [chi, FittedTrend] = R1rocking(params)

for q=1:5;
T=Temp(q);
S2s=params(1);
S2f=params(2);
tau0s=params(3);
tau0f=params(4);
Eas=params(5);
Eaf=params(6);
Csi = C_shifts(a,1);
Nsi = N_shifts(a,1);

[CR1,CR1rho,NR1,NR1rho]=EMF_13C_15N_R1_R1rho(field,S2s,S2f,tau0s,tau0f,Eas,Eaf,T,Csi,Nsi)

chiCR1(q)= (((CR1-(CR1_INPUT(a,2*q)))^2)/((CR1_INPUT(a,1+2*q))^2));
chiCR1rho(q)= (((CR1rho-(CR1rho_INPUT(a,2*q)))^2)/((CR1rho_INPUT(a,1+2*q))^2));
chiNR1rho(q)= (((NR1rho-(NR1rho_INPUT(a,2*q)))^2)/((NR1rho_INPUT(a,1+2*q))^2));
chiNR1(q)= (((NR1-(NR1_INPUT(a,2*q)))^2)/((NR1_INPUT(a,1+2*q))^2));
end

chi=sum(chiCR1) + sum(chiNR1) + sum(chiCR1rho) + sum(chiNR1rho)
end

Output(a,1) = S2s
Output(a,2) = S2f
Output(a,3) = tau0s
Output(a,4) = tau0f
Output(a,5) = Eas
Output(a,6) = Eaf
Output(a,7) = chi
end

```

Using the Above Script for Multiple Peptide Planes

```

for a=1:55
global Output
[estimates, model,chi] =FITMIN_EMF_13C_15N_R1_R1rho(600, Temp, 0.99,0.95,10E-10, 10E-12,
15000,15000, a, CR1_INPUT, CR1rho_INPUT, NR1_INPUT, NR1rho_INPUT, C_shifts, N_shifts)
end

```

Appendix E

Investigating the Effects of “Antifreeze” Compounds on Ice Growth Using Solid-State NMR

E.1 1D ^1H Spectra of the Antifreeze Solutions as Solids and Liquids

As each sample in H_2O freezes the ^1H water peak dramatically decreases in intensity due to the decrease in motion. In most of the liquid spectra, the water peak dwarfs any antifreeze peaks so that they are often not visible. However when the water peak drops in intensity (due to freezing) it sometimes becomes possible to also see peaks due to the antifreeze. The liquid and solid water give significantly different ^1H chemical shifts (see Figure E.1).

Examples of the 1D ^1H spectra of the antifreeze solutions as solids and liquids are shown in Figures E.2 - E.7.

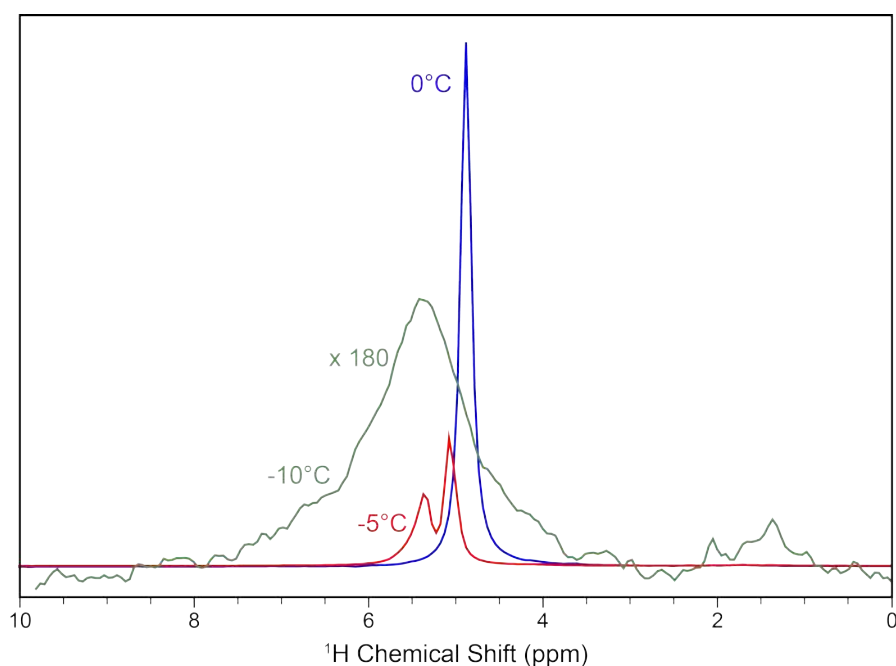


Figure E.1: 1D ^1H spectra of 1 mg/ml DP150 PVA solution at 0.0 $^{\circ}\text{C}$ (blue), -5.0 $^{\circ}\text{C}$ (green) and -10.0 $^{\circ}\text{C}$ (red). The intensity of the -10 $^{\circ}\text{C}$ spectrum has been scaled by 180, in comparison to the -5.0 and 0.0 $^{\circ}\text{C}$ spectra, so that the water peak is visible. It is clear that the liquid and solid water peaks have distinct ^1H chemical shifts. Both can be seen in the -5.0 $^{\circ}\text{C}$ spectrum as the sample freezes.

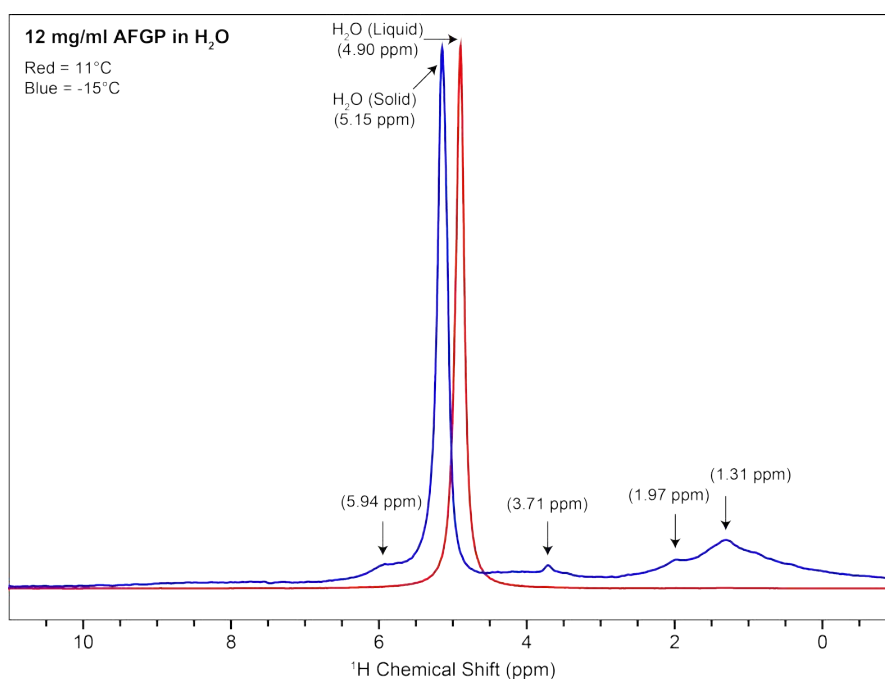


Figure E.2: Assigned 1D ^1H spectra of 12.0 mg/ml AFGP in H_2O at 11 $^{\circ}\text{C}$ (red) and -15 $^{\circ}\text{C}$ (blue). The intensity of the -15 $^{\circ}\text{C}$ spectrum has been scaled by 225, in comparison to the 11 $^{\circ}\text{C}$ spectrum, so that the peaks are visible.

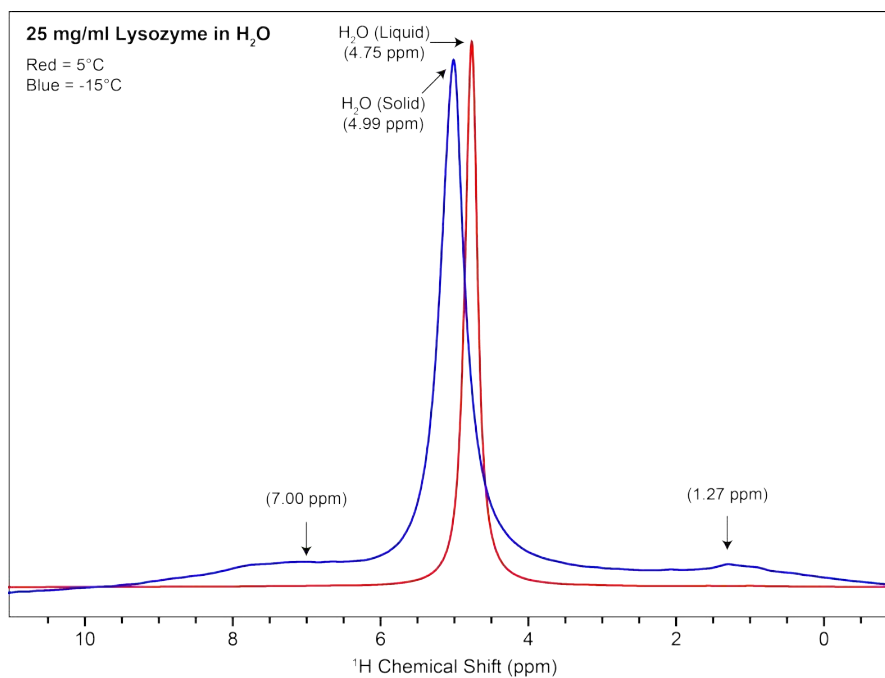


Figure E.3: Assigned 1D ¹H spectra of 25.0 mg/ml Lysozyme in H₂O at 5°C (red) and -15°C (blue). The intensity of the -15°C spectrum has been scaled by 225, in comparison to the 5°C spectrum, so that the peaks are visible.

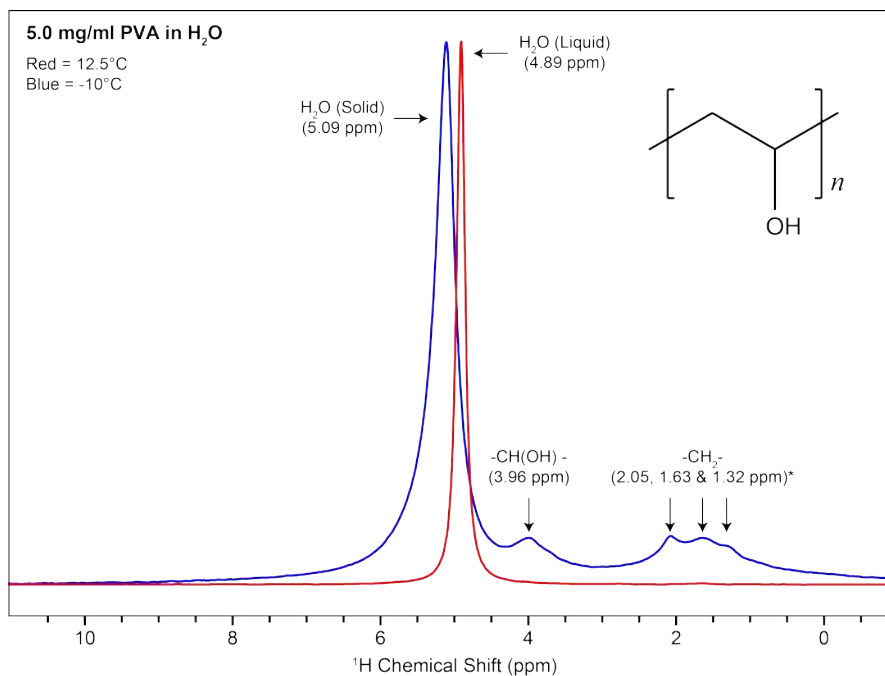


Figure E.4: Assigned 1D ¹H spectra of 5.0 mg/ml PVA in H₂O at 12.5°C (red) and -10°C (blue). *The -CH₂- group produces a multiplet due to the tacticity of the polymer.

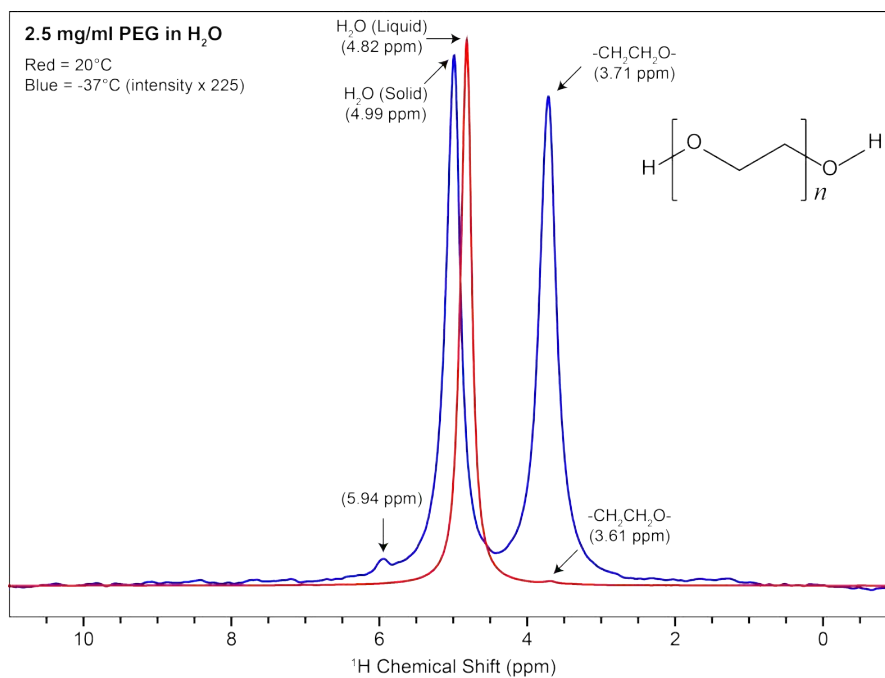


Figure E.5: Assigned 1D ¹H spectra of 2.5 mg/ml PEG in H₂O at 20°C (red) and -30°C (blue). The intensity of the -30°C spectrum has been scaled by 225, in comparison to the 20°C spectrum, so that the peaks are visible.

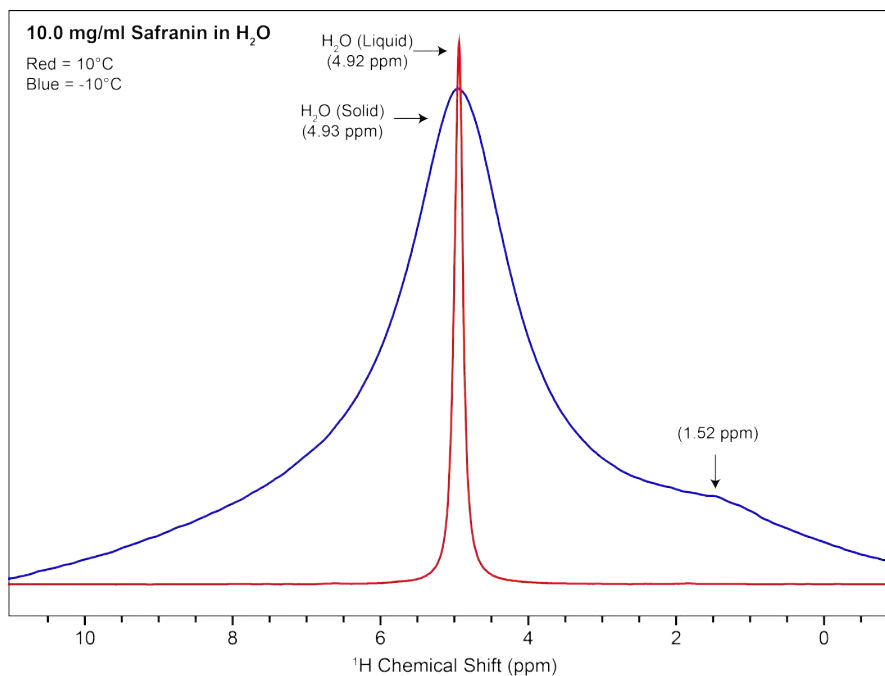


Figure E.6: Assigned 1D ¹H spectra of 10.0 mg/ml Safranin in H₂O at 10°C (red) and -10°C (blue).

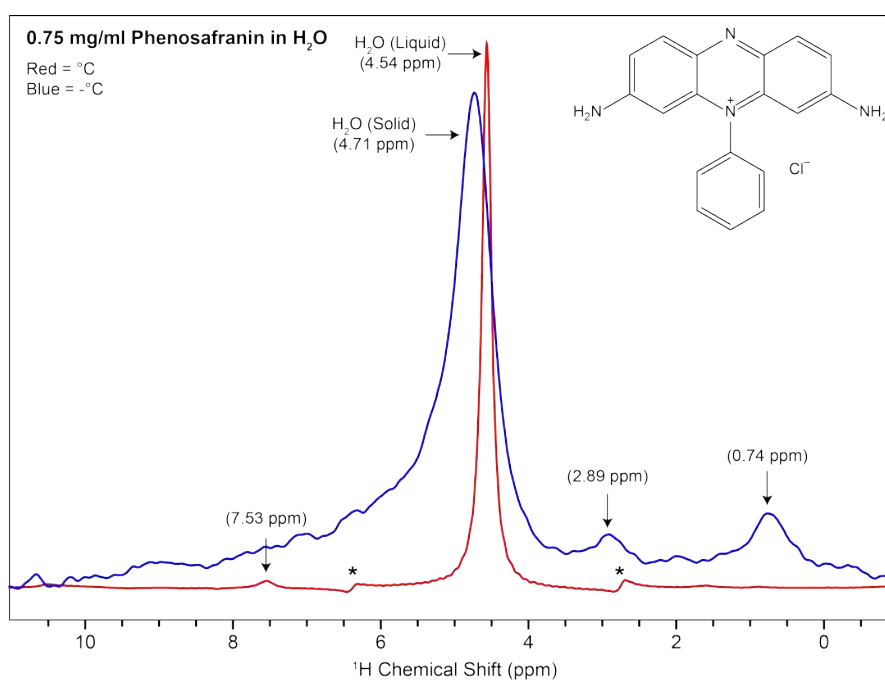


Figure E.7: Assigned 1D ¹H spectra of 0.75 mg/ml Phenosafranin in H₂O at 10°C (red) and -10°C (blue). The asterisks represent spinning side bands since the rotor would not spin stably at 10 kHz so this measurement on the liquid was taken at 1 kHz MAS.

Bibliography

- ¹ Aneta T Petkova, Yoshitaka Ishii, John J Balbach, Oleg N Antzutkin, Richard D Leapman, Frank Delaglio, and Robert Tycko. A structural model for alzheimer's -amyloid fibrils based on experimental constraints from solid state nmr. *Proceedings of the National Academy of Sciences*, 99(26):16742–16747, 2002.
- ² Oleg N Antzutkin, John J Balbach, Richard D Leapman, Nancy W Rizzo, Jennifer Reed, and Robert Tycko. Multiple quantum solid-state nmr indicates a parallel, not antiparallel, organization of -sheets in alzheimer's -amyloid fibrils. *Proceedings of the National Academy of Sciences*, 97(24):13045–13050, 2000.
- ³ Marcus D Tuttle, Gemma Comellas, Andrew J Nieuwkoop, Dustin J Covell, Deborah A Berthold, Kathryn D Kloepper, Joseph M Courtney, Jae K Kim, Alexander M Barclay, and Amy Kendall. Solid-state nmr structure of a pathogenic fibril of full-length human -synuclein. *Nature structural molecular biology*, 23(5):409, 2016.
- ⁴ Patrick C.A. van der Wel. New applications of solid-state nmr in structural biology. *Emerging Topics in Life Sciences*, 2(1):57–67, 2018.
- ⁵ Jonathan M. Lamley, Dinu Iuga, Carl ster, Hans-Juergen Sass, Marco Rogowski, Andres Oss, Jaan Past, Andres Reinhold, Stephan Grzesiek, Ago Samoson, and Jzef R. Lewandowski. Solid-state nmr of a protein in a precipitated complex with a full-length antibody. *Journal of the American Chemical Society*, 136(48):16800–16806, 2014.
- ⁶ J. M. Lamley, C. Oster, R. A. Stevens, and J. R. Lewandowski. Intermolecular interactions and protein dynamics by solid-state nmr spectroscopy. *Angew. Chem. Int. Ed.*, 54(51):15374–15378, 2015.
- ⁷ K. Henzler-Wildman and D. Kern. Dynamic personalities of proteins. *Nature*, 450:964–72, 2007.
- ⁸ David D Boehr, H Jane Dyson, and Peter E Wright. An nmr perspective on enzyme dynamics. *Chemical reviews*, 106(8):3055–3079, 2006.
- ⁹ Katherine A Henzler-Wildman, Ming Lei, Vu Thai, S Jordan Kerns, Martin Karplus, and Dorothee Kern. A hierarchy of timescales in protein dynamics is linked to enzyme catalysis. *Nature*, 450(7171):913, 2007.
- ¹⁰ Robert G Bryant. The nmr time scale. *Journal of Chemical Education*, 60(11):933, 1983.
- ¹¹ V. Agarwal, Y. Xue, B. Reif, and N. R. Skrynnikov. Protein side-chain dynamics as observed by solution- and solid-state nmr spectroscopy: A similarity revealed. *J. Am. Chem. Soc.*, 130:16611–21, 2008.

- ¹² O Jardetzky and NG Wade-Jardetzky. Comparison of protein structures by high resolution solid state and solution nmr. *FEBS letters*, 110(1):133–135, 1980.
- ¹³ W. T. Franks, D.H. Zhou, B.J. Wylie, B.G. Money, D.T. Graesser, H.L. Frericks, G. Sahota, and C.M. Rienstra. Magic-angle spinning solid-state nmr spectroscopy of the beta-1 immunoglobulin binding domain of protein g (gb1): ¹⁵n and ¹³c chemical shift assignments and conformational analysis. *JACS*, 127:12291–305, 2005.
- ¹⁴ Veniamin Chevelkov, Yi Xue, Rasmus Linser, Nikolai R Skrynnikov, and Bernd Reif. Comparison of solid-state dipolar couplings and solution relaxation data provides insight into protein backbone dynamics. *Journal of the American Chemical Society*, 132(14):5015–5017, 2010.
- ¹⁵ Atsuo Tamura, Michio Matsushita, Akira Naito, Shuichi Kojima, KinIchiro Miura, and Kazuyuki Akasaka. Dynamics of the three methionyl side chains of streptomyces subtilisin inhibitor. deuterium nmr studies in solution and in the solid state. *Protein Science*, 5(1):127–139, 1996.
- ¹⁶ Jonathan M. Lamley and Jzef R. Lewandowski. *Relaxation-Based Magic-Angle Spinning NMR Approaches for Studying Protein Dynamics*. John Wiley and Sons, Ltd, 2016.
- ¹⁷ V. Chevelkov, A. Diehl, and B. Reif. Quantitative measurement of differential ¹⁵nha/b t2 relaxation rates in a perdeuterated protein by mas solid-state nmr spectroscopy. *Magn. Reson. Chem.*, 45(S1):156–60, 2007.
- ¹⁸ Edward M Purcell, H Co Torrey, and Robert V Pound. Resonance absorption by nuclear magnetic moments in a solid. *Physical review*, 69(1-2):37, 1946.
- ¹⁹ F.; Block, W.W. Hansen, and M. Packard. *Physical Review*, 70:474, 1946.
- ²⁰ E. R. Andrew, A. Bradbury, and R. G. Eades. Nuclear magnetic resonance spectra from a crystal rotated at high speed. *Nature*, 182:1659, 1958.
- ²¹ I. J. Lowe. Free induction decays of rotating solids. *Physical Review Letters*, 2(7):285–287, 1959.
- ²² Ago Samoson, Tiit Tuherm, Jean Past, Andres Reinhold, Tiit Anupld, and Ivo Heinmaa. *New Horizons for Magic-Angle Spinning NMR*, pages 15–31. Springer Berlin Heidelberg, Berlin, Heidelberg, 2005.
- ²³ V. Agarwal, S. Penzel, K. Szekely, R. Cadalbert, E. Testori, A. Oss, J. Past, A. Samoson, M. Ernst, A. Bockmann, and B. H. Meier. De novo 3d structure determination from sub-milligram protein samples by solid-state 100 khz mas nmr spectroscopy. *Angew. Chem. Int. Ed.*, 53:1–5, 2014.
- ²⁴ Yoshitaka Ishii, Ayesha Wickramasinghe, Isamu Matsuda, Yuki Endo, Yuji Ishii, Yusuke Nishiyama, Takahiro Nemoto, and Takayuki Kamihara. Progress in proton-detected solid-state nmr (ssnmr): Super-fast 2d ssnmr collection for nano-mole-scale proteins. *Journal of Magnetic Resonance*, 286:99–109, 2018.
- ²⁵ Susanne Penzel, Albert A. Smith, Vipin Agarwal, Andreas Hunkeler, Mai-Liis Org, Ago Samoson, Anja Bckmann, Matthias Ernst, and Beat H. Meier. Protein resonance assignment at mas frequencies approaching 100khz: a quantitative comparison of j-coupling and dipolar-coupling-based transfer methods. *Journal of Biomolecular NMR*, 63(2):165–186, 2015.

- ²⁶ J. R. Lewandowski. Advances in solid-state relaxation methodology for probing site-specific protein dynamics. *Acc. Chem. Res.*, 46(9):2018–27, 2013.
- ²⁷ S. F. Lienin, T. Bremi, B. Brutscher, R. Bruschweiler, and R. R. Ernst. Anisotropic intramolecular backbone dynamics of ubiquitin characterized by nmr relaxation and md computer simulation. *J. Am. Chem. Soc.*, 120:9870–9879, 1998.
- ²⁸ G. Lipari and A. Szabo. Model-free approach to the interpretation of nuclear magnetic resonance relaxation in macromolecules. 1. theory and range of validity. *J. Am. Chem. Soc.*, 104(17):4546–59, 1982.
- ²⁹ G. Lipari and A. Szabo. Model-free approach to the interpretation of nuclear magnetic resonance relaxation in macromolecules. 2. analysis of experimental results. *J. Am. Chem. Soc.*, 104:4559–70, 1982.
- ³⁰ J. R. Lewandowski, M. E. Halse, M. Blackledge, and L. Emsley. Direct observation of hierarchical protein dynamics. *Science*, 348(6234):578–81, 2015.
- ³¹ J. Keeler. *Understanding NMR Spectroscopy*. John Wiley and Sons Ltd, UK, 2010.
- ³² M. H. Levitt. *Spin Dynamics: Basics of Nuclear Magnetic Resonance*. John Wiley and Sons Ltd, UK, 2008.
- ³³ Peter J Hore. *Nuclear magnetic resonance*. Oxford University Press, USA, 2015.
- ³⁴ Peter Hore, Jonathan Jones, and Stephen Wimperis. *NMR: The toolkit: How pulse sequences work*. Oxford University Press, USA, 2015.
- ³⁵ David C Apperley, Robin K Harris, and Paul Hodgkinson. *Solid-state NMR: Basic principles and practice*. Momentum Press, 2012.
- ³⁶ Melinda J Duer. *Introduction to solid-state NMR spectroscopy*. Wiley-Blackwell, 2005.
- ³⁷ Anne E McDermott and Tatyana Polenova. *Solid state NMR studies of biopolymers*. John Wiley and Sons, 2012.
- ³⁸ J Mason. Conventions for the reporting of nuclear magnetic shielding (or shift) tensors suggested by participants in the nato arw on nmr shielding constants at the university of maryland, college park, july 1992. *Solid state nuclear magnetic resonance*, 2(5):285, 1993.
- ³⁹ Yusuke Nishiyama. Fast magic-angle sample spinning solid-state nmr at 60100 khz for natural abundance samples. *Solid State Nuclear Magnetic Resonance*, 78:24–36, 2016.
- ⁴⁰ S. Hediger, B. H. Meier, and M. Ernst. Adiabatic passage hartmann-hahn cross polarization in nmr under magic angle sample spinning. *Chem. Phys. Lett.*, 240:449–456, 1995.
- ⁴¹ Ren Verel and Beat H. Meier. Polarization-transfer methods in solid-state magic-angle-spinning nmr: Adiabatic cn pulse sequences. 5(6):851–862, 2004.
- ⁴² G. Metz, X. L. Wu, and S. O. Smith. Ramped-amplitude cross polarization in magic-angle-spinning nmr. *Journal of Magnetic Resonance, Series A*, 110(2):219–227, 1994.

- ⁴³ Diane Cala-De Paepe, Jan Stanek, Kristaps Jaudzems, Kaspars Tars, Loren B. Andreas, and Guido Pintacuda. Is protein deuteration beneficial for proton detected solid-state nmr at and above 100khz magic-angle spinning? *Solid State Nuclear Magnetic Resonance*, 87:126–136, 2017.
- ⁴⁴ Geoffrey Bodenhausen and David J. Ruben. Natural abundance nitrogen-15 nmr by enhanced heteronuclear spectroscopy. *Chemical Physics Letters*, 69(1):185–189, 1980.
- ⁴⁵ Yoshitaka Ishii, James P. Yesinowski, and Robert Tycko. Sensitivity enhancement in solid-state ¹³c nmr of synthetic polymers and biopolymers by ¹h nmr detection with high-speed magic angle spinning. *Journal of the American Chemical Society*, 123(12):2921–2922, 2001.
- ⁴⁶ B. Reif and R. G. Griffin. ¹h detected ¹h,¹⁵n correlation spectroscopy in rotating solids. *Journal of Magnetic Resonance*, 160(1):78–83, 2003.
- ⁴⁷ Andrew E. Bennett, Chad M. Rienstra, Michle Auger, K. V. Lakshmi, and Robert G. Griffin. Heteronuclear decoupling in rotating solids. 103(16):6951–6958, 1995.
- ⁴⁸ Mrignayani Kotecha, Nalinda P. Wickramasinghe, and Yoshitaka Ishii. Efficient low-power heteronuclear decoupling in ¹³c high-resolution solid-state nmr under fast magic angle spinning. *Magnetic Resonance in Chemistry*, 45(S1):S221–S230, 2007.
- ⁴⁹ A. J. Shaka, James Keeler, and Ray Freeman. Evaluation of a new broadband decoupling sequence: Waltz-16. *Journal of Magnetic Resonance (1969)*, 53(2):313–340, 1983.
- ⁵⁰ Zhe Zhou, Rainer Kmmmerle, Xiaohua Qiu, David Redwine, Rongjuan Cong, Angela Taha, Dan Baugh, and Bill Winniford. A new decoupling method for accurate quantification of polyethylene copolymer composition and triad sequence distribution with ¹³c nmr. *Journal of Magnetic Resonance*, 187(2):225–233, 2007.
- ⁵¹ Donghua H. Zhou and Chad M. Rienstra. High-performance solvent suppression for proton detected solid-state nmr. *Journal of Magnetic Resonance*, 192(1):167–172, 2008.
- ⁵² David M. LeMaster and Diana M. Kushlan. Dynamical mapping of e. coli thioredoxin via ¹³c nmr relaxation analysis. *Journal of the American Chemical Society*, 118(39):9255–9264, 1996.
- ⁵³ P. Lundstrom, K. Teilum, T. Carstensen, I. Bezsonova, S. Wiesner, D. Fleming Hansen, T. L. Religa, M. Akke, and L. E. Kay. Fractional ¹³c enrichment of isolated carbons using 1 ¹³c or 2 ¹³c glucose facilitates the accurate measurement of dynamics at backbone ca and side chain methyl positions in proteins. *J. Biomol. NMR*, 38:199–212, 2007.
- ⁵⁴ F. Castellani, B. van Rossum, A. Diehl, M. Schubert, K. Rehbein, and H. Oschkinat. Structure of a protein determined by solid-state magic-angle-spinning nmr spectroscopy. *Nature*, 420:98–102, 2002.
- ⁵⁵ Victoria A. Higman, Jeremy Flinders, Matthias Hiller, Stefan Jehle, Stefan Markovic, Sebastian Fiedler, Barth-Jan van Rossum, and Hartmut Oschkinat. Assigning large proteins in the solid state: a mas nmr resonance assignment strategy using selectively and extensively ¹³c-labelled proteins. *Journal of Biomolecular NMR*, 44(4):245–260, 2009.

- ⁵⁶ M. Hong and K. Jakes. Selective and extensive ^{13}C labeling of a membrane protein for solid-state nmr investigations. *Journal of Biomolecular NMR*, 14(1):71–74, 1999.
- ⁵⁷ Alexey G. Krushelnitsky, Gnter Hempel, and Detlef Reichert. Simultaneous processing of solid-state nmr relaxation and 1d-mas exchange data: the backbone dynamics of free vs. binase-bound barstar. *Biochimica et Biophysica Acta (BBA) - Proteins and Proteomics*, 1650(1):117–127, 2003.
- ⁵⁸ D. Marion and K. Wthrich. Application of phase sensitive two-dimensional correlated spectroscopy (cosy) for measurements of 1h-1h spin-spin coupling constants in proteins. *Biochemical and Biophysical Research Communications*, 113(3):967–974, 1983.
- ⁵⁹ G. M. Clore, A. Szabo, A. Bax, L. E. Kay, P. C. Driscoll, and A. M. Gronenborn. Deviations from the simple two-parameter model-free approach to the interpretation of nitrogen-15 nuclear magnetic relaxation of proteins. *J. Am. Chem. Soc.*, 112(12):4989–91, 1990.
- ⁶⁰ Jeffrey L Evelhoch and Joseph JH Nmr t1 measurements in inhomogeneous b1 with surface coils. 53(1):52–64, 1983. (1969).
- ⁶¹ Ray Freeman and HDW Fourier transform study of nmr spinlattice relaxation by progressive saturation. 54(8):3367–3377, 1971.
- ⁶² Dennis A. Torchia. The measurement of proton-enhanced carbon-13 t1 values by a method which suppresses artifacts. *Journal of Magnetic Resonance (1969)*, 30(3):613–616, 1978.
- ⁶³ George G McDonald and John S Leigh Jr. A new method for measuring longitudinal relaxation times. *Journal of Magnetic Resonance*, 9(3):358–362, 1973. (1969).
- ⁶⁴ John L Markley, William J Horsley, and Melvin P Klein. Spinlattice relaxation measurements in slowly relaxing complex spectra. *The Journal of Chemical Physics*, 55(7):3604–3605, 1971.
- ⁶⁵ N. Bloembergen, E. M. Purcell, and R.V. Pound. Relaxation effects in nuclear magnetic resonance absorption. *Physical Review*, 73(7):679 – 712, 1948.
- ⁶⁶ I. R. Kleckner and M. P. Foster. An introduction to nmr-based approaches for measuring protein dynamics. *Biochimica et Biophysica Acta*, pages 942–68, 2011.
- ⁶⁷ J. M. B. H. Jeener, B. H. Meier, P. Bachmann, and R. R. Ernst. Investigation of exchange processes by twodimensional nmr spectroscopy. *The Journal of chemical physics*, 71(11):4546–4553, 1979.
- ⁶⁸ A. Krushelnitsky, T. Brauniger, and D. Reichert. ^{15}N spin diffusion rate in solid-state nmr of totally enriched proteins: The magic angle spinning frequency effect. *J. Magn. Reson.*, 182(2):339–42, 2006.
- ⁶⁹ N. Giraud, M. Blackledge, A. Bockmann, and L. Emsley. The influence of nitrogen-15 proton-driven spin diffusion on the measurement of nitrogen-15 longitudinal relaxation times. *J. Magn. Reson.*, 184(1):51–61, 2007.
- ⁷⁰ J. R. Lewandowski, J. Sein, H. J. Sass, S. Grzesiek, M. Blackledge, and L. Emsley. Measurement of site-specific ^{13}C spin-lattice relaxation in a crystalline protein. *J. Am. Chem. Soc.*, 132:8252–54, 2010.

- ⁷¹ V. Chevelkov, A. Diehl, and B. Reif. Measurement of ^{15}N - t_1 relaxation rates in a perdeuterated protein by magic angle spinning solid-state nuclear magnetic resonance spectroscopy. *J. Chem. Phys.*, 218(128):052316, 2008.
- ⁷² A. A. Smith, E. Testori, R. Cadalbert, B. H. Meier, and M. Ernst. Characterization of fibril dynamics on three timescales by solid-state nmr. *J. Biomol. NMR*, 2016.
- ⁷³ K. M. Ward, A. H. Aletras, and R. S. Balaban. A new class of contrast agents for mri based on proton chemical exchange dependent saturation transfer (cest). *Journal of Magnetic Resonance*, 143(1):79–87, 2000.
- ⁷⁴ Peter C. M. van Zijl and Nirbhay N. Yadav. Chemical exchange saturation transfer (cest): what is in a name and what isn't? *Magnetic resonance in medicine : official journal of the Society of Magnetic Resonance in Medicine / Society of Magnetic Resonance in Medicine*, 65(4):927–948, 2011. 21337419[pmid] Magn Reson Med.
- ⁷⁵ Shanrong Zhang, Matthew Merritt, Donald E. Woessner, Robert E. Lenkinski, and A. Dean Sherry. Paracest agents: modulating mri contrast via water proton exchange. *Accounts of Chemical Research*, 36(10):783–790, 2003.
- ⁷⁶ Mark Woods, Donald E. Woessner, and A. Dean Sherry. Paramagnetic lanthanide complexes as paracest agents for medical imaging. *Chemical Society Reviews*, 35(6):500–511, 2006.
- ⁷⁷ Jinyuan Zhou and Peter C. M. van Zijl. Chemical exchange saturation transfer imaging and spectroscopy. *Progress in Nuclear Magnetic Resonance Spectroscopy*, 48(2-3):109–136, 2006.
- ⁷⁸ A. Dean Sherry and Mark Woods. Chemical exchange saturation transfer contrast agents for magnetic resonance imaging. *Annu. Rev. Biomed. Eng.*, 10:391–411, 2008.
- ⁷⁹ Enzo Terreno, Daniela Delli Castelli, Claudia Cabella, Walter Dastr, Alberto Sanino, Joseph Stancanella, Lorenzo Tei, and Silvio Aime. Paramagnetic liposomes as innovative contrast agents for magnetic resonance (mr) molecular imaging applications. *Chemistry and biodiversity*, 5(10):1901–1912, 2008.
- ⁸⁰ Silvio Aime, Daniela Delli Castelli, and Enzo Terreno. Lanthanide-loaded paramagnetic liposomes as switchable magnetically oriented nanovesicles. *Methods in enzymology*, 464:193–210, 2009.
- ⁸¹ Enzo Terreno, Joseph Stancanella, Dario Longo, Daniela Delli Castelli, Luciano Milone, Honorius M. H. F. Sanders, Maarten B Kok, Fulvio Uggeri, and Silvio Aime. Methods for an improved detection of the mricest effect. *Contrast media and molecular imaging*, 4(5):237–247, 2009.
- ⁸² Ileana Hancu, W. Thomas Dixon, Mark Woods, Elena Vinogradov, A. Dean Sherry, and Robert E. Lenkinski. Cest and paracest mr contrast agents. *Acta radiologica*, 51(8):910–923, 2010.
- ⁸³ Enzo Terreno, Daniela Delli Castelli, and Silvio Aime. Encoding the frequency dependence in mri contrast media: the emerging class of cest agents. *Contrast media and molecular imaging*, 5(2):78–98, 2010.
- ⁸⁴ Enzo Terreno, Daniela Delli Castelli, Alessandra Viale, and Silvio Aime. Challenges for molecular magnetic resonance imaging. *Chemical reviews*, 110(5):3019–3042, 2010.

- ⁸⁵ Nicolas L. Fawzi, Jinfa Ying, Dennis A. Torchia, and G. Marius Clore. Probing exchange kinetics and atomic resolution dynamics in high-molecular-weight complexes using dark-state exchange saturation transfer nmr spectroscopy. *Nature Protocols*, 7:1523, 2012.
- ⁸⁶ Nicolas L. Fawzi, Jinfa Ying, Rodolfo Ghirlando, Dennis A. Torchia, and G. Marius Clore. Atomic-resolution dynamics on the surface of amyloid- protofibrils probed by solution nmr. *Nature*, 480:268, 2011.
- ⁸⁷ Ashok Sekhar and Lewis E. Kay. Nmr paves the way for atomic level descriptions of sparsely populated, transiently formed biomolecular conformers. *Proceedings of the National Academy of Sciences*, 110(32):12867–12874, 2013.
- ⁸⁸ dm Fizil, Zoltn Gspri, Terzia Barna, Florentine Marx, and Gyula Batta. invisible conformers of an antifungal disulfide protein revealed by constrained cold and heat unfolding, cestnmr experiments, and molecular dynamics calculations. *Chemistry A European Journal*, 21(13):5136–5144, 2015.
- ⁸⁹ Binhan Yu and Daiwen Yang. Coexistence of multiple minor states of fatty acid binding protein and their functional relevance. *Scientific reports*, 6:34171, 2016.
- ⁹⁰ Lewis E. Kay. New views of functionally dynamic proteins by solution nmr spectroscopy. *Journal of molecular biology*, 428(2):323–331, 2016.
- ⁹¹ Pramodh Vallurupalli, Guillaume Bouvignies, and Lewis E. Kay. Studying invisible excited protein states in slow exchange with a major state conformation. *Journal of the American Chemical Society*, 134(19):8148–8161, 2012.
- ⁹² Guillaume Bouvignies and Lewis E. Kay. Measurement of proton chemical shifts in invisible states of slowly exchanging protein systems by chemical exchange saturation transfer. *The Journal of Physical Chemistry B*, 116(49):14311–14317, 2012.
- ⁹³ Ashok Sekhar, Jessica A. O. Rumfeldt, Helen R. Broom, Colleen M. Doyle, Guillaume Bouvignies, Elizabeth M. Meiering, and Lewis E. Kay. Thermal fluctuations of immature sod1 lead to separate folding and misfolding pathways. *Elife*, 4, 2015.
- ⁹⁴ VA Daragan, TN Khazanovich, and AU Stepanyants. Cross-correlation effects in multiplet spectra of ¹³c. *Chemical Physics Letters*, 26(1):89–92, 1974.
- ⁹⁵ Claudio Dalvit and Geoffrey Bodenhausen. Evidence for dipolar cross-correlation from triple-quantum-filtered two-dimensional exchange nmr spectroscopy. *Journal of the American Chemical Society*, 110(23):7924–7926, 1988.
- ⁹⁶ M. Gueron, J. L. Leroy, and R. H. Griffey. Proton nuclear magnetic relaxation of nitrogen-15-labeled nucleic acids via dipolar coupling and chemical shift anisotropy. *Journal of the American Chemical Society*, 105(25):7262–7266, 1983.
- ⁹⁷ Bernhard Brutscher. Principles and applications of cross-correlated relaxation in biomolecules. *Concepts in Magnetic Resonance*, 12(4):207–229, 2000.
- ⁹⁸ Anil Kumar, R. Christy Rani Grace, and P. K. Madhu. Cross-correlations in nmr. *Progress in Nuclear Magnetic Resonance Spectroscopy*, 37(3):191–319, 2000.
- ⁹⁹ Anil Kumar and P. K. Madhu. Cross-correlations in multispin relaxation. *Concepts in Magnetic Resonance*, 8(2):139–160, 1996.

- ¹⁰⁰ Daniel Canet. *Cross-relaxation and Cross-correlation Parameters in NMR: Molecular Approaches*, book section Introduction to Nuclear Spin Cross Relaxation and Cross Correlation Phenomena in Liquids, pages 1–60. The Royal Society of Chemistry, 2017.
- ¹⁰¹ Daiwen Yang, Anthony Mittermaier, Yu-Keung Mok, and Lewis E. Kay. A study of protein side-chain dynamics from new ²h auto-correlation and ¹³c cross-correlation nmr experiments: application to the n-terminal sh3 domain from drk1 edited by p. e. wright. *Journal of Molecular Biology*, 276(5):939–954, 1998.
- ¹⁰² Nico Tjandra, Attila Szabo, and Ad Bax. Protein backbone dynamics and ¹⁵n chemical shift anisotropy from quantitative measurement of relaxation interference effects. *Journal of the American Chemical Society*, 118(29):6986–6991, 1996.
- ¹⁰³ Bernd Reif, Mirko Hennig, and Christian Griesinger. Direct measurement of angles between bond vectors in high-resolution nmr. *Science*, 276(5316):1230–1233, 1997.
- ¹⁰⁴ Konstantin Pervushin, Roland Riek, Gerhard Wider, and Kurt Wuthrich. Attenuated t₂ relaxation by mutual cancellation of dipole-dipole coupling and chemical shift anisotropy indicates an avenue to nmr structures of very large biological macromolecules in solution. *Proceedings of the National Academy of Sciences*, 94(23):12366–12371, 1997.
- ¹⁰⁵ M. W. Fischer, L. Zeng, Y. Pang, W. Hu, A. Majumdar, and E. R. P. Zuiderweg. Experimental characterization of models for backbone picosecond dynamics in proteins. quantification of nmr auto- and cross-correlation relaxation mechanisms involving different nuclei of the peptide plane. *J. Am. Chem. Soc.*, 119:12629–12642, 1997.
- ¹⁰⁶ Radovan Fiala, Naa pakov, Silvie Foldynov-Trantek, Ji pener, Vladimr Sklen, and Luk Trantek. Nmr cross-correlated relaxation rates reveal ion coordination sites in dna. *Journal of the American Chemical Society*, 133(35):13790–13793, 2011.
- ¹⁰⁷ Jonathan Boyd, Ulrich Hommel, and Iain D. Campbell. Influence of cross-correlation between dipolar and anisotropic chemical shift relaxation mechanisms upon longitudinal relaxation rates of ¹⁵n in macromolecules. *Chemical Physics Letters*, 175(5):477–482, 1990.
- ¹⁰⁸ Abhishek Mandal, Jennifer C. Boatz, Travis B. Wheeler, and Patrick C. A. van der Wel. On the use of ultracentrifugal devices for routine sample preparation in biomolecular magic-angle-spinning nmr. *Journal of Biomolecular NMR*, 67(3):165–178, 2017.
- ¹⁰⁹ Rachel W. Martin and Kurt W. Zilm. Preparation of protein nanocrystals and their characterization by solid state nmr. *Journal of Magnetic Resonance*, 165(1):162–174, 2003.
- ¹¹⁰ Patrick Alexander, Stephen Fahnstock, Timothy Lee, John Orban, and Philip Bryan. Thermodynamic analysis of the folding of the streptococcal protein g igg-binding domains b1 and b2: why small proteins tend to have high denaturation temperatures. *Biochemistry*, 31(14):3597–3603, 1992.
- ¹¹¹ I. Idiyatullin, D. Nesmelova, V. A. Daragan, and K. H. Mayo. Heat capacities and a snapshot of the energy landscape in protein gb1 from the pre-denaturation temperature dependence of backbone nh nanosecond fluctuations. *J. Mol. Biol.*, 325:149–62, 2003.

- ¹¹² B Akerström, TH Brodin, K Reis, and L Björck. Protein g: a powerful tool for binding and detection of monoclonal and polyclonal antibodies. *The Journal of Immunology*, 135(4):2589–2592, 1985.
- ¹¹³ Angela M Gronenborn, David R Filpula, Nina Z Essig, Aniruddha Achari, Marc Whitlow, Paul T Wingfield, and G Marius Clore. A novel, highly stable fold of the immunoglobulin binding domain of streptococcal protein g. *Science*, 253(5020):657–661, 1991.
- ¹¹⁴ Travis Gallagher, Patrick Alexander, Philip Bryan, and Gary L Gilliland. Two crystal structures of the b1 immunoglobulin-binding domain of streptococcal protein g and comparison with nmr. *Biochemistry*, 33(15):4721–4729, 1994.
- ¹¹⁵ H. L. Frericks Schmidt, L. J. Sperling, Y. Gui Gao, B. J. Wylie, J. M. Boettcher, S. R. Wilson, and C. M. Rienstra. Crystal polymorphism of protein gb1 examined by solid-state nmr spectroscopy and x-ray diffraction. *J. Phys. Chem. B.*, 111(51):14362–9, 2007.
- ¹¹⁶ John Orban, Patrick Alexander, Philip Bryan, and Devesh Khare. Assessment of stability differences in the protein g b1 and b2 domains from hydrogen-deuterium exchange: comparison with calorimetric data. *Biochemistry*, 34(46):15291–15300, 1995.
- ¹¹⁷ Naohiro Kobayashi, Shinya Honda, Hirofumi Yoshii, Hatsuho Uedaira, and Eisuke Munekata. Complement assembly of two fragments of the streptococcal protein g b1 domain in aqueous solution. *FEBS letters*, 366(2-3):99–103, 1995.
- ¹¹⁸ Soon-Ho Park, Karyn T O’Neil, and Heinrich Roder. An early intermediate in the folding reaction of the b1 domain of protein g contains a native-like core. *Biochemistry*, 36(47):14277–14283, 1997.
- ¹¹⁹ Felix B Sheinerman and Charles L Brooks III. Calculations on folding of segment b1 of streptococcal protein g1. *Journal of molecular biology*, 278(2):439–456, 1998.
- ¹²⁰ Stephan G. Zech, A. Joshua Wand, and Ann E. McDermott. Protein structure determination by high-resolution solid-state nmr spectroscopy: application to microcrystalline ubiquitin. *Journal of the American Chemical Society*, 127(24):8618–8626, 2005.
- ¹²¹ Rachel W. Martin and Kurt W. Zilm. Preparation of protein nanocrystals and their characterization by solid state nmr. *Journal of Magnetic Resonance*, 165(1):162–174, 2003.
- ¹²² Andi Mainz, Tomasz L. Religa, Remco Sprangers, Rasmus Linser, Lewis E. Kay, and Bernd Reif. Nmr spectroscopy of soluble protein complexes at one mega-dalton and beyond. *Angewandte Chemie International Edition*, 52(33):8746–8751, 2013.
- ¹²³ Ivano Bertini, Claudio Luchinat, Giacomo Parigi, Enrico Ravera, Bernd Reif, and Paola Turano. Solid-state nmr of proteins sedimented by ultracentrifugation. *Proceedings of the National Academy of Sciences*, 108(26):10396–10399, 2011.
- ¹²⁴ Ivano Bertini, Claudio Luchinat, Giacomo Parigi, and Enrico Ravera. Sednmr: On the edge between solution and solid-state nmr. *Accounts of Chemical Research*, 46(9):2059–2069, 2013.

- ¹²⁵ Jutta Pauli, Barth van Rossum, Hans Frster, Huub J. M. de Groot, and Hartmut Oschkinat. Sample optimization and identification of signal patterns of amino acid side chains in 2d rfdr spectra of the -spectrin sh3 domain. *Journal of Magnetic Resonance*, 143(2):411–416, 2000.
- ¹²⁶ John A. Rupley and Giorgio Careri. *Protein Hydration and Function*, volume 41, pages 37–172. Academic Press, 1991.
- ¹²⁷ Hans Frauenfelder, P. W. Fenimore, and B. H. McMahon. Hydration, slaving and protein function. *Biophysical Chemistry*, 98(1):35–48, 2002.
- ¹²⁸ Zhengfeng Zhang, Yanke Chen, Xinqi Tang, Jianping Li, Liying Wang, and Jun Yang. Solid-state nmr shows that dynamically different domains of membrane proteins have different hydration dependence. *The Journal of Physical Chemistry B*, 118(32):9553–9564, 2014.
- ¹²⁹ P. W. Fenimore, H. Frauenfelder, B. H. McMahon, and F. G. Parak. Slaving: Solvent fluctuations dominate protein dynamics and functions. *Proceedings of the National Academy of Sciences*, 99(25):16047, 2002.
- ¹³⁰ Giorgio Schir, Yann Fichou, Francois-Xavier Gallat, Kathleen Wood, Frank Gabel, Martine Moulin, Michael Hrtlein, Matthias Heyden, Jacques-Philippe Colletier, Andrea Orecchini, Alessandro Paciaroni, Joachim Wuttke, Douglas J Tobias, and Martin Weik. Translational diffusion of hydration water correlates with functional motions in folded and intrinsically disordered proteins. *Nature Communications*, 6:6490, 2015.
- ¹³¹ Joe Wolfe and Gary Bryant. Freezing, drying, and/or vitrification of membrane solutewater systems. *Cryobiology*, 39(2):103–129, 1999.
- ¹³² Abhishek Mandal and PatrickC A. vanderWel. Mas 1h nmr probes freezing point depression of water and liquid-gel phase transitions in liposomes. *Biophysical Journal*, 111(9):1965–1973, 2016.
- ¹³³ Gary Bryant, Karen L. Koster, and Joe Wolfe. Membrane behaviour in seeds and other systems at low water content: the various effects of solutes. *Seed Science Research*, 11(1):17–25, 2007.
- ¹³⁴ Huiru Tang, Peter S. Belton, Annie Ng, and Peter Ryden. 13c mas nmr studies of the effects of hydration on the cell walls of potatoes and chinese water chestnuts. *Journal of Agricultural and Food Chemistry*, 47(2):510–517, 1999.
- ¹³⁵ Gemma Comellas, Luisel R. Lemkau, Andrew J. Nieuwkoop, Kathryn D. Kloepper, Daniel T. Lador, Reika Ebisu, Wendy S. Woods, Andrew S. Lipton, Julia M. George, and Chad M. Rienstra. Structured regions of -synuclein fibrils include the early-onset parkinson’s disease mutation sites. *Journal of Molecular Biology*, 411(4):881–895, 2011.
- ¹³⁶ Alexander McPherson. Introduction to protein crystallization. *Methods*, 34(3):254–265, 2004.
- ¹³⁷ Hiller Matthias, Krabben Ludwig, Vinothkumar Kutti R., Castellani Federica, van Rossum BarthJan, Khlbrandt Werner, and Oschkinat Hartmut. Solidstate magicangle spinning nmr of outermembrane protein g from escherichia coli. *Chem-BioChem*, 6(9):1679–1684, 2005.

- ¹³⁸ Grant S. Hisao, Michael A. Harland, Robert A. Brown, Deborah A. Berthold, Thomas E. Wilson, and Chad M. Rienstra. An efficient method and device for transfer of semisolid materials into solid-state nmr spectroscopy rotors. *Journal of Magnetic Resonance*, 265:172–176, 2016.
- ¹³⁹ Shu-Shen Lu, Takaaki Inada, Akira Yabe, Xu Zhang, and Svein Grandum. Microscale study of poly(vinyl alcohol) as an effective additive for inhibiting recrystallization in ice slurries. *International Journal of Refrigeration*, 25(5):562–568, 2002.
- ¹⁴⁰ Arne H. Linden, W. Trent Franks, mit Akbey, Sascha Lange, Barth-Jan van Rossum, and Hartmut Oschkinat. Cryogenic temperature effects and resolution upon slow cooling of protein preparations in solid state nmr. *Journal of Biomolecular NMR*, 51(3):283, 2011.
- ¹⁴¹ Nabanita Das, Dylan T. Murray, and Timothy A. Cross. Lipid bilayer preparations of membrane proteins for oriented and magic-angle spinning solid-state nmr samples. *Nat. Protocols*, 8(11):2256–2270, 2013.
- ¹⁴² A. Bockmann, C Gardiennet, R. Verel, A. Hunkeler, A. Loquet, G. Pintacuda, L. Em-sley, B. H. Meier, and A. Lesage. Characterization of different water pools in solid-state nmr protein samples. *J. Biomol. NMR*, 45:319–327, 2009.
- ¹⁴³ Ivano Bertini, Frank Engelke, Leonardo Gonnelli, Benno Knott, Claudio Luchinat, David Osen, and Enrico Ravera. On the use of ultracentrifugal devices for sedimented solute nmr. *Journal of Biomolecular NMR*, 54(2):123–127, 2012.
- ¹⁴⁴ Carole Gardiennet, Anne K. Schtz, Andreas Hunkeler, Britta Kunert, Laurent Ter-radot, Anja Bckmann, and Beat H. Meier. A sedimented sample of a 59kda dode-cameric helicase yields high-resolution solid-state nmr spectra. *Angewandte Chemie International Edition*, 51(31):7855–7858, 2012.
- ¹⁴⁵ Ioannis Gelis, Veronika Vitzthum, Neha Dhimole, Marc A. Caporini, Andreas Schedl-bauer, Diego Carnevale, Sean R. Connell, Paola Fucini, and Geoffrey Bodenhausen. Solid-state nmr enhanced by dynamic nuclear polarization as a novel tool for ribosome structural biology. *Journal of Biomolecular NMR*, 56(2):85–93, 2013.
- ¹⁴⁶ Beckman Coulter. Mla-150 fixed angle rotor used in the beckman coulter optima max-xp ultracentrifuge. 2007.
- ¹⁴⁷ Beckman Coulter. Mls-50 rotor used in beckman coulter optima max, max-xp, and max-e tabletop ultracentrifuges, 2008.
- ¹⁴⁸ Georgina Charlton. *Development of sample preparation methods to study antibody-drug conjugates*. Thesis, 2016.
- ¹⁴⁹ Sren Lundh. Concentrated protein solutions in the analytical ultracentrifuge. *Journal of Polymer Science: Polymer Physics Edition*, 18(9):1963–1978, 1980.
- ¹⁵⁰ Sren Lundh. Ultracentrifugation of concentrated biopolymer solutions and effect of ascorbate. *Archives of Biochemistry and Biophysics*, 241(1):265–274, 1985.
- ¹⁵¹ Harold P Erickson. Size and shape of protein molecules at the nanometer level deter-mined by sedimentation, gel filtration, and electron microscopy. *Biological procedures online*, 11(1):32, 2009.

- ¹⁵² Yvonne Th van den Hoogen, Stevin J Treurniet, Harlof CPF Roelen, Erik de Vroom, Gijs A van der Marel, Jacques H van Boom, and Cornelis Altona. Conformational analysis of the tetranucleotides m62am62aum62a (m62a= n6dimethyladenosine) and um62aum62a and of the hybrid dar (ua) a oneand twodimensional nmr study. *European journal of biochemistry*, 171(12):155–162, 1988.
- ¹⁵³ David S Wishart, Colin G Bigam, Jian Yao, Frits Abildgaard, H Jane Dyson, Eric Oldfield, John L Markley, and Brian D Sykes. ¹h, ¹³c and ¹⁵n chemical shift referencing in biomolecular nmr. *Journal of biomolecular NMR*, 6(2):135–140, 1995.
- ¹⁵⁴ A. Pines, M. G. Gibby, and J. S. Waugh. Protonenhanced nuclear induction spectroscopy. a method for high resolution nmr of dilute spins in solids. *The Journal of Chemical Physics*, 56(4):1776–1777, 1972.
- ¹⁵⁵ A. Mittermaier and L. E. Kay. New tools provide new insights in nmr studies of protein dynamics. *Science*, 312:224–8, 2006.
- ¹⁵⁶ V. A. Jarymowycz and M. J. Stone. Fast time scale dynamics of protein backbones: nmr relaxation methods, applications, and functional consequences. *Chem. Rev.*, 106:1624–1671, 2006.
- ¹⁵⁷ V. A. Daragan and Kevin H. Mayo. Motional model analyses of protein and peptide dynamics using ¹³c and ¹⁵n nmr relaxation. *Prog. Nucl. Magn. Reson. Spectrosc.*, 31:63–105, 1997.
- ¹⁵⁸ J. M. Lamley, M.J Lougher, H. J. Sass, M. Rogowski, S. Grzesiek, and J. R. Lewandowski. Unraveling the complexity of protein backbone dynamics with combined ¹³c and ¹⁵n solid-state nmr relaxation measurements. *Phys. Chem. Chem. Phys.*, 17:21997–22008, 2015.
- ¹⁵⁹ T. Zinkevich, V. Chevelkov, B. Reif, K. Saalwachter, and A. Krushelnitsky. Internal protein dynamics on ps to ls timescales as studied by multi-frequency ¹⁵n solid state nmr relaxation. *J. Biomol. NMR*, 57:219–35, 2013.
- ¹⁶⁰ J. R. Lewandowski, J. Sein, M. Blackledge, and L. Emsley. Anisotropic collective motion contributes to nuclear spin relaxation in crystalline proteins. *J. Am. Chem. Soc.*, 132:1246–8, 2010.
- ¹⁶¹ N. Giraud, M. Blackledge, M. Goldman, A. Bockmann, A. Lesage, F. Penin, and L. Emsley. Quantitative analysis of backbone dynamics in a crystalline protein from nitrogen ¹⁵ spin lattice relaxation. *J. Am. Chem. Soc.*, 127:18190–201, 2005.
- ¹⁶² N. Bloembergen. On the interaction of nuclear spins in a crystalline lattice. *Physica*, 15(3-4):386–426, 1949.
- ¹⁶³ A. Grommek, B. H. Meier, and M. Ernst. Distance information from proton-driven spin diffusion under mas. *Chem. Phys. Lett.*, 427:404–409, 2006.
- ¹⁶⁴ Mikhail Veshtort and Robert G. Griffin. Proton-driven spin diffusion in rotating solids via reversible and irreversible quantum dynamics. *The Journal of Chemical Physics*, 135(13):134509, 2011.
- ¹⁶⁵ S. Asami, J. Porter, O. F. Lange, and B. Reif. Access to c backbone dynamics of biological solids by ¹³c t1 relaxation and molecular dynamics simulation. *J. Am. Chem. Soc.*, 137:1094–1100, 2015.

- ¹⁶⁶ D. Suter and R. R. Ernst. Spin diffusion in resolved solid-state nmr spectra. *Physical Review B*, 32(9):5608–5627, 1985. PRB.
- ¹⁶⁷ Nathaniel J. Traaseth, T. Gopinath, and Gianluigi Veglia. On the performance of spin diffusion nmr techniques in oriented solids: Prospects for resonance assignments and distance measurements from separated local field experiments. *The journal of physical chemistry. B*, 114(43):13872–13880, 2010.
- ¹⁶⁸ Wurong Zhang and DG Cory. First direct measurement of the spin diffusion rate in a homogenous solid. *Physical review letters*, 80(6):1324, 1998.
- ¹⁶⁹ Federica Castellani, Barth-Jan van Rossum, Annette Diehl, Kristina Rehbein, and Hartmut Oschkinat. Determination of solid-state nmr structures of proteins by means of three-dimensional ^{15}N ^{13}C ^{13}C dipolar correlation spectroscopy and chemical shift analysis. *Biochemistry*, 42(39):11476–11483, 2003.
- ¹⁷⁰ W. Trent Franks, Benjamin J. Wylie, Heather L. Frericks Schmidt, Andrew J. Nieuwkoop, Rebecca-Maria Mayrhofer, Gautam J. Shah, Daniel T. Graesser, and Chad M. Rienstra. Dipole tensor-based atomic-resolution structure determination of a nanocrystalline protein by solid-state nmr. *Proceedings of the National Academy of Sciences*, 105(12):4621–4626, 2008.
- ¹⁷¹ Theofanis Manolikas, Torsten Herrmann, and Beat H. Meier. Protein structure determination from ^{13}C spin-diffusion solid-state nmr spectroscopy. *Journal of the American Chemical Society*, 130(12):3959–3966, 2008.
- ¹⁷² Antoine Loquet, Benjamin Bardiaux, Carole Gardiennet, Christophe Blanchet, Marc Baldus, Michael Nilges, Thrse Malliavin, and Anja Bckmann. 3d structure determination of the crh protein from highly ambiguous solid-state nmr restraints. *Journal of the American Chemical Society*, 130(11):3579–3589, 2008.
- ¹⁷³ Christian Wasmer, Adam Lange, Hlne Van Melckebeke, Ansgar B. Siemer, Roland Riek, and Beat H. Meier. Amyloid fibrils of the het-s(218289) prion form a solenoid with a triangular hydrophobic core. *Science*, 319(5869):1523–1526, 2008.
- ¹⁷⁴ J. R. Lewandowski, H. J. Sass, S. Grzesiek, M. Blackledge, and L. Emsley. Site-specific measurement of slow motions in proteins. *J. Am. Chem. Soc.*, 133:16762–5, 2011.
- ¹⁷⁵ V. Chevelkov, B. J. van Rossum, F. Castellani, K. Rehbein, A. Diehl, M. Hohwy, S. Steuernagel, F. Engelke, H. Oschkinat, and B. Reif. ^1H detection in mas solid-state nmr spectroscopy of biomacromolecules employing pulsed field gradients for residual solvent suppression. *J. Am. Chem. Soc.*, 125:7788–7789, 2003.
- ¹⁷⁶ E. K. Paulson, C. R. Morcombe, V. Gaponenko, B. Danccheck, R. A. Byrd, and K.W. Zilm. Sensitive high resolution inverse detection nmr spectroscopy of proteins in the solid state. *J. Am. Chem. Soc.*, 125:15831–6, 2003.
- ¹⁷⁷ B. Reif, C. P. Jaroniec, C. M. Rienstra, M. Hohwy, and R. G. Griffin. ^1H ^1H mas correlation spectroscopy and distance measurements in a deuterated peptide. *Journal of Magnetic Resonance*, 151(2):320–327, 2001.
- ¹⁷⁸ V. Chevelkov, K. Rehbein, A. Diehl, and B. Reif. Ultrahigh resolution in proton solid-state nmr spectroscopy at high levels of deuteration. *Angew. Chem. Int. Ed.*, 45:3878–81, 2006.

- ¹⁷⁹ Nils-Alexander Lakomek, Susanne Penzel, Alons Lends, Riccardo Cadalbert, Matthias Ernst, and Beat H. Meier. Microsecond dynamics in ubiquitin probed by solid-state ^{15}N nmr spectroscopy r1 relaxation experiments under fast mas (60110khz). *Chemistry A European Journal*, 23(39):9425–9433, 2017.
- ¹⁸⁰ A. Krushelnitsky, T. Zinkevich, D. Reichert, V. Chevelkov, and B. Reif. Microsecond time scale mobility in a solid protein as studied by the ^{15}N r1rho site-specific nmr relaxation rates. *J. Am. Chem. Soc.*, 132:11850–3, 2010.
- ¹⁸¹ P. Ma, J. D. Haller, J. Zajakala, P. Macek, A. C. Sivertsen, D. Willbold, J. Boissbouvier, and P. Schanda. Probing transient conformational states of proteins by solid-state r1rho relaxation-dispersion nmr spectroscopy. *Angew. Chem. Int. Ed.*, 53:4312–7, 2014.
- ¹⁸² Y. Ishii and R. Tycko. *J. Magn. Reson.*, 204(1):199, 2000.
- ¹⁸³ G. Zhou, D. H. Shah, M. Cormos, C. Mullen, D. Sandoz, and C. M. Rienstra. Proton-detected solid-state nmr spectroscopy of fully protonated proteins at 40 khz magic-angle spinning. *J. Am. Chem. Soc.*, 129:11791–801, 2007.
- ¹⁸⁴ J. R. Lewandowski, J. N. Dumez, U. Akbey, S. Lange, L. Emsley, and H. Oschkinat. Enhanced resolution and coherence lifetimes in the solid-state nmr spectroscopy of perdeuterated proteins under ultrafast magic-angle spinning. *J. Phys. Chem. Lett.*, 2(17):2205–2211, 2011.
- ¹⁸⁵ Alessandro Marchetti, Stefan Jehle, Michele Felletti, Michael J. Knight, Yao Wang, Zhi-Qiang Xu, Ah Young Park, Gottfried Otting, Anne Lesage, Lyndon Emsley, Nicholas E. Dixon, and Guido Pintacuda. Backbone assignment of fully protonated solid proteins by ^1H detection and ultrafast magic-angle-spinning nmr spectroscopy. *Angewandte Chemie International Edition*, 51(43):10756–10759, 2012.
- ¹⁸⁶ Songlin Wang, Sudhakar Parthasarathy, Yiling Xiao, Yusuke Nishiyama, Fei Long, Isamu Matsuda, Yuki Endo, Takahiro Nemoto, Kazuo Yamauchi, Tetsuo Asakura, Mitsuhiro Takeda, Tsutomu Terauchi, Masatsune Kainosho, and Yoshitaka Ishii. Nano-mole scale sequential signal assignment by ^1H -detected protein solid-state nmr. *Chemical Communications*, 51(81):15055–15058, 2015.
- ¹⁸⁷ Meaghan E. Ward, Shenlin Wang, Sridevi Krishnamurthy, Howard Hutchins, Michael Fey, Leonid S. Brown, and Vladimir Ladizhansky. High-resolution paramagnetically enhanced solid-state nmr spectroscopy of membrane proteins at fast magic angle spinning. *Journal of Biomolecular NMR*, 58(1):37–47, 2014.
- ¹⁸⁸ Donghua H. Zhou, Andrew J. Nieuwkoop, Deborah A. Berthold, Gemma Comellas, Lindsay J. Sperling, Ming Tang, Gautam J. Shah, Elliott J. Brea, Luisel R. Lemkau, and Chad M. Rienstra. Solid-state nmr analysis of membrane proteins and protein aggregates by proton detected spectroscopy. *Journal of Biomolecular NMR*, 54(3):291–305, 2012.
- ¹⁸⁹ Loren B. Andreas, Jan Stanek, Tanguy Le Marchand, Andrea Bertarello, Diane Calade Paepe, Daniela Lalli, Magdalena Krejckov, Camille Doyen, Carl ster, Benno Knott, Sebastian Wegner, Frank Engelke, Isabella C. Felli, Roberta Pierattelli, Nicholas E. Dixon, Lyndon Emsley, Torsten Herrmann, and Guido Pintacuda. Protein residue linking in a single spectrum for magic-angle spinning nmr assignment. *Journal of Biomolecular NMR*, 62(3):253–261, 2015.

- ¹⁹⁰ mit Akbey, Sascha Lange, W. Trent Franks, Rasmus Linser, Kristina Rehbein, Anne Diehl, Barth-Jan van Rossum, Bernd Reif, and Hartmut Oschkinat. Optimum levels of exchangeable protons in perdeuterated proteins for proton detection in mas solid-state nmr spectroscopy. *Journal of Biomolecular NMR*, 46(1):67, 2009.
- ¹⁹¹ K. Takegoshie, S. Nakamura, and T. Terao. ^{13}C \rightarrow ^1H dipolar-driven ^{13}C \rightarrow ^{13}C recoupling without ^{13}C rf irradiation in nuclear magnetic resonance of rotating solids. *J. Chem. Phys.*, 118(5):2325–41, 2003.
- ¹⁹² Eric K Paulson, Corey R Morcombe, Vadim Gaponenko, Barbara Dancheck, R Andrew Byrd, and Kurt W Zilm. High-sensitivity observation of dipolar exchange and noes between exchangeable protons in proteins by 3d solid-state nmr spectroscopy. *Journal of the American Chemical Society*, 125(47):14222–14223, 2003.
- ¹⁹³ Lewis E. Kay, Linda K. Nicholson, F. Delaglio, A. Bax, and D. A. Torchia. Pulse sequences for removal of the effects of cross correlation between dipolar and chemical-shift anisotropy relaxation mechanisms on the measurement of heteronuclear t_1 and t_2 values in proteins. *Journal of Magnetic Resonance (1969)*, 97(2):359–375, 1992.
- ¹⁹⁴ P. Ma, Y. Xue, N. Coquelle, J. D. Haller, T. Yuwen, I. Ayala, Oleg Mikhailovskii, D. Willbold, J. Colletier, N. R. Skrynnikov, and P. Schanda. Observing the overall rocking motion of a protein in a crystal. *Nat. Commun.*, 6(8361):1–10, 2015.
- ¹⁹⁵ Jennifer Lippincott-Schwartz, Erik Snapp, and Anne Kenworthy. Studying protein dynamics in living cells. *Nature reviews Molecular cell biology*, 2(6):444, 2001.
- ¹⁹⁶ A. Krushelnitsky and D. Reichert. Solid-state nmr and protein dynamics. *Prog. Nucl. Magn. Reson. Spectrosc.*, 47:1–25, 2005.
- ¹⁹⁷ A. Krushelnitsky, D. Reichert, and K. Saalwachter. Solid-state nmr approaches to internal dynamics of proteins: From picoseconds to microseconds and seconds. *Acc. Chem. Res.*, 46(9):2028–36, 2013.
- ¹⁹⁸ P. Schanda. Solid-state nmr studies of protein dynamics: New approaches and applications to crystalline proteins and large molecular assemblies, 2014.
- ¹⁹⁹ Bjarne F Rasmussen, Ann M Stock, Dagmar Ringe, and Gregory A Petsko. Crystalline ribonuclease a loses function below the dynamical transition at 220 k. *Nature*, 357(6377):423, 1992.
- ²⁰⁰ Martin Weik and J-P Colletier. Temperature-dependent macromolecular x-ray crystallography. *Acta Crystallographica Section D: Biological Crystallography*, 66(4):437–446, 2010.
- ²⁰¹ Anna B Loveland and Andrei A Korostelev. Structural dynamics of protein s1 on the 70s ribosome visualized by ensemble cryo-em. *J Methods*, 137:55–66, 2018.
- ²⁰² John L Rubinstein. Cryo-em captures the dynamics of ion channel opening. *J Cell*, 168(3):341–343, 2017.
- ²⁰³ Dina Schneidman-Duhovny and Michal Hammel. *Modeling Structure and Dynamics of Protein Complexes with SAXS Profiles*, pages 449–473. Springer, 2018.
- ²⁰⁴ Tadayuki Ogawa and Nobutaka Hirokawa. Multiple analyses of protein dynamics in solution. *J Biophysical reviews*, pages 1–8, 2017.

- ²⁰⁵ Xavier Michalet, Shimon Weiss, and Marcus Jger. Single-molecule fluorescence studies of protein folding and conformational dynamics. *J Chemical reviews*, 106(5):1785–1813, 2006.
- ²⁰⁶ Haw Yang, Guobin Luo, Pallop Karnchanaphanurach, Tai-Man Louie, Ivan Rech, Sergio Cova, Luying Xun, and X Sunney Xie. Protein conformational dynamics probed by single-molecule electron transfer. *J Science*, 302(5643):262–266, 2003.
- ²⁰⁷ Andrea Pavlou, Hideaki Yoshimura, Shigetoshi Aono, and Eftychia Biophysical journal Pinakoulaki. Protein dynamics of the sensor protein hemat as probed by time-resolved step-scan ftir spectroscopy. 114(3):584–591, 2018.
- ²⁰⁸ Ayanjeet Ghosh, Joshua S Ostrander, and Martin T Zanni. Watching proteins wiggle: Mapping structures with two-dimensional infrared spectroscopy. *J Chemical reviews*, 117(16):10726–10759, 2017.
- ²⁰⁹ M Schmid, P Changenet-Barret, and F Hache. Multiscale conformational dynamics probed by time-resolved circular dichroism. In *Organic Photonic Materials and Devices XX*, volume 10529, page 1052911. International Society for Optics and Photonics.
- ²¹⁰ Hassane S Mchaourab, Michael A Lietzow, Kalman Hideg, and Wayne L Hubbell. Motion of spin-labeled side chains in t4 lysozyme. correlation with protein structure and dynamics. *J Biochemistry*, 35(24):7692–7704, 1996.
- ²¹¹ Gurusamy Balakrishnan, Colin L Weeks, Mohammed Ibrahim, Alexandra V Soldatova, and Thomas G Spiro. Protein dynamics from time resolved uv raman spectroscopy. *J Current opinion in structural biology*, 18(5):623–629, 2008.
- ²¹² Thomas G Spiro. Resonance raman spectroscopy as a probe of heme protein structure and dynamics. *J Adv Protein Chem*, 37:111–159, 1985.
- ²¹³ Linda Columbus and Wayne L Hubbell. A new spin on protein dynamics. *J Trends in biochemical sciences*, 27(6):288–295, 2002.
- ²¹⁴ Likai Song, Zahra Hayati, Mengtian Liu, Mikyung Kim, and Ellis Reinherz. Protein-lipid interactions on the hiv membrane defined by epr spectroscopy. *J Biophysical Journal*, 114(3):198a, 2018.
- ²¹⁵ Aaron Holmes and Kathleen Howard. Site-directed spin-label epr spectroscopy of influenza a m2 protein. *J Biophysical Journal*, 114(3):237a, 2018.
- ²¹⁶ Dennis Vitkup, Dagmar Ringe, Gregory A Petsko, and Martin Karplus. Solvent mobility and the protein’glass’ transition. *J. Nature Structural Molecular Biology*, 7(1):34, 2000.
- ²¹⁷ M Tarek and DJ Tobias. Role of protein-water hydrogen bond dynamics in the protein dynamical transition. *J Physical Review Letters*, 88(13):138101, 2002.
- ²¹⁸ M. J. Seewald, K. Pichumani, C. Stowell, B. V. Tibbals, L. Regan, and M. J. Stone. The role of backbone conformational heat capacity in protein stability: Temperature dependent dynamics of the b1 domain of streptococcal protein g. *Protein Sci.*, 9:1177–93, 2000.

- ²¹⁹ M. Tollinger, A. C. Sivertsen, B. H. Meier, M. Ernst, and P. Schanda. Site-resolved measurement of microsecond-to-millisecond conformational-exchange processes in proteins by solid-state nmr spectroscopy. *J. Am. Chem. Soc.*, 134:14800–7, 2012.
- ²²⁰ Y. Xue, M. S. Pavlova, Y. E. Ryabov, B. Reif, and N. Skrynnikov. Methyl rotation barriers in proteins from 2h relaxation data implications for protein structure. *J. Am. Chem. Soc.*, 129:6827–38, 2007.
- ²²¹ S. Chang and N. Tjandra. Temperature dependence of protein backbone motion from carbonyl ¹³c and amide ¹⁵n nmr relaxation. *Journal of Magnetic Resonance*, 174:43–53, 2005.
- ²²² T. Wang, S. Cai, and E. R. P. Zuiderweg. Temperature dependence of anisotropic protein backbone dynamics. *J. Am. Chem. Soc.*, 125(8639-43), 2003.
- ²²³ B. J. Wylie, L. J. Sperling, A. J. Nieuwkoop, W. T. Franks, E. Oldfield, and C. M. Rienstra. Ultrahigh resolution protein structures using nmr chemical shift tensors. *Proc. Natl. Acad. Sci. U. S. A.*, 108(41):16974–9, 2011.
- ²²⁴ H. Allard and T. Hard. Nmr relaxation mechanisms for backbone carbonyl carbons in a ¹³c,¹⁵n-labeled protein. *J. Magn. Reson.*, 126:48–57, 1997.
- ²²⁵ B. J. Wylie, W. T. Franks, D. T. Graesser, and C. M. Rienstra. Site-specific ¹³c chemical shift anisotropy measurements in a uniformly-¹⁵n,¹³c-labeled microcrystalline protein by 3d magic-angle spinning nmr spectroscopy. *J. Am. Chem. Soc.*, 127(34):11946–7, 2005.
- ²²⁶ P. Schanda, B. H. Meier, and M. Ernst. Quantitative analysis of protein backbone dynamics in microcrystalline ubiquitin by solid-state nmr spectroscopy. *J. Am. Chem. Soc.*, 132:15957–67, 2010.
- ²²⁷ P. Schanda, B. H. Meier, and M. Ernst. Accurate measurement of one-bond h-x heteronuclear dipolar couplings in mas solid-state nmr. *J. Magn. Reson.*, 210:246–59, 2011.
- ²²⁸ V. Chevelkov, U. Fink, and B. Reif. Accurate determination of order parameters from ¹h,¹⁵n dipolar couplings in mas solid-state nmr experiments. *J. Am. Chem. Soc.*, 131:14018–22, 2009.
- ²²⁹ Thomas Congdon, Rebecca Notman, and Matthew I. Gibson. Antifreeze (glyco)protein mimetic behavior of poly(vinyl alcohol): Detailed structure ice recrystallization inhibition activity study. *Biomacromolecules*, 14(5):1578–1586, 2013.
- ²³⁰ Vincent Bouvet and Robert N. Ben. Antifreeze glycoproteins. *Cell Biochemistry and Biophysics*, 39(2):133–144, 2003.
- ²³¹ Caroline I. Biggs, Trisha L. Bailey, Graham Ben, Christopher Stubbs, Alice Fayter, and Matthew I. Gibson. Polymer mimics of biomacromolecular antifreezes. *Nature Communications*, 8(1):1546, 2017.
- ²³² I. K. Voets. From ice-binding proteins to bio-inspired antifreeze materials. *Soft Matter*, 13(28):4808–4823, 2017.
- ²³³ Donald L Hall, S Michael Sterner, and Robert J Bodnar. Freezing point depression of nacl-kcl-h₂o solutions. *Economic Geology*, 83(1):197–202, 1988.

- ²³⁴ Leonard B Lane. Freezing points of glycerol and its aqueous solutions. *Industrial and Engineering Chemistry*, 17(9):924–924, 1925.
- ²³⁵ Siegfried Rebsdat and Dieter Mayer. Ethylene glycol. *Ullmann’s Encyclopedia of Industrial Chemistry*, 2000.
- ²³⁶ DOW. What are the freeze points of propylene glycol solutions?, 25/07/2017 2017.
- ²³⁷ S. S. Lu, T. Inada, A. Yabe, X. Zhang, and S. Grandm. Effective additives for preventing recrystallization in ice-slurry systems. In P. Cheng, editor, *Symposium on Energy Engineering in the 21st Century (SEE2000)*, volume 2, pages 860–865.
- ²³⁸ Carsten Budke and Thomas Koop. Ice recrystallization inhibition and molecular recognition of ice faces by poly(vinyl alcohol). *ChemPhysChem*, 7(12):2601–2606, 2006.
- ²³⁹ Ran Drori, Chao Li, Chunhua Hu, Paolo Raiteri, Andrew L. Rohl, Michael D. Ward, and Bart Kahr. A supramolecular ice growth inhibitor. *Journal of the American Chemical Society*, 138(40):13396–13401, 2016.
- ²⁴⁰ Sylvain Deville, Cline Viazzi, and Christian Guizard. Ice-structuring mechanism for zirconium acetate. *Langmuir*, 28(42):14892–14898, 2012.
- ²⁴¹ Ortal Mizrahy, Maya Bar-Dolev, Shlomit Guy, and Ido Braslavsky. Inhibition of ice growth and recrystallization by zirconium acetate and zirconium acetate hydroxide. *PloS one*, 8(3):e59540, 2013.
- ²⁴² Sylvain Deville, Cline Viazzi, Jrme Leloup, Audrey Lasalle, Christian Guizard, Eric Maire, Jrme Adrien, and Laurent Gremillard. Ice shaping properties, similar to that of antifreeze proteins, of a zirconium acetate complex. *PLOS ONE*, 6(10):e26474, 2011.
- ²⁴³ Moreno Marcellini, Francisco M. Fernandes, Dmytro Dedovets, and Sylvain Deville. Water/ice phase transition: The role of zirconium acetate, a compound with ice-shaping properties. *The Journal of Chemical Physics*, 146(14):144504, 2017.
- ²⁴⁴ Daniel E. Mitchell, Guy Clarkson, David J. Fox, Rebecca A. Vipond, Peter Scott, and Matthew I. Gibson. Antifreeze protein mimetic metallohelices with potent ice recrystallization inhibition activity. *Journal of the American Chemical Society*, 139(29):9835–9838, 2017.
- ²⁴⁵ Hongya Geng, Xing Liu, Guosheng Shi, Guoying Bai, Ji Ma, Jingbo Chen, Zhuangyuan Wu, Yanlin Song, Haiping Fang, and Jianjun Wang. Graphene oxide restricts growth and recrystallization of ice crystals. *Angewandte Chemie International Edition*, 56(4):997–1001, 2017.
- ²⁴⁶ W. H. Bragg. The crystal structure of ice. *Proceedings of the Physical Society of London*, 34(1):98, 1921.
- ²⁴⁷ C Lobban, JL Finney, and WF Kuhs. The structure of a new phase of ice. *Nature*, 391(6664):268, 1998.
- ²⁴⁸ Luuk LC Olijve, Konrad Meister, Arthur L DeVries, John G Duman, Shuaiqi Guo, Huib J Bakker, and Ilja K Voets. Blocking rapid ice crystal growth through non-basal plane adsorption of antifreeze proteins. *Proceedings of the National Academy of Sciences*, 113(14):3740–3745, 2016.

- ²⁴⁹ Charles Blagden. Blagden's law (freezing point depresssion). *Phil. Trans. Roy. Soc.*, 78(125):277, 1788.
- ²⁵⁰ Charles A Knight and Arthur L DeVries. *The prevention of ice crystal growth from water by antifreeze proteins*, pages 717–720. Springer, 1988.
- ²⁵¹ Charles A Knight, John Hallett, and AL DeVries. Solute effects on ice recrystallization: an assessment technique. *Cryobiology*, 25(1):55–60, 1988.
- ²⁵² Matthew I. Gibson. Slowing the growth of ice with synthetic macromolecules: beyond antifreeze(glyco) proteins. *Polymer Chemistry*, 1(8):1141–1152, 2010.
- ²⁵³ Omar A Karim and ADJ Haymet. The ice/water interface: A molecular dynamics simulation study. *The Journal of chemical physics*, 89(11):6889–6896, 1988.
- ²⁵⁴ Jeffry D Madura, Kelli Baran, and Andrzej Wierzbicki. Molecular recognition and binding of thermal hysteresis proteins to ice. *Journal of Molecular Recognition*, 13(2):101–113, 2000.
- ²⁵⁵ Jennifer A Hayward and ADJ Haymet. The ice/water interface: orientational order parameters for the basal, prism, 202-1, and 21-1-0 interfaces of ice Ih. *Physical chemistry chemical physics*, 4(15):3712–3719, 2002.
- ²⁵⁶ H Nada and Y Furukawa. Anisotropy in growth kinetics at interfaces between proton-disordered hexagonal ice and water: A molecular dynamics study using the six-site model of h₂O. *Journal of crystal growth*, 283(1-2):242–256, 2005.
- ²⁵⁷ Arthur L. DeVries and Donald E. Wohlschlag. Freezing resistance in some antarctic fishes. *Science*, 163(3871):1073–1075, 1969.
- ²⁵⁸ Maya Bar Dolev, Ido Braslavsky, and Peter L Davies. Ice-binding proteins and their function. *Annual review of biochemistry*, 85:515–542, 2016.
- ²⁵⁹ Maya Bar-Dolev, Yeliz Celik, J. S. Wettlaufer, Peter L. Davies, and Ido Braslavsky. New insights into ice growth and melting modifications by antifreeze proteins. *Journal of The Royal Society Interface*, 9(77):3249–3259, 2012.
- ²⁶⁰ Anneloes S. Oude Vrielink, Antonio Aloï, Luuk L. C. Olijve, and Ilja K. Voets. Interaction of ice binding proteins with ice, water and ions. *Biointerphases*, 11(1):018906, 2016.
- ²⁶¹ Peter L. Davies. Ice-binding proteins: a remarkable diversity of structures for stopping and starting ice growth. *Trends in Biochemical Sciences*, 39(11):548–555, 2014.
- ²⁶² Laurie A. Graham, Rod S. Hobbs, Garth L. Fletcher, and Peter L. Davies. Helical antifreeze proteins have independently evolved in fishes on four occasions. *PLOS ONE*, 8(12):e81285, 2013.
- ²⁶³ Chi-Hing C Cheng. Evolution of the diverse antifreeze proteins. *Current opinion in genetics and development*, 8(6):715–720, 1998.
- ²⁶⁴ K. V. Ewart, Q. Lin, and C. L. Hew. Structure, function and evolution of antifreeze proteins. *Cellular and Molecular Life Sciences CMLS*, 55(2):271–283, 1999.
- ²⁶⁵ John M. Logsdon and W. Ford Doolittle. Origin of antifreeze protein genes: A cool tale in molecular evolution. *Proceedings of the National Academy of Sciences*, 94(8):3485–3487, 1997.

- ²⁶⁶ C. A. Knight, C. C. Cheng, and A. L. DeVries. Adsorption of alpha-helical antifreeze peptides on specific ice crystal surface planes. *Biophysical Journal*, 59(2):409–418, 1991.
- ²⁶⁷ Jason Baardsnes, Leslie H. Kondejewski, Robert S. Hodges, Heman Chao, Cyril Kay, and Peter L. Davies. New ice-binding face for type i antifreeze protein. *FEBS Letters*, 463(1):87–91, 1999.
- ²⁶⁸ Tianjun Sun, Feng-Hsu Lin, Robert L Campbell, John S Allingham, and Peter L Davies. An antifreeze protein folds with an interior network of more than 400 semi-clathrate waters. *Science*, 343(6172):795–798, 2014.
- ²⁶⁹ Michael E Houston, Heman Chao, Robert S Hodges, Brian D Sykes, Cyril M Kay, Frank D Snnichsen, Michele C Loewen, and Peter L Davies. Binding of an oligopeptide to a specific plane of ice. *Journal of Biological Chemistry*, 273(19):11714–11718, 1998.
- ²⁷⁰ Alfred A Antson, Derek J Smith, David I Roper, Sally Lewis, Leo SD Caves, Chandra S Verma, Sarah L Buckley, Peter J Lillford, and Roderick E Hubbard. Understanding the mechanism of ice binding by type iii antifreeze proteins. *Journal of molecular biology*, 305(4):875–889, 2001.
- ²⁷¹ Yee-Foong Mok, Feng-Hsu Lin, Laurie A Graham, Yeliz Celik, Ido Braslavsky, and Peter L Davies. Structural basis for the superior activity of the large isoform of snow flea antifreeze protein. *Biochemistry*, 49(11):2593–2603, 2010.
- ²⁷² Steffen P. Graether, Michael J. Kuiper, Stphane M. Gagn, Virginia K. Walker, Zongchao Jia, Brian D. Sykes, and Peter L. Davies. -helix structure and ice-binding properties of a hyperactive antifreeze protein from an insect. *Nature*, 406:325, 2000.
- ²⁷³ Peter L Davies, Jason Baardsnes, Michael J Kuiper, and Virginia K Walker. Structure and function of antifreeze proteins. *Philosophical Transactions of the Royal Society of London B: Biological Sciences*, 357(1423):927–935, 2002.
- ²⁷⁴ C. A. Knight, E. Driggers, and A. L. DeVries. Adsorption to ice of fish antifreeze glycopeptides 7 and 8. *Biophysical Journal*, 64(1):252–259, 1993.
- ²⁷⁵ A. Wierzbicki, M. S. Taylor, C. A. Knight, J. D. Madura, J. P. Harrington, and C. S. Sikes. Analysis of shorthorn sculpin antifreeze protein stereospecific binding to (21 0) faces of ice. *Biophysical Journal*, 71(1):8–18, 1996.
- ²⁷⁶ Heman Chao, Michael E. Houston, Robert S. Hodges, Cyril M. Kay, Brian D. Sykes, Michle C. Loewen, Peter L. Davies, and Frank D. Snnichsen. A diminished role for hydrogen bonds in antifreeze protein binding to ice. *Biochemistry*, 36(48):14652–14660, 1997.
- ²⁷⁷ Jason Baardsnes and Peter L. Davies. Contribution of hydrophobic residues to ice binding by fish type iii antifreeze protein. *Biochimica et Biophysica Acta (BBA) - Proteins and Proteomics*, 1601(1):49–54, 2002.
- ²⁷⁸ Alexander Jorov, Boris S Zhorov, and Daniel SC Yang. Theoretical study of interaction of winter flounder antifreeze protein with ice. *Protein Science*, 13(6):1524–1537, 2004.
- ²⁷⁹ Carl I. DeLuca, Rebecca Comley, and Peter L. Davies. Antifreeze proteins bind independently to ice. *Biophysical Journal*, 74(3):1502–1508, 1998.

- ²⁸⁰ Wolfram Gronwald, Heman Chao, D Venkat Reddy, Peter L Davies, Brian D Sykes, and Frank D Snnichsen. Nmr characterization of side chain flexibility and backbone structure in the type i antifreeze protein at near freezing temperatures. *Biochemistry*, 35(51):16698–16704, 1996.
- ²⁸¹ A. D. J. Haymet, Leanne G. Ward, and Margaret M. Harding. Winter flounder antifreeze proteins: synthesis and ice growth inhibition of analogues that probe the relative importance of hydrophobic and hydrogen-bonding interactions. *Journal of the American Chemical Society*, 121(5):941–948, 1999.
- ²⁸² C. Allen Bush, Robert E. Feeney, David T. Osuga, Suresh Ralapati, and Y. I. N. Yeh. Antifreeze glycoprotein. conformational model based on vacuum ultraviolet circular dichroism data. *International Journal of Peptide and Protein Research*, 17(1):125–129, 1981.
- ²⁸³ Margaret M. Harding, Pia I. Anderberg, and A. D. J. Haymet. antifreeze glycoproteins from polar fish. *European Journal of Biochemistry*, 270(7):1381–1392, 2003.
- ²⁸⁴ David T Osuga, Milton S Feather, Mena J Shah, and Robert E Feeney. Modification of galactose and n-acetylgalactosamine residues by oxidation of c-6 hydroxyls to the aldehydes followed by reductive amination: Model systems and antifreeze glycoproteins. *Journal of protein chemistry*, 8(4):519–528, 1989.
- ²⁸⁵ Yuki Tachibana, Garth L. Fletcher, Naoki Fujitani, Sakae Tsuda, Kenji Monde, and Shin-Ichiro Nishimura. Antifreeze glycoproteins: Elucidation of the structural motifs that are essential for antifreeze activity. *Angewandte Chemie*, 116(7):874–880, 2004.
- ²⁸⁶ BN Rao and C Allen Bush. Comparison by 1hnmr spectroscopy of the conformation of the 2600 dalton antifreeze glycopeptide of polar cod with that of the high molecular weight antifreeze glycoprotein. *Biopolymers*, 26(8):1227–1244, 1987.
- ²⁸⁷ J A Raymond and A L DeVries. Adsorption inhibition as a mechanism of freezing resistance in polar fishes. *Proceedings of the National Academy of Sciences*, 74(6):2589–2593, 1977.
- ²⁸⁸ CC Cheng and AL DeVries. *The role of antifreeze glycopeptides and peptides in the freezing avoidance of cold-water fish*, pages 1–14. Springer, 1991.
- ²⁸⁹ Christopher P Garnham, Aditya Natarajan, Adam J Middleton, Mike J Kuiper, Ido Braslavsky, and Peter L Davies. Compound ice-binding site of an antifreeze protein revealed by mutagenesis and fluorescent tagging. *Biochemistry*, 49(42):9063–9071, 2010.
- ²⁹⁰ Natalya Pertaya, Christopher B Marshall, Carlos L DiPrinzio, Larry Wilen, Erik S Thomson, JS Wettlaufer, Peter L Davies, and Ido Braslavsky. Fluorescence microscopy evidence for quasi-permanent attachment of antifreeze proteins to ice surfaces. *Biophysical journal*, 92(10):3663–3673, 2007.
- ²⁹¹ Kazunori Miura, Satoru Ohgiya, Tamotsu Hoshino, Nobuaki Nemoto, Tetsuya Sue-take, Ai Miura, Leo Spyropoulos, Hidemasa Kondo, and Sakae Tsuda. Nmr analysis of type iii antifreeze protein intramolecular dimer. *Journal of biological chemistry*, 276(2):1304–1310, 2001.

- ²⁹² CA Knight and AL DeVries. Ice growth in supercooled solutions of a biological antifreeze, afgp 15: An explanation in terms of adsorption rate for the concentration dependence of the freezing point. *Physical Chemistry Chemical Physics*, 11(27):5749–5761, 2009.
- ²⁹³ Michael J Kuiper, Craig J Morton, Sneha E Abraham, and Angus Gray-Weale. The biological function of an insect antifreeze protein simulated by molecular dynamics. *Elife*, 4:e05142, 2015.
- ²⁹⁴ Yeliz Celik, Ran Drori, Natalya Pertaya-Braun, Aysun Altan, Tyler Barton, Maya Bar-Dolev, Alex Groisman, Peter L Davies, and Ido Braslavsky. Microfluidic experiments reveal that antifreeze proteins bound to ice crystals suffice to prevent their growth. *Proceedings of the National Academy of Sciences*, 110(4):1309–1314, 2013.
- ²⁹⁵ Ran Drori, Peter L. Davies, and Ido Braslavsky. When are antifreeze proteins in solution essential for ice growth inhibition? *Langmuir*, 31(21):5805–5811, 2015.
- ²⁹⁶ Konrad Meister, Arthur L DeVries, Huib J Bakker, and Ran Drori. Antifreeze glycoproteins bind irreversibly to ice. *Journal of the American Chemical Society*, 2018.
- ²⁹⁷ Salvador Zepeda, Etsuro Yokoyama, Yukihiko Uda, Chihiro Katagiri, and Yoshinori Furukawa. In situ observation of antifreeze glycoprotein kinetics at the ice interface reveals a two-step reversible adsorption mechanism. *Crystal Growth and Design*, 8(10):3666–3672, 2008.
- ²⁹⁸ Yong Ba, Jeff Wongsakhaluang, and Jiabo Li. Reversible binding of the hplc6 isoform of type i antifreeze proteins to ice surfaces and the antifreeze mechanism studied by multiple quantum filteringspin exchange nmr experiment. *Journal of the American Chemical Society*, 125(2):330–331, 2003.
- ²⁹⁹ TS Burcham, DT Osuga, Y Yeh, and RE Feeney. A kinetic description of antifreeze glycoprotein activity. *Journal of Biological Chemistry*, 261(14):6390–6397, 1986.
- ³⁰⁰ Mark R Anklaam and Abbas Firoozabadi. An interfacial energy mechanism for the complete inhibition of crystal growth by inhibitor adsorption. *The Journal of chemical physics*, 123(14):144708, 2005.
- ³⁰¹ Denver G Hall and Alexander Lips. Phenomenology and mechanism of antifreeze peptide activity. *Langmuir*, 15(6):1905–1912, 1999.
- ³⁰² Junjie Liu and Qianzhong Li. Theoretical model of antifreeze proteinice adsorption: Binding of large ligands to a two-dimensional homogeneous lattice. *Chemical physics letters*, 422(1-3):67–71, 2006.
- ³⁰³ PW Wilson. Explaining thermal hysteresis by the kelvin effect. *Cryoletters*, 14:31–36, 1993.
- ³⁰⁴ Erlend Kristiansen and Karl Erik Zachariassen. The mechanism by which fish antifreeze proteins cause thermal hysteresis. *Cryobiology*, 51(3):262–280, 2005.
- ³⁰⁵ Charles A Knight. Structural biology: adding to the antifreeze agenda. *Nature*, 406(6793):249, 2000.
- ³⁰⁶ Gerald W. Sears. Effect of poisons on crystal growth. *The Journal of Chemical Physics*, 29(5):1045–1048, 1958.

- 307 SS Brenner, RH Doremus, BW Roberts, and D Turnbull. Growth and perfection of crystals. In *Cooperstown Conference, New York*, page 157.
- 308 Noriaki Kubota. Effects of cooling rate, annealing time and biological antifreeze concentration on thermal hysteresis reading. *Cryobiology*, 63(3):198–209, 2011.
- 309 S Zepeda, H Nakaya, Y Uda, E Yokoyana, and Y Furukawa. Diffusion, incorporation, and segregation of antifreeze glycoproteins at the ice/solution interface surfaces. In *Physics and Chemistry of Ice*, page 669.
- 310 Andrew N Lane, Lisa M Hays, Nelly Tsvetkova, Robert E Feeney, Lois M Crowe, and John H Crowe. Comparison of the solution conformation and dynamics of antifreeze glycoproteins from antarctic fish. *Biophysical journal*, 78(6):3195–3207, 2000.
- 311 Aleksandr Noy, Salvador Zepeda, Christine A Orme, Yin Yeh, and James J De Yoreo. Entropic barriers in nanoscale adhesion studied by variable temperature chemical force microscopy. *Journal of the American Chemical Society*, 125(5):1356–1362, 2003.
- 312 Yukihiro Uda, Salvador Zepeda, Fumitoshi Kaneko, Yoshiki Matsuura, and Yoshinori Furukawa. Adsorption-induced conformational changes of antifreeze glycoproteins at the ice/water interface. *The Journal of Physical Chemistry B*, 111(51):14355–14361, 2007.
- 313 Ning Du, Xiang Y Liu, and Choy L Hew. Aggregation of antifreeze protein and impact on antifreeze activity. *The Journal of Physical Chemistry B*, 110(41):20562–20567, 2006.
- 314 Xiang Yang Liu and Ning Du. Zero-sized effect of nano-particles and inverse homogeneous nucleation: principles of freezing and antifreeze. *Journal of Biological Chemistry*, 2003.
- 315 Choy L Hew and Daniel SC Yang. Protein interaction with ice. *European Journal of Biochemistry*, 203(12):33–42, 1992.
- 316 David R Nutt and Jeremy C Smith. Dual function of the hydration layer around an antifreeze protein revealed by atomistic molecular dynamics simulations. *Journal of the American Chemical Society*, 130(39):13066–13073, 2008.
- 317 Eli Ochshorn and Will Cantrell. Ice nucleation on hydrophilic silicon. *The Journal of chemical physics*, 128(13):134701, 2008.
- 318 Kim A Sharp. The remarkable hydration of the antifreeze protein maxi: A computational study. *The Journal of Chemical Physics*, 141(22), 2014.
- 319 Christopher P. Garnham, Robert L. Campbell, and Peter L. Davies. Anchored clathrate waters bind antifreeze proteins to ice. *Proceedings of the National Academy of Sciences*, 108(18):7363–7367, 2011.
- 320 A. B. Siemer, K. Huang, and A. E. McDermott. Protein-ice interaction of an antifreeze protein observed with solid-state nmr. *Proc. Natl. Acad. Sci. U. S. A.*, 107(41):17580–17585, 2010.
- 321 Ansgar B Siemer, Kuo-Ying Huang, and Ann E McDermott. Protein linewidth and solvent dynamics in frozen solution nmr. *PLoS One*, 7(10):e47242, 2012.

- ³²² Ansgar B. Siemer and Ann E. McDermott. Solid-state nmr on a type iii antifreeze protein in the presence of ice. *Journal of the American Chemical Society*, 130(51):17394–17399, 2008.
- ³²³ Yougang Mao and Yong Ba. Insight into the binding of antifreeze proteins to ice surfaces via ¹³c spin lattice relaxation solid-state nmr. *Biophysical journal*, 91(3):1059–1068, 2006.
- ³²⁴ Takaaki Inada and Shu-Shen Lu. Thermal hysteresis caused by non-equilibrium antifreeze activity of poly(vinyl alcohol). *Chemical Physics Letters*, 394(4):361–365, 2004.
- ³²⁵ Robert C Deller, Jeffrey E Pessin, Manu Vatish, Daniel A Mitchell, and Matthew I Gibson. Enhanced non-vitreous cryopreservation of immortalized and primary cells by ice-growth inhibiting polymers. *Biomaterials science*, 4(7):1079–1084, 2016.
- ³²⁶ Daniel E Mitchell, Joseph R Lovett, Steven P Armes, and Matthew I Gibson. Combining biomimetic block copolymer worms with an iceinhibiting polymer for the solvent-free cryopreservation of red blood cells. *Angewandte Chemie International Edition*, 55(8):2801–2804, 2016.
- ³²⁷ Robert C. Deller, Manu Vatish, Daniel A. Mitchell, and Matthew I. Gibson. Synthetic polymers enable non-vitreous cellular cryopreservation by reducing ice crystal growth during thawing. *Nature Communications*, 5:3244, 2014.
- ³²⁸ Takaaki Inada and Shu-Shen Lu. Inhibition of recrystallization of ice grains by adsorption of poly(vinyl alcohol) onto ice surfaces. *Crystal Growth and Design*, 3(5):747–752, 2003.
- ³²⁹ Carsten Budke, Axel Dreyer, Jasmin Jaeger, Kerstin Gimpel, Thomas Berkemeier, Anna S. Bonin, Lilly Nagel, Carolin Plattner, Arthur L. DeVries, Norbert Sewald, and Thomas Koop. Quantitative efficacy classification of ice recrystallization inhibition agents. *Crystal Growth and Design*, 14(9):4285–4294, 2014.
- ³³⁰ Nicholas S Vail, Christopher Stubbs, Caroline I Biggs, and Matthew I Gibson. Ultralow dispersity poly (vinyl alcohol) reveals significant dispersity effects on ice recrystallization inhibition activity. *ACS macro letters*, 6(9):1001–1004, 2017.
- ³³¹ Robert G Solomon, Rudi Appels, and purification. Stable, high-level expression of a type i antifreeze protein in *Escherichia coli*. *Protein expression*, 16(1):53–62, 1999.
- ³³² Robert C. Deller, Thomas Congdon, Mohammed A. Sahid, Michael Morgan, Manu Vatish, Daniel A. Mitchell, Rebecca Notman, and Matthew I. Gibson. Ice recrystallization inhibition by polyols: comparison of molecular and macromolecular inhibitors and role of hydrophobic units. *Biomaterials Science*, 1(5):478–485, 2013.
- ³³³ Chantelle J. Capicciotti, Mathieu Leclere, Frederic A. Perras, David L. Bryce, Hilary Paulin, James Harden, Yun Liu, and Robert N. Ben. Potent inhibition of ice recrystallization by low molecular weight carbohydrate-based surfactants and hydrogelators. *Chemical Science*, 3(5):1408–1416, 2012.
- ³³⁴ Guoying Bai, Dong Gao, and Jianjun Wang. Control of ice growth and recrystallization by sulphur-doped oxidized quasi-carbon nitride quantum dots. *Carbon*, 124:415–421, 2017.

- 335 Caroline I Biggs, Christopher Packer, Steven Hindmarsh, Marc Walker, Neil R Wilson, Jonathan P Rourke, and Matthew I Gibson. Impact of sequential surface-modification of graphene oxide on ice nucleation. *Physical Chemistry Chemical Physics*, 19(33):21929–21932, 2017.
- 336 Zhiyuan He, Kai Liu, and Jianjun Wang. Bioinspired materials for controlling ice nucleation, growth, and recrystallization. *Accounts of Chemical Research*, 51(5):1082–1091, 2018.
- 337 Thomas F Whale, Martin Rosillo-Lopez, Benjamin J Murray, and Christoph G Salzmann. Ice nucleation properties of oxidized carbon nanomaterials. *The journal of physical chemistry letters*, 6(15):3012–3016, 2015.
- 338 Kyle A. Soltys, Arun K. Batta, and Baburao Koneru. Successful nonfreezing, subzero preservation of rat liver with 2,3-butanediol and type i antifreeze protein. *Journal of Surgical Research*, 96(1):30–34, 2001.
- 339 Folkert O Belzer and James H Southard. Principles of solid-organ preservation by cold storage. *Transplantation*, 45(4):673–676, 1988.
- 340 Kelvin GM Brockbank, Lia H Campbell, Elizabeth D Greene, Matthew CG Brockbank, and John G Duman. Lessons from nature for preservation of mammalian cells, tissues, and organs. *In Vitro Cellular and Developmental Biology-Animal*, 47(3):210–217, 2011.
- 341 Jennie G Briard, Jessica S Poisson, Tracey R Turner, Chantelle J Capicciotti, Jason P Acker, and Robert N Ben. Small molecule ice recrystallization inhibitors mitigate red blood cell lysis during freezing, transient warming and thawing. *Scientific reports*, 6:23619, 2016.
- 342 Martin Heisig, Sarah Mattessich, Alison Rembisz, Ali Acar, Martin Shapiro, Carmen J Booth, Girish Neelakanta, and Erol Fikrig. Frostbite protection in mice expressing an antifreeze glycoprotein. *PloS one*, 10(2):e0116562, 2015.
- 343 Joseph Bakhach. The cryopreservation of composite tissues: principles and recent advancement on cryopreservation of different type of tissues. *Organogenesis*, 5(3):119–126, 2009.
- 344 Girish Neelakanta, Andrew M Hudson, Hameeda Sultana, Lynn Cooley, and Erol Fikrig. Expression of ixodes scapularis antifreeze glycoprotein enhances cold tolerance in drosophila melanogaster. *PLoS One*, 7(3):e33447, 2012.
- 345 AV Makarevich, E Kuboviov, M Popelkov, D Fabian, iko, J Pivko, and P Chrenek. Several aspects of animal embryo cryopreservation: anti-freeze protein (afp) as a potential cryoprotectant. *Zygote*, 18(2):145–153, 2010.
- 346 Atsushi Ideta, Yoshito Aoyagi, Kanami Tsuchiya, Yuuki Nakamura, Kou Hayama, Atsushi Shirasawa, Kenichiro Sakaguchi, Naomi Tominaga, Yoshiyuki Nishimiya, and Sakae Tsuda. Prolonging hypothermic storage (4 c) of bovine embryos with fish antifreeze protein. *Journal of Reproduction and Development*, 61(1):1–6, 2015.
- 347 Gabriel Amir, Boris Rubinsky, Liana Horowitz, Liron Miller, Jonathan Leor, Yigal Kassif, David Mishaly, Aram K Smolinsky, and Jacob Lavee. Prolonged 24-hour sub-zero preservation of heterotopically transplanted rat hearts using antifreeze proteins derived from arctic fish. *The Annals of thoracic surgery*, 77(5):1648–1655, 2004.

- 348 Haydar Bagis, Digdem Aktoprakligil, Hande Odaman Mercan, Nevzat Yurdusev, Gazi Turgut, Sakir Sekmen, Sezen Arat, and Seyfettin Cetin. Stable transmission and transcription of newfoundland ocean pout type iii fish antifreeze protein (afp) gene in transgenic mice and hypothermic storage of transgenic ovary and testis. *Molecular Reproduction and Development: Incorporating Gamete Research*, 73(11):1404–1411, 2006.
- 349 Jennifer L Chaytor, Jacqueline M Tokarew, Luke K Wu, Mathieu Leclre, Roger Y Tam, Chantelle J Capicciotti, Louise Guolla, Elisabeth von Moos, C Scott Findlay, and David S Allan. Inhibiting ice recrystallization and optimization of cell viability after cryopreservation. *Glycobiology*, 22(1):123–133, 2011.
- 350 Jan Huebinger, Hong-Mei Han, Oliver Hofnagel, Ingrid R Vetter, Philippe IH Bastiaens, and Markus Grabenbauer. Direct measurement of water states in cryopreserved cells reveals tolerance toward ice crystallization. *Biophysical journal*, 110(4):840–849, 2016.
- 351 Chantelle J Capicciotti, Malay Doshi, and Robert N Ben. *Ice recrystallization inhibitors: from biological antifreezes to small molecules*. InTech, 2013.
- 352 Dirk K Hinch, Arthur L De Vries, and Jrgen M Schmitt. Cryotoxicity of antifreeze proteins and glycoproteins to spinach thylakoid membranescomparison with cryotoxic sugar acids. *Biochimica et Biophysica Acta (BBA)-Biomembranes*, 1146(2):258–264, 1993.
- 353 Robert E. Feeney and Yin Yeh. Antifreeze proteins: Current status and possible food uses. *Trends in Food Science and Technology*, 9(3):102–106, 1998.
- 354 Majid Hassas-Roudsari and H. Douglas Goff. Ice structuring proteins from plants: Mechanism of action and food application. *Food Research International*, 46(1):425–436, 2012.
- 355 James F Crilly, Andrew B Russell, Andrew R Cox, and Deryck J Cebula. Designing multiscale structures for desired properties of ice cream. *Industrial and Engineering Chemistry Research*, 47(17):6362–6367, 2008.
- 356 A Regand and HD Goff. Ice recrystallization inhibition in ice cream as affected by ice structuring proteins from winter wheat grass. *Journal of dairy science*, 89(1):49–57, 2006.
- 357 Chuan-Mei Yeh, Bi-Yu Kao, and Hsuan-Jung Peng. Production of a recombinant type 1 antifreeze protein analogue by l. lactis and its applications on frozen meat and frozen dough. *Journal of agricultural and food chemistry*, 57(14):6216–6223, 2009.
- 358 Steven R Payne and Owen A Young. Effects of pre-slaughter administration of antifreeze proteins on frozen meat quality. *Meat Science*, 41(2):147–155, 1995.
- 359 N Cochet and P Widehem. Ice crystallization by pseudomonas syringae. *Applied microbiology and biotechnology*, 54(2):153–161, 2000.
- 360 Waraporn Boonsupthip and TungChing Lee. Application of antifreeze protein for food preservation: Effect of type iii antifreeze protein for preservation of gelforming of frozen and chilled actomyosin. *Journal of Food Science*, 68(5):1804–1809, 2003.
- 361 Ravi Gupta and Renu Deswal. Antifreeze proteins enable plants to survive in freezing conditions. *Journal of biosciences*, 39(5):931–944, 2014.

- ³⁶² John G Duman and Michael J Wisniewski. The use of antifreeze proteins for frost protection in sensitive crop plants. *Environmental and Experimental Botany*, 106:60–69, 2014.
- ³⁶³ Harjeet K Khanna and Grant E Daggard. Targeted expression of redesigned and codon optimised synthetic gene leads to recrystallisation inhibition and reduced electrolyte leakage in spring wheat at sub-zero temperatures. *Plant cell reports*, 25(12):1336–1346, 2006.
- ³⁶⁴ Christine Malmos Perfeldt, Pei Cheng Chua, Nagu Daraboina, Dennis Friis, Erlend Kristiansen, Hans Ramlv, John M Woodley, Malcolm A Kelland, and Nicolas von Solms. Inhibition of gas hydrate nucleation and growth: efficacy of an antifreeze protein from the longhorn beetle rhagium mordax. *Energy and Fuels*, 28(6):3666–3672, 2014.
- ³⁶⁵ Devin Tonelli, Chantelle J Capicciotti, Malay Doshi, and Robert N Ben. Inhibiting gas hydrate formation using small molecule ice recrystallization inhibitors. *RSC Advances*, 5(28):21728–21732, 2015.
- ³⁶⁶ Manabu Fukushima, Sakae Tsuda, and Yuichi Yoshizawa. Fabrication of highly porous alumina prepared by gelation freezing route with antifreeze protein. *Journal of the American Ceramic Society*, 96(4):1029–1031, 2013.
- ³⁶⁷ SG Weissberg, Robert Simha, and S Rothman. Viscosity of dilute and moderately concentrated polymer solutions. *Journal of Research of the National Bureau of Standards*, 47(3):2257–2274, 1951.
- ³⁶⁸ MVS Rao. Viscosity of dilute to moderately concentrated polymer solutions. *Polymer*, 34(3):592–596, 1993.
- ³⁶⁹ RF Fedors. An equation suitable for describing the viscosity of dilute to moderately concentrated polymer solutions. *Polymer*, 20(2):225–228, 1979.
- ³⁷⁰ Graeme Moad, Ezio Rizzardo, and San H Thang. Radical additionfragmentation chemistry in polymer synthesis. *Polymer*, 49(5):1079–1131, 2008.